REPORT DOCUMENTATION PAGE	Form Approved OMB NO. 0704-0188

1. REPORT DATE (DD-MM-YYYY)	2. REPORT TYPE	3. DATES COVERED (From - To)
21-12-2015	Final Report	20-Aug-2014 - 19-Aug-2015

4. TITLE AND SUBTITLE	5a. CONTRACT NUMBER
Final Report: U.S. Workshop on the Physics and Chemistry of II-VI Materials (a.k.a. II-VI Workshop) - ARO Research Area 9: Materials Science - Physical Properties of Materials	W911NF-14-1-0544
	5b. GRANT NUMBER
	5c. PROGRAM ELEMENT NUMBER
	611102

6. AUTHORS	5d. PROJECT NUMBER
Sivalingam Sivananthan	
	5e. TASK NUMBER
	5f. WORK UNIT NUMBER

7. PERFORMING ORGANIZATION NAMES AND ADDRESSES	8. PERFORMING ORGANIZATION REPORT NUMBER
University of Illinois - Chicago MB 502, M/C 551 809 S. Marshfield Avenue Chicago, IL 60612 -4305	

9. SPONSORING/MONITORING AGENCY NAME(S) AND ADDRESS (ES)	10. SPONSOR/MONITOR'S ACRONYM(S) ARO
U.S. Army Research Office P.O. Box 12211 Research Triangle Park, NC 27709-2211	11. SPONSOR/MONITOR'S REPORT NUMBER(S) 66241-MS-CF.1

12. DISTRIBUTION AVAILIBILITY STATEMENT

Approved for Public Release; Distribution Unlimited

13. SUPPLEMENTARY NOTES
The views, opinions and/or findings contained in this report are those of the author(s) and should not contrued as an official Department of the Army position, policy or decision, unless so designated by other documentation.

14. ABSTRACT
The 2014 II?VI Workshop was successfully held from October 20 ? October 23, 2014 at the Sheraton Baltimore Hotel in Baltimore, MD. The Workshop was attended by a total of 109 scientists from Academia, Government Labs, and Industry both nationally and internationally. There was a total of 52 presentations. Students contributed 32 of the total number of presentations. The full details of what was presented can be found in the extended abstract book(See attached).
The $10K funds provided under Army Research Office under Grant W911NF2142120544 was used to support

15. SUBJECT TERMS
US Workshop II-VI Materials Conference Proceedings - Final Report

16. SECURITY CLASSIFICATION OF:			17. LIMITATION OF ABSTRACT	15. NUMBER OF PAGES	19a. NAME OF RESPONSIBLE PERSON
a. REPORT	b. ABSTRACT	c. THIS PAGE	UU		Sivalingam Sivananthan
UU	UU	UU			19b. TELEPHONE NUMBER 312-996-5092

Standard Form 298 (Rev 8/98)
Prescribed by ANSI Std. Z39.18

Report Title

Final Report: U.S. Workshop on the Physics and Chemistry of II-VI Materials (a.k.a. II-VI Workshop) - ARO
Research Area 9: Materials Science - Physical Properties of Materials

ABSTRACT

The 2014 II?VI Workshop was successfully held from October 20 ? October 23, 2014 at the Sheraton Baltimore Hotel in Baltimore, MD. The Workshop was attended by a total of 109 scientists from Academia, Government Labs, and Industry both nationally and internationally. There was a total of 52 presentations. Students contributed 32 of the total number of presentations. The full details of what was presented can be found in the extended abstract book(See attached).

The $10K funds provided under Army Research Office under Grant W911NF?14?1?0544 was used to support University student travel totaling $7,500 and to cover the advance program, abstract book, and call for papers, which were given to each attendee of the Workshop, totaling $2,500.

Enter List of papers submitted or published that acknowledge ARO support from the start of the project to the date of this printing. List the papers, including journal references, in the following categories:

(a) Papers published in peer-reviewed journals (N/A for none)

<u>Received</u>   <u>Paper</u>

TOTAL:

Number of Papers published in peer-reviewed journals:

(b) Papers published in non-peer-reviewed journals (N/A for none)

<u>Received</u>   <u>Paper</u>

TOTAL:

Number of Papers published in non peer-reviewed journals:

(c) Presentations

Number of Presentations: 52.00

Non Peer-Reviewed Conference Proceeding publications (other than abstracts):

<u>Received</u>   <u>Paper</u>

TOTAL:

Number of Non Peer-Reviewed Conference Proceeding publications (other than abstracts):

Peer-Reviewed Conference Proceeding publications (other than abstracts):

<u>Received</u>   <u>Paper</u>

TOTAL:

Number of Peer-Reviewed Conference Proceeding publications (other than abstracts):

(d) Manuscripts

<u>Received</u>   <u>Paper</u>

TOTAL:

Number of Manuscripts:

Books

Received   Book

   TOTAL:

Received   Book Chapter

   TOTAL:

Patents Submitted

Patents Awarded

Awards

Graduate Students

NAME	PERCENT_SUPPORTED
FTE Equivalent:	
Total Number:	

Names of Post Doctorates

NAME	PERCENT_SUPPORTED
FTE Equivalent:	
Total Number:	

Names of Faculty Supported

NAME	PERCENT_SUPPORTED

FTE Equivalent:
Total Number:

Names of Under Graduate students supported

NAME	PERCENT_SUPPORTED

FTE Equivalent:
Total Number:

Student Metrics
This section only applies to graduating undergraduates supported by this agreement in this reporting period

The number of undergraduates funded by this agreement who graduated during this period: 0.00

The number of undergraduates funded by this agreement who graduated during this period with a degree in science, mathematics, engineering, or technology fields:...... 0.00

The number of undergraduates funded by your agreement who graduated during this period and will continue to pursue a graduate or Ph.D. degree in science, mathematics, engineering, or technology fields:...... 0.00

Number of graduating undergraduates who achieved a 3.5 GPA to 4.0 (4.0 max scale):...... 0.00

Number of graduating undergraduates funded by a DoD funded Center of Excellence grant for Education, Research and Engineering:...... 0.00

The number of undergraduates funded by your agreement who graduated during this period and intend to work for the Department of Defense 0.00

The number of undergraduates funded by your agreement who graduated during this period and will receive scholarships or fellowships for further studies in science, mathematics, engineering or technology fields:...... 0.00

Names of Personnel receiving masters degrees

NAME

Total Number:

Names of personnel receiving PHDs

NAME

Total Number:

Names of other research staff

NAME	PERCENT_SUPPORTED

FTE Equivalent:
Total Number:

Sub Contractors (DD882)

1 a. Palisades Convention Management   1 b. 411 Lafayette Street

                                                                            New York   NY   100037032

Sub Contractor Numbers (c):
Patent Clause Number (d-1):
Patent Date (d-2):
Work Description (e): Facilitated the II-VI Materials Workshop.
Sub Contract Award Date (f-1): 8/20/14 12:00AM
Sub Contract Est Completion Date(f-2): 8/19/15 12:00AM

1 a. Palisades Convention Management   1 b. 411 Lafayette Street

                                                                            New York   NY   100037032

Sub Contractor Numbers (c):
Patent Clause Number (d-1):
Patent Date (d-2):
Work Description (e): Facilitated the II-VI Materials Workshop.
Sub Contract Award Date (f-1): 8/20/14 12:00AM
Sub Contract Est Completion Date(f-2): 8/19/15 12:00AM

Inventions (DD882)

Scientific Progress

Technology Transfer

FINAL PROCEDINGS FOR THE
2014 U.S. WORKSHOP ON THE PHYSICS AND CHEMISTRY OF II-VI MATERIALS

OCTOBER 20 - OCTOBER 23, 2014

Baltimore, MD

The 2014 II-VI Workshop was successfully held from October 20 - October 23, 2014 at the Sheraton Baltimore Hotel in Baltimore, MD. The Workshop was attended by a total of 109 scientists from Academia, Government Labs, and Industry both nationally and internationally. There was a total of 52 presentations. Students contributed 32 of the total number of presentations. The full details of what was presented can be found in the extended abstract book (See attached).

TABLE OF CONTENTS

Session 3: MMA

Session 4: Solar Cells I

Poster Session

Session 5: Materials I

Session 6:   Devices II

Session 7:   Materials II

Session 8: Devices III and Late-News Papers

Session 9: nBn / SLS

Session 10: Solar Cells II

Session 11: Devices IV

Student Papers

Late-News Student Papers

8.5: *Late-News Paper:* **Progress towards II-VI Based Broadband Quantum Cascade Detectors**
A. P. Ravikumar, C. Gmachl, *Princeton University, Princeton, NJ, USA*
J. De Jesus, T. A. Garcia, M. Tamargo, *Graduate Center and City College of New York, NY, USA*

Student Poster Papers

P.2: **Characterization of CdTe Growth on GaAs by Using Different Etching Techniques**
E. Bilgilisoy, M. Günnar, S. Özden, M. Polat, Y. Selamet, *Izmir Institute of Technology, Izmir, Turkey*

P.4: **Minimization of the Surface Leakage Currents in High-Resistivity (Cd,Mn)Te Crystal Plates**
A. Markowska, *Warsaw University of Technology, Warsaw, Poland and Institute of Physics, Polish Academy of Sciences, Warsaw, Poland*
M. Witkowska-Baran, D. Kochanowska, A. Mycielski, *Institute of Physics, Polish Academy of Sciences, Warsaw, Poland*

P.5 **Floating-Gate Nonvolatile Memory Structure Using Cladded Germanium Quantum-Dot Channel (QDC)**
J. Kondo, M. Lingalugari, P-Y. Chan, F. Jain, *University of Connecticut, Storrs, CT, USA*
E. Heller, *Synopsis, Inc., Ossining, NY, USA*

High Performance MWIR HgCdTe on Si Substrate Focal Plane Array Development

R. Bommena[1], S. Ketharanathan[1], P.S. Wijewarnasuriya[2], N.K. Dhar[3],
R. Kodama[1], J. Zhao[1], C. Buurma[1], J.D. Bergeson[1], F. Aqariden[1], S. Velicu[1]

[1]*EPIR Technologies, Inc., Bolingbrook, Illinois*
[2]*Army Research Laboratory, Adelphi, Maryland*
[3]*DARPA MTO, Arlington, Virginia*

Abstract

We report the develop ment of low noise equivale nt difference t emperature (NEDT), high operabilit y midwave infrared (MWIR) focal plane arrays (FPAs) fabricated from molecular beam epitaxial (MBE)-grown HgCdTe on Si-based substrates. High quality n-type MWIR HgCdTe (cutoff wavelength ~4.90 µm at 77 K, carrier concentration $1.0\ 5x10^{15}$ cm^{-3}) layers were grown on CdTe/Si substrates by MBE. High degrees of uniformity in composition and thickness over 3-inch areas (Figure 1) were demonstrated, and low surface defect densities (voids ~$5x10^{\ 2}$ cm^{-2}, micro-defects ~ $5x10^{\ 3}$ cm^{-2}) and etch pit densit y (~$3.5x10^6$ cm^{-2}) were measured. This m aterial was used to fabricate 320 x 256 format, 30 µm pitch FPAs with a planar device archit ecture[1] using arsenic implantation to achieve p-type doping. Radiometric and noise characterization were perform ed. A low NEDT of 13.8 m K at 100 K for a 1 ms integration time with f#2 opt ics was measured. The dark current operability was 99.85% (Figure 2) and the noise operability was 99.4% (Figure 3), with a mean dark current of $4.97x10^{-10}$ A/pixel and a mean dark current noise of $8.14x10^{-13}$ A/pixel at 120 K. High qualit y thermal imaging was obtained fro m the FPA (Figure 4). Temperature-dependent NEDT characterization is underway and will be reported.

Presenter: Ramana Bommena, rbommena@epir.com, 630-771-0203 (phone), 630-771-0204 (fax)

EPIR Technologies, Inc., 590 Territorial Drive, Bolingbrook, IL 60440

---

[1] R. Bo mmena, J. Berg eson, P.S. Wijewarnasuriya, N.K. Dhar, R. Ko dama, S. Velicu and F. Aqaride n, "High Performance SWIR HgCdTe FPA development on silicon substrates", SPIE DSS Baltimore (2014)
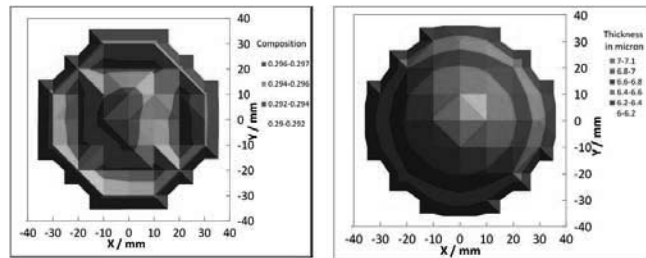
Figure 1: (left) FTIR map of Cd composition of MWIR HgCdTe grown by MBE on a 3-inch CdTe/Si substrate. (right) Thickness map of a MWIR HgCdTe on CdTe/Si sample.
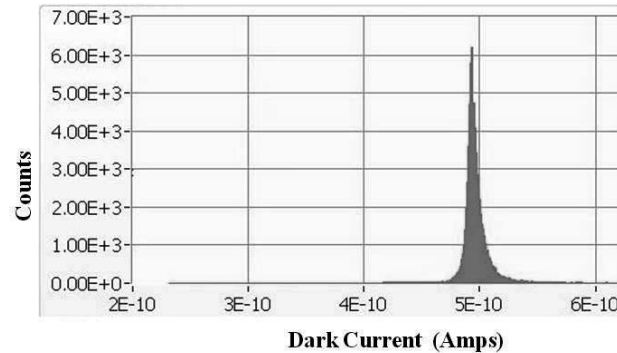
Figure 2: Dark current distribution at 120 K of a 320 x 256 format, 30 µm pitch MWIR FPA fabricated from MBE-grown HgCdTe on CdTe/Si.
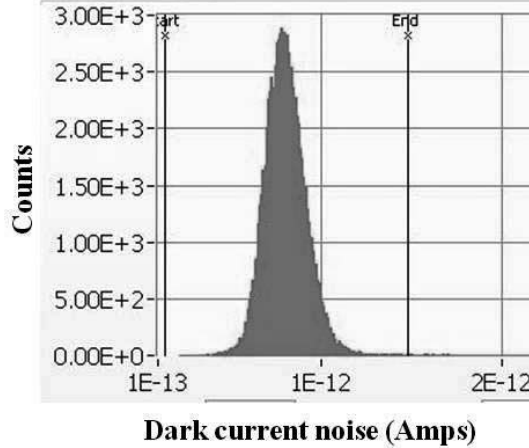
Figure 3: Dark current noise distribution at 120 K of a 320 x 256 format, 30 µm pitch MWIR FPA fabricated from MBE-grown HgCdTe on CdTe/Si.
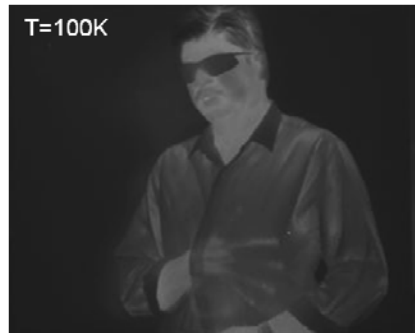
Figure 4: Thermal image taken with a MWIR HgCdTe on CdTe/Si FPA at a 100 K operating temperature.

Latest developments in long and very long wavelength infrared detection with p-on-n HgCdTe

N. Baier[a*], C. Cervera[a], O. Gravrand[a], L. Mollard[a], G. Destefanis[a], G. Bourgeois[a], J.P. Zanatta[a], O. Boulade[b], V. Moreau[b]

[a]*CEA-LETI, MINATEC, F38054 Grenoble – France;*
[b]*CEA-IRFU, Orme des Merisiers, 91191 Gif-sur-Yvette – France;*
nicolas.baier@cea.fr, phone: +33 (0)4 38 78 93 21, fax: +33 (0)4 38 78 51 67

This paper presents recent developments done at CEA-LETI Infrared Laboratory on processing and characterization of p-on-n HgCdTe planar infrared focal plane arrays (FPAs) in LWIR and VLWIR spectral bands. These FPAs have been grown using liquid phase epitaxy (LPE) on a lattice matched CdZnTe substrate and processed with p-on-n technology developed since 2005 in the scope of the DEFIR joint laboratory between CEA-LETI and SOFRADIR[1][2]. This technology presents lower dark current and lower serial resistance in comparison with n-on-p architecture and is well adapted for low flux detection or high operating temperature. This architecture has been evaluated for space applications in LWIR and VLWIR spectral bands with cutoff wavelengths from 10µm up to 15µm at 78K[3]. Innovations have been introduced to the technological process to lower dark current at low temperature. This has been performed by decreasing the transition temperature from diffusion limited to generation-recombination limited dark current. Other developments tend to improve the modulation transfer function (MTF). Large diffusion length which characterizes low doped n-type HgCdTe affect MTF, as optical cross-talk between pixels may be important. An evolution of the process has been brought to lower this cross-talk to improve MTF. Electro-optical characterizations on p-on-n photodiodes have been performed on test arrays and on half-VGA format FPAs with 25µm and 30µm pixel pitches. Results show excellent operabilities in current and responsivity, with low dispersion and noise limited by current shotnoise. Dark current densities follow the heuristic prediction law "Rule07"[4]. Part of these studies has been funded by French National Space Studies Center (CNES).
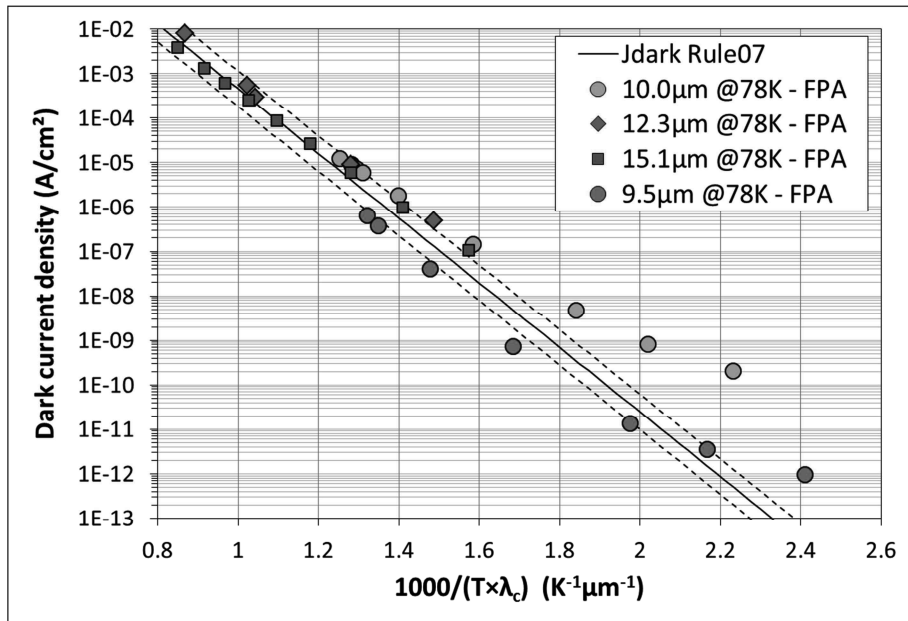
Fig. 1. Dark current density vs. 1000/(T×λ$_c$) measured on various LPE p-on-n HgCdTe FPAs manufactured at CEA-LETI, in comparison with the heuristic "Rule07" law.

[1]   Mollard, L. et al., "HgCdTe FPAs made by Arsenic-ion implantation," Proc. SPIE 6940, 69400F (2008).
[2]   Bubulac, L.O., Lo, D.S., Tennant, W.E., Edwall, D.D., Chen, J.C., Ratusnik, J., Robinson, J.C. and Bostrup, G., "p on n ion-implanted junctions in liquid phase epitaxy HgCdTe layers on CdTe substrates," Appl. Phys. Lett. 50, 1586-1588 (1987).
[3]   Baier, N. et al., "MCT planar p-on-n LW and VLW IRFPAs," Proc. SPIE 8704, 87042P (2013).
[4]   Tennant, W.E., Lee, D., Zandian, M., Piquette, E. and Carmody, M., "MBE HgCdTe Technology: A Very General Solution to IR Detection, Described by "Rule 07", a Very Convenient Heuristic," Journal of Electronic Materials 37, 1406-1410 (2008).

COMPLEX BEHAVIOUR OF TIME RESPONSE OF HgCdTe HOT PHOTODETECTORS

J. Pawluczyk[a], J. Piotrowski[a], W. Pusz[a,b], A. Koźniewski[a], M. Romanis[a], Z. Orman[a], W. Gawron[a,b]

and A. Piotrowski[a]

jpawluczyk@vigo.com.pl

[a] *Vigo System SA, Ożarów Mazowiecki, Poland*

[b] *Institute of Applied Physics, Military University of Technology, Warsaw, Poland*

Abstract: In this paper we report on time response of near room temperature (HOT) fast LWIR (8-14 µm long cutoff wavelength) photodetectors, based on MOVPE-grown HgCdTe. Time constants in 100 ps-100 ns range are observed in the time response of some devices. Mechanisms of the origin of fast and slow components are simulated and discussed.

Keywords: HgCdTe, mid-infrared, LWIR, photo-detectors, room temperature, HOT

1. Introduction

Wideband (~1 GHz or higher) and sensitive detection in 2-14 µm spectral range is demanded for numerous important applications, including various forms of laser spectroscopy, plasma diagnosis and particle physics. Moreover, HOT operation is often preferred due to inconvenience and cost associated with cryogenic cooling. Recent considerations of the fundamental mechanisms suggest that, in principle, near perfect detection can be achieved without cryogenic cooling[1].

2. Mechanisms of fast response

Fast detector response can be achieved in two different ways:[2,3]

- fast recombination of optically generated carriers in material with short lifetime of carriers, e.g. in wideband photoresistors with highly doped narrow bandgap HgCdTe absorber;[4,5]

- fast transport, diffusion or drift, of optically generated carriers to contacts.

The use of material with a short recombination time entails large generation-recombination noise. Therefore, fast carrier collection devices are preferable, e.g. wideband photodiodes.[6,7]

Time response is also affected by parasitic impedances, such as device capacitance and series resistance.[8]

3. HOT detector design

Fig.1 shows schematic cross-sections of 3 types od wideband, highly sensitive LWIR detectors:[2] a modified PIN photodiode, photoconductor and a cascade photovoltaic device – consisting of multiple small volume photovoltaic cells connected in series.

According to a HOT detector concept developed over the last two decades at Vigo,[2] the detectors are equipped with the following elements: immersion microlense – infrared (IR) concentrator, monolithically integrated with detection structure, IR retroreflector so as to further enhance IR absorption and shield against background radiation, IR p-type absorber with bandgap, composition and thickness optimized for the best compromise between efficient use of IR (absorption, collection of optically generated carriers) and low thermal generation, graded bandgap absorber interfaces and wide gap heavily doped contacts to suppress thermal generation and minimize parasitic impedances. The p-type HgCdTe alloy is a material of choice for the fast response devices.[2]

4. Time response

The time response measurements have been carried out using an optical parametric oscillator (OPO) as a source of short (~25 ps) pulses of radiation, tunable in a wide spectral range from UV to 16 µm, and quantum cascade lasers (QCL) producing longer (4-100 ns) pulses. The detectors were coupled to microwave preamplifiers (e.g. Mini-Circuits ERA-3+) integrated with detector bias circuit and matched to detector. 50 ohm preamplifier output was connected to 50 ohm input of a scope. The scopes featured up to 8 GHz bandwidth, 40 GS/s single-shot sample rate and <9 ps rise time.

PIN photodiodes: Reverse bias and cooling improve the time response. The near exponential signal decay was observed of <150 ps time constant, using the reverse biased devices with 8 µm cut-off wavelength, a 4-stage Peltier cooler and the pulse from OPO (fig.2 a). Fig. 2 b shows their response time limited by QCL pulser at excitation by 10 to 50 ns pulses of the focused beam from QCL. However, the significant long time constant (~19 ns) component appeared when moving the focal point of the QCL

beam outside of detector optical sensitive area (fig. 2c). A distinct peak before signal decay, which always occurs, is a characteristic of QCL.

Photoconductors: The near exponential signal decay was obtained in 300-200 K (fig. 3). Time constants ~0.6 ns were obtained for the uncooled devices having 11 µm cut-off wavelength.[4,5] Time constant increases few times with cooling and depends on composition and doping of absorber material.

Cascade photodiodes: At 0 V bias, the near exponential signal decay was obtained of 0.5 ns time constant with the uncooled devices characterized by 12.5 µm cut-off wavelength at 293 K (fig.4 a). Two time constants of 0.16 ns and 2.6 ns were visible in some cooled devices at 190-200 K (fig.4 b). There were no significant changes of the time response with reverse bias.

5. Figures
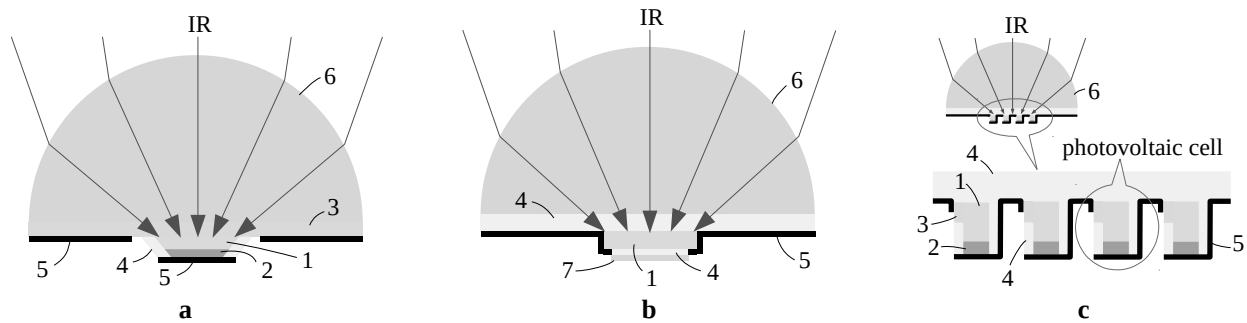
Fig. 1: Schematic cross-sections of wideband HgCdTe HOT immersed devices: a – modified PIN photodiode, b – photoconductor, c – cascade photodiode. References: 1 – IR p-type absorber, 2 – P$^+$ – anode, 3 – N$^+$ – cathode, 4 – passivation, 5 – contact pads, 6 – GaAs immersion microlense, 7 – IR reflector.
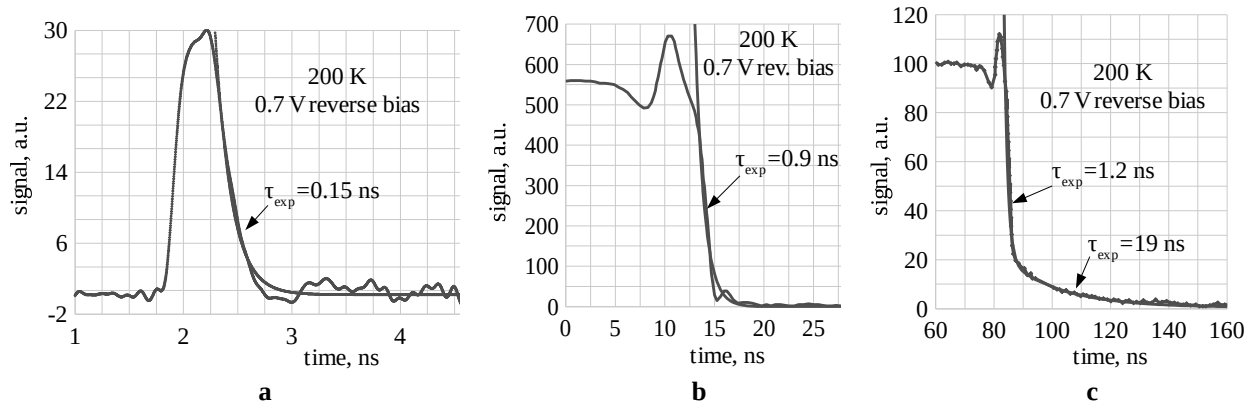
Fig. 2: Time response of reverse biased PIN photodiode: a – in parallel beam from OPO, b – in focal point of QCL beam, c – outside the focal point of the QCL beam.
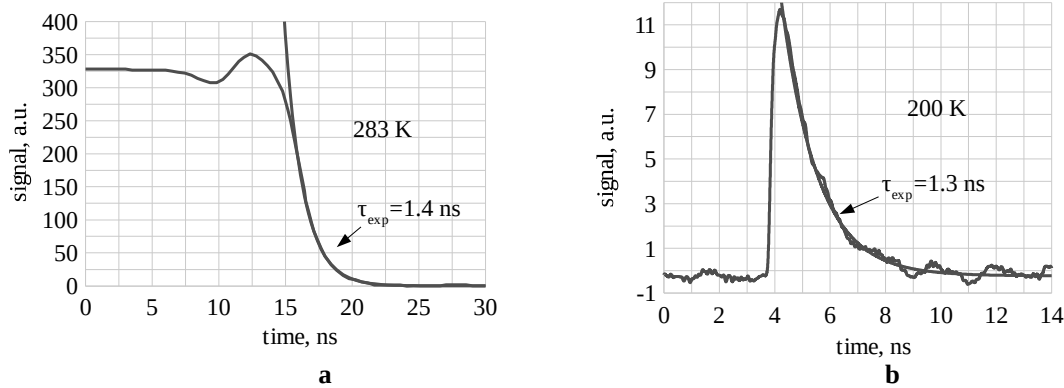
Fig. 3: Photoconductors signal decays: a – in focal point of QCL beam, b – in parallel beam from OPO.
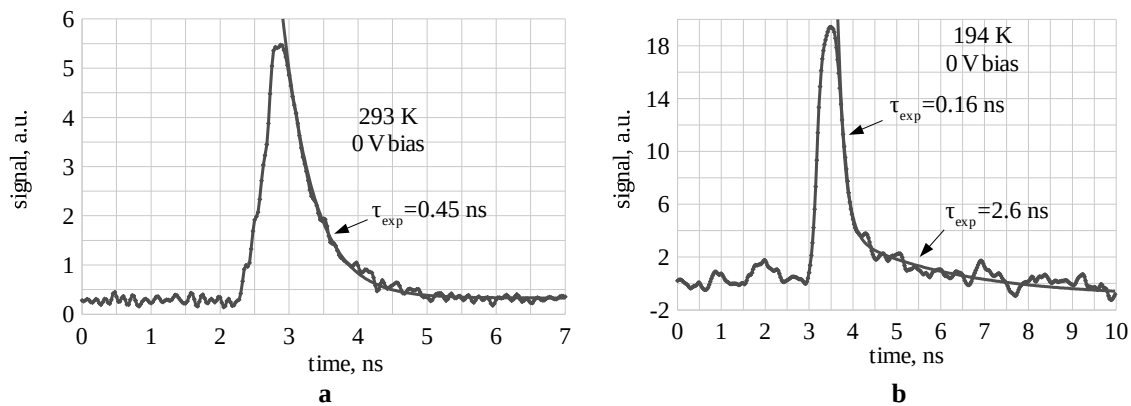
Fig. 4: Time response of cascade photodiode in a parallel beam from OPO.

6. References

1. Kinch M. *Fundamentals of Infrared Detector Materials* (2007), *SPIE Tutorial Texts*, *Opt. Eng.*, **TT76**, Bellingham.
2. Piotrowski J., Rogalski A. High-operating-temperature Infrared Photodetectors (2007), *SPIE*, Bellingham.
3. Piotrowski J., Piotrowski A. *Room Temperature IR Photodetectors* (2011), in *Mercury Cadmium Telluride Growth, Properties and Applications*, edited by Capper P. and Garland J., Wiley.
4. Piotrowski A., Kłos K., Gawron W., Pawluczyk J., Orman Z., Piotrowski J. *Uncooled or Minimally Cooled 10 µm Photodetectors with Subnanosecond Response Time* (2007), *Proc. SPIE*, **6542**, 65421B.
5. Bocci A., Marcelli A., Pace E., Drago A., Piccinini M., Cestelli Guidi M., de Sio A., Sali D., Morini P., Piotrowski J. *Fast Infrared Detectors for Beam Diagnostics with Synchrotron Radiation* (2007), *Nuclear Instr. and Methods Phys. Res. A*, **580** (1, 21), 190 – 193.
6. Stanaszek D., Piotrowski J., Piotrowski A., Gawron W., Orman Z., Paliwoda R., Brudnowski M., Pawluczyk J., Pędzińska M. *Mid and Long Infrared Detection Modules for Picosecond Range Measurements* (2009), *Proc. SPIE*, **7482**, 74820M – 74820M-11.
7. Piotrowski J., Gawron W., Orman Z., Pawluczyk J., Kłos K., Stępień D., Piotrowski A. *Dark currents, responsivity, and response time in graded gap HgCdTe structures* (2010), *SPIE, Infr.Tech. and Appl.* XXXVI, **7660** (1), 766031-8.
8. Hobbs P. *Building Electro-Optical Systems: Making it All Work* (2000), Wiley.

Dislocations as a noise source in LWIR HgCdTe photodiodes

Krzysztof Jóźwikowski[a], Alina Jóźwikowska[b], Andrzej Martyniuk[a]

kjozwikowski@wat.edu.pl

a) Institute of Applied Physics, Military Univ. of Technology, 2 Kaliskiego Str. 00-908, Warsaw, Poland

b) The Faculty of Applied Informatics and Mathematics, University of Life Science,166 Nowoursynowska Str. 02-787, Warsaw, Poland

Abstract: The effect of dislocation on the 1/f noise current in long-wavelength (LWIR) HgCdTe photodiodes working at T= 77K was analyzed theoretically by using phenomenological model of dislocations as an additional SHR generation-recombination (G-R) channel in heterostructure. Numerical analysis was involved to solve the set of transport equations to find steady state values of physical parameters of the heterostructure. Next the set of transport equation for fluctuations (TEFF) were formulated and solved to obtain spectral densities (SD) of fluctuations of electrical potential, quasi-Fermi levels and temperature. The expressions for SD of 1/f fluctuations of G-R processes were derived. The SD of mobility fluctuations, shot G-R noise and thermal noise were also taken into account in TEFF. Numerical values of SD of noise current were compared with experimental results of Johnson at al. Theoretical analysis has shown that despite the fact that dislocations increase the 1/f G-R noise the main cause of 1/f current noise in LWIR LN photodiodes are 1/f fluctuations of carriers mobility. Dislocations cause the growth of G-R dark current and in this way the growth of noise current, which is always proportional to the total diode current.

1. INTRODUCTION

The minimum radiant power that can be detected by any detector is limited by some form of noise. The fundamental types of internal noise are Johnson (sometimes called thermal) noise, generation-recombination (G-R) noise, and 1/f noise [1]. At present, due to the development of MBE and MOCVD technology in manufacturing of MCT heterostructures, as well as the theories of fluctuation phenomena, we try to find the ways to limit G-R noise without LN cooling of detectors. Two examples of such solutions are small area non-cooled 2-11 μm IR photovoltaic detectors optically immersed [2], or a method proposed by British scientists[3,4], which is based on the non equilibrium mode of operation. However one of the main issues in MCT heterostructures are misfit dislocations, which strongly influence on decreasing of the detector performance[5-7].In 8 we presented and discussed model of dislocation band formed by the dangling bonds of atoms of a dislocation core.   In addition to the fact that dislocations strongly influencing G-R rates in devices, they are also sources of the shot noise and 1/f noise. The mechanism of the shot noise is well understood, but there are different views on the origin of 1/f noise In our opinion, the most simple and reasonable is however a model based on Handel's theory[9], confirmed by the measurements of Hooge's parameters α_H of 1/f noise in electronics devices[10,11]. The basic concept of his theory is that "moderated" electrons emit photons with a 1/f spectrum of their energy. These emitted photons interact back with other electrons producing current 1/f

noise. The photon-electron interaction is described by the energy law. Electron is moderated (or accelerated) in G-R events as well as in scattering events. This is why both, fluctuations of G-R rates and mobility fluctuations, seems to be the main reason of the 1/f noise in devices (see Fig.1).

2. METHOD OF ANALYSIS AND RESULTS OF CALCULATIONS

To explain why dislocations lead to the growth of the 1/f noise we have developed the model of dislocations to obtain, first expressions for α_H for 1/f noise, and then to derive the spectral densities of fluctuations of effective G-R rates. Next we have applied our numerical program enabling modeling of fluctuation phenomena in devices by using the Langevine-like method to solve the set of TEFF[12]. In TEFF all physical quantities are expanded in the Taylor series around their steady state values, e.g. electron concentration $n(\vec{r},t) = n_0(\vec{r}) + \delta n(\vec{r},t)$. Here we treat $\delta n(\vec{r},t)$ as a fluctuation of n. On the other hand the fluctuation of n may be expressed by:

$$\delta n(\vec{r},t) = \frac{\partial n(\vec{r},t)}{\partial \Psi(\vec{r},t)}\delta\Psi(\vec{r},t) + \frac{\partial n(\vec{r},t)}{\partial \Phi_n(\vec{r},t)}\delta\Phi_n(\vec{r},t) + \frac{\partial n(\vec{r},t)}{\partial T(\vec{r},t)}\delta T(\vec{r},t) \qquad (1)$$

Similarly $\delta p(\vec{r},t)$, fluctuation of p (hole concentration):

$$\delta p(\vec{r},t) = \frac{\partial p(\vec{r},t)}{\partial \Psi(\vec{r},t)}\delta\Psi(\vec{r},t) + \frac{\partial p(\vec{r},t)}{\partial \Phi_p(\vec{r},t)}\delta\Phi_p(\vec{r},t) + \frac{\partial p(\vec{r},t)}{\partial T(\vec{r},t)}\delta T(\vec{r},t) \qquad (2)$$

The electron and hole mobility is not only the function of Ψ, Φ_n, Φ_p and T, but is additionally dependent on the type and density of scattering centers. For theoretical calculations we have adopted the relaxation time approach after Ref. 13.

$$\mu_n = \mu_n\left(\Phi_n, \Phi_p, \Psi, T, \tau_{rel}^e\right) \rightarrow \delta\mu_n = \frac{\partial\mu_n}{\partial\Phi_n}\delta\Phi_n + \frac{\partial\mu_n}{\partial\Phi_p}\delta\Phi_p + \frac{\partial\mu_n}{\partial\Psi}\delta\Psi + \frac{\partial\mu_n}{\partial T}\delta T + \frac{\partial\mu_n}{\partial\tau_{rel}^e}\delta\tau_{rel}^e \qquad (3)$$

$$\mu_p = \mu_p\left(\Phi_n, \Phi_p, \Psi, T, \tau_{rel}^h\right) \rightarrow \delta\mu_p = \frac{\partial\mu_p}{\partial\Phi_n}\delta\Phi_n + \frac{\partial\mu_p}{\partial\Phi_p}\delta\Phi_p + \frac{\partial\mu_p}{\partial\Psi}\delta\Psi + \frac{\partial\mu_p}{\partial T}\delta T + \frac{\partial\mu_p}{\partial\tau_{rel}^h}\delta\tau_{rel}^h \qquad (4)$$

We have denoted the relaxation time for electrons and holes as τ_{rel}^e and τ_{rel}^h. Spectral densities of $\delta\tau_{rel}^e$ and $\delta\tau_{rel}^h$ fluctuations have spectrum 1/f. Kousik at. al.[14] based on 1/f Handel's theory of 1/f noise, obtained theoretically the spectral intensity of relaxation time in the case of silicon. We have adopted their results for HgCdTe in some previous works[12,15]. The fluctuations of G-R processes are caused by two sources of noise, the shot noise and the 1/f noise. However , G-R processes are dependent on carrier concentration, so the fluctuations of carrier concentration produce also the G-R noise. In the overall case one can write:

$$\delta(G-R) = \delta(G-R)_{SHOT} + \delta(G-R)_{1/f} + \frac{\partial(G-R)}{\partial n}\left[\frac{\partial n}{\partial\Psi}\delta\Psi + \frac{\partial n}{\partial\Phi_n}\delta\Phi_n + \frac{\partial n}{\partial T}\delta T\right]$$

$$+ \frac{\partial(G-R)}{\partial p}\left[\frac{\partial p}{\partial\Psi}\delta\Psi + \frac{\partial p}{\partial\Phi_p}\delta\Phi_p + \frac{\partial p}{\partial T}\delta T\right] \qquad (5)$$

Fig 3 shows a plot of calculated noise current (AHz$^{1/2}$) at 1Hz of photodiode presented in Fig.2 versus dislocation density at 77 K. Experimental data (points) for LWIR photodiodes (Junction area=$7x10^{-6}cm^2$, T=77K, bias=20mV) are taken after Johnson at. al.[5]. Fig. 4 refers to device with dislocation density $N_{DIS} =$

$5x10^7 cm^{-2}$. One may notice that SD of noise power density   is practically generated in regions where built-in electric field $\vec{E}$ exists. In these regions strong gradients of quasi-Fermi levels ($\nabla\Phi_n$ and $\nabla\Phi_p$) are found.

The noise power density is here treated as a result of the fluctuations of the quasi-Fermi levels as well as fluctuations current density, i.e.

$$\delta\rho_P = \vec{j}_n \cdot \delta(\nabla\Phi_n) + \nabla\Phi_n \cdot \delta\vec{j}_n + \vec{j}_p \cdot \delta(\nabla\Phi_p) + \nabla\Phi_p \cdot \delta\vec{j}_p \qquad (6)$$

The fluctuations of the total noise power density may be expressed by

$$\delta P_N = \int_V \delta\rho_P \, dV = \delta UI + U\delta I \approx U\delta I \qquad (7)$$

Fluctuation of density of Joule's heat power $\delta\rho_P$ is now considered as a noise power density.

Taking into account the energy balance of Eq. (7), one may write an expression for the effective SD of the total noise current:

$$S_I = \frac{1}{U^2} S_{P_N} \qquad (8)$$

Here S_{P_N} is SD of the Joule noise power.

Numerical results show, that the dislocations are not only the direct source of 1/f noise via 1/f G-R noise, but also mainly increase it through their effect on G-R currents. All these results confirm Johnson's assumption[5], that dislocations are not the direct source of 1/f noise in LWIR 77K photodides, but rather increase it only through their effect on leakage current.

3. REFERENCES

1.A. van der Ziel, "Fluctuation Phenomena in Semiconductors"(Butterworths Scientific, London,1959).
2.e.mail, info@vigo.com.pl
3.T. Ashley and TC.T. Elliott,Electron. Lett.21,451,(1985).
4.T. Ashley at al. , Infrared. Phys.26,303,(1986).
5.S.M. Johnson at al. J. Vac. Sci. Technol. B 10(4),1499, (1992).
6.A.T.Paxton at al., J.Electron. Mater.25,529,(1995).
7.K. Jóźwikowski and A. Rogalski, J.Electron. Mater.29,736,(2000).
8. K. Jóźwikowski at al., Infrared Physics &Technology,55,98, (2012).
9.P.H. Handel, Pys. Rev.Lett. 34,1497,(1975).
10. A. van der Ziel,in 9th Inter.Conference on Noise in Phys. Systems, ed. by C.M. van Vliet(World Scientific,Sigaphoure,1987)
11.A. van der Ziel, JAP 63,(7),2456 (1988).
12. K, Jóźwikowski, JAP,90,1318,(2001).
13. B.R. Nag,"Electron Transport in Compound Semiconductors",Brlin, Springer (1980).
14.G.S. Kousik at al.,Advanced in Physics, 34, 6,663,(1985).
15.K, Jóźwikowski at al., Solid St. Electronics,48,13, (2004).

4. FIGURES
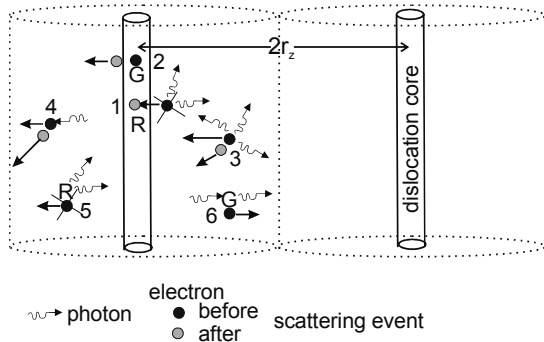
Fig.1. Examples of G-R and scattering processes in which soft photons are emitted and absorbed. $2r_z$ is the mean distance between dislocation cores. . Digit 1 – recombination in dislocation core, 2- generation, 3- scattering of electron, 4-absorption of photon by electron, 5-bulk recombination, 6-bulk recombination

Fig.2.Geometry, CdTe mole fraction profile, and carrier concentration profiles across LWIR P-on-n photodiode operated at 77K. Distribution of particular functions are shown across the line A-B marked in the inside figure.

Fig. 3. Noise current (AHz$^{1/2}$) at 1Hz vs. dislocation density
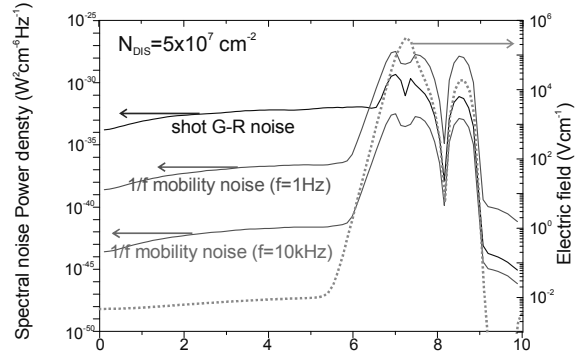
Fig.4. Spatial distribution (along AB cross section) of noise power density caused by different noise sources for dislocation density 5x10^7 cm^{-2}. Shot G-R noise – black line, 1/f mobility noise (red line at frequency f=1Hz, blue line f=10 kHz). Distribution of electric field strength - dotted green line.

$Mg_xZn_{1-x}O$ Thin Film Transistor-Based UV Photodetector with Enhanced Photoresponse

Chieh-Jen Ku, <u>Pavel Reyes</u>, Ziqing Duan, Wen-Chiang Hong, Rui Li, and Yicheng Lu*

Department of Electrical and Computer Engineering, Rutgers University

94 Brett Road, Piscataway, NJ 08854. *pavelrey@rci.rutgers.edu (presenting author)

Abstract: We demonstrate a UV photodetector based on $Mg_xZn_{1-x}O$ (MZO) thin film transistor (TFT). The device has low dark current (2×10^{-14} A) and an ON/OFF ratio of 10^{11}. We show that by using small composition of Mg (5%) in the MZO TFT channel, we are able to significantly improve the photoresponse recovery time of the photodetector to 13.3 ms compared with 46.9 ms recovery time of a similar TFT with 0% Mg. We also observed a shift in the cutoff wavelength from 377.21nm in the 0% Mg TFT photodetector down to 370.96 nm for the MZO TFT photodetector.

Introduction

ZnO is a promising material for UV photodetection due to its wide bandgap and superior radiation hardness. However, it has been found that the performance of ZnO-based devices such as that of the ZnO-based thin film transistors can be strongly impacted by the native defects like oxygen vacancies [1]. Based on our recent work, it has been shown that Mg doping in ZnO to form its ternary alloy $Mg_xZn_{1-x}O$ (MZO) enhances the thermal and electrical properties of ZnO-based thin film transistors (TFT) due to the suppression of the O_2 vacancies [2].

Various types of UV photodetectors based on ZnO have been reported mainly utilizing two-terminal devices including photoconductive [3-4], and Schottky [5-6] types. More recent ZnO-based photodetectors have been demonstrated based on the TFT devices [7]. The TFT-based UV photodetector as a three-terminal device provides intrinsic advantage over its two-

terminal counterpart by allowing bias control and signal gain. Moreover, ZnO TFTs can be integrated into arrays and can be fabricated on various substrates including glass. This makes it well suited for constructing photodetector-arrays for UV imaging applications. However, as previously stated, devices based on purely ZnO materials suffer from poor performance including the low mobility, high operating voltages, and especially, slow recovery speeds caused by oxygen vacancies. We have previously reported significant recovery time improvement of a pure-ZnO TFT UV photodetector through O_2 plasma surface treatment of the ZnO TFT channel [8] to minimize persistent photoconductivity (PPC).

Device Structure and Static Characteristic

In this paper, we demonstrate the enhanced UV photoresponse by introducing low Mg composition MZO as the channel to form the MZO TFT-based UV photodetector. The MZO TFT UV photodetector consists of a bottom gate configuration TFT fabricated on heavily doped n-type Si wafers with a 100 nm thermally-grown SiO_2. The MZO channel has a 50 nm thickness with a ~5% Mg composition. The MZO channel is grown by metal-organic chemical vapor deposition (MOCVD) at 450 °C using diethyl zinc (DEZn) as the Zn precursor and bis-(methylcyclopentadienyl)-magnesium (MCp_2Mg) as the Mg precursor. The source and drain metallizations consist of 100 nm Ti/50 nm Au. The active layer of the device had an aspect ratio of W/L = 150μm/5μm. To provide a control device for comparison, we fabricated a similar TFT with 0% Mg doping. The inset of Fig. 1 shows the schematic of the TFT. We measured the I_{DS}-V_{GS} transconductance curve of both photodetectors under dark conditions as shown in Fig. 1. Both devices have a low dark current of ~10^{-14} at -10V gate bias, however, the MZO device with 5% composition exhibited higher on current (1×10^{-3} A) compared to 1×10^{-5} A dark current of the 0% Mg device. The MZO TFT UV photodetector exhibited a high ON/OFF ratio of 10^{11}. The spectral response of both UV TFT photodetectors (0% Mg and 5% Mg) was measured by illuminating the exposed TFT channel with a broadband UV lamp through a tunable

monochromator (Oriel Optics MS257). The wavelength was varied from 300 nm to 400 nm. The I-V characteristics of both devices were measured for each wavelength step of 5nm. The drain was held constant at +10V and the gate at -10V for the whole duration of the measurements. The resulting spectral photoresponse of both devices are shown in Fig. 2. We observed a shift in the cutoff wavelength from 377.21nm in the 0% Mg TFT photodetector down to 370.96 nm for the 5% Mg doped MZO TFT photodetector verifying the increase in the energy bandgap of the MZO TFT compared to the pure ZnO device.

Enhancement of UV Photoresponse in the MZO-based TFT UV Photodetector

The dynamic photoresponse of the ZnO TFT UV photodetector was measured using a Laser Science VSL 337ND-S nitrogen pulsed-laser as the optical source. It was operated at 40 ns optical pulse duration averaged at 60 Hz. The laser wavelength is 337 nm, which was externally triggered at 10% duty cycle burst mode. Fig. 3 shows the photocurrent as a function of time of both devices with the same optical excitation. We show that by using small composition Mg (5%) in MZO TFT channel, we are able to significantly improve the photoresponse recovery time of the photodetector to 15 ms compared with 42 ms recovery time of a similar TFT with 0% Mg. The PPC in ZnO and related materials is due to slow process of the optically excited state (Vo^{2+} metastable states) returning to its ground state. To return to ground state, the metastable state must be first thermally activated across its energy barrier and, simultaneously, an electron must be captured from the conduction band. Simultaneously meeting these two conditions to attain a return to ground state results in a slower decay of PPC. The improvement of dynamic photo response for MZO TFTs could be attributed to the suppression of V_0 in the channel layer due to the Mg doping. The incorporation of certain metal ions that have a stronger oxygen affinity than Zn in ZnO (like Mg) can suppress the oxygen vacancies since the formation energy of oxygen vacancies partially depends on the M-O/Zn-O bonding energy [9]. The demonstrated

MZO TFT UV photodetector with enhanced photoresponse is a promising device for applications in deep-UV sensors and imaging arrays.

References:

[1] C. T. Tsai, et al., Appl. Phys. Lett. 96, 242105, (2010).
[2] C. J. Ku, et al., Appl. Phys. Lett. 98, 123511, (2011).
[3] C. Soci, et al., Nano Lett. 7(4) 1003–1009 (2007).
[4] Y. Liu, et al., J. Electron. Mater. 29, 69 (2000).
[5] S. Liang, et al., J. Cryst. Growth, 225, 110 (2001).
[6] D. Jiang, et al., Solid-State Electron 52, 679–682 (2008).
[7] H. Bae, et al., Jpn. J. Appl. Phys. 47(7), 5362–5364 (2008).
[8] P. Reyes et al., Appl. Phys. Lett., 101, 031118, (2012).
[9] S. Lany, et al., Phys. Rev. B 72, 035215, (2005).

Figures
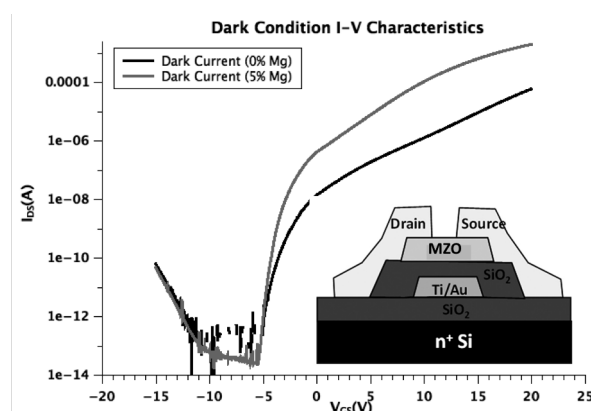
Fig. 1. I-V characteristics of the MZO TFT (red) pure ZnO TFT (black) UV photodetector at dark conditions, (inset: schematic of the TFT UV photodetector).
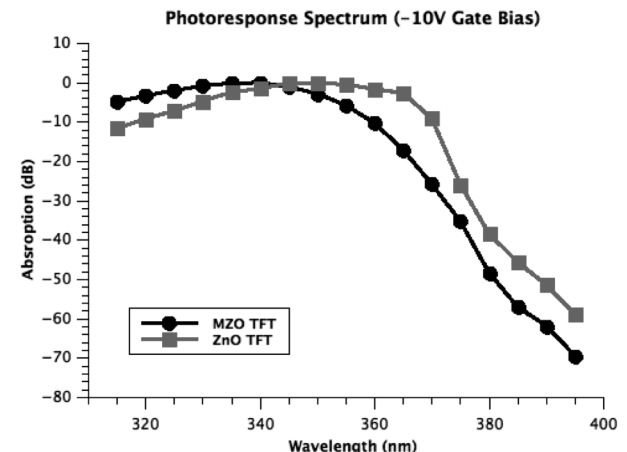
Fig. 2. Photoresponse spectrum of the the MZO TFT (black) pure ZnO TFT (red) UV photodetector.
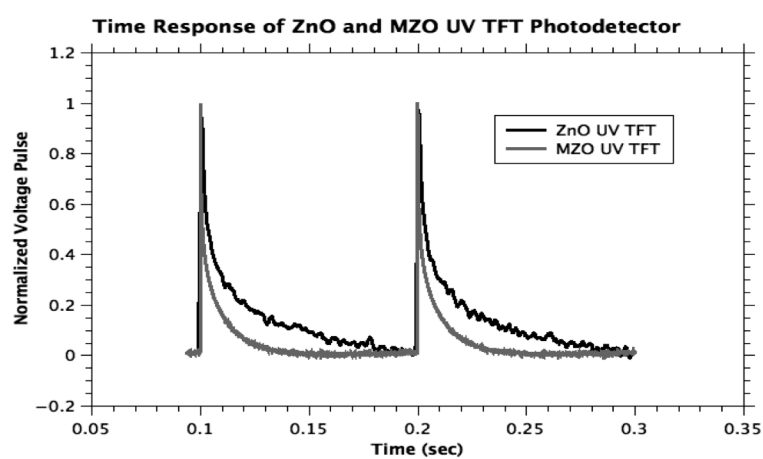
Fig. 3. Time response of the MZO TFT (red) pure ZnO TFT (black) UV photodetector for a 340nm laser pulse with 10Hz repetition rate.

Infrared Materials, Processing, and Device Development at the Army Research Laboratory

Phil Perconti

U.S. Army Research Laboratory

A review will be given of the unique capabilities found at the Army Research Laboratory (ARL) for the understanding and development of enabling infrared materials, devices, and focal plane arrays for next generation IR systems. This will include a discussion of ARL's HgCdTe research portfolio, alternative IR materials, advanced processing capabilities using atomic layer deposition (ALD), fundamental modeling of devices, and our vision of where the greatest areas of impact lie for the Army with respect to infrared research and Army unique requirements.

A Computational Investigation of Random Angle Grain Boundaries for CdTe Solar Cells

C Buurma*[1], M K Y Chan[2], R Klie[1], S Sivananthan[1]

[1] University of Illinois at Chicago
[2] Argonne National Laboratory, Center for Nanoscale Materials.
*630-771-0203, cbuurm2@uic.edu

Abstract

Grain boundaries (GB) in poly-CdTe solar cells play an important role in species diffusion, segregation, defect formation, and carrier recombination. Many studies on GBs in CdTe focus on either entire grain-boundary networks found in complete poly-CdTe devices, those exhibiting high symmetry such as the coincident site lattice (CSL) or symmetric tilt or twist, or on very small scale Scanning-Tunneling Electron Microscope (STEM) viewable interfaces and dislocations. The topic of this talk is a symmetry comprehensive survey of the grain boundary parameter space regardless of the degree of symmetry found and whether the STEM channeling condition is satisfied. Our survey encompasses both near-CSL or vicinal grain boundaries decorated with nearby dislocations, as well as mixed tilt and twist interfaces with all possible symmetrically inequivalent grain boundary planes.

Atomistic calculations using a Stillinger-Weber[1] potential will be presented on a large representative sample of random-angle GBs. Trends in interfacial energies and atomistic structures as a function of tilt/twist/displacement parameters will be investigated. First principles density functional theory (DFT) calculations will be performed on a subset of these GBs to reveal their electronic structures and their implications towards PV performance.

[1]   D. K. Ward, X. W. Zhou, B. M. Wong, F. P. Doty, and J. a Zimmerman, "Accuracy of existing atomic potentials for the CdTe semiconductor compound." *J. Chem. Phys.*, vol. 134, no. 24, p. 244703, Jun. 2011.
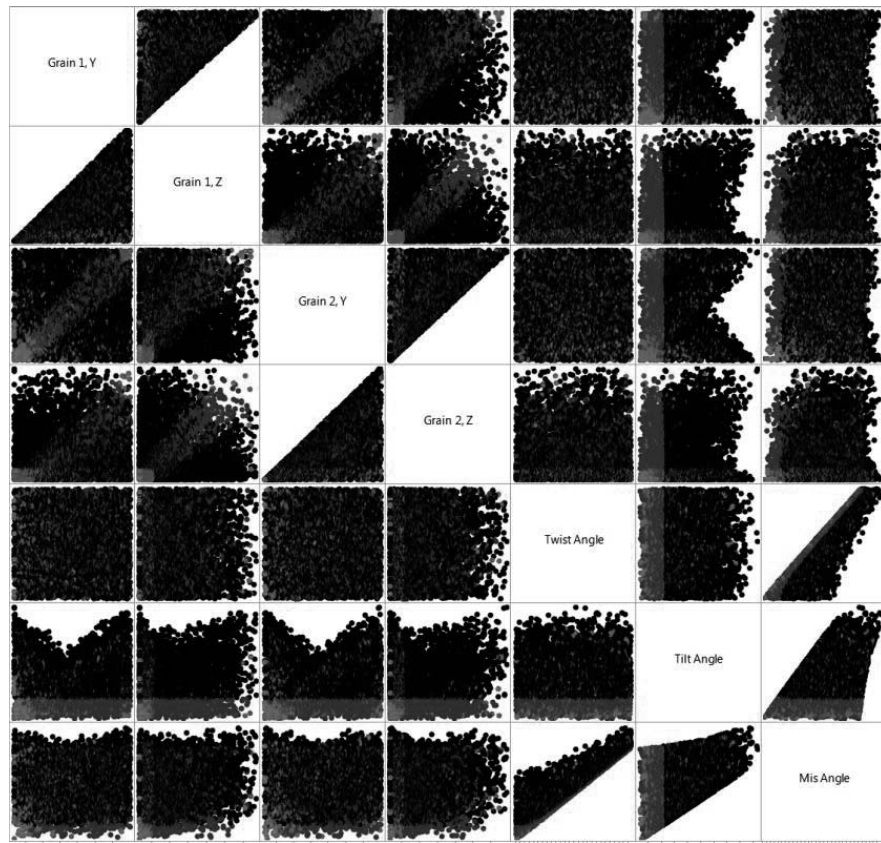
Figure 1. Grain boundary macroscopic parameter space (with 5 DoF) which are symmetrically inequivalent, along with tilt and misorientation angles. STEM Viewable GBs are in red, low tilt angles are in blue, and the intersection of both subsets is in green.
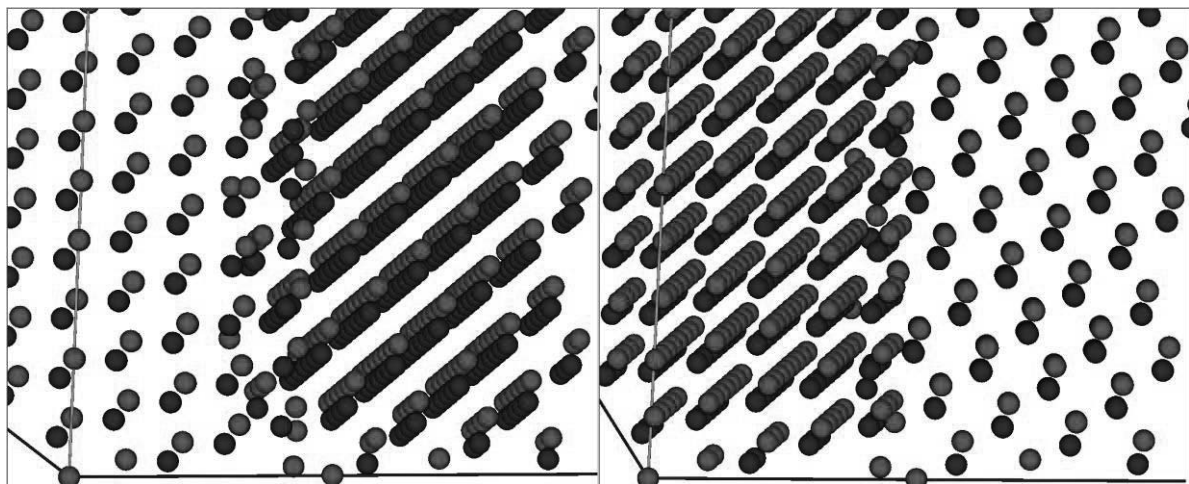
Figure 2. A (11°)[6,5,3] [6,5,2] random angle (13.8°) GB viewed along two directions near [1,1,0] to visualize each side of the GB which cannot be resolved by STEM.

Student Paper   Advisor: Yong-Hang Zhang

Monocrystalline ZnTe/CdTe/MgCdTe double-heterostructure solar cells grown on InSb using Molecular Beam Epitaxy

Ying-Shen Kuo[1,2], Jacob Becker[1,2], Yuan Zhao[1,2], Michael J. DiNezza[1,2], Xin-Hao Zhao[1,3], Shi Liu[1,2], Calli Campbell[1,3], Xinyu Liu[4], Jacek K. Furdyna[4], and Yong-Hang Zhang[1,2,a]

[1]Center for Photonics Innovation, Arizona State University, Tempe, AZ 85287

[2]School of Electrical, Computer and Energy Engineering, Arizona State University, Tempe, AZ 85287

[3]School for Engineering of Matter, Transport and Energy, Arizona State University, Tempe, AZ 85287

[4]Department of Physics and Center for Materials Fabrication & Nanotechnology, University of Notre Dame, Notre Dame, Indiana 46556

[a] Contact information: Phone: 480-965-2562; Fax: 480-965-0775; Email: yhzhang@asu.edu

Introduction

Monocrystalline CdTe has been utilized for photovoltaic applications with a maximum reported cell efficiency of 13.4% in 1987 [1], and polycrystalline CdS/CdTe solar cells have recently reached a 21.0% record efficiency demonstrated by First Solar [2]; however, both are far from the detailed balanced limit of 32.1%. By comparing these values with single-junction monocrystalline and polycrystalline GaAs solar cells with record efficiencies of 18.4% and 28.8% [3], respectively, as shown in Table 1, it is believed that the monocrystalline CdTe solar cell should be able to achieve an even higher efficiency than the current record. We have recently demonstrated high-quality monocrystalline CdTe/MgCdTe double heterostructures (DHs) grown on lattice-matched InSb (001) substrates using Molecular Beam Epitaxy (MBE), with Shockley-Read-Hall (SRH) lifetimes of 179 ns and 86 ns [4,5] for 2-μm- and 1-μm-thick CdTe layers, respectively. This work shows our further exploration of using this high-quality monocrystalline CdTe to demonstrate single-junction CdTe solar cells with improved efficiency.

The design, growth, processing and characterization of monocrystalline p-ZnTe/n-CdTe/n-MgCdTe DH solar cells on n-InSb substrates are carefully studied.

Experimental results and discussion

The sample, of which the layer structure is shown in Fig. 1 (a), is firstly grown at ASU using a VG V80H dual-chamber MBE system with separate III-V and II-VI growth chambers connected by a UHV transfer chamber. Details of the growth conditions have been reported previously for undoped DH [4]. The sample is capped with a 100-nm-thick Arsenic layer to protect the surface during sample shipment from ASU to University of Notre Dame, where the p-ZnTe:N layer was grown after the Arsenic cap was thermally desorbed (Fig. 1 (b)). Further processing and characterization as described in Fig. 1 (c) ~ Fig. 1(f) was then carried out at ASU.

A 1-μm-thick CdTe base layer, giving an absorbance of 97.5% as shown in Fig. 2, is used in the design as the absorber. Fig. 3 plots the energy conversion efficiency as a function of the total non-radiative carrier lifetime in the CdTe, which considers both the interface recombination velocity and bulk SRH recombination lifetime. An efficiency of 27.4% is expected for a sample with a total non-radiative carrier lifetime of 97 ns for 1-μm-thick CdTe/MgCdTe DH. A high quality CdTe absorber layer with an X-ray diffraction (XRD) FWHM of 18 arcseconds is measured as shown in Fig. 4. It is noted that the ZnTe is almost completely relaxed, which results in large densities of misfit dislocations and non-radiative recombination centers at or near the ZnTe/CdTe interface. The current density vs. voltage (J-V) characteristics of a finished device without an anti-reflection (AR) coating is shown in Fig. 5. The J-V curve shows a typical PN junction rectifying behavior in dark and exhibits an efficiency of 6.11% under AM1.5G 1 sun illumination. The low efficiency results from low open-circuit voltage (V_{OC}) that is primarily attributed to strong non-radiative recombination at the ZnTe/CdTe interface, and low short-

circuit current density (J_{SC}) that is due to the absence of AR coating. A surface reflection of roughly 30% is observed and the reflection spectrum is shown along with the internal and external quantum efficiencies in Fig. 7. The internal and external quantum efficiencies show a considerable drop in the wavelength range above the ZnTe bandgap which are due to the parasitic absorption loss in ZnTe emitter layer and surface/interface recombination. Additional characterization and analysis will be presented at the conference.

Summary

In summary, monocrystalline ZnTe/CdTe/MgCdTe double-heterostructure solar cells are demonstrated on lattice-matched InSb substrates by MBE growth for the first time. Preliminary results show an V_{OC} of 556 mV, a J_{SC} of 15.5 mA/cm^2 and a power conversion efficiency of 6.11% under AM 1.5G one sun illumination.

Table and Figures

Material	Polycrystalline	Monocrystalline	Detailed balance limit
GaAs	18.4 %	28.8 %	33.2 %
CdTe	21.0 %	13.4 %	32.1 %

Table 1. Record efficiencies and detailed balance limits of GaAs and CdTe single-junction solar cell.
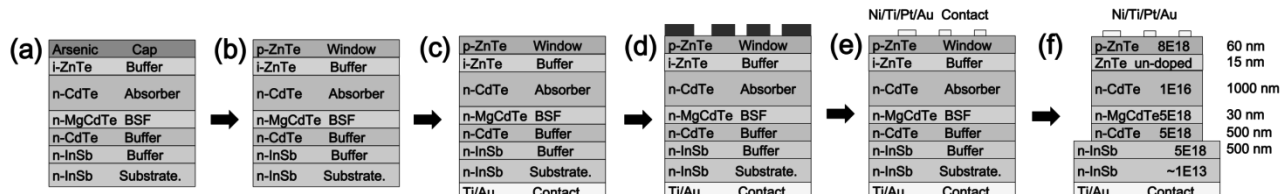
Fig. 1. Design and process flow of the proposed solar cell. Solar cell structure is (a) firstly grown at ASU and then (b) p-ZnTe is grown at University of Notre Dame. The processing starts with oxide removal and (c) back Ti/Au contact deposition by E-beam evaporation. The front contact grid (area <5%) is then defined by (d) photolithography, (e) front Ni/Ti/Pt/Au metal deposition and lift-off process. Solar cell sizes ranging from 0.6 mm × 0.6 mm to 5 mm × 5 mm are obtained after (f) mesa etching.
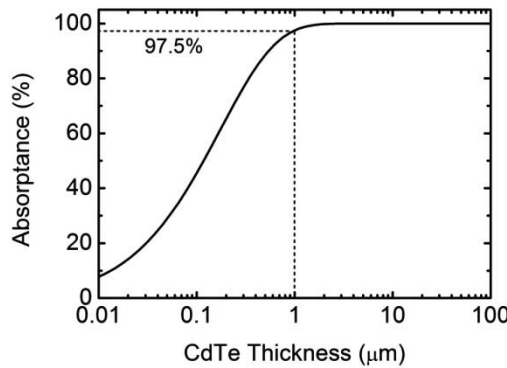
Fig. 2. Calculated absorptance versus layer thickness for CdTe single-junction solar cell.
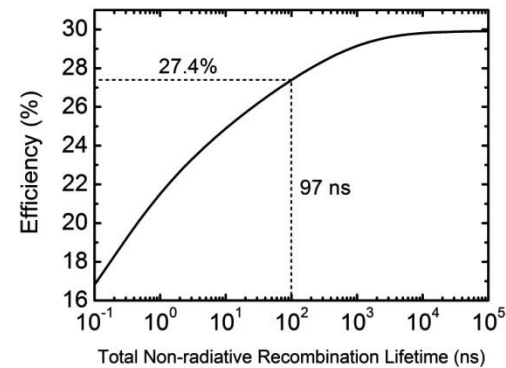
Fig. 3. Simulated energy conversion efficiency as a function of CdTe total non-radiative recombination lifetime for the structure shown in Fig. 1 (f).
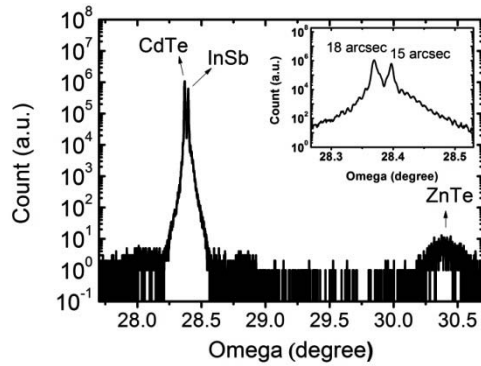
Fig. 4. XRD pattern of the grown solar cell structure shown in Fig. 1 (b). Inset figure shows the zoom in peaks of CdTe and InSb.
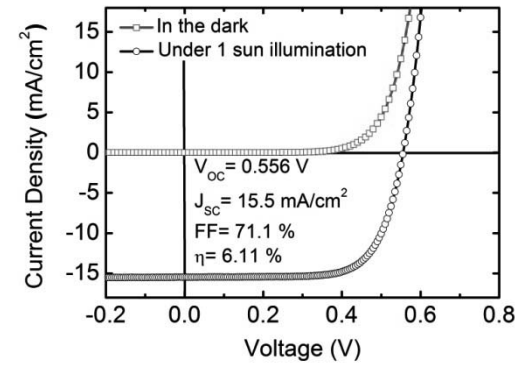
Fig. 5. J-V characteristic of a ZnTe/CdTe/MgCdTe solar cell measured in the dark and under AM 1.5G one sun illumination at room temperature.

References

[1] T. Nakazawa, K. Takamizawa, and K. Ito, Appl. Phys. Letts. 50, 279 (1987).

[2] First Solar Press Release, 5 August 2014, (accessed at http://investor.firstsolar.com on 5 September 2014).

[3] M. A. Green, K. Emery, Y. Hishikawa, W. Warta and E. D. Dunlop. Prog. Photovolt: Res. Appl. 2014; 22:701–710

[4] M. J. DiNezza, X.-H. Zhao, S. Liu, A. P. Kirk, and Y.-H. Zhang, Appl. Phys. Letts. 103, 193901 (2013).

[5] X.-H Zhao, Michael J. DiNezza, Shi Liu, Su Lin, Yuan Zhao, and Yong-Hang Zhang, J. Vac. Sci. Technol., B, 32, 040601 (2014).

Fig. 6. Measured EQE, reflectance, and IQE of the ZnTe/CdTe/MgCdTe solar cell.

Low interface recombination velocity in MBE grown

CdTe/MgCdTe double heterostuctrures

Xin-Hao Zhao[1,2], Michael J. DiNezza[1,3], Shi Liu[1,3], Ying-Shen Kuo[1,3], Calli Campbell[1,3],

Yuan Zhao[1,3], Yong-Hang Zhang[1,3,a]

[1]Center for Photonics Innovation, Arizona State University, Tempe, AZ 85287

[2]School for Engineering of Matter, Transport, and Energy, Arizona State University, Tempe, AZ 85287

[3]School of Electrical, Computer, and Energy Engineering, Arizona State University, Tempe, AZ 85287

[a] Contact information: Phone: 480-965-2562; Fax: 480-965-0775; Email: yhzhang@asu.edu

Introduction

Cd(Zn)Te is not only a suitable virtual substrate for Mercury Cadmium Telleride detectors, but also a promising material for solar cells because of its large absorption coefficients and the favorable bandgap of CdTe (1.50 eV). Recently we demonstrated CdTe and CdTe/MgCdTe double heterostructures (DHs) grown on InSb substrates using molecular beam epitaxy (MBE), with excellent crystalline qualities, very low defect density and a record long carrier lifetime of 86 ns.[1,2,3] First Solar has demonstrated polycrystalline CdTe solar cells with a record efficiency of 20.4%,[4] and it is expected that monocrystalline CdTe with much better material quality should enable even higher efficiencies. The heterostructure solar cell efficiency is not only limited by the bulk carrier lifetime, but also by interface and surface recombination. This paper focuses on the study of interface recombination velocity in MBE grown CdTe/MgCdTe DHs.

Experimental results and discussion

The double heterostructures (DHs) were grown using a dual-chamber MBE system as reported previosly.[1] With MgCdTe barrier layers providing effective carrier confinement and reducing surface recombinations for CdTe, the samples provide a strong photoluminescence (PL) intensity and long minority carrier lifetimes.[1,2,3] Time-resolved PL results for recently grown samples with different CdTe middle layer thickness are shown in Fig. 1. A new record lifetime of 179 ns is observed for the 2 μm thick sample at room temperature. The wafer has some degree of non-uniformity and lifetimes are measured at 3 different

positions on the wafer. On average, the thinner samples have shorter carrier lifetimes indicating stronger interface recombiantion. The interface recombination velocity is determined to be 461 cm/s by fitting the thickness dependent carrier lifetimes. The measured interface recombintaion velocity is approaching the typical value (210 cm/s) of GaAs/AlGaAs DHs,[5] suggesting that the interface of CdTe/MgCdTe has excellent quality. The bulk carrier lifetime is estimated to be at least on the order of hundreds of nanoseconds. Such a long bulk carrier lifetime indicates the superior material quality of the epitaxial CdTe layer compared with polycrystalline CdTe. PL spectra are measured for samples with different CdTe layer thickness under the same condition (Fig 2). It is found that the PL peak shifts to longer wavelength with thicker CdTe layer thickness. This is because the photon recycling effect is stronger for shorter wavelength photons, which have a higher probablity of being reabsorbed by the CdTe layer before they are emitting from the sample. Theoretically, under low excitation levels during PL measurement, the PL intensity is proportional to $(1-\gamma)\tau_{eff}$. The calculated effective lifetime τ_{eff} and 1-γ (photon recyling factor) is shown in Fig 3 (left). The measured PL intensity agrees very well with the theoretical prediction as shown in Fig 3 (right).

Summary

In summary, very high quality CdTe/MgCdTe double heterostructures are demonstrated by using lattice matched InSb substrate and molecular beam epitaxy growth. The interface recombination velocity is determined to be 461 cm/s, and the bulk lifetime is determined to be on the order of hundreds of nanoseconds. Such a high quality CdTe bulk material could enable high efficiency solar cells, and the MgCdTe layer could be a potential surface passivation layer for CdTe.

Figures
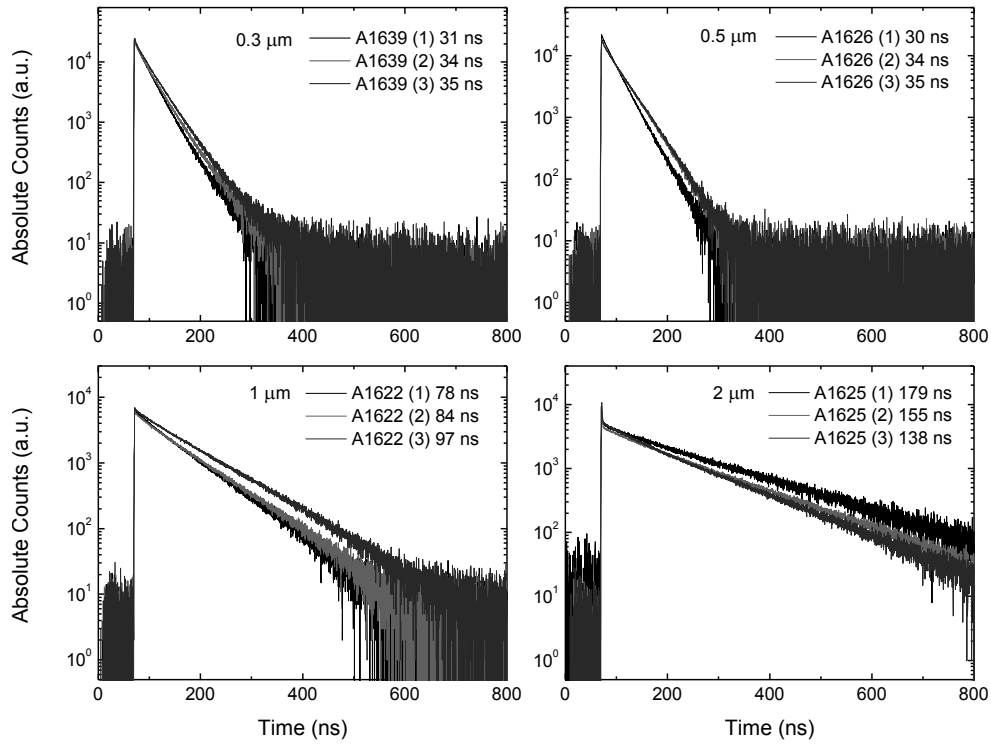
Figure 1. Time-resolved photoluminescence measurements of CdTe/MgCdTe double heterostructures with different CdTe layer thickness. For each wafer, the lifetimes are measured from the center to the edge of the wafer with equal spacing, corresponding to label (1)~(3). Averaged lifetimes are used for the interface recombination study. The thicker the sample, the longer the lifetime, indicating that interface recombination is an important part of the total lifetime.
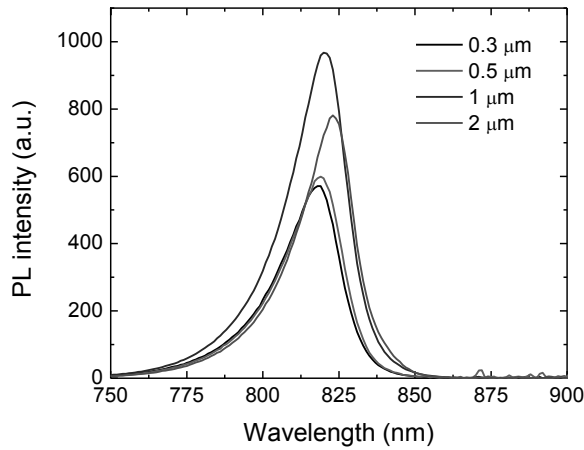
Figure 2. Photoluminescence spectra study of CdTe/MgCdTe double heterostructures with different CdTe layer thickness. The thicker the CdTe layer, the longer the peak wavelength is, indicating a strong photon recycling effect.
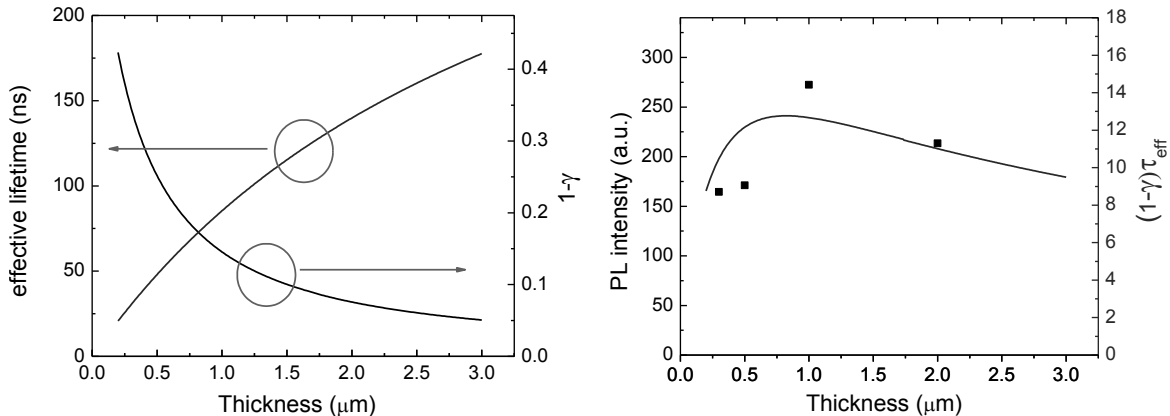
Figure 3. (Left) Calculated effective lifetime τ_{eff} and 1- γ (photon recycling factor) as a function of CdTe layer thickness. (Right) Photoluminescence intensity is proportional to $(1-\gamma)\tau_{eff}$ under low excitation levels as predicted by theory.

References

[1] M. J. DiNezza, X.-H. Zhao, S. Liu, A. P. Kirk and Y.-H. Zhang, Applied Physics Letters **103**, 193901 (2013).

[2] X.-H. Zhao, M. J. DiNezza, S. Liu, S. Lin, Y. Zhao, and Y.-H. Zhang, Journal of Vacuum Science & Technology B, **32**, 040601 (2014).

[3] X.-H. Zhao, M. J. DiNezza, S. Liu, P. A. Jayathilaka, O. C. Noriega, T. H. Myers, Y. Zhao and Y.-H. Zhang, in proceedings of PVSC, 2014.

[4] http://investor.firstsolar.com/releasedetail.cfm?ReleaseID=828273.

[5] J. M. Olson, R. K. Ahrenkiel, D. J. Dunlavy, B. Keyes and A. E. Kibbler, Applied Physics Letters, **55**, 1208 (1989).

Structural Characterization of GaAs (211)B/CdTe Composite Substrate

Mustafa Polat, Ozan Arı, Orhan Öztürk and Yusuf Selamet

mustafapolat@iyte.edu.tr - *90 537 706 2633*

Izmir Institute of Technology, Departmant of Physics, Izmir 35430, TURKEY

Abstract: In this study, we focused on structural characterization of CdTe epilayer grown on GaAs (211)B substrate with the help of different techniques of X-ray diffraction (XRD). We found that mosaicity exists in 1.6 micrometer-thick CdTe epilayer according to reciprocal space map (RSM) of symmetric (422) peak. CdTe epilayer had a few degrees of misorientation relative to GaAs (211)B substrate. Subgrain boundaries were revealed as shoulders in rocking curve (RC) peak shapes for some of the thicker CdTe epilayers. Ga_2O_3oxide was not completely stripped from GaAs (211)B surface after thermal desorption process with respect to X-ray reflectivity (XRR) fit result.

Keywords: CdTe/GaAs (211)B, Reciprocal Space Map, X-ray Reflectivity, Rocking Curve.

1. INTRODUCTION

GaAs (211)B is superior to other alternative substrates such as Si and Ge in terms of having low lattice mismatch with CdTe, polarity, easy surface preparation process, direct growth of CdTe without nucleation layer or transition layer such as ZnTe by using molecular beam epitaxy (MBE). Growth of CdTe buffer layer on epiready GaAs (211)B substrate can be started immediately after thermal stripping of oxide layer(s). CdTe epilayer grown on GaAs (211)B substrate must be characterized in great detail whether it is suitable for the growth of HgCdTe.

XRD is a versatile, well-established, and non-destructive structural characterization technique. There are limited number of studies devoted to structural analysis of CdTe epilayers grown on GaAs (211)B substrate using XRD. RC map is a very useful and most common technique for this structure that can be used to show variation of crystal quality on the surface of CdTe epilayer. RC map of CdTe epilayer grown on GaAs (211)B substrate can be found in several studies [1, 2]. The effect of growth temperature on crystal orientations was determined by XRD in a study for CdTe/GaAs (211)B [3]. Residual film stress [4], tilting of CdTe with respect to GaAs (211)B substrate [5], and RC peak shape of bulk growth CdTe on GaAs (211)B [6] were reported in the literature. In this study, XRD analysis was employed with different

techniques such as Gonio Scan and XRR in low resolution and RSM and RC in high resolution to understand structural characteristics of thin CdTe epilayers grown on GaAs (211)B substrate in great detail.

2. EXPERIMENTAL

A. MBE Growth

CdTe epilayers were grown on GaAs (211)B substrate by using Veeco GEN20MZ MBE system. Thermal oxide desorption process of GaAs (211)B substrate before direct growth of CdTe was monitored by reflection high energy electron diffraction (RHEED). Growth temperature of CdTe epilayers was measured with the help of band edge measurement system. Thicknesses of CdTe epilayers were measured by ex-situ spectroscopic ellipsometry (SE). Thicknesses and growth temperatures of CT8 and CT9 can be given as 1.9 and 1.6 μm and 310 ^{o}C and 315°C, respectively and with Te:Cd=3:1 flux ratios.

B. XRD Measurements

PANalytical Pro Material Research Diffractometer (MRD) was used as XRD diffraction instrument for all of the measurements. High and low resolution with line focus tube alignment were employed to characterize CdTe epilayer grown on GaAs (211)B substrate. XRR was measured in low resolution for incidence angle (ω) in between 0.15^o and 6°. Experimental raw data of XRR was fitted with PANalytical X'Pert Reflectivity software supplied by PANanalytical. RC measurement of symmetric (422) peak of CdTe was measured in high resolution in the range of ± 0.5^o about the peak position. Optical apparatus such as four crystal Ge (220) monochromator with 10 mm x 10 mm spot size on the incident beam side and analyzer crystal on the diffracted beam side were used in order to increase resolution of RC setup by selecting Cu K$_{\alpha 1}$. RSM of CdTe (422) peak was measured as a 2D map with omega-2theta and omega scans whose ranges were ± 0.6^o and ± 0.5^o, respectively.

3. RESULTS AND DISCUSSION

Symmetric (422) peak of CdTe was observed with an offset to the incident angle for some RC measurements. This offset as a deviation from (422) peak position was attributed to misoriented CdTe epilayer accroding to GaAs (211)B substrate as illustrated in Figure 1 (a). Large lattice mismatch between GaAs (211)B substrate and CdTe epilayer leads to this misorientation. Intrinsically, CdTe epilayers behave this way to reduce lattice mismacth with GaAs (211)B lattice. A weak correlation observed with the offset & crystal quality might be due to the variation of growth paramaters such as nucleation and growth temperature.

Reciprocal space map of symmetric (422) reflection of 1.6 micrometer-thick sample (CT9) can be seen from Figure 1 (b). Secondary flat of GaAs substrate is ($\bar{1}$11) and it is parallel to the incident beam for this measurement. Elongation along Q_x can be interpreted as existence of mosaicity in CdTe epilayer. This result also demonstrates the formation of low-angle subgrain boundaries in CdTe epilayer due to moasicity.

(422) peak which was obtained from 1.9 micrometer-thick sample (CT8) has an asymmetric peak shape as shown in Figure 2 (a). Asymmetric peak shape demonstrates that low-angle grain boundaries (LAGB) or subgrain boundaries exist in the crystal structure. We infer that low-angle grain boundaries in CdTe are formed by a mixture of twist and tilt boundaries as components of moasicity and supported by dislocation arrays in crystal structure. FWHM of this peak obtained from PearsonVII function fitting is about 250 arsec.

According to XRR results table of CT 23 given in Figure 2 (b), Ga_2O_3 was still present at the surface of GaAs (211)B substrate after thermal desorption process which suggests that higher temperature might be needed for complete desorption. Thickness and roughness of CdTe epilayer can be approximately given as 294 and 1 nm, respectively. The data analysis also suggests, Tellirium dioxide and oxygen were formed on the surface of CdTe epilayer.

4. FIGURES
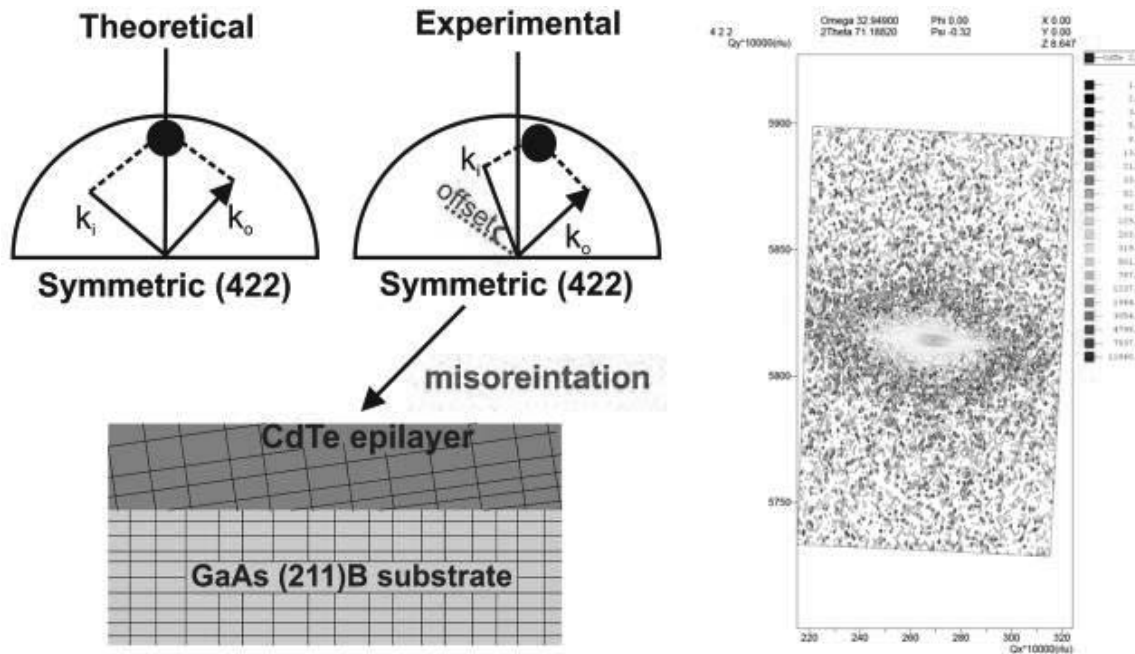
Figure 1. Misorientation illustration of CdTe epilayer according to GaAs (211)B substrate (a-left) and RSM of symmetric (422) peak of CdTe (b-right) for the same sample (CT9).

Figure 2. Asymmetric shape of (422) peak of CdTe (a-left) for sample CT8 and XRR measurement (blue) with fit data (red) and result table (b-right) for sample CT23.
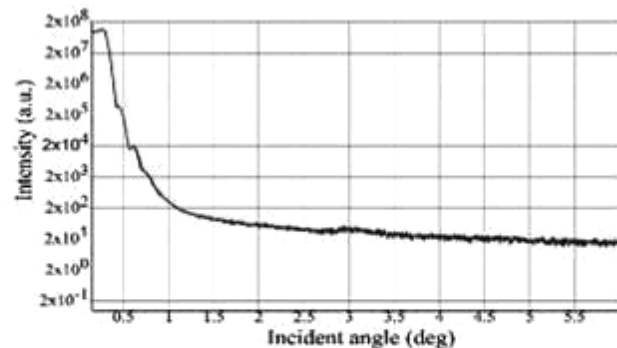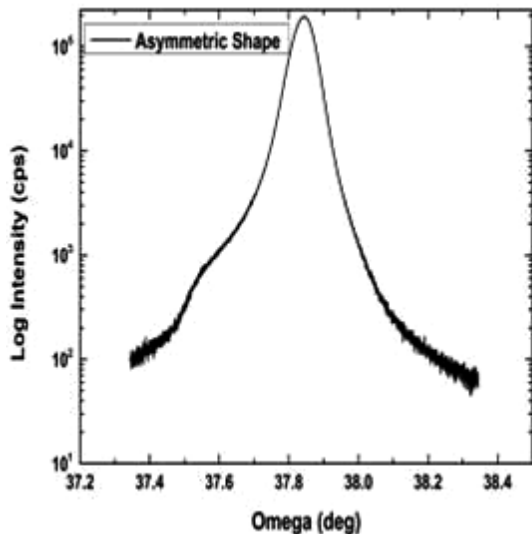
Layer	Layer description	Density (g/cm^3)	Thickness (nm)	Roughness (nm)	Delta (e^{-5})
Substrate	GaAs	5.316	650000	0.041	0
1	Ga_2O_3	6.705	1.957	0.932	1.91302
2	CdTe	5.86	294.82	1.048	1.5618
3	TeO_2	5.806	1.271	3.257	1.65665
4	Oxygen	1.448	30.446	2.526	0.4667

5. REFERENCES

1. Jacobs, R., et al., *Development of MBE II–VI Epilayers on GaAs (211) B.* Journal of Electronic Materials, 2012. **41**(10): p. 2707-2713.
2. Lennon, C., et al., *Real-Time In Situ Monitoring of GaAs (211) Oxide Desorption and CdTe Growth by Spectroscopic Ellipsometry.* Journal of Electronic Materials, 2012. **41**(10): p. 2965-2970.
3. Ryu, Y.S., T.W. Kang, and T.W. Kim, *Structural properties and interfacial atomic arrangements in CdTe thin films grown on GaAs (211) B substrates.* Journal of Materials Science, 2005. **40**(17): p. 4699-4702.
4. Jacobs, R., et al., *Comparative study of thermal mismatch effects in CdTe/Si, CdTe/Ge, and CdTe/GaAs composite structures.*
5. He, L., et al., *MBE HgCdTe on Si and GaAs substrates.* Journal of Crystal Growth, 2007. **301–302**(0): p. 268-272.
6. Choubey, A., et al. *Heteroepitaxial growth and properties of crystals of CdTe on GaAs substrates.* in *Proc. of SPIE Vol.* 2007.

Growth of in-situ Arsenic doped of CdTe/Si by MBE

S. Farrell[1], J. Park[2], T, Barns[1], R. Kodama[2], R. Reedy[1], T. Gessert[1], S. Sivanathan[2], W. Metzger[1]

[1]National Renewable Energy Laboratory (NREL), Golden, CO 80401, USA
[2]EPIR Technologies, Inc. Bolingbrook, IL 60440
[*]Contact: stuart.farrell@nrel.gov

We present the work that NREL has performed on in-situ arsenic (As) doping of CdTe layers grown on silicon by MBE. Arsenic is a promising p-type dopant for the absorber layer in CdTe solar cells if carrier concentrations of at least 10^{16} cm^{-3} can be reproducibly achieved. We have shown high quality layers can be grown with uniform As incorporation of mid to high 10^{16} cm^{-3}. As grown, the As is electrically inactive and requires an ex-situ activation anneal. After activation anneal (~500°C for 10 min) under Hg or Cd over pressures, these layers realize a 50% activation efficiency leading to carrier concentrations in the low to mid 10^{16} cm^{-3}. Following the ex-situ activation anneal, select layers have been coated with an indium doped n-type CdTe layer to form junctions. Preliminary results of these devices will also be presented.

Several parameters have been explored to study the challenges of As incorporation in CdTe. These include the very low sticking coefficient of As (<0.001%), and the tendency for As to induce defects in the crystal structure. We have studied the critical CdTe:As growth parameters, including substrate temperature, Cd over pressure, growth rate, As cracking conditions (flux and temperature), and in-situ annealing cycles. These parameters were optimized to increase As incorporation while retaining high crystal quality. We also provide insights into avoiding run-away As incorporation that can lead to highly defective and/or amorphous layers.

SINGLE CRYSTAL CdTe HOMOJUNCTION STRUCTURES FOR SOLAR CELL APPLICATIONS

Peng-Yu Su[1]*, Rajendra Dahal[1], Gwo-Ching Wang[2], Toh-Ming Lu[2] and Ishwara B. Bhat[1]

[1]Electrical, Computer and Systems Engineering Department

[2]Physics, Applied Physics and Astronomy Department

Rensselaer Polytechnic Institute, Troy, NY 12180

*Corresponding author, Peng-Yu Su. Phone: 518 276 2786; Fax: 518 276 6261; Email: sup@rpi.edu

Cadmium telluride (CdTe) thin film solar cells are very promising because of their low cost and high efficiency. Till date, thin film polycrystalline CdS/CdTe solar cell with 20.4% efficiency has been announced [1]. However, the performance of CdTe solar cells can still be further improved according to theoretical calculation, especially the open circuit voltage (V_{oc}). The low p-type CdTe doping concentration and low minority carrier lifetime are the main reasons resulting in V_{oc} lower than the theoretical prediction. Also, the device performance could be degraded due to the bandgap offset between CdTe and CdS. With use of single crystal CdTe, both high minority carrier lifetimes and high doping concentration can be achieved. Single crystal CdTe/ZnTe/GaAs heterojunction structures have been studied and presented in the 2013 workshop. Amorphous CdS/single crystal CdTe solar cells have also been demonstrated. Nevertheless, the solar cell performance was still limited by the high density of dislocations and non-optimized junctions [2]. In this work, CdTe homojunction structures for solar cell applications grown on GaAs substrates and bulk CdTe substrates will be demonstrated.

The CdTe crystal growth took place in a vertical cold wall CVD reactor equipped with a 3" rotating quartz heater/substrate holder. Dimethylcadmium (DMCd), diethylzinc (DEZn), and diisopropyltelluride (DIPTe) were used as the precursors of Cd, Zn and Te, respectively. Ethyliodide (EI) and arsine (AsH_3) were used as the iodine and arsenic sources for n-type and p-type doping respectively. The growth temperature and pressure were varied from 300℃ to 400℃ and 100 Torr to 500 Torr, respectively. The substrates we used for CdTe growth were GaAs(100) wafers. Before CdTe growth, thin ZnTe buffer layers were first grown on GaAs to ensure the (100) orientated CdTe growth. Other experimental details have been published earlier [2]. With use of arsine as the arsenic source for p-type CdTe, very abrupt doping profile has been observed. Figure 1 shows the secondary ion mass spectrometry (SIMS) analysis results of a specific CdTe structure grown at 400℃ containing an undoped CdTe

buffer layer and five As-doped CdTe layers with different arsine flows varied from 1 standard cubic centimeter per minute (sccm) to 19 sccm. It is clear that five distinct CdTe layers with different As concentrations were observed. This demonstrated that the arsenic atoms are stable in CdTe at the growth temperature of 400℃. Moreover, the arsenic incorporation efficiency in CdTe was a linear function of introduced arsine flows in this range. As compared to using tris(dimethylamino)arsine (TDMAAs) as the As source, arsine was found to provide higher activation efficiency. However, post growth annealing in N_2 ambient at 450℃ for 30 s was still required to activate the dopants. The highest hole concentration obtained from CdTe:As was ~6×10^{16} cm^{-3}.

On the other hand, the properties of iodine-doped n-type CdTe were very sensitive to the growth conditions. The as-grown CdTe:I grown at 400℃ and 100 Torr was very resistive. Post-growth annealing at 550℃ under Cd-overpressure was required to activate the dopant. It resulted in a doping concentration of 2.4×10^{16} cm^{-3} and mobility of 735 cm^2/Vs. With higher growth temperature, the Cd-vacancies in CdTe may compensate the dopants and thus result in high resistive as-grown CdTe. After annealing in Cd-overpressure, the Cd-vacancies were anhilated and the sample became more n-type. However, the high temperature processes are not desirable due to the undesirable diffusion of dopants. Instead, the CdTe:I grown at 300℃ and 500 Torr showed n-type behavior without additional post-growth annealing. The electron concentration and mobility was 1.7×10^{16} cm^{-3} and 570 cm^2/Vs, respectively. It's worth noting that these n-type CdTe samples are not stable at higher temperature. The n-type CdTe samples became highly resistive after annealing at 450℃ for 30 s in N_2 ambient. Table 1 summarizes the Hall measurement data before and after annealing. Both mobility and carrier concentration decreased after annealing. Further results and discussion of device fabrication and characterizations are being carried out and will be presented in the conference.
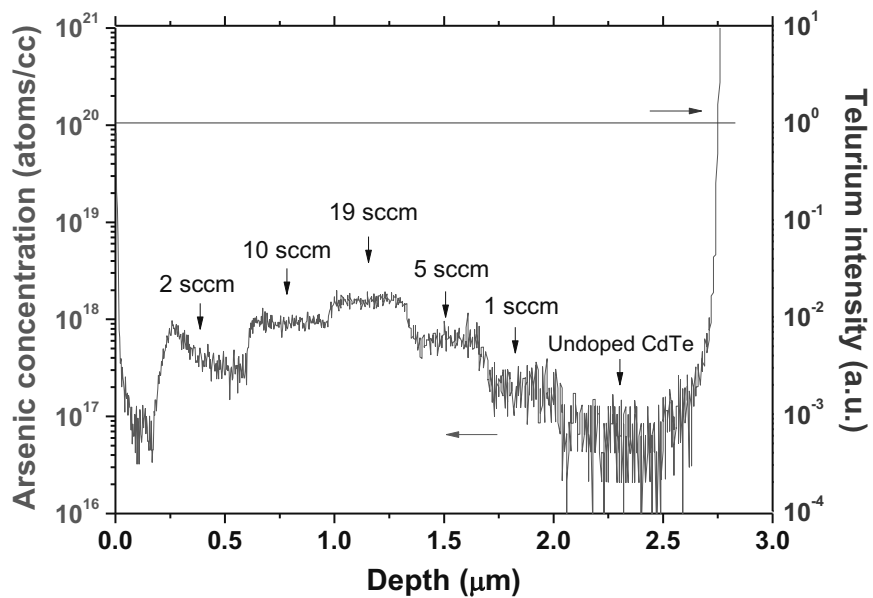
Figure 1. SIMS results of a specific CdTe structure grown at 400℃ containing an undoped CdTe layer and five As-doped CdTe layers with different arsine flows varied from 1 sccm to 19 sccm.

	Resistivity (Ω-cm)	Mobility (cm^2/Vs)	Concentration (cm^{-3})
Before annealing	0.7	567.3	1.7×10^{16}
After annealing	136.2	286.4	1.6×10^{14}

Table 1. Hall measurement results of n-type iodine-doped CdTe before and after annealing at 450℃, 30 s.

References

[1] "First Solar Sets Thin-Film Module Efficiency World Record of 17.0 Percent." http://investor.firstsolar.com/releasedetail.cfm?ReleaseID=833971. Accessed 19 March 2014.

[2] P.-Y. Su, C. Lee, G.-C. Wang, T.-M. Lu and I. Bhat, J. Electron. Mater., DOI: 10.1007/s11664-014-3142-1 (2014).

Optimization of HgCdTe-based nBn detectors for MWIR applications

N. Dehdashti Akhavan*, G. Jolley, G. Umana-Membreno, J. Antoszewski, L. Faraone

M018, University of Western Australia, 35 Stirling Hwy, Crawley, WA, 6009

*phone: +61864883748 , Fax: +61864881095 , email: nima.dehdashti@uwa.edu.au

Abstract

We present theoretical modelling and optimization of mercury cadmium telluride (HgCdTe) unipolar n-type/Barrier/n-type (nBn) infrared detectors for applications in the mid-wave infrared band (3~5µm). The calculations, implemented using the commercial Synopsis TCAD simulation platform, included all dominant generation-recombination (G-R) mechanisms that affect the operation of practical HgCdTe detectors, including: Shockley-Read-Hall (SRH), band-to-band tunneling, trap-assisted tunneling (TAT), as well as radiative and Auger processes [1]. Temperature-dependent, field-dependent and-doping dependent carrier mobility models were also included. The results indicate that optimization of the barrier composition, barrier doping, and barrier width in HgCdTe nBn detectors can enable performance levels similar to ideal p-n photodiodes even in the presence of the valence band discontinuity at the absorber/barrier heterojuction. For absorber doping densities higher than 10^{16} cm^{-3}, detector performance was found to be limited by BTBT and Auger processes. These two mechanisms lead to increasingly higher dark current levels as the absorber doping level is increased beyond 10^{16} cm^{-3}. Figures 1 and 2 show the dark current density and detectivity versus temperature. We can observe that the dark current in our modelled nBn is close to the values predicted by Rule 07 [2]. Figure 3 shows the dynamic resistance which corroborates with those predicted by Rule 07 and saturates for absorber doping level of 10^{16} cm^{-3} [2,3]. Figure 4 shows that our simulation results are in good agreement with previously published data available for HgCdTe based nBn detectors operating at 5µm cut-off wavelength [2,3,4].

References

[1] A. M. Itsuno, J. D. Phillips, and S. Velicu, Journal of Electronic Materials, vol. 40, no. 8, pp. 1624-1629, 2011..

[2] W. E. Tennant , Journal of Electronic Materials, Volume 39, Issue 7, pp 1030-1035, 2010.

[3] P. MARTYNIUK,1,2 W. GAWRON,1 and A. ROGALSKI, Journal of ELECTRONIC MATERIALS, Vol. 42, No. 11, 2013.

[4] Anne M. Itsuno et. Al, Appl. Phys. Lett. 100, 161102 (2012); doi: 10.1063/1.4704359.
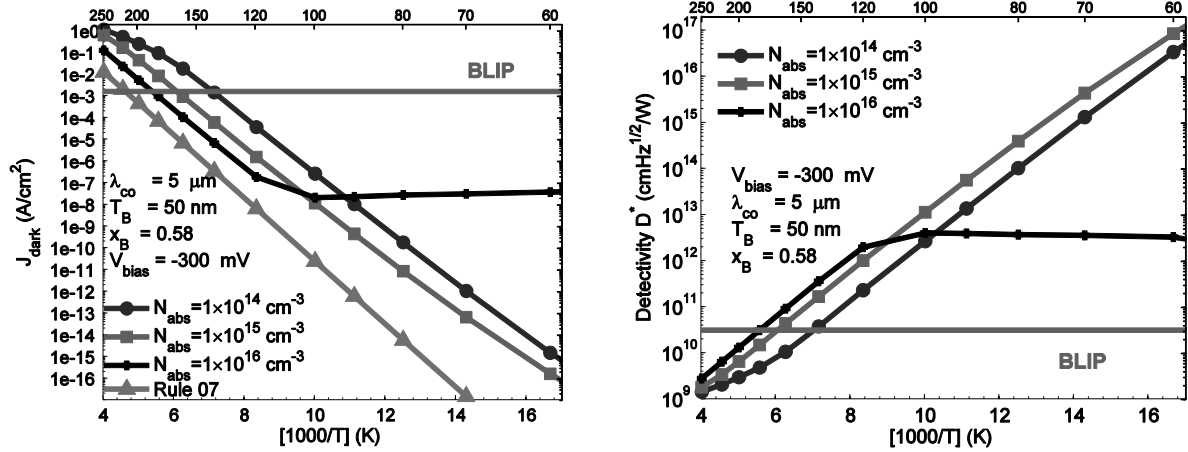
Figure 1 and 2. (left) Total dark current *vs.* temperature MWIR *n*B*n* detector at cut-off wavelength of 5 *μ*m and comparison with Rule 07. (Right) Detectivity *vs.* temperature for MWIR nBn detector with different absorber doping density. Auger, BTBT generation-recombination mechanisms degrade the performance of detector for absorber doping densities larger than 10^{16} cm^{-3}.
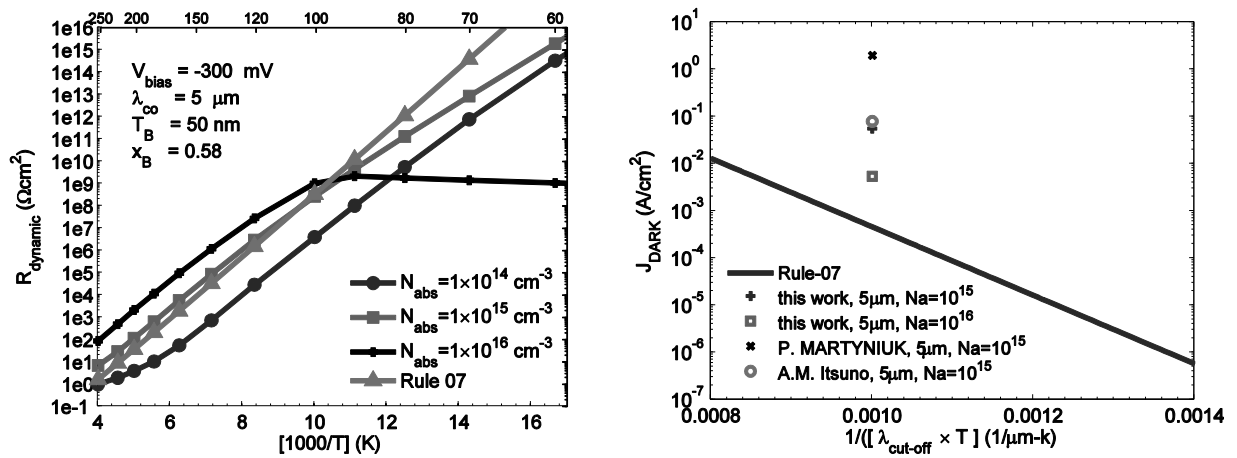
Figure 3 and 4. (left) Dynamic resistance *vs.* temperature for MWIR nBn detector at cut-off wavelength of 5 *μ*m and comparison with Rule 07. (Right) Comparison of dark current for MWIR *n*B*n* detector from different theoretical studies at T=200 K. P. Martinuk has reported higher dark current compare to this work and A.M. Itsuno due to incorporation of inappropriate barrier parameters.

A new nBn IR detection concept using HgCdTe material

O. Gravrand, F. Boulard, A. Ferron, Ph. Ballet, W. Hassis

CEA-LETI-Minatec Campus
17 rue des martyrs, 38054 Grenoble France

Olivier.gravrand@cea.fr

We present here a new HgCdTe based heterostructure to perform quantum IR detection. This structure is based on the unipolar barrier concept, imagined by White in the 80[th][*A. M. White, "IR detector," Patent, vol. US4679063, 1987*.] The driving idea is the use of a large gap barrier layer to impede the flow of majority carriers (electrons on the conduction band in the case of a N type material) while facilitating the transport of minority (photo) carriers (holes on the valence band). The issue encountered here is the formation of a small potential barrier on the valence band, blocking photocarriers and therefore killing the quantum efficiency. The idea here is to optimize the structure with the design of an asymmetric barrier: abrupt on the contact side to efficiently block the majority carriers, and gradual on the absorption layer side to plane down the remaining potential barrier for the photocarriers. The concept has been studied by FEM simulation and showed promising results. An optimal design has been identified in the MW band and few MBE layers have been grown then processed. First experimental characterization of the EO properties of such structures will be presented.

MEASUREMENT OF VERTICAL AND HORIZONTAL TRANSPORT PARAMETERS IN TYPE-II SUPERLATTICES

C. H. Swartz* and T. H. Myers

Materials Science, Engineering, & Commercialization Program, Texas State University

RFM 3205, Texas State University, 601 University Drive, San Marcos, TX 78666

*v: (512) 245-1839; f: (512) 245-3675; <u>*craig.swartz@txstate.edu*</u>

Abstract: A novel magnetotransport method is developed which determines both vertical and horizontal mobilities in a strained-layer superlattice (SLS). GaSb/InAs-based LWIR SLS structures were characterized using this method. A very high horizontal-to-vertical mobility anisotropy ratio was evident for conduction electrons.

In a strained-layer superlattice (SLS), carrier mobility (μ) can vary strongly between the vertical and horizontal directions. [1] While the horizontal mobility can be found from standard Hall effect techniques, sometimes by employing a variable magnetic field, [2] the measurement of vertical mobility in a thin film is much more challenging.

A novel magnetotransport method is developed which determines both vertical and horizontal mobilities in any anisotropic film, including a SLS. [3] To carry it out, one fabricates a circular mesa of radius r, leaving a thin contact layer to be covered by a large area ohmic contact. A second ohmic contact is deposited on top of the mesa. When a magnetic field B is applied at an angle θ, The total resistance between the contacts becomes:

$$R_{TOT} = \frac{R_S}{2\pi}\left[\frac{L_T}{r}\frac{I_0(r/L_T)}{I_1(r/L_T)} + \frac{K_0(r/L_T)}{K_1(r/L_T)}\frac{L_T}{r+d} + \ln\left(1+\frac{d}{r}\right)\right] \tag{1}$$

Where

$$L_T{}^2 = t\frac{1+\left(\mu_{\parallel}B\cos\theta\right)^2 + \mu_{\parallel}\mu_{\perp}B^2\sin^2\theta}{R_S\sigma_0\left(1+\left(\mu_{\parallel}B\cos\theta\right)^2\right)} \tag{2}$$

And

$$R_S = \frac{1+(\mu_S B\cos\theta)^2}{\sigma_{S0}} \tag{3}$$

The gap between the mesa and a large area metallization is d, and I and K are the modified Bessel functions of the first and second kind.^Error! Bookmark not defined. Fortunately, the Bessel function ratios simplify to one for $r \gg L_T$. The thickness is t, and σ_o and σ_{So} are the volume and sheet conductivities of the film and contact layer, respectively.

The intensity and the angle of an applied magnetic field are varied, and a single analysis routine yields the horizontal and vertical transport parameters. If a bottom contact layer is deposited under the SLS, it may be characterized as well. The method may be extended to any anisotropic thin film with arbitrary substrate conductivity.

GaSb/InAs-based LWIR SLS structures, doped in the n-i-n pattern, were characterized using this magnetotransport method. A very high horizontal-to-vertical mobility anisotropy ratio was evident for conduction electrons, as well as evidence of a dependence of mobility on carrier concentration, as predicted from theory. [1]
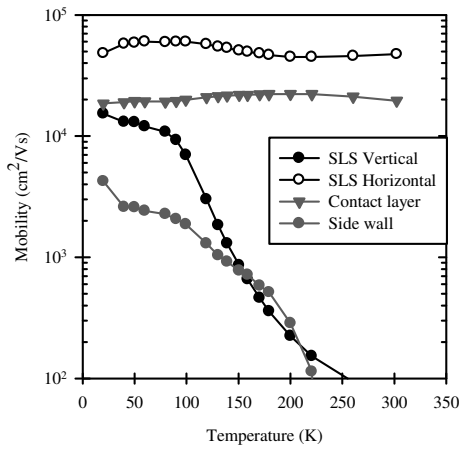
Fig. 1 –Extracted mobility as a function of temperature, including both horizontal and vertical mobilities. The very high predicted horizontal-to-vertical mobility anisotropy ratio is evident.
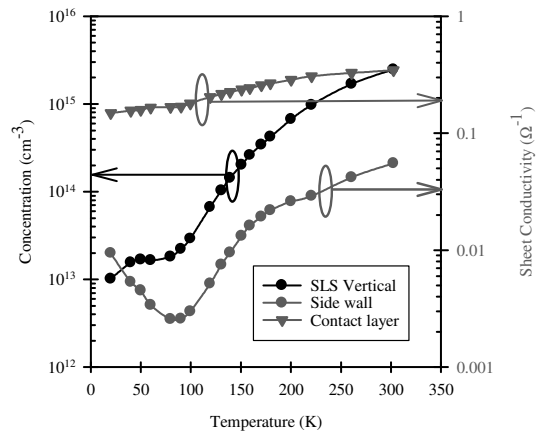
Fig. 2 – Extracted carrier concentration (n) as a function of temperature. For the thin side wall and bottom contact layers, carrier concentration was expressed in terms of sheet conductivity.
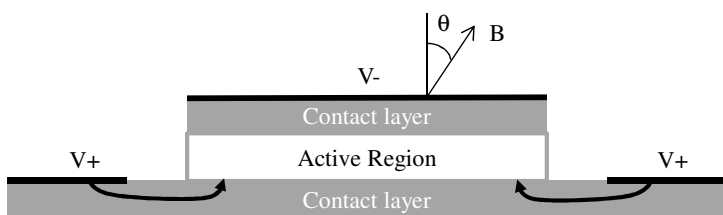
Fig. 3. A sandwich structure for GMR. Contact layers, often heavily doped, surround an Active Region (AR), such as a SLS.
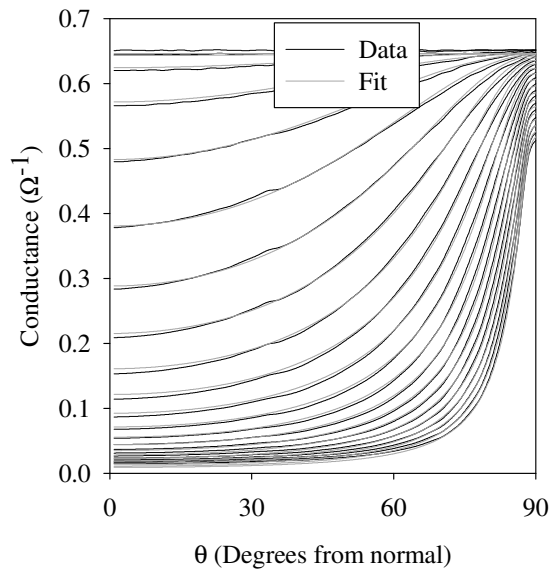
Fig. 4 – Angular dependence of geometric

magnetoresistance at 20 values of the magnetic

field from 0 to 9 Tesla.

---

[1] F. Szmulowicz, H. J. Haugan, S. Elhamri, and G. J. Brown, Phys. Rev. B 84, 155307 (2011).

[2] T. V. Chandrasekhar Rao, J. Antoszewski, L. Faraone, J. B. Rodriguez, E. Plis, and S. Krishna, Appl. Phys. Lett. 92, 012121 (2008)

[3] C. H. Swartz and T. H. Myers, Phys. Rev. B 89, 075305 (2014).

Minority Carrier Extraction in Unipolar Barrier Infrared Detectors

D. Z. Ting*, A. Soibel, L. Höglund, and S. D. Gunapala

Center for Infrared Photodetectors, NASA Jet Propulsion Laboratory

California Institute of Technology, 4800 Oak Grove Drive, Pasadena, CA 91109, USA

*David.Z.Ting@jpl.nasa.gov; phone 1.818.354.1549

ABSTRACT

We examine some issues related to minority carrier collection in unipolar barrier infrared photodetectors theoretically. In a barrier infrared detector such as the nBn [1] and the CBIRD [2], the barrier should block only majority carriers and allow the un-impeded flow of minority carriers. However, an imperfect barrier would also block minority carriers, resulting in higher turn-on bias as has been observed in both MWIR and LWIR devices [2, 3].   Minority carrier blocking can be caused by (1) barrier doping, and/or (2) un-intended band offset between the barrier and the absorber. The distinct manner in which these two mechanisms affect device performance are seen in Figure 1, which shows the calculated energy band diagrams and current density-voltage characteristics for two sets of nBn devices, one with different barrier doping levels, the other with different barrier-absorber valence band offsets.   The results are clarified by examining the Shockley-Read-Hall recombination rates, and electron and hole densities, shown in Fig. 2. Under the right conditions, barrier doping can reduce generation-recombination dark current without affecting minority carrier extraction.   Minority carrier transport also depends on lifetime and mobility. It is a commonly held belief that hole mobility in an n-doped type-II superlattice (T2SL) is very low because of the extremely large vertical effective mass. Yet MWIR and LWIR n-type T2SL detectors have shown reasonable optical responses [4, 5].   A closer inspection of the T2SL band structure offers a possible explanation as to why the hole mobility (while still low) may not be as poor as suggested by the simple effective mass picture.

Keywords: infrared detector, type-II superlattice, unipolar barrier, mid-wavelength infrared, long-wavelength infrared

[1] S. Maimon and G. W. Wicks, *Appl. Phy. Lett.* **89**, 151109 (2006).

[2] D. Z.-Y. Ting, C. J. Hill, A. Soibel, S. A. Keo, J. M. Mumolo, J. Nguyen, and S. D. Gunapala, *Appl. Phy. Lett.* **95**(2), 023508 (2009).

[3] D. Z.-Y. Ting, A. Soibel, S. A. Keo, A. Khoshakhlagh, C. J. Hill, L. Höglund, J. M. Mumolo, S. D. Gunapala, *J. Elect. Mat*. 42(11) 3071-3079 (2013).

[4] J. B. Rodriguez, E. Plis, G. Bishop, Y. D. Sharma, H. Kim, L. R. Dawson, and S. Krishna, *Appl. Phy. Lett.* **91**, 043514 (2007).

[5] H. S. Kim, O. O. Cellek, Zhi-Yuan Lin, Zhao-Yu He, Xin-Hao Zhao, Shi Liu, H. Li, and Y.-H. Zhang, , *Appl. Phy. Lett.* **101**, 161114 (2012).
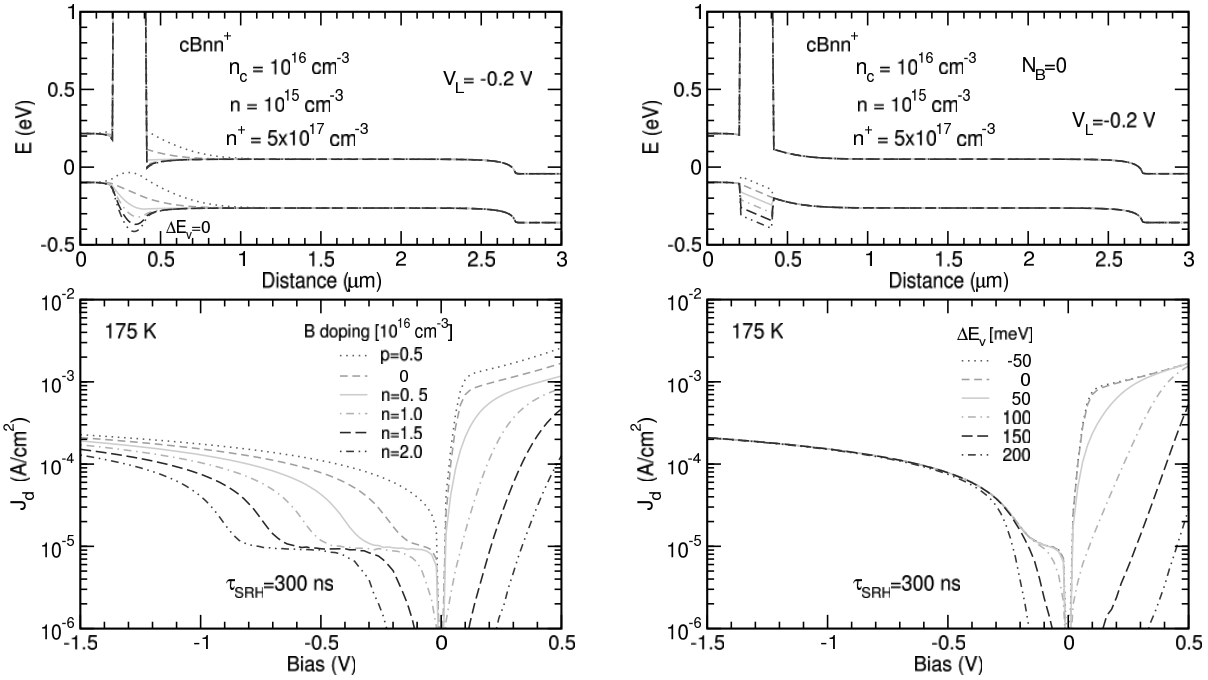
Figure 1 Calculated energy band diagrams (-0.2 V) and current density-voltage characteristics for nBn structures with different barrier doping (left) and different barrier-absorber valence band offset (right).
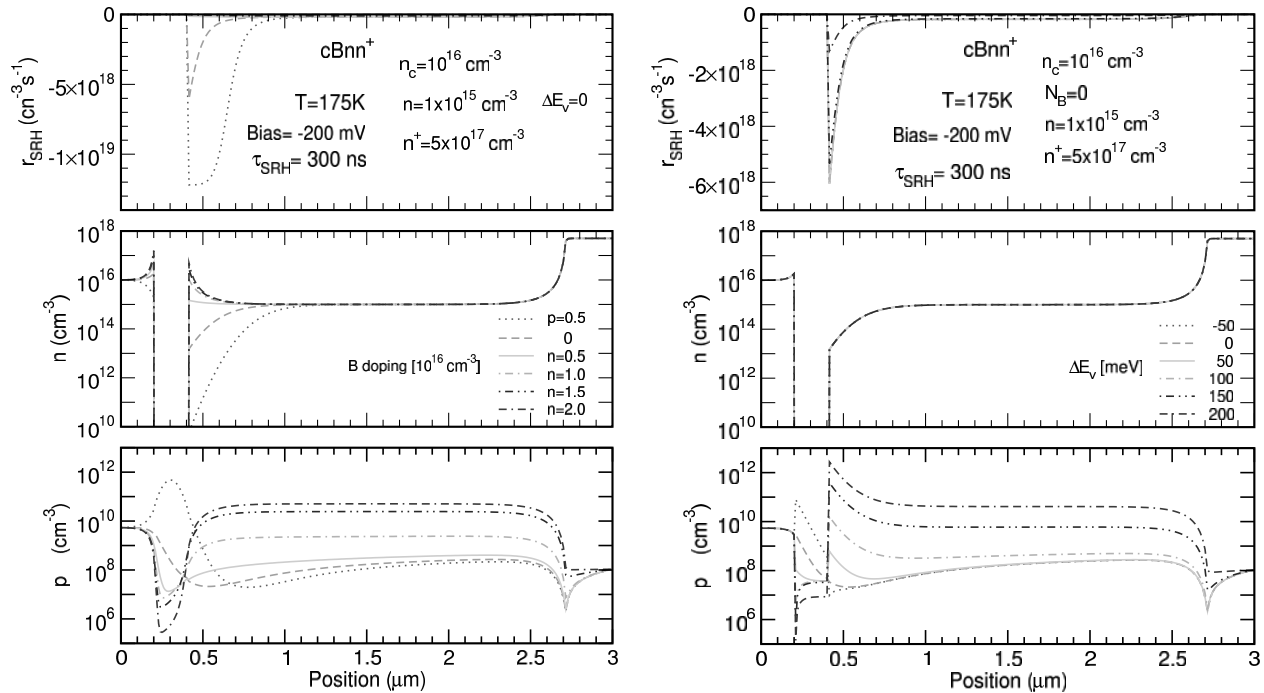
Figure 2 Calculated SRH recombination rate and carrier densities for nBn structures with different barrier doping (left) and different barrier-absorber valence band offset (right). The applied bias is -0.2 V.

Electronic transport characterization of InAs/InGaSb superlattices for VLWIR

Hemendra Kala (1), Gilberto A. Umana-Membreno (1), Mikhail Patrashin (2),
Iwao Hosako (2), Kouichi Akahane(2), Jarek Antoszewski (1), Lorenzo Faraone (1)

1. School of EEC Eng., The University of Western Australia,
35 Stirling Hwy, Crawley WA 6009

2. National Institute of Information and Communications Technology,
4-2-1 Nukui-Kitamachi, Koganei, Tokyo 1848795, JAPAN

InAs/(In)GaSb Type-II superlattices are an important material system for high-performance infrared radiation detectors, with performance levels that are predicted to rival those of HgCdTe. For applications in the very long wavelength infrared (VLWIR) and terahertz region of the electromagnetic spectrum, InAs/(In)GaSb Type-II superlattices (T2SL) offer flexible tunability of their effective bandgap which is easier to achieve than in conventional HgCdTe-based detectors. [1] There are however few report on the electronic properties of InAs/(In)GaSb Type-II superlattices designed for very long wavelength sensing.

In this work, we present results of a study of in-plane electronic transport in InAs/InGaSb Type-II superlattices designed for VLWIR. The samples studied were grown by molecular beam epitaxy on (100) GaSb substrates, and consisted of 500nm GaSb buffer layer, followed by 40 superlattice periods, and terminated with a 20 nm InAs cap layer. The superlattice period was defined by 4.21 nm InAs and 2.51 nm $In_{0.35}Ga_{0.65}Sb$.

In order to unambiguously discriminate the transport characteristics of the superlattice region from the p-type substrate, magnetic field dependent measurements and high resolution mobility spectrum analysis (HR-MSA) were performed on the same wafer before and after wet-chemical removal of the superlattice material. In the material without the SL layer, two hole carrier peaks were detected which are attributable to heavy and light holes. Although the contribution from substrate holes was found to dominate sample conductivity (representing over 95% of total conductivity at 300K), two additional electron species with mobilities of 8,200cm^2/Vs and 15,630cm^2/Vs were detected at 300K in the sample with the superlattice layers (Fig. 1). These electron species have been attributed to the 20nm InAs cap layer and the 269nm superlattice region, respectively.

From the temperature dependence of electron sheet density (Fig. 2), the superlattice miniband was found to transition from a semiconductor with a energy bandgap of 25meV at T ~ 60K, to a semi-metal with a negative bandgap for T > 150K. These results are consistent with the calculated temperature dependent bandgap using 8-band k.p simulations (Fig. 3), and yield parameters that are consistent with Varshni parameters reported for relatively wider bandgap InAs/(In)GaSb Type-II superlattices [2].

[1] A. Rogalski, Opto-Elect. Rev. 16, pp. 458–482, 2008.

[2] B. Klein, E. Plis, M. N. Kutty, N. Gautam, A. Albrecht, S. Myers, and S. Krishna, J. Phys. D 44(7), 075102, 2011.
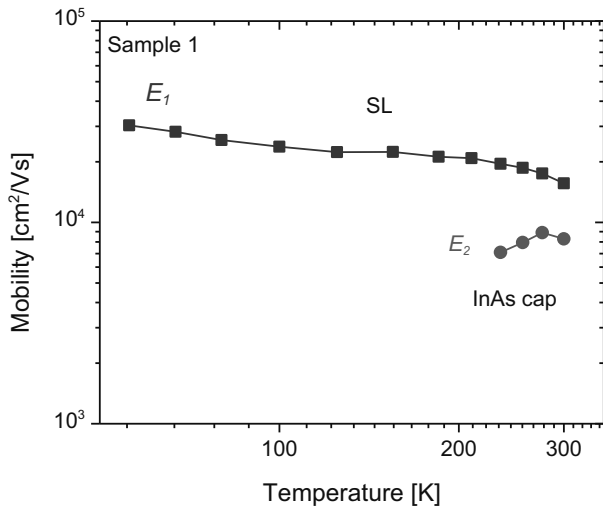
Fig. 1 Temperature dependence of the mobility of the electron species detected by HR-MSA
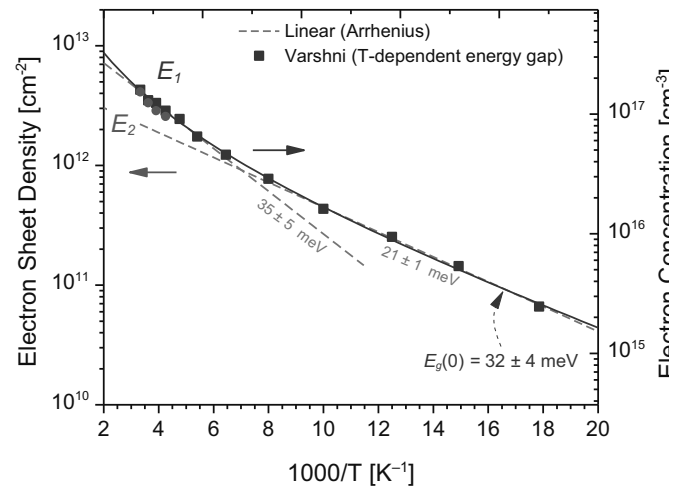
Fig.2 Electron concentration and sheet density for electrons attributed to the T2SL layer and InAs cap layer, respectively. The electron concentration in the superlattice exhibited a Varshni-like energy dependence.
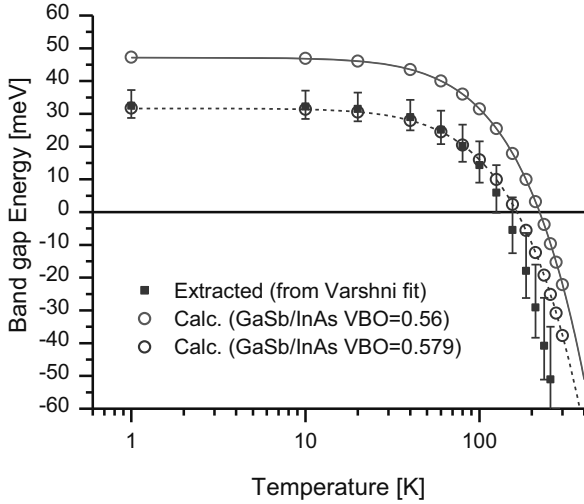
Fig.3 Temperature dependence of the superlattice bandgap energy from the extracted Varshni parameters, and from 8-band k.p calculations. For the calculations, a small adjustment to the InAs/GaSb valence band offset yields results that are in excellent agreement with experimentally determined values.

Development of Long Wavelength Imaging Using Type-II Superlattice Based Complementary Barrier Infrared Detectors

C.J. Hill, A. Fisher, L. Höglund, S. A. Keo, A. Khoshakhlagh, J. Liu, J. Mumolo,
S. B. Rafol, A. Soibel, D. Z. Ting, and S. D. Gunapala

cory.j.hill@jpl.nasa.gov – 818 393 7121

Jet Propulsion Laboratory, California Institute of Technology, Pasadena, California 91109, USA.

Abstract: The InAs/GaSb type-II superlattice-based complementary barrier infrared detector (CBIRD) has previously demonstrated excellent performance in long-wavelength infrared (LWIR) detection. Progress in the design and material growth of these detectors has enabled LWIR devices with cutoffs near 10 μm that have near zero bias operation and exhibit a dark current density of less than 1×10^{-5} A/cm^2 at 77 K. In this paper we report on the growth, material characterization, single device and array performance of typical infrared photodetectors using the CBIRD design.

Keywords: superlattice, infrared, focal plane array, photodetectors, GaSb, InAs.

1. INTRODUCTION

The antimonide material system consists of the nearly lattice-matched semiconductors of InAs, GaSb, and AlSb (and their pseudomorphic alloys with InSb, AlAs, and GaAs). It is often referred to as the 6.1 Å material system[1], since InAs, GaSb, and AlSb all have lattice constants of approximately 6.1 Å. High quality, epitaxy-ready GaSb substrates commercially available in 50, 75 and 100mm diameters have enabled the development of a variety of semiconductor devices grown by techniques such as Molecular Beam Epitaxy (MBE). Additionally, the antimonides have emerged recently as a highly effective platform for the development of sophisticated heterostructure-based mid-wavelength infrared (MWIR) and long-wavelength infrared (LWIR) detectors, as exemplified by the high-performance double heterostructure (DH)[2], nBn[3], XBn[4], and type-II superlattice (SL) infrared detectors[5-8]. A key enabling design element is the unipolar barrier[9], which is used to implement the barrier infrared detector (BIRD) design for increasing the collection efficiency of photo-generated carriers, and reducing dark current generation without impeding photocurrent flow. In this paper, we examine the growth, material quality, device and array performance of LWIR antimonide superlattice detectors based on the complementary barrier infrared detector (CBIRD) design.

2. COMPLEMENTARY BARRIER INFRARED DETECTOR (CBIRD)

The active region of the CBIRD design consists of a p-type InAs/GaSb long wave-length infrared (LWIR) absorber SL sandwiched between an n-type InAs/AlSb hole-barrier (hB) SL (which also serves as the top contact) and a p-type InAs/GaSb electron-barrier (eB) SL. The hB SL and the eB SL are respectively designed to have approximately zero conduction and valence subband offset with respect to the absorber SL, i.e., they act as a pair of complementary unipolar barriers with respect to the absorber SL. Underneath the active region is a ~ 1μm thick highly n-doped InAsSb bottom contact region, which is connected to the eB SL via a broken-gap tunnel junction. The entire structure, as depicted in *Figure 1*, is grown on a GaSb substrate via MBE, with an n-type GaSb buffer layer which is not electrically active.

3. DEVICE CHARACTERISTICS

Photoluminescence (PL), Quantum Efficiency (QE), and dark current density (J_d) measurements for a CBIRD device are shown in *Figure 2*. The CBIRD structure[10] was grown on a Te-doped GaSb(100) substrate in a Veeco Applied-Epi Gen-III molecular beam epitaxy chamber equipped with valved cracking sources for the group V Sb2 and As2 fluxes. The active region of the structure consists of a 300-period (44Å, 21Å)-InAs/GaSb absorber SL sandwiched between an 80-period (46Å,12Å)-InAs/AlSb hole barrier SL on top and a 60-period (22Å, 21Å)-InAs/GaSb electron barrier SL on the bottom. At 77K the LWIR mesa devices exhibited a peak PL at 9.6μm, a 50% peak QE cutoff at 9.8μm with the device fully turned on at zero bias. At a bias of 0.1V, which is in the range typically necessary for imaging uniformity in focal plane array (FPA) operation, the device exhibited a dark current density of $8x10^{-6}$ A/cm^2.

4. ARRAY PERFORMANCE

An older CBIRD device structure grown on a 100 mm GaSb wafer was used to fabricate a 320 × 256 LWIR Focal Plane Array (FPA). The detector array was hybridized to a FLIR/Indigo ISC0903 Read Out Integrated Circuit (ROIC) and the hybridized FPA was epoxy under-filled and the substrate was completely removed with the removal process ending on an epitaxially grown etch-stop layer. The FPA was thermally cycled more than 30 times and no noticeable physical or electro-optical degradations were observed. The array displayed a maximum QE of 54% at 5.4μm, and a cut-off wavelength (50% of peak QE) near 8.8μm, with a QE Full-Width-Half-Maximum (FWHM) from roughly from 4.4μm to 8.8μm.

Sample imagery as well as the experimentally measured Noise Equivalent Temperature difference (NEΔT) histograms distributions of the CBIRD FPA at 78 K operating temperature, 128 mV bias, and 370 μsec integration time, with blackbody temperature at 298 K and an f/2 cold stop is shown in *Figure 3*[11]. A mean NEΔT of 18.6 mK and 12 mK was achieved at FPA operating temperature of 78 K and 65 K, respectively. The results demonstrate that the antimonide-based CBIRD structure can be used to produce imaging arrays with performance characteristics suitable for many challenging LWIR applications.

5. FIGURES
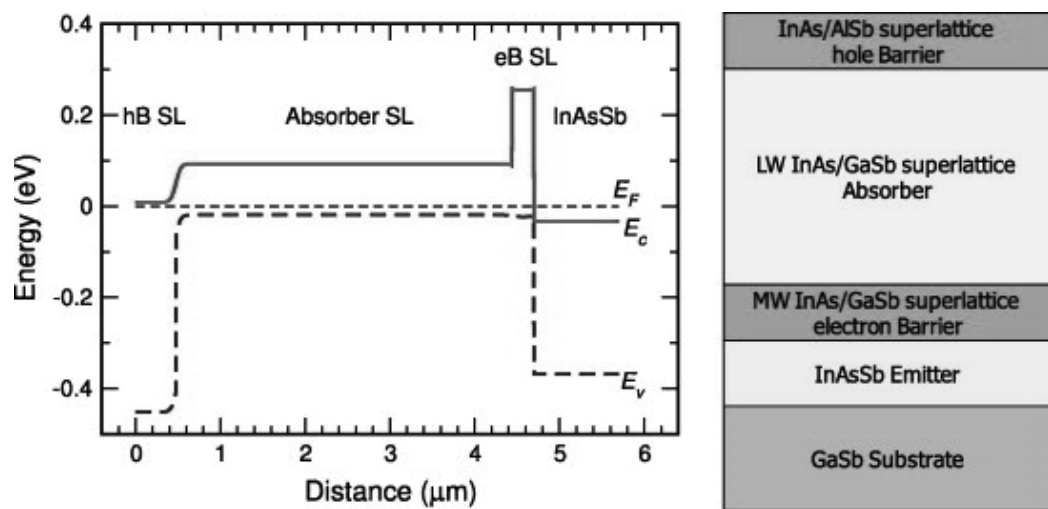
Figure 1: (left) Calculated zero-bias energy band diagram and (right) a schematic device structure layer diagram for the CBIRD.
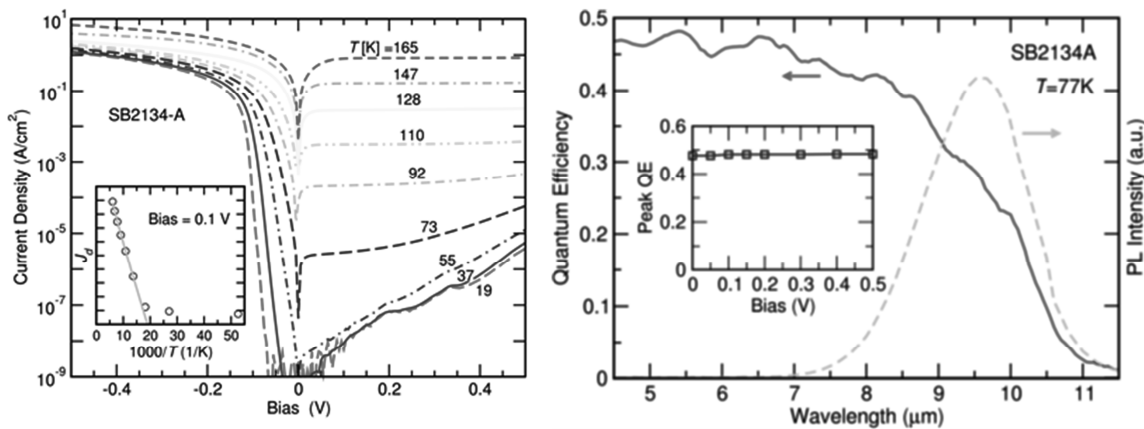
Figure 2: (left) Dark current density (J_d) as a function of applied bias at various temperatures. Inset shows the temperature dependence of J_d at a bias of 0.1V. (right) 77K photoluminescence spectrum and QE. Inset shows top-illuminated spectral QE as a function of applied bias.
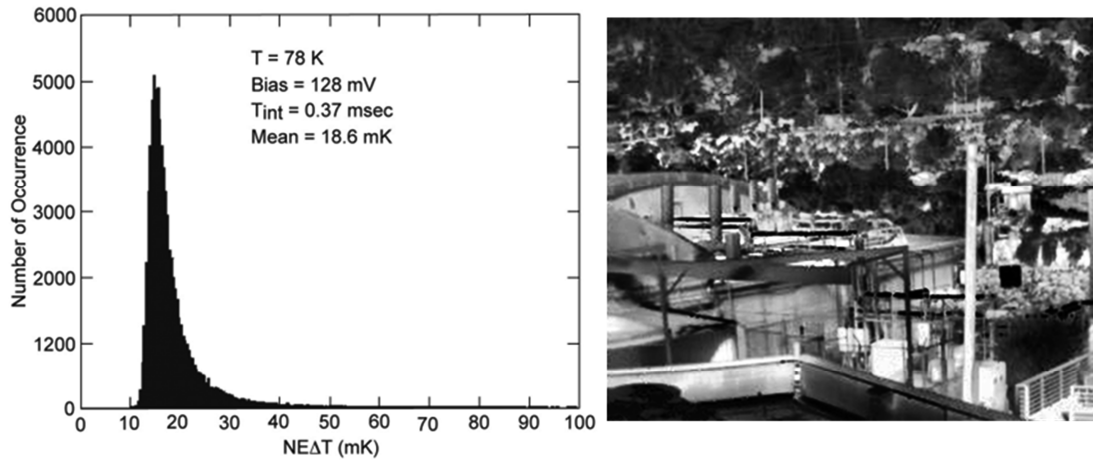
Figure 3: (left) 78K NEΔT *histogram and (right) contrast-optimized outdoor imagery from a 320x256 LWIR CBIRD array.*

6. REFERENCES

[1] H. Kroemer, Physica E, **20** 196 (2004).

[2] M. Carras, J.L. Reverchon, G. Marre, C. Renard, B. Vinter, X. Marcadet, V. Berger, Appl. Phys. Lett., **87** 102103 (2005).

[3] S. Maimon, G.W. Wicks, Appl. Phys. Lett., **89** 151109 (2006).

[4] P. Klipstein, Proc. SPIE, **6940** 69402U (2008).

[5] F. Fuchs, U. Weimer, W. Pletschen, J. Schmitz, E. Ahlswere, M. Walter, J. Wagner, P. Koidl, Appl. Phys. Lett., **71** 3251 (1997).

[6] P.-Y. Delaunay, B.M. Nguyen, D. Hoffman, E.K.-W. Huang, M. Razeghi, IEEE J. Quantum Electron., **45** 157 (2009).

[7] C.L. Canedy, E.H. Aifer, I. Vurgaftman, J.G. Tischler, J.R. Meyer, J.H. Warner, E.M. Jackson, J. Electron. Mater., **36** (8) 852 (2007).

[8] C.J. Hill, A. Soibel, S.A. Keo, J.M. Mumolo, S.D. Gunapala, D.R. Rhiger, R.E. Kvaas, S.F. Harris Proc. SPIE, **6940** 69400C (2008).

[9] D.Z.-Y. Ting, C.J. Hill, A. Soibel, S.A. Keo, J.M. Mumolo, J. Nguyen, S.D. Gunapala Appl. Phys. Lett., **95** 023508 (2009).

[10] D.Z.-Y. Ting, A. Soibel, A. Khoshakhlagh, J. Nguyen, L. Höglund, S.A. Keo, J.M. Mumolo, S.D. Gunapala, Appl. Phys. Lett., **102** 121109 (2013).

[11.] S.B. Rafol, A. Soibel, A. Khoshakhlagh, J. Nguyen, J.K. Liu, J.M. Mumolo, S.A. Keo, L. Höglund, D.Z.-Y. Ting, S.D. Gunapala, IEEE J. Quant. Electron., **48** 878 (2012).

Interfacial Defects and Elemental Composition of Chemically Treated CdZnTe Crystals

A. Hossain, A. E. Bolotnikov, G. S. Camarda, Y. Cui, R. Gul, U. N. Roy, G. Yang, and

R. B. James

Brookhaven National Laboratory, Upton, NY

EXTENDED ABSTRACT

Cadmium Zinc Telluride (CZT) is the leading semiconductor material used for X- and gamma-ray detectors operating at room temperature [1-2]. In addition, it often is used as a substrate material for infra-red active/passive sensor devices due to its lattice-match with mercury cadmium-telluride epilayers [3-4]. However, some problems remain related to its bulk- and surface-properties that affect its widespread deployment in both applications. In this work, we focused on exploring various defects that extend into the near-surface region, and also investigated the surface- and interface-structures after processing the sample via mechanical- and chemical-polishing. We investigated different methods for generating an ideal, smooth, non-conductive surface for growing thin films and depositing contacts. We determined the surface's features and chemical species by the following methods: atomic force microscopy (AFM), X-ray photoelectron spectroscopy (XPS), and scanning electron-microscopy (SEM), coupled with energy-dispersive spectroscopy (EDS) and wavelength-dispersive spectroscopy (WDS). Also, we revealed various defects on the CZT crystals' surfaces after employing selected chemical etchants, and then analyzed these defects by high-spatial-resolution X-ray response mapping, X-ray diffraction, and scanning electron-microscopy (SEM).

We scanned for the presence of compositional elements over the surface area ($2x2$ cm^2) of the chemically treated CZT surface using electron dispersive spectroscopy in the high current mode. Fig. 1 displays the distribution of individual elements composing the CZT's surface. We compared the distribution of Cd and Te and their ratio before and after the chemical treatment. We localized the compositional variations in Cd and Te at the nanoscale level in our particular detector-crystal. The variations likely were due to material-strain field and secondary-phase defects. Ultimately, we are working to correlate compositional variation with the material's non-uniformity and eventually to determine the influence of such material features on the response of the fabricated detectors.
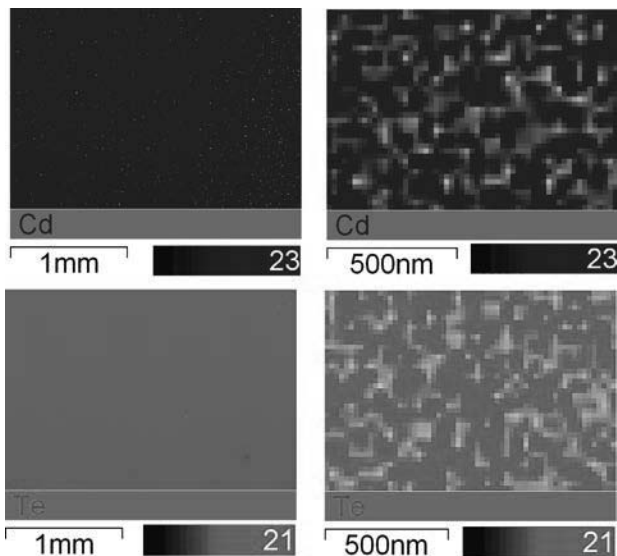
Fig. 1. Images of elemental mapping of a CZT crystal by electron dispersive spectroscopy. Non-homogeneous elemental distribution was revealed in nano-scale mapping.

Also, we obtained XPS measurements of untreated- and treated-CZT surfaces and compared the ratio of Te/Cd to observe the change of the surface chemistry of CZT

surfaces (Fig. 2). The stoichiometric ratio of (Te/Cd) of a chemical-etched surface was estimated as 1.20 that decreased to 1.07 after passivation by the NH_4F agent.
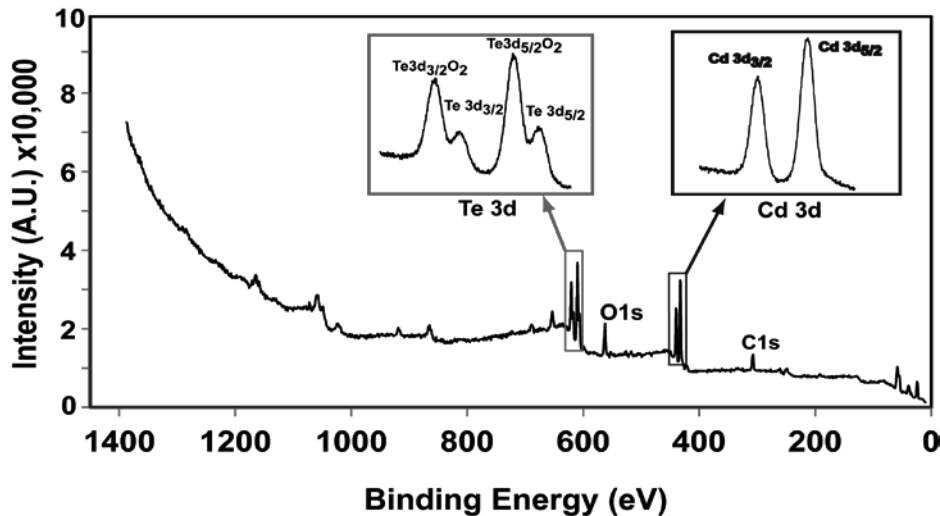
Fig. 2. The spectra from x-ray photoelectron spectroscopy measurements of a chemically treated CZT crystal. The Tellurium 3d doublet is partially shifted to a higher binding energy forming a stable TeO_2, but the Cd 3d doublet remained the same.

We also analyzed the diffusion profile of the contact metals that were deposited on the chemically treated surfaces. Fig. 3 demonstrates some of our results on the oxidation of chemically treated surfaces and the diffusion of metals at the interface.
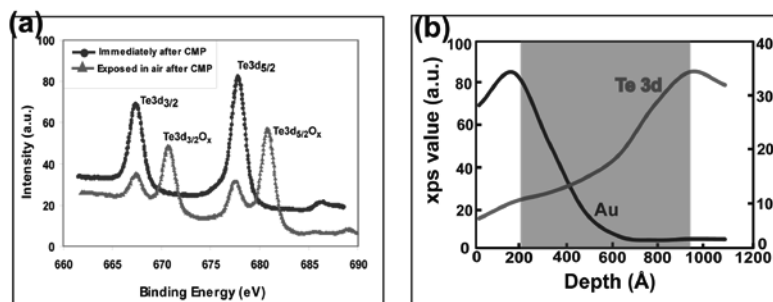
Fig. 3: (a) CZT surfaces were oxidized after chemical polishing. (b) Depth profile of Au into CZT surface. Mutual diffusion occurs after depositing Au by e-beam evaporation.

Our experimental data imply that surface defects and chemical species induced by chemical processing alter the interfacial behavior and ultimately exert a significant influence on the performance of radiation detectors.

REFERENCES:

[1] R. B. James, T. E. Schlesinger, J. C. Lund, and M. Schieber, "Cadmium Zinc Telluride Spectrometers for Gamma and X-Ray Applications", in Semiconductors for Room Temperature Nuclear Detector Applications, Vol. 43, edited by R. B. James and T. E. Schlesinger (Academic Press, New York, 1995), p. 334.

[2] C. Szeles, "Advances in the Crystal Growth and Device Fabrication Technology of CdZnTe Room Temperature Radiation Detectors", *IEEE Trans. Nucl. Sci.* NS-51 (2004) 1242.

[3] J. Garland and R. Sporken, *Mercury Cadmium Telluride Growth, Properties and Applications*, edited by Peter Capper and James Garland, John Wiley & Sons, 2011.

[4] R. Singh, S. Velicu, J. Crocco, et al., Molecular beam epitaxy growth of high-quality HgCdTe LWIR layers on polished and repolished CdZnTe substrates, *J. Electron Mater.,* Vol. 34, (2005) pp. 885-890.

A NOVEL METHOD FOR INSITU ESTIMATION OF $Hg_{1-x}Cd_xTe$ ETCH RATE IN REAL TIME

Palash Apte, Raytheon Vision Systems, Goleta CA

Abstract

A novel and non-invasive method to estimate the insitu etch rate (ER) of the Inductively Coupled Plasma (ICP) etched $Hg_{1-x}Cd_xTe$ in real time is described. Correlations between the chuck DC bias and 2 different flavors of $Hg_{1-x}Cd_xTe$ detector wafers are reported with R≥0.94. Estimates of the $Hg_{1-x}Cd_xTe$ ER for all the samples based on the new method are presented and compared with the actual Hg1-xCdxTe ER. The results show ≤ 3% differential between the actual Hg1-xCdxTe ER and the estimated insitu Hg1-xCdxTe ER.

Introduction

Fabrication of 3rd gen infrared detectors requires the ICP deep dry etching of mesa trenches to delineate the individual pixels whose depth is critical to the proper functioning of the detectors[1]. The current methods of achieving this involve either having an etch stop layer beneath the Hg1-xCdxTe layer for end pointing or breaking the etch into 2 parts. The first method isn't usually applicable as typically, the thickness of the Hg1-xCdxTe layer is much deeper than the target trench depth. The second currently used method suffers from long cycle times, higher cost of wafer processing, increased risk of damage to wafer and increased risk of reduced yield. Since the $Hg_{1-x}Cd_xTe$ ER depends upon a variety of factors (which can vary from wafer to wafer) including but not limited to the photolithography step prior to etch[1], the trench width[1], chuck DC bias voltage[1], $Hg_{1-x}Cd_xTe$ x value[2], variable amount of inert gas during etch[3], and wafer

temperature[4] and since the etch process exhibits process drift and unpredictable shifts in behavior due to chamber conditioning, incoming wafer variability and other unpredictable effects of chamber maintenance activities, one cannot assume a constant Hg1-xCdxTe ER for a particular group of wafers as this could lead to a scrap event. Hence a method is required which is easy to implement, non-invasive, accurate, and reduces cost and saves money. Such a method to estimate the ER of the $Hg_{1-x}Cd_xTe$ in real time is described. In this work, the output parameters from the ICP etcher are evaluated for their correlation with the $Hg_{1-x}Cd_xTe$ ER. The chuck DC bias voltage is seen to correlate with the $Hg_{1-x}Cd_xTe$ ER significantly for the 2 different flavors of samples. Estimates of the $Hg_{1-x}Cd_xTe$ ER using the new method are compared against the actual $Hg_{1-x}Cd_xTe$ ER.

<div align="center">Experimental</div>

Two different flavors of detector designs were used for this study. Both samples A and B are Long Wave (LW) MBE Hg1-xCdxTe grown on a Cadmium Zinc Telluride (CZT) substrate with sample B having a different array pattern than sample A. All sample wafers were processed in identical fashion prior to etch. After ICP plasma dry etching, the ground etch depth of the $Hg_{1-x}Cd_xTe$ samples was measured (using a confocal laser microscope\optical profilometer) from which the average $Hg_{1-x}Cd_xTe$ ER was calculated. All sample data was collected over a period of about a year during which time, the ICP etcher was vented for scheduled\unscheduled maintenance. The ICP process chamber utilizes two 1.2 KW RF generators supplying power to the antenna coil and the wafer electrode respectively. A mechanical clamping mechanism allows Helium to flow between the wafer carrier and the water cooled electrode and thus provides cooling during wafer processing. All samples were etched using a Hydrogen based etch recipe.

Results and Discussions

The output parameters which were changing from run to run and thought to affect the

$Hg_{1-x}Cd_xTe$ ER from the tool were identified. They included the chuck backside gas pressure, the

chuck DC bias Voltage, the throttle valve angle and the chuck RF power matching network

tuning and matching capacitors. As expected, the Hg1-xCdxTe ER best correlated ($R \geq 0.94$) with

the chuck DC bias voltage (figures 1 and 2). Figures 3 and 4 show a $\leq 3\%$ differential between

the actual ER and the estimated Hg1-xCdxTe ER for samples A and B. The estimated Hg1-

xCdxTe ER was calculated by measuring the average chuck DC bias voltage at a time

significantly shorter than the total etch time and using that value in the correlation equation to

estimate the Hg1-xCdxTe ER. Thus, if one were to run another of the sample A or B, all we

would have to do would be to measure the average DC bias at any time during the run and then

use the regression equation to estimate the $Hg_{1-x}Cd_xTe$ ER and hence the time to endpoint at the

required etch depth.

Conclusions

It has been shown that the chuck DC bias voltage can be used to estimate the $Hg_{1-x}Cd_xTe$ ER in

real time. The methods Hg1-xCdxTe ER estimate is accurate to within 3% of the actual

Hg1-xCdxTe ER. The ability to measure the Hg1-xCdxTe ER insitu and endpoint the etch at the

targeted depth would be invaluable to production $Hg_{1-x}Cd_xTe$ etch processes as this method

would reduce cycle time, cost and wafer damage and potentially improve yield. Although the

data presented here is specific to the tool and the samples, the technique is robust enough to

allow its application to create similar regression fits for samples in other etch tools to estimate

the Hg1-xCdxTe ER in real time.

Figures
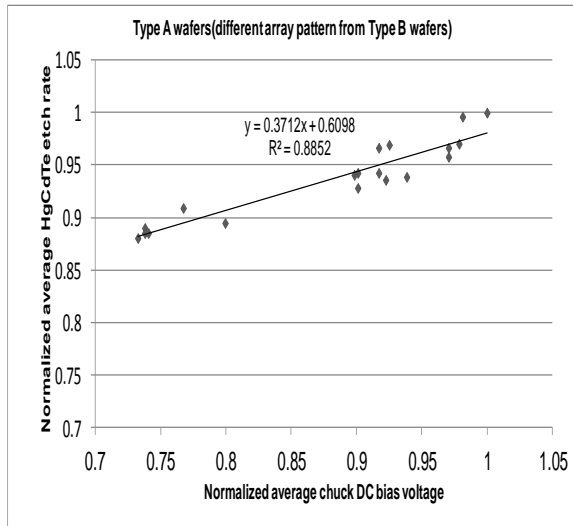
Figure 1
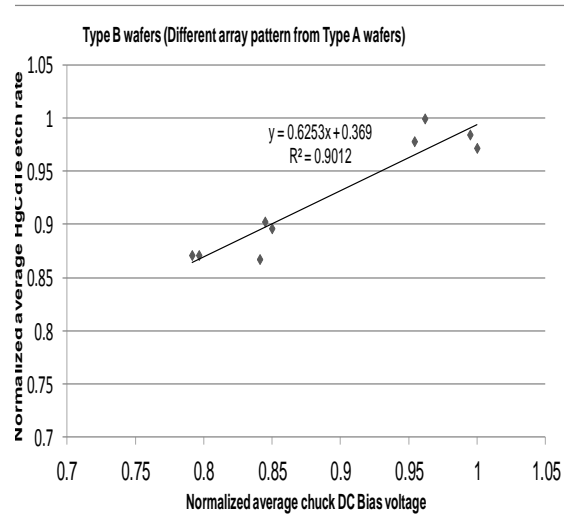
Figure 2
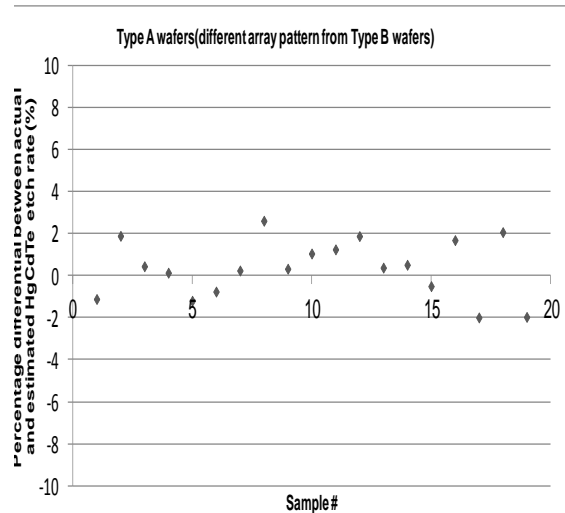
Figure 3
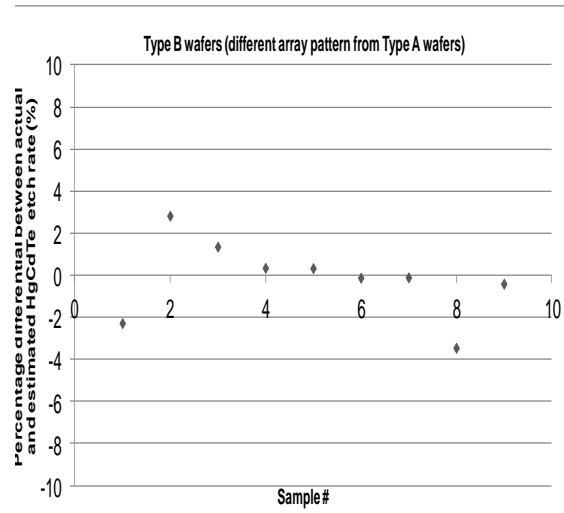
Figure 4

References

[1]V.Srivastav, R.Pal, H.P.Vyas, Opto-Electron. Rev., 13, no.3, 2005,pp 197-211
[2]E.P.G.Smith et al., Journal of Electronic Materials, Vol. 34, No. 6, 2005, pp 746-753
[3]Patrick Verdonck, "Plasma Etching",
(http://wcam.engr.wisc.edu/Public/Reference/PlasmaEtch/Plasma%20paper.pdf)
[4]C.R.Eddy, JR. et al., Journal of Electronic Materials, Vol. 28, No. 4, 1999 pp 347-354

Progress Towards II-VI Based Broadband Quantum Cascade Detectors

Arvind P. Ravikumar*[1], Joel De Jesus[2], Thor A. Garcia[3], Maria Tamargo[3], and Claire Gmachl[1]

[1]*Department of Electrical Engineering, Princeton University, Princeton, NJ 08544, USA*
[2]*Department of Physics, The Graduate Center and The City College of New York, NY 11080, USA*
[3]*Department of Chemistry, The Graduate Center and The City College of New York, NY 11080, USA*
*Presenter's information: Ph: 609-456-7097 Fax: 609-258-6279 email: aravikum@princeton.edu

Abstract

Quantum Cascade (QC) detectors are better suited than Quantum Well Infrared Photo-detectors (QWIPs) for imaging and high speed applications owing to their operation at zero bias resulting in much lower noise components. The II-VI ZnCdSe / ZnCdMgSe material system, with a lattice matched conduction band offset of up to 1.12 eV, offers the possibility of developing broadband and multicolor IR detectors. In this work, we report recent results on the development of the first II-VI based broadband QC detector.

The broadband QC detector design spans the wavelength region from about 4 μm to about 10 μm and consists of three impedance matched active cores centered at 5 μm, 6.8 μm, and 8 μm respectively. Fig. 1 shows a portion of the conduction band of the 5 μm core – the upper detector state is a doublet to improve the typically low carrier escape probability.

As shown in Fig. 2(a), the dark current density decreases by 3 orders of magnitude from about 10 mA/cm^2 at 300 K, to about 10 μA/cm^2 at 80 K. The dark current density at 300 K is over 2 orders of magnitude smaller than those observed in QWIPs operating at similar wavelength [*Appl. Phys. Lett. 102, 161107 (2013)*]. It can also be noted that the flat IV curves at higher applied bias is indicative of very good noise properties in the detector. Fig. 2 (b) shows an Arrhenius plot of the resistance-area product, indicative of the Johnson noise in the detectors. An activation energy of 147 meV is extracted, which corresponds to the electron leakage path E_{13} (155 meV), as shown in Fig. 1.
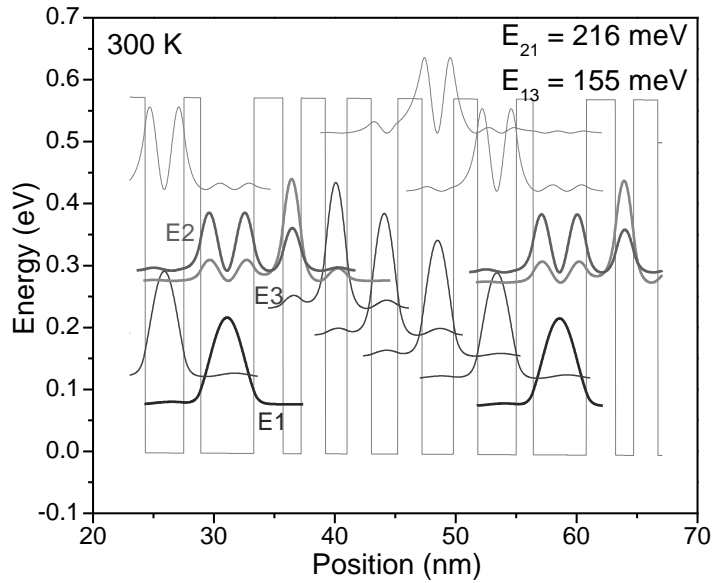
Figure 1: A portion of the conduction band of the 5 µm core of the II − VI broadband QCD at zero applied bias. Starting from the widest well on the left, the layer thicknesses (in Angstroms) of one period of the active region are: **44**/24/**15**/20/**18**/20/**22**/20/**26**/20/**32**/14. The $Zn_{0.51}Cd_{0.49}Se$ wells are in bold and the $Zn_{0.29}Cd_{0.26}Mg_{0.45}Se$ barriers are in normal text. The 4.4 nm detection well is doped to a doping density of 10^{18} cm^{-3}.
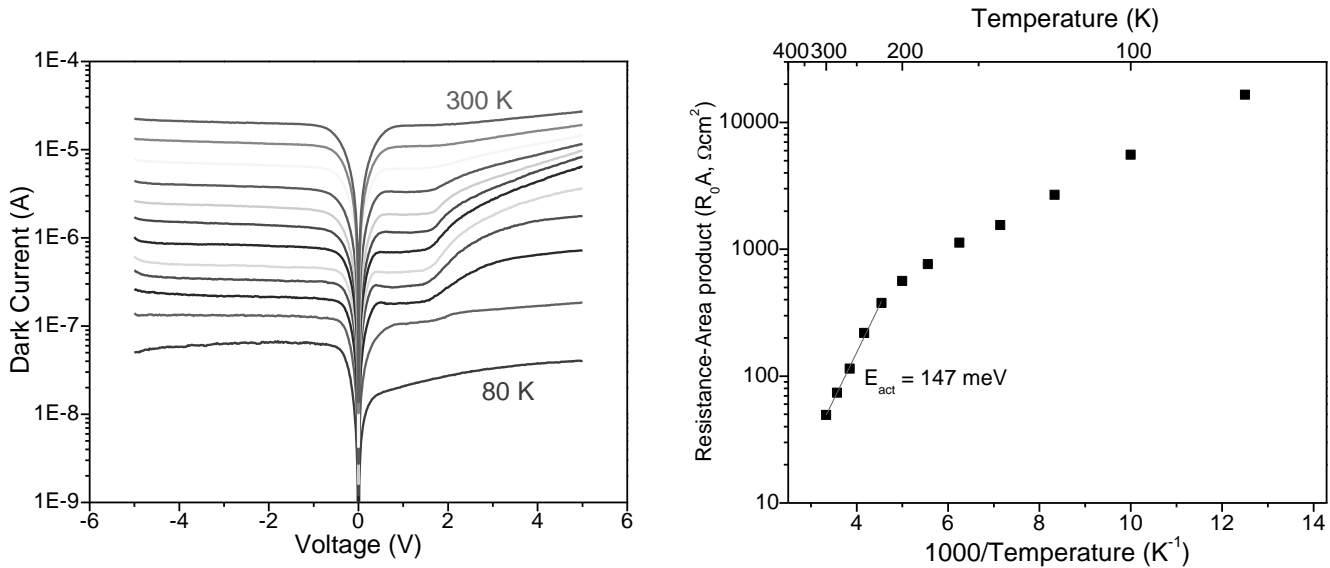
Figure 2: (a) Dark current characteristics as a function of temperature. The 300 K dark current density is about 10 mA/cm^2, about 2 orders of magnitude smaller than QWIP based detectors at similar wavelength. (b) Arrhenius plot of the resistance-area product, indicative of the Johnson noise in the detectors, yield an activation energy of 147 meV.

Dislocation Etching Solutions of HgCdSe

Kevin Doyle[1,A] and Sudhir Trivedi[2]

[1]U.S. Army Research Laboratory, SEDD. 2800 Powder Mill Rd, Adelphi MD 20783.

[2]Brimrose Corporation. 19 Loveton Circle, Hunt Valley Loveton Center, Sparks MD 21152.

The bandgap of HgCdSe can be tuned across the infrared (IR) spectrum, and it is closely lattice-matched to GaSb which is available as a large area substrate. Thus HgCdSe could be grown on GaSb substrates with low dislocation densities, making it suitable for long wave infrared (LWIR) applications. Etching solutions typically used for etch pit density (EPD) measurement of CdTe and HgCdTe, such as the Everson etch and Benson etch, proved ineffective for HgCdSe. Thus a new preferential etching solution for (211)B HgCdSe needs to be developed.

Solutions of HNO_3, HCl, and various buffering agents were found to produce trapezoid-shaped pits on (211)B HgCdSe as seen in Figure 1. These pits were regularly shaped and oriented in the same direction, suggesting they are related to the crystallography, but the pits often had flat or curved bottoms rather than converging to a single point as expected. One solution of $HNO_3:HCl:H_3PO_4$ (20:10:5) managed to produce hexagonal pits, as seen in Figure 2. While some of these pits appear to contain debris, other pits are clear and converge to a single point as expected. This could suggest that the curved or flat bottoms observed previously were due to re-deposition of material during the etching process. Further work is being performed to produce a more consistent etching solution for EPD measurement of HgCdSe.

[A] **kevin.j.doyle30.ctr@mail.mil**
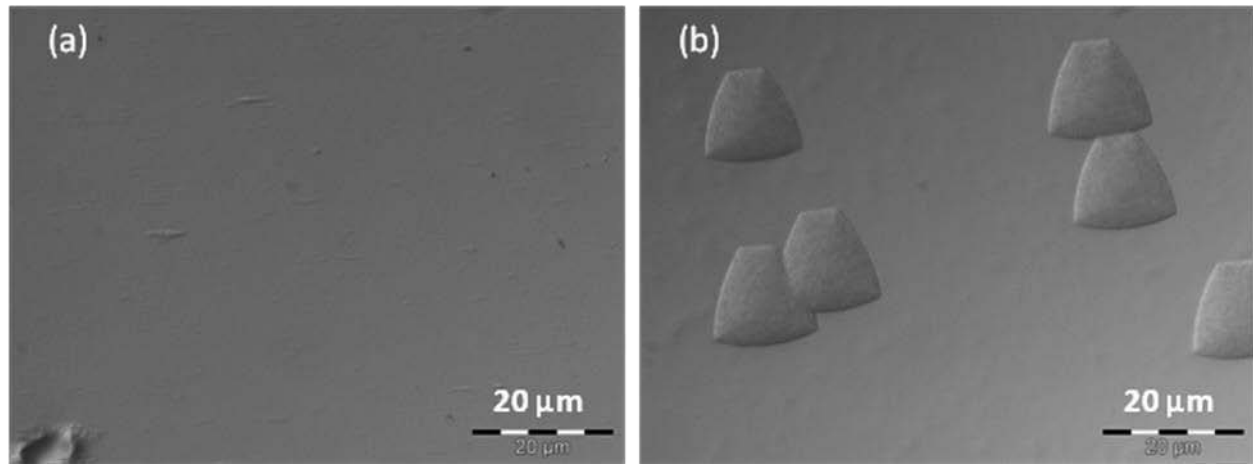
Figure 1: $Hg_{0.84}Cd_{0.16}Se$ sample viewed under Nomarski 100×, (a) unetched and (b) etched 20 s in HNO_3:HCl (2:1), then 20 s in 50% H_2SO_4.
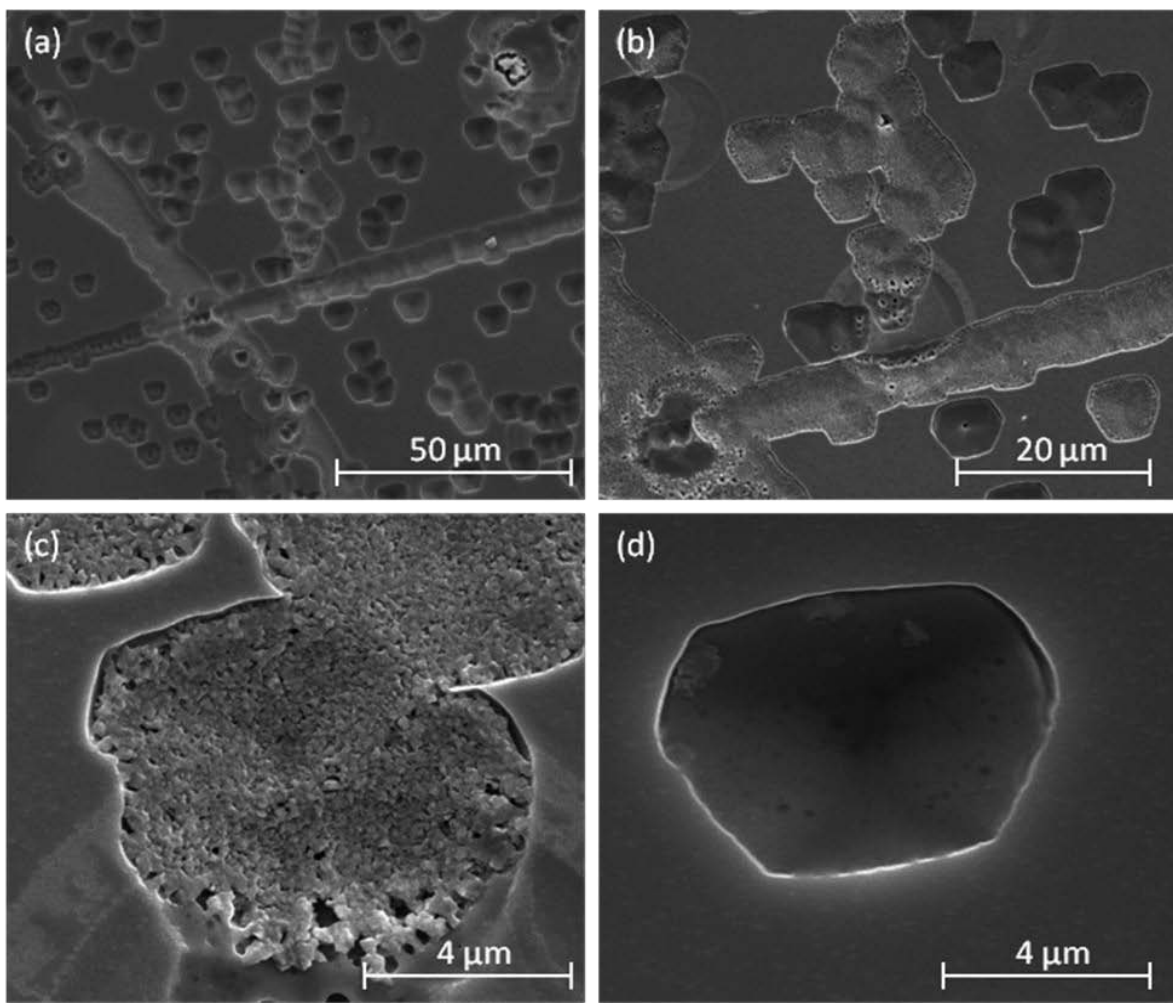
Figure 2: HgCdSe Sample etched 20s in HNO_3:HCl:H_3PO_4 (20:10:5) viewed under (a) Scanning electron microscopy (SEM) 1,196×, (b) SEM 2,554× (c) SEM 13,526×, and (d) SEM, and (f) SEM 16,098×.

150

Electro-Optical Characteristics of P$^+$n In$_{0.53}$Ga$_{0.47}$As Hetero-Junction Photodiodes in Large Format Dense Focal Plane Arrays

R. DeWames[‡], R. Littleton[†], K. Witte[†], A. Wichman[§], E.Bellotti[§], and J. Pellegrino[†]

‡ Fulcrum Company, Centerville, VA 20120, † U.S. Army RDECOM CERDEC NVESD Fort Belvoir VA 2206-5806, § Boston University, Boston MA, 02215.

Abstract

This paper is concerned with focal plane array, FPA, data and applying analytical and three dimensional numerical simulation methods to capture the right physical effects and processes limiting performance. For shallow homojunction p$^+$n designs the temperature dependence of the dark current data for T <300K depends on the intrinsic carrier concentration of the In$_{0.53}$Ga$_{0.47}$As material implying G-R currents of origins in the depletion regions of the double layer planar heterostructure, DLPH, photodiode. In the analytical model the variations are modeled with a G-R like perimeter dependent shunt current conjectured to be of origin at the InP/InGaAs interface. In this description the fitting parameter is the effective conductivity $\sigma_{eff}(T)$ in mhos-cm^{-1}. Variation in the data suggests, $\sigma_{eff}(300K)$ values (1.2•10^{-11}- 4.6•10^{-11} mhos-cm^{-1}). Substrate removal extends the QE spectral band into the visible, however, dead layer effects limit the QE to 10% at a wavelength of 0.5 μm. For star light-no moon illumination conditions, the Signal/Noise ratio is estimated to be 50 at an operating temperature of 300K A major result of the 3D numerical simulation of the device is the prediction of a perimeter G-R current not associated with the properties of the metallurgical interface. Another is the prediction that for junction positioned in the larger band gap InP cap layer the QE is bias dependent and that relatively large reverse bias ≥ 0.9 Volts are needed for the value to saturate to the shallow homojunction value. At this higher bias the dark current is larger than the shallow homojunction value. 3D numerical model and the analytical model agree in predicting and explaining the measured radiatively limited diffusion current of origin in the n-side of the junction. The calculations of the area dependent G-R current for the condition studied, is also in agreement. A unique value of 3D numerical simulation methods is the capability to mimic real device architectures, achieve a deeper understanding of the real physical effects associated with the various methods of junction formation and predict how device designs will function.

Dense array effects in SWIR HgCdTe arrays

A. R. Wichman[*], B. Pinkie[*], E.Bellotti[*]

[*] Electrical & Computer Engineering Department, Boston University, 8 St. Mary's Street, Boston MA, 02215. Contact: belloti@bu.edu, 617.358.1576

Abstract

The relatively easily tuned bandgap in HgCdTe photodetecting arrays makes it an interesting candidate for extended range short wave infrared detection. Recent publications report short wave infrared HgCdTe-based focal plane arrays with 15 μm pitch. [1–3] Depending on doping levels and operation, the minority carrier diffusion lengths for these arrays may exceed the pixel dimensions. [4–6] In these domains, neighboring junctions in the dense array geometry can suppress minority carrier densities and gradients and reduce lateral diffusion currents. [7] In radiatively-limited lattice-matched dense P^+n InGaAs on InP arrays, for example, the dark diffusion current falls in proportion to the pixel volume (area), and dark diffusion currents can be expressed analytically as a function of pitch, diffusion length, junction radius, and material constants. [7] *See* Figure 1, *infra*. Unlike InGaAs photodetecting arrays, Auger recombination makes important, if not necessarily dominant, contributions to intrinsic current in short wave infrared HgCdTe photodetectors. Carrier dynamics relating specifically to dense array geometry in short wave HgCdTe detectors, however, have not been expressly studied but instead are often suppressed in reported data by averaging dark currents over pixel areas.

Using three-dimensional quantitative modeling for dense arrays in convention double layer planar heterostructures, in this study we investigate geometrical influence on minority carrier distributions and intrinsic diffusion in dense short wave infrared HgCdTe

DLPH arrays. This approach highlights several geometric effects, including Auger

suppression, negative luminescence, and negative differential resistance. Understanding

these mechanisms lends insight into device design and operation for higher temperature.
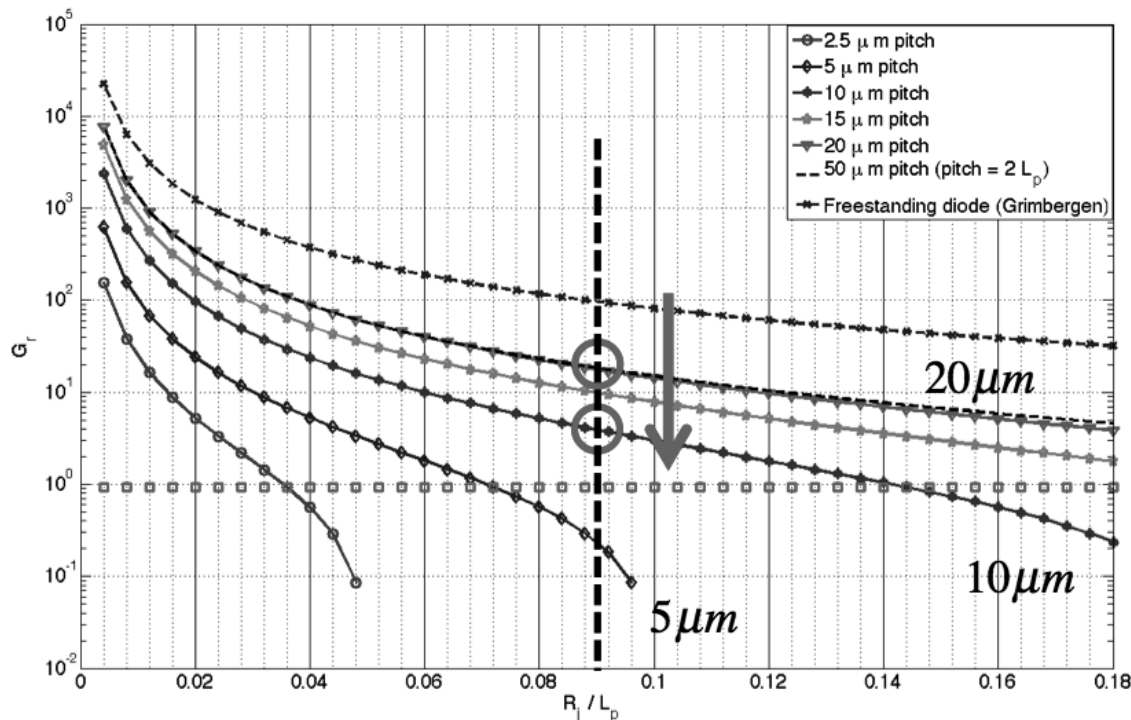
Fig. 1: Radial geometry factors for intrinsic dark current suppression with pitch in P$^+$n
InGaAs on InP dense photodiode array given L_p = 25 μm.

References

1. L. Melkonian, J. Bangs, L. Elizondo, R. Ramey, and E. Guerrero, in *Proc. SPIE* (2010), p. 76602W–76602W–11.

2. O. Gravrand, N. Baier, a. Ferron, F. Rochette, J. Berthoz, L. Rubaldo, and R. Cluzel, J. Electron. Mater. (2014).

3. O. Gravrand, L. Mollard, O. Boulade, V. Moreau, E. Sanson, and G. Destefanis, J. Electron. Mater. **41**, 2686 (2012).

4. J. Jia, G. Chen, X. Li, and H. Gong, in *Proc. SPIE 5640* (2005), pp. 1–10.

5. M. Kinch, F. Aqariden, and D. Chandra, J. Electron. Mater. **34**, 880 (2005).

6. A. Rogalski, Reports Prog. Phys. **68**, 2267 (2005).

7. A. R. Wichman, R. E. DeWames, and E. Bellotti, in *Proc. SPIE 9070* (2014), p. forthcoming.

LINEAR MODE HGCDTE AVALANCHE PHOTODIODES FOR PHOTON COUNTING APPLICATIONS*

William Sullivan III, Jeff Beck, Richard Scritchfield, Mark Skokan, and Pradip Mitra

DRS Technologies, C4ISR Group, 13544 N. Central Expressway, Dallas, Texas, 75243

Xiaoli Sun and James Abshire

NASA Goddard Space Flight Center, Greenbelt, Maryland 20771

Darren Carpenter and Barry Lane

A/DIC Inc., 740 Florida Central Parkway, Longwood, FL 32750

An overview of recent improvements in the understanding and maturity of linear mode photon counting (LMPC) with HgCdTe electron-initiated APDs is presented. The first HgCdTe LMPC 2x8 format array with 64 μm pitch was a remarkable success in terms of demonstrating a high single photon signal to noise ratio (SNR) of 13.7 with an excess noise factor of 1.3-1.4, a 7 ns minimum time between events (MTBE), and a broad spectral response extending from 0.4 μm to 4.2 μm [1-3]. The main limitations were a greater than 10x higher false event rate (FER) than expected of > 1 MHz, a 5-7x lower than expected APD gain, and a photon detection efficiency (PDE) of only 50% when greater than 60% was expected. This paper discusses the reasons behind these limitations and the implementation of their mitigations with new results.

Fabricating focal plane arrays (FPAs) with a mirror metal shield to block the readout integrated circuit (ROIC) glow and optimizing ROIC biases to minimize the glow resulted in FER almost an order of magnitude lower than the original LMPC results. Increased APD gains of 1910 and the reduced FER enabled single photon PDEs of 60-75% at "ROIC glow" limited FERs of less than 200 kHz across the entire array, as shown in Figs. 1 and 2. These higher PDEs are close to theoretical predictions. Five FPAs were characterized and the 16-pixel mean PDE vs. FER of each is shown in Fig. 2. The three FPAs with the mirror blocking metal exhibited a 5x decrease in FER compared to the two without it. All of the FPAs shown in Fig. 2 were vacancy doped except A8327-8-2 which was copper + vacancy doped and had a

slightly higher PDE due to its expected longer electron diffusion length. Also, all of the FPAs shown had a single layer anti-reflection (AR) coating of ZnS which was ~92% efficient, except A8327-20-2 which had a double layer AR coating of ZnS/SiO_2 with an efficiency of greater than 98%. PDE vs. FER was compared on sister FPAs A8327-14-1 and A8327-14-2 which were identical except A8327-14-1 had the mirror blocking metal. Each pixel's FER is $\leq$ 200 kHz on A8327-14-1 at the optimum threshold of 4.8 mV yielding PDE $\geq$ 50% across all pixels as shown in Fig. 3. Further reductions in the ROIC-glow generated photons are expected to decrease the FER to few tens of kHz or less, limited only by detector dark current as shown in Fig. 4. A model was generated which explains the PDE vs. FER curve, including the downwards trend after the peak PDE is reached. Excellent fits to measured data were obtained, as shown in Fig. 5.
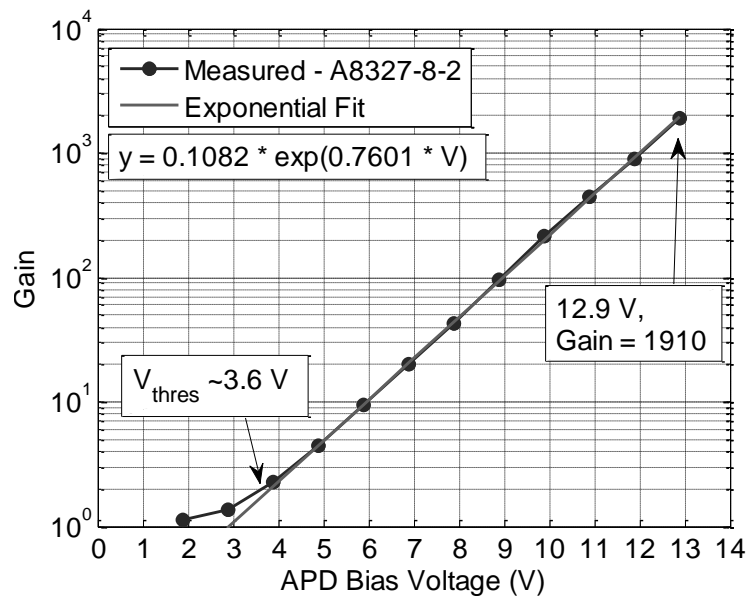
Figure 1: Measured gain vs. voltage curve on Pixel 1,1 of A8327-8-2.
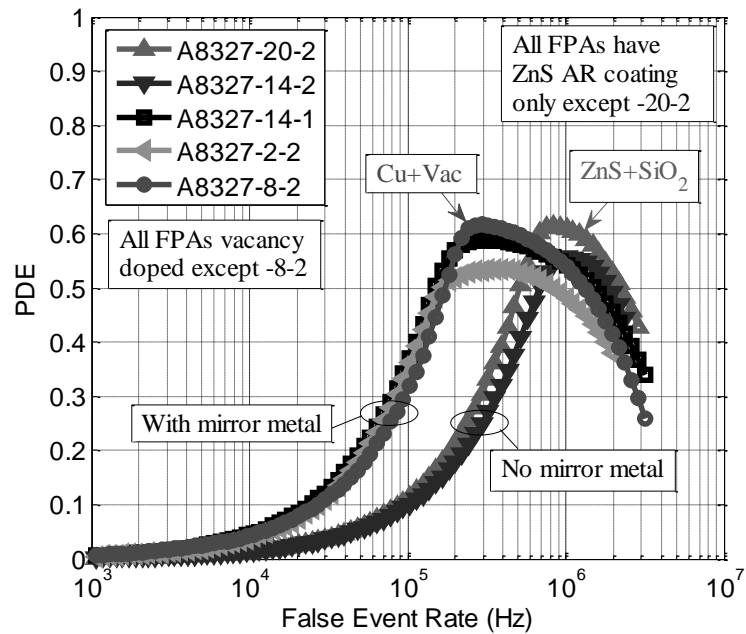
Figure 2: 16 pixel mean PDE vs FER for 5 different 2x8 FPA's at an APD bias of 12.9 V. The 3 FPAs with the mirror blocking metal exhibited a 5x decrease in FER compared to the 2 FPAs without it.
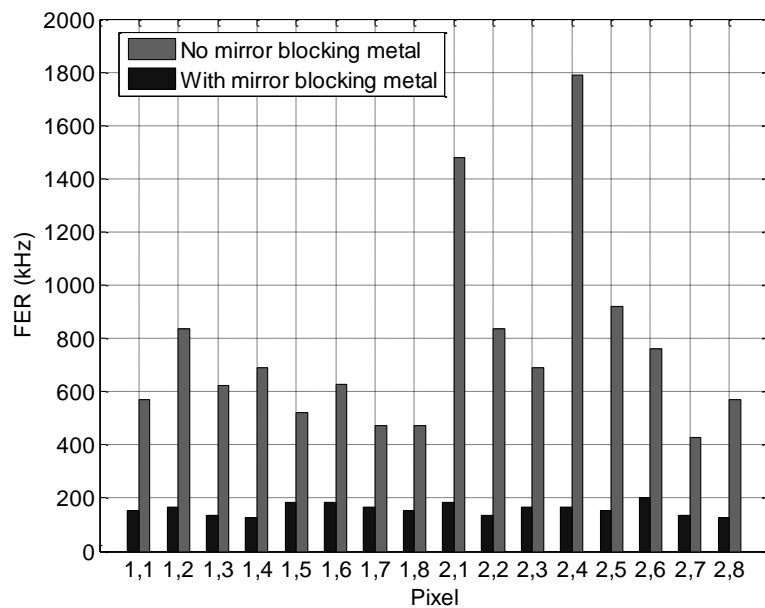
Figure 3: FER vs. pixel at the optimum threshold of 4.8 mV yielding ≥ 50% PDE across all pixels on both FPAs.

Input Referred Dark Current Electrons/Second
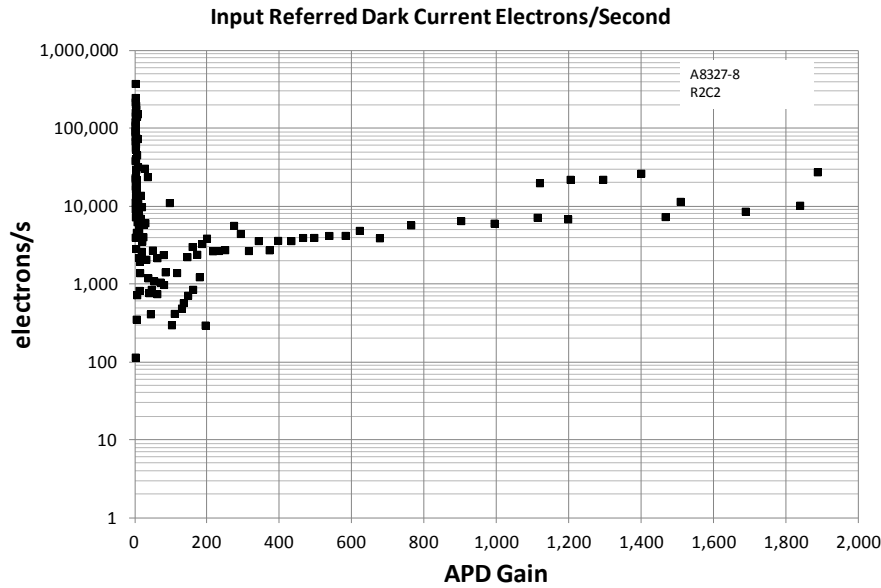
Figure 4: Gain normalized dark current of test diodes showing a maximum effective dark count rate of less than 30 kHz at gains up to 1900.
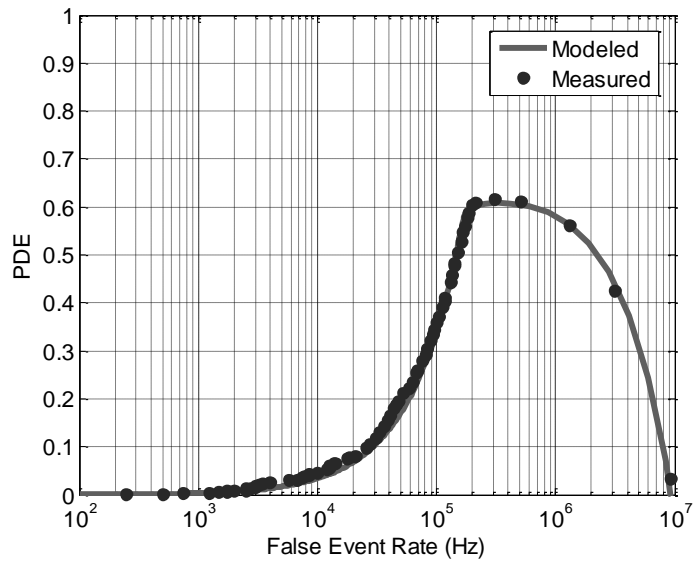
Figure 5: Modeled and measured PDE vs. FER data on A8327-14-1.

References:

[1] J. D. Beck, R. Scritchfield, P. Mitra, W. Sullivan III, A. D. Gleckler, R. Strittmatter, R. J. Martin, *Proc. SPIE* 8033, 80330N (2011).

[2] J. D. Beck, R. Scritchfield, P. Mitra, W. W. Sullivan III, A. D. Gleckler, R. Strittmatter, R. J. Martin, *Opt. Eng*. 53(8), 081905 (2014).

[3] J. D. Beck, M. Kinch, X. Sun, *Opt. Eng*. 53(8), 081906, (2014).

Si and InGaAs Spatial Wavefunction Switched (SWS) FETs with II-VI Gate Insulators

F. Jain[1], P-Y. Chan[1], M. Lingalugari[1], J. Kondo[1], E. Suarez[1], P. Gogna[1,2], J. Chandy[1], E. Heller[3]

[1]ECE Dept., UConn, Storrs, CT 06269, [2]Intel, Hudson, MA, [3]Synopsys, Ossining, NY 10562

Electron wavefunctions are switched spatially from one quantum well to the other by varying the gate voltage V_g in SWS-FETs, which comprise coupled quantum wells serving as the transport channel. The presence of charge in a particular well is used to encode four states 00, 01, 10, 11. This unique property is used for 2-bit processing, resulting in ultra-compact high-speed logic circuits and static random access memory (SRAM) devices. Experimental data including capacitance-voltage peaks in Si and InGaAs (Fig. 1) multiple quantum well channel SWS-FETs has verified the SWS phenomenon. Recent simulations have shown that increased barrier heights, such as in Ge-ZnSSe quantum well SWS FETs, enhances the contrast and noise margins (Fig.2). In addition, wavefunction switching has been experimentally observed in 4 InGaAs well SWS devices (Fig. 3 and Fig. 4) where multiple C-V peaks indicate transfer of carriers.

Replacing quantum wells by quantum dot superlattice (QDSL) layers enhances the contrast and noise margin in SWS-FETs. This paper presents I-V (Fig. 5b) and C-V (Fig. 5c) characteristics of a twin-drain SWS-FET (Fig. 5a) comprising 4 layers of self-assembled SiO_x-Si quantum dots forming two quantum dot superlattice layers (QDSL), serving as transport channels. ID-VD shows lower dot layer conducting when gate voltage is in the range of 1.8-2.0V and the upper channel conducting above 2.3V. The C-V plot of a SWS MOS capacitor manifests peaks in inversion and accumulation (left arrows) due to carrier switching from lower to upper channel. The quantum simulations are presented (Fig. 5d) with carriers switching from Dot Layer 4 ($V_g = 0.2V$) to Dot Layer 1 at $V_g=0.9V$.

Quantum simulation and experimental characteristics of InGaAs SWS-MOS devices comprising

of two-to-four quantum well channels, fabricated using II-VI gate insulator in our laboratory, are

also presented. SPICE and BSIM models are also being developed for SWS circuits.

Fig. 1(a) MOCVD growth run file for a 2-channel InGaAs SWS with InGaAs wells and AlInAs barriers.	Fig.1(b) Capacitance *vs* gate voltage in a 2-well InGaAs SWS-MOS device.	Fig.1(c) Low frequency C-V of 4-well InGaAs SWS MOS device.
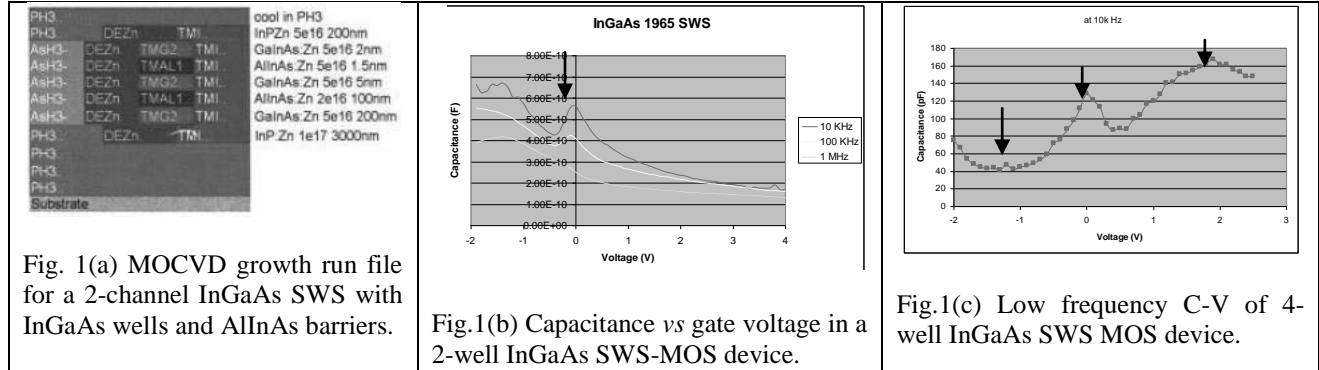
Simulation of 3-channel Ge well/ZnSSe barrier SWS-FET:

Fig.2(a). Wavefunction in Ge well W3 for SWS-FET of Fig. 7.	Fig.2(b).Wavefunction in well W1. Note higher confinement than Fig. 1c.	Fig. 3(c) Carrier density in quantum wells QW3 and QW1.
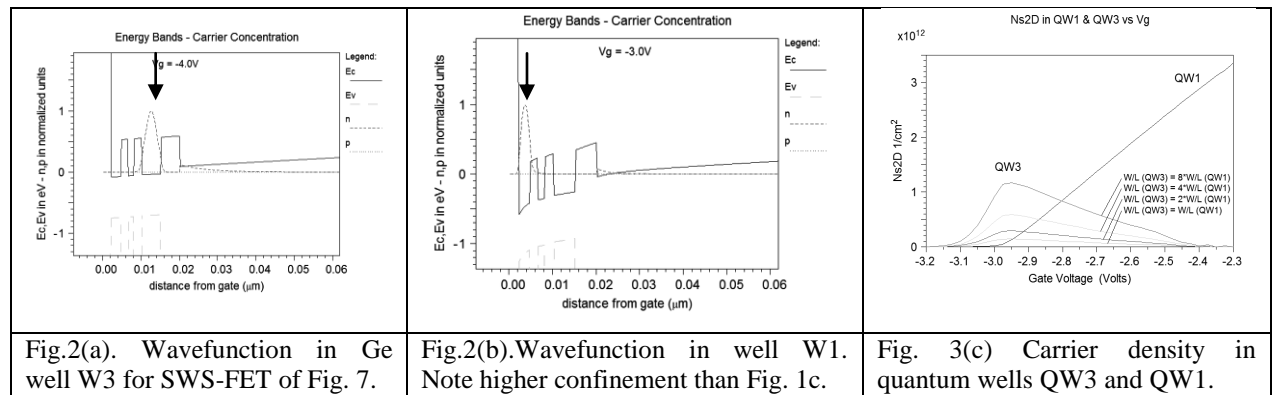
Simulation of 4-channel InGaAs SWS-FETs:

Fig. 3(a). Carriers mostly in well InGaAs W3 (Vg=1.7V).	Fig. 3(b) Carriers mostly in InGaAs well W1 (Vg=1.9V).	Fig.4 Experimental C-V characteristic of a 4-well InGaAs SWS MOS in inversion.
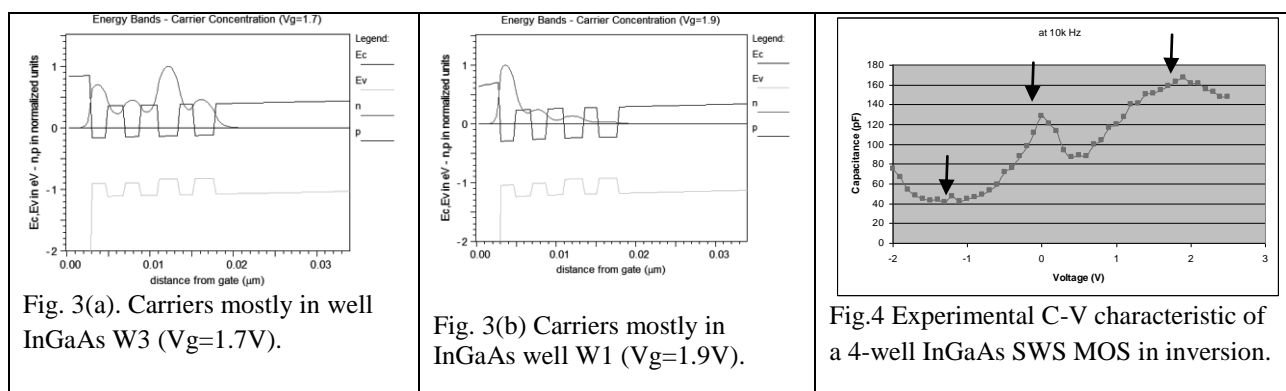
Quantum Dot Superlattice Layer (QDSL) Si SWS-FETs: Experimental and Simulations

Fig.5(a) High contrast 4- channel 2-drain QDSL-SWSFET.	Fig. 5b ID-VD of 2-drain QDSL-SWSFET	Fig.5(c) C-V showing peaks in fabricated QDSL-SWS Si.	Fig. 5(d) Simulation $N_{s2D}=1.0x10^{11}$ cm^{-2} in W4 at $V_g = 0.2V$.
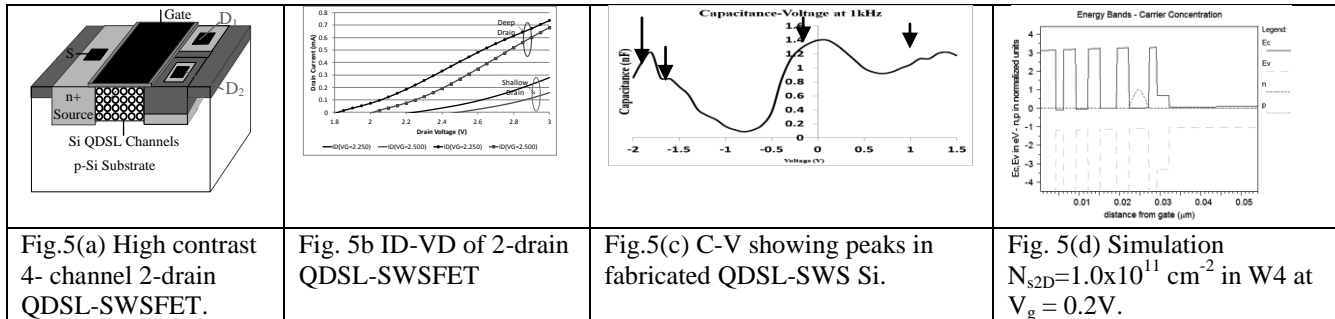
References: 1. F. C. Jain, B. Miller, E. Suarez, P-Y. Chan, S. Karmakar, F. Al-Amoody, M .Gogna, J. Chandy, and E. Heller, "Spatial Wavefunction-Switched (SWS) InGaAs FETs with II-VI Gate Insulators", J. Electronic Materials, 40, 1717, 2011.

2. P. Gogna, M. Lingalugari, J. Chandy, E. Heller, E-S. Hasaneen and F. Jain, "Quaternary logic and applications using multiple quantum well based SWSFETS", International Journal of VLSI design & Communication Systems (VLSICS) Vol.3, No.5, pp. 27-42, October 2012.

Intrinsic broadening of the mobility distribution of bulk n-type HgCdTe

G. Jolley*, G. Umana-Membreno, N. D. Akhavan, J. Antoszewski and L. Faraone

School of Electrical, Electronic and Computer Engineering, University of Western Australia, Perth, WA, Australia, 6009

*phone: +61864883748, email: gregory.jolley@uwa.edu.au

Abstract

Quantitative Mobility Spectrum Analysis techniques have been applied to the study of numerous semiconductor structures due to the ability to simultaneously resolve the contributions of various conduction mechanisms such as bulk and surface conduction. However, there is a severe lack of reported studies on theoretical calculations of the mobility distributions of semiconductor structures or devices. We present a fundamental study of the mobility distribution of n-type bulk HgCdTe by numerically solving the Boltzmann's transport equation taking polar optical phonon, acoustic phonon, ionized impurity and alloy scattering into consideration. The shape of the mobility distribution is found to be considerably complex and dependent on the nature of the scattering interaction. It is found that polar optical phonon scattering results in multiple peaks in the mobility distribution resulting from electron conductivity in only the Γ conduction band, see figures 1 and 2 for computational results of $Hg_{0.7}Cd_{0.3}Te$ at a temperature of 120K and an electron concentration 1×10^{15} cm^{-3}. The computation results provide insight into the nature of electron mobility distributions and can assist in the interpretation of experimental Quantitative Mobility Spectrum Analysis.

References

[1] W.A. Beck and J.R. Anderson, J. Appl. Phys. vol. 62, pp. 541 (1987)

[2] I. Vurgaftman, J. R. Meyer, C. A. Hoffman, D. Redfern, J. Antoszewski, L. Faraone, and J. R. Lindemuth, J. Appl. Phys., vol. 84, pp. 4966 (1998)

[3] D. Chrastina, J. P. Hague, and D. R. Leadley, J. Appl. Phys., vol. 94, pp. 6583 (2003)

[4] S. Kiatgamolchai, M. Myronov, O. A. Mironov, V. G. Kantser, E. H. C. Parker, and T. E. Whall, Phys. Rev. E, vol. 66, pp. 036705 (2002)

[5] J. Rothman, J. Meilhan, G Perrais, J.P. Bellie and O. Gravrand, J. Electronic Material, vol. 35, pp. 1174 (2006)

[6] J. Antoszewski, L. Faraone, I. Vurgaftman, J.R. Meyer, and C.A. Hoffman, Journal of electronic materials, vol. 33, pp. 673, (2004)

[7] G. A. Umana-Membreno, J. Antoszewski, L. Faraone, E. P. G. Smith, G. M. Venzor, S. M. Johnson, and V. Phillips, vol. 39, pp. 1023 (2010)
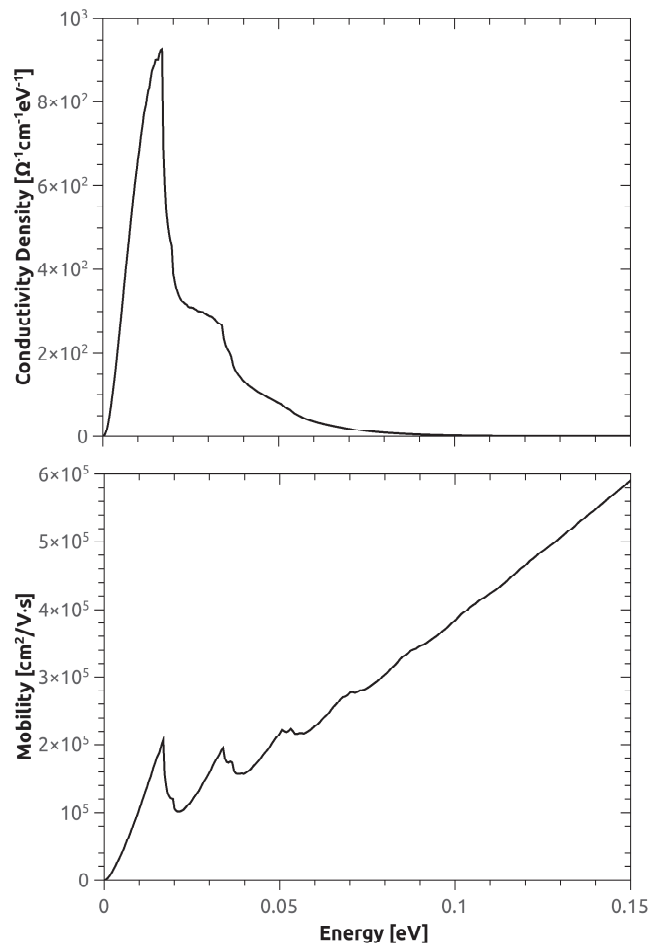
Figure 1: Calculated conductivity density and mobility as a function of electron energy of bulk $Hg_{0.7}Cd_{0.3}Te$ at a temperature of 120 K and an electron concentration of 1×10^{15} cm^{-3}.
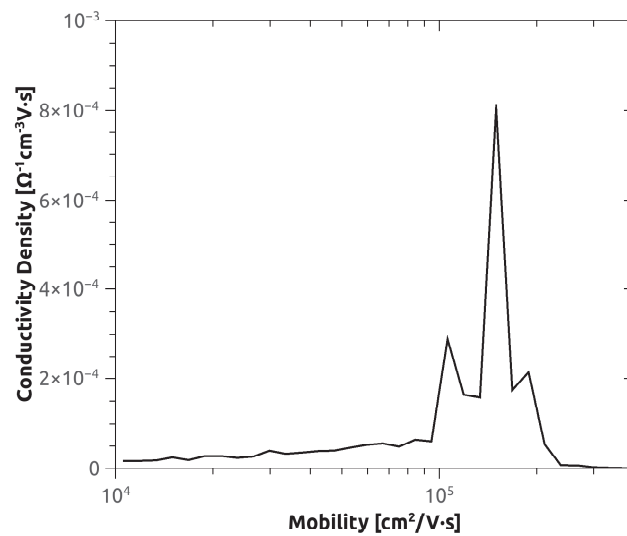
Figure 2: Calculated mobility distribution of bulk $Hg_{0.7}Cd_{0.3}Te$ at a temperature of 120 K and an electron concentration of 1×10^{15} cm^{-3}.

The Evolution of Kinetically-Limited Lattice Relaxation and Threading Dislocation in Temperature-Graded ZnSe/GaAs (001) Metamorphic Heterostructures

T. Kujofsa and J. E. Ayers[†], Electrical and Computer Engineering Department, University of Connecticut, Storrs, CT 06269-4157.

I. Abstract

Metamorphic buffer layers allow tremendous flexibility to design novel semiconductor heterostructures for application in various microelectronic and optical devices. However, device fabrication, reliability and performance are limited by dislocation defects associated with the growth of highly mismatched systems such as ZnSe on GaAs substrate. Thus, understanding kinetically-limited lattice relaxation and development of a plastic flow model applicable to multilayered and compositionally graded heterostructure is desirable to provide guidance in designing ZnSe/GaAs devices. Previously, we reported a plastic flow model for ZnS_ySe_{1-y}/GaAs (001) heterostructures which predicts the non-equilibrium strain relaxation as well as misfit dislocation and threading dislocation densities by accounting for (i) the time evolution of kinetically-limited and equilibrium strain relaxation, (ii) thermal activation of glide, and (iii) misfit-threading dislocation interactions. In this work, we have studied the evolution of kinetically-limited in-plane strain and threading dislocation densities in ZnSe/GaAs (001) metamorphic buffer layers with arbitrary temperature grading profile. In addition, we have investigated the effect of forward versus reverse temperature grading cases on the relaxation mechanism. For each structure, we have studied the temperature grading coefficient dependence on the average and surface kinetically-limited in-plane strain and threading dislocation density. Moreover we show that the use of temperature graded buffer layers

---

[†] Tel: (617)-383-1514. FAX: (860)-486-2447. e-mail: tedi.kujofsa@gmail.com.

enables the design of ZnSe/GaAs (001) heterostructures with high surface strain values which enhance the sweeping of threading defects and therefore yielding device structures with lower defect densities.

II. Kinetically-Limited Lattice Relaxation and Dislocation Dynamics Model

The foundation for the kinetic model used in this work is derived in [1]. The model predicts lattice relaxation and threading dislocation behavior in (001) zinc blende heteroepitaxial layers of arbitrary thickness and compositional profile. In a general semiconductor heterostructure with lattice mismatch profile $f(z)$, the rate of lattice relaxation at a distance z from the interface is determined by the glide of dislocations in the underlying material, and is given by

$$\frac{d\gamma(z)}{dt} = KBb \sin \alpha \cos \lambda \tau_{eff}^2(z) \exp\left(-\frac{U}{kT}\right) \int_0^z \left[\rho_A(\zeta) + \rho_0\right] d\zeta , \tag{1.}$$

where K and B are constants, b is the length of the Burgers vector, α is the angle between the Burgers vector and line vector, λ is the angle between the Burgers vector and the direction in the interface which is perpendicular to the intersection of the glide plane and the interface, τ_{eff} is the effective stress which is determined by the difference of actual and equilibrium strain, U is the activation energy for dislocation glide, k is the Boltzmann constant, T is the temperature, ρ_A is the areal density of misfit dislocations, ρ_0 is a constant which represents the initial sources of dislocations, and ζ is the variable of integration. The effective stress is determined by the difference of the actual and equilibrium strain profiles in the material above, given by

$$\tau_{eff}(z) = \left[\frac{2\cos\psi\cos\lambda}{h-z}\right] \int_z^h \left\{\frac{\mu(1-\nu)\left[\varepsilon_{||}(\zeta) - \varepsilon_{eq}(\zeta)\right]}{(1+\nu)}\right\} d\zeta , \tag{2.}$$

where h is the layer thickness, ψ is the angle between the surface normal and the slip plane, μ is the shear modulus, ν is the Poisson ratio, $\varepsilon_{||}$ is the in-plane strain, and ε_{eq} is the

equilibrium in-plane strain. Embedded within the kinetic model we have included minimum energy calculations to determine the equilibrium structure after the deposition of each sublayer.

Complementing the lattice relaxation model we have also included dislocation interactions: the basic types of dislocation interactions are (i) introduction of half loops, (ii) bending over of existing dislocations, (iii) annihilation, and (iv) coalescence. Therefore the resulting differential equation for the threading dislocation density is

$$\frac{dD(z)}{dz} = \frac{4\rho_A(z)}{L_{MD}(z)sign\int_0^z \rho_A(\zeta)d\zeta} - C_2 D^2(z) , \tag{3.}$$

where $L_{MD}(z)$ is the length of misfit dislocation segments, and C_2 is a constant. The first term in (3) accounts for the interactions between misfit and threading dislocations. Considering mechanism (i), new misfit dislocations are introduced via half loops if the new misfit dislocations have the same sense (relax the same sign of lattice mismatch) as the underlying misfit segments. This corresponds to the case of $sign(\rho_A(z)) = sign\int_0^z \rho_A(\zeta)d\zeta$ and results in positive $dD(z)/dz$. With respect to mechanism (ii), misfit dislocations are produced by the bending of existing threading dislocations if these misfit dislocations have the opposite sense (relax the opposite sign of mismatch) compared to the underlying misfit segments).

III. In-plane Strain and Threading Dislocations

Lattice relaxation in II-VI devices exhibits a three regime (sluggish, rapid, saturation) behavior as observed in many experimental studies. More importantly, strain relaxation of ZnSe/GaAs (001) occurs much more gradually than predicted by the Matthews and Blakeslee equilibrium theory. In addition, at around 400°C growth of ZnSe layers will exhibit a transition from compressive to tensile strain as the thickness is increased; this is expected on the basis of the differential thermal expansion and is observed experimentally in this material system. Therefore, controlling the defect density is crucial in designing devices with fewer threading dislocations. Moreover, the kinetic model predicts a two regime behavior for the evolution of

the threading dislocation density; first, there exists an initial build-up of the threading dislocation density associated with layers which are beyond the critical layer thickness and as the layer epilayer thickness is further increased, D is inversely proportion to thickness. In this work, we will show how varying the temperature grading coefficient and grading direction effects the kinetically-limited in-plane strain and the surface threading dislocation density. Moreover, we will show how controlling the temperature grading period could lead to lower threading densities.

IV. References

[1] T. Kujofsa, W.Yu, S. Cheruku, B. Outlaw, F. Obst, D. Sidoti, B. Bertoli, P. B. Rago, E. N. Suarez, F. C. Jain and J. E. Ayers, J. Electron. Mater. 41, 2993 (2012).

MBE growth of HgCdTe layers on GaSb alternative substrates

W. Lei*, R.J. Gu, J. Antoszewski, J. Dell, L. Faraone

School of Electrical, Electronic and Computer Engineering, The University of Western Australia, 35 Stirling Highway,

Crawley WA 6009, Australia

*Tel: 61-8-6488 1848, fax: 61-8-6488 1065, email: wen.lei@uwa.edu.au

Abstract

Recently, GaSb has been proposed as a new alternative substrate for growing HgCdTe epitaxial layers for next generation infrared detectors. The principal advantage is that GaSb is better matched with HgCdTe with respect to lattice constant and/or CTE in comparison with other alternative substrates currently under consideration, such as Si, GaAs and Ge. In our recent study, CdTe buffer layers grown on GaSb substrates *via* molecular beam epitaxy (MBE) demonstrate a material quality comparable to CdTe grown on GaAs substrates that have been developed in our lab in terms of crystal quality, despite the fact that the growth conditions of CdTe buffer layers on GaSb were not fully optimized. In order to be suitable for device applications, high quality HgCdTe layers must be achieved on GaSb alternative substrates. In this paper, we present a preliminary study of MBE growth and structural characterization of mid-wave infrared HgCdTe layers on CdTe/GaSb alternative substrates. Generally, the HgCdTe layers grown on GaSb substrates demonstrate material quality comparable to MBE grown HgCdTe on GaAs substrates developed in our lab in terms of reflection high-energy electron diffraction (RHEED) pattern during material growth, full width at half maximum of X-ray diffraction (XRD) peak, and etch pit density (EPD), the details of which are summarized in Table 1. Furthermore, transmission electron microscopy (TEM) and electron backscatter diffraction (EBSD) mapping analysis indicates that most of the misfit dislocations generated close to the interface between the CdTe buffer layers and GaSb substrates are relaxed within 500~650 nm away from the interface. More importantly, the misfit dislocations generated near the interface between the CdTe buffer layers and HgCdTe layers are relaxed almost completely within 160~200 nm away from the interface, indicating a high quality HgCdTe epilayer can be achieved if the growth conditions of the CdTe buffer layer and HgCdTe layer are optimized. These results demonstrate the great potential of GaSb as the next generation alternative substrate for MBE growth of HgCdTe infrared detector materials.

Table 1 Some characteristics of mid-wave infrared $Hg_{1-x}Cd_xTe$ layers grown on GaSb and GaAs substrates*.

Alternative substrates	x valve of $Hg_{1-x}Cd_xTe$ layers	HgCdTe layer thickness (um)	CdTe buffer thickness (um)	XRD FWHM (arc sec)	RHEED pattern during growing CdTe buffer layer	EPD ($\times 10^6$ cm^{-2})
GaSb	0.27 ~ 0.32	4.5 ~ 5.3	5.3 ~ 5.7	122 ~ 139	long and uniform streaks	2 ~ 10
GaAs	0.26 ~ 0.32	5.7 ~ 6.7	5.7 ~ 6.7	98 ~ 155	long and uniform streaks	8 ~ 40

* representative experimental data will be shown in the supporting material - Figure 1.
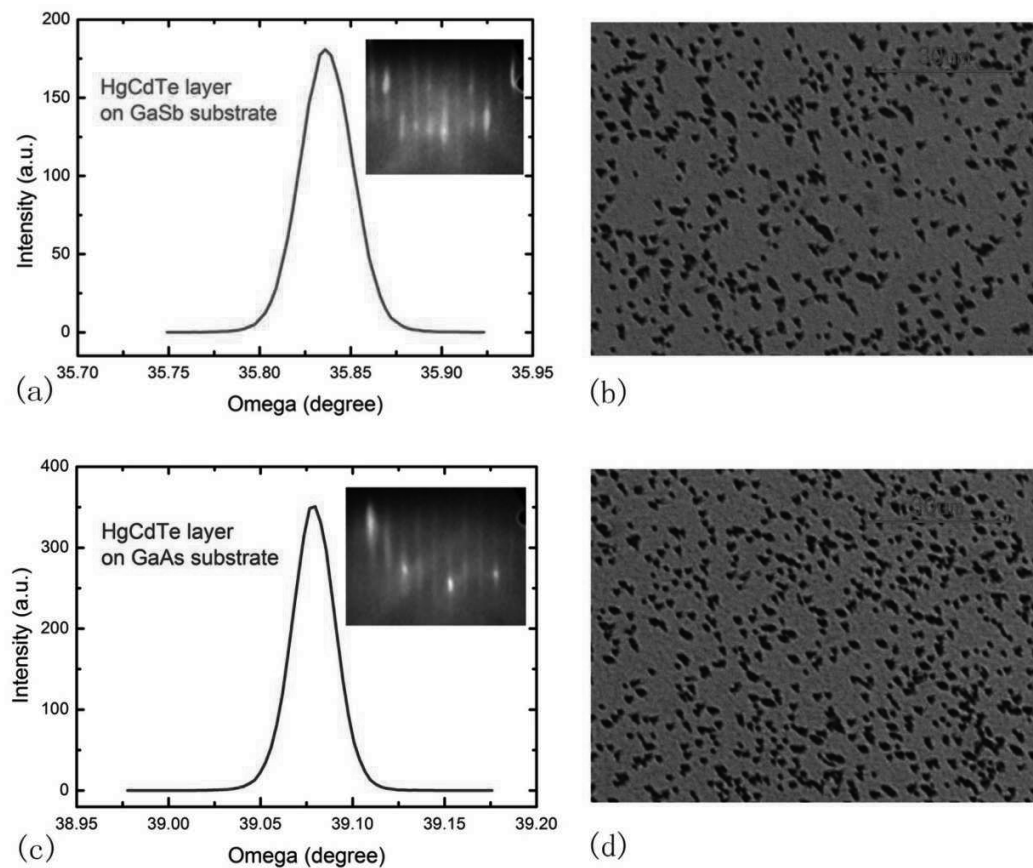
Figure 1 Representative XRD rocking curves and surface images (after EPD etching) of $Hg_{1-x}Cd_xTe$ (x=0.32) layers on GaSb ((a) and (b)) and GaAs ((c) and (d)) substrates. Insets of (a) and (c) show typical RHEED pattern during the growth of $Hg_{1-x}Cd_xTe$ (x=0.32) layers on GaSb and GaAs, respectively.

RADIATIVE AND NON-RADIATIVE RECOMBINATION IN MBE-GROWN CDTE HETEROSTRUCTURES

C. H. Swartz,[1,]* O. C. Noriega,[1] P. A. R. D. Jayathilaka,[1] M. Edirisooriya,[1]

T. H. Myers,[1] and Katherine N. Zaunbrecher[2]

[1]*Materials Science, Engineering, & Commercialization Program, Texas State University*

[2]*National Renewable Energy Laboratory*

RFM 3205, Texas State University, 601 University Drive, San Marcos, TX 78666

v: (512) 245-1839; f: (512) 245-3675; craig.swartz@txstate.edu

Abstract: Double heterostructures were produced consisting of a CdTe film between two wide band gap barriers of Cd1-xMgxTe alloy. A combined method examining both the excitation intensity dependence and the time dependence of photoluminescence (PL) was developed to quantify both radiative and non-radiative recombination.

1. Introduction

The non-radiative recombination of carriers in CdTe is largely attributable to surfaces and interfaces. The resulting short lifetimes harm various aspects of device performance, such as the open circuit voltages of solar cells. [1,2] An understanding of both radiative and non-radiative recombination rates is crucial for predicting device performance. [3]

Wide band gap barriers of $Cd_{1-x}Mg_xTe$ alloy are known to greatly reduce non-radiative recombination in CdTe by passivation of the surface.[4] To better understand both radiative and non-radiative recombination, double heterostructures were produced by molecular beam epitaxy (MBE). A method was developed to characterize interface-related recombination and estimate the non-radiative recombination coefficient.

2. Barriers

These heterostructures consist of a CdTe film between two 30 nm thick layers of CdMgTe, capped by a 10 nm thick layer of CdTe to prevent oxidation of the Mg. Photoluminescence (PL) was measured as a function of excitation intensity (PL-I) using a nm argon ion laser. PL was measured as a function of time after a fast laser pulse (TRPL) using a 640 nm fast pulse laser.

To determine the band gap and composition of the barriers, high-resolution X-ray diffraction (HR-XRD) and angle-dependent spectroscopic ellipsometry were employed, with the second proving to be well-suited to characterizing such thin layers. The barrier was modeled as a collection of Cody-Lorentz oscillators[5] which resulted in wavelength-dependent optical properties that could be fit to the ellipsometric data. Assuming that the gap corresponded with a maximum in the real refractive index of the barrier, we found that films with the high PL intensity were achieved with CdMgTe barriers having a band gap around 2.1 eV.

3. PL Intensity and Lifetime

Films with the highest PL intensity also had the longest TRPL lifetime, as would be expected from a reduction in non-radiative recombination. The PL intensity is shown in *Fig*. 1 as a function of excitation.

The fact that PL intensity increases with film thickness suggests that interfacial recombination continues to be the primary recombination pathway with these barriers. To properly characterize this situation, as seen in *Fig*. 2, trap charging must be accounted for, in addition to drift, diffusion, generation, and recombination. Minority carrier lifetime and surface recombination velocity are not

useful approximations in high injection, preventing an analytical solution. A numerical simulation algorithm was created to simulate the PL intensity, both in steady-state and as a function of time.[6]

The simulation quantitatively reveals interfacial trap densities of $N_T = 2\times10^{10}$ cm^{-2}. In addition to interfacial (Shockley-Read-Hall) recombination, direct band-to-band radiative recombination occurs, although Auger recombination is expected to be negligible for CdTe. Given the carrier concentrations n and p, the rate of radiative recombination is simply found from $R = Bnp$. Reported values of the recombination parameter B have ranged from 2-4$\times10^{-9}$ cm^{-3}s^{-1}.[7,8, and 9] However, the Van Roosbroeck-Shockley (VRS) relationship between absorption and recombination gives B = 1-3$\times10^{-10}$ cm^{-3}s^{-1} depending on the absorption data used. [3,10]

We have found that using the VRS relationship allows us to predict the TRPL trace of our films with striking accuracy, using the value N_T from the PL-I, without free parameters. (*Fig*. 3.) According to these calculations, the larger values of B in the literature do not allow for the possibility of the observed decays and the observed PL-I dependencies. A value of $B \approx 1\times10^{10}$ cm^{3}s^{-1} appears to best suit both datasets.
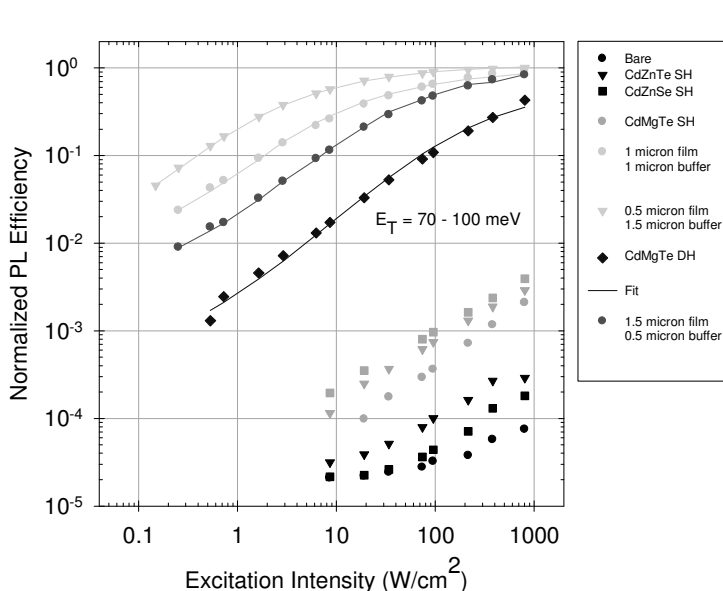
Fig. 1 – PL excitation intensity dependence shows the effectiveness of double CdMgTe barriers (DH). Also shown is the result of removing the back barrier, forming a single heterostructures (SH) and allowing the photocarriers to diffuse into the bulk substrate.
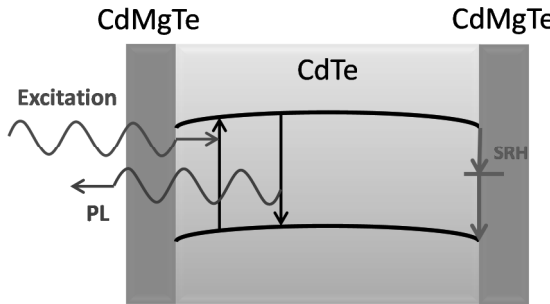
Fig. 2 Schematic of recombination at the interfaces of a CdMgTe /CdTe double heterostructure.
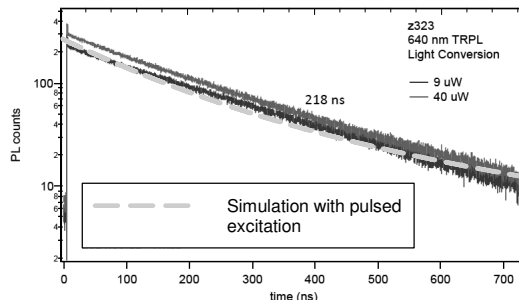
Fig. 3 – The trap parameters resulting from the fit to the PL-I data were used to simulate the time dependent distribution of carriers after a pulse of generated electron-hole pairs – without the use of any additional parameters. The relationship between simulated PL intensity and time yields a decay consistent with the experimental time-resolved PL (TRPL) lifetimes in these heterostructures.

[1] C. J. Bridge, P. Dawson, P. D. Buckle, and M. E. Özsan, J. Appl. Phys., 88, pp. 6451-6456, (2000).

[2] M. Gloeckler and J. R. Sites, Thin Solid Films, 480 pp. 241 – 245, (2005).

[3] A. P. Kirk, M. J. DiNezza, S. Liu, X.-H. Zhao, and Y.-H. Zhang, IEEE 39th Photovoltaic Specialists Conference (PVSC), pp. 2515-2517, (2013).

[4] M. J. DiNezza, X.-H. Zhao, S. Liu, A. P. Kirk, and Y.-H. Zhang, Appl. Phys. Lett. 103, 193901 (2013).

[5] J. Price1, P. Y. Hung, T. Rhoad1, B. Foran and A. C. Diebold, Appl. Phys. Lett. 85, 1701 (2004).

[6] C.H. Swartz, O.C. Noriega, P.A.R.D. Jayathilaka, M. Edirisooriya, X.-H. Zhao, M. J. DiNezza, S. Liu, Y.-H. Zhang, and T. H. Myers, IEEE 40th Photovoltaic Specialists Conference (PVSC) (2014).

[7] R. Cohen, V. Lyahovitskaya, E. Poles, A. Liu, and Y. Rosenwaks, Appl. Phys. Lett. , 73, pp. 1400-1402, (1998).

[8] R. K. Ahrenkiel, B. M. Keyes, D. L. Levi, K. Emery, T. L. Chu, and S. S. Chu, Appl. Phys. Lett., 64, pp. 2879 – 2881, (1994).

[9] X.-H. Zhao, M. J. DiNezza, S. Liu, S. Lin, Y.-H. Zhang, and Y. Zhao, J. Vac. Sci. Technol. B, 32, p. 040601, (2014).

[10] A. E. Rakhashani, J. Appl. Phys., 81, pp. 7988-7993, (1997).

Atomic structure of the CdTe (001) bonded interfaces

Ce Sun[1], Guoda Lian[1], Jinguo Wang[1], Robert F. Klie[2], and Moon J. Kim[1]

[1.] Department of Materials Science and Engineering, The University of Texas at Dallas, Richardson, Texas 75080, USA

[2.] Department of Physics, University of Illinois at Chicago, Chicago, Illinois 60607, USA

CdTe grain boundaries are the key to high efficiency solar cells, and also affect the optical and electrical properties. To understand how these occur, a direct correlation of the atomic and electronic structure of grain boundaries is critical. Wafer bonding, which enables the direct integration of two or more single crystal wafers with controlled surfaces and orientation, is a key technique in creating a single boundary with well defined crystallographic orientations. In this study, we demonstrate the fabrication of a single boundary between two identical CdTe (001) single crystals by wafer bonding. Interfacial morphology and atomic arrangement were analyzed using HRTEM and HAADF-STEM. HRTEM image of the bonded pair with a relative rotation angle of 0° shows a well-bonded single boundary along the [011] zone axis. The diffraction patterns from two portions of bonded pair indicates that the crystallographic orientation relationship of the bonded pair was (001)//(001) and [011]//[011]. The HAADF-STEM image and HAADF intensity profile show the atomic arrangement at the interface.

Presenter: Ce Sun, Tel: 214-240-7610, Fax: 972-883-5725, e-mail: ce.sun@utdallas.edu

Mid-infrared graphene detectors with antenna enhanced light absorption and photo-carrier collection

Yu Yao[1], Raji Shankar[1], Patrick Rauter[1], Yi Song[2], Jing Kong[2], Marko Loncar[1], and Federico Capasso[1,*]

[1]*School of Engineering and Applied Sciences, Harvard University, Cambridge, Massachusetts, 02138, USA*
[2]*Department of Electrical Engineering and Computer Science, Massachusetts Institute of Technology, Cambridge, 02139, USA*
yuyao@seas.harvard.edu

Abstract: We demonstrated antenna-assisted mid-infrared graphene detectors at room temperature with more than 200 times enhancement of responsivity (0.4 V/W at λ_0=4.45 μm) compared to devices without antennas (<2 mV/W).

1. Introduction

Graphene is an attractive material for optical detection due to its broad absorption spectrum and ultrafast response time. However, high-speed graphene detectors so far are still limited by low responsivity due to the weak optical absorption (only 2.3% in the monolayer graphene sheet) and short photocarrier lifetime (< 1 ps) [1]. Here we show that metallic nanoantenna structures can be designed to simultaneously improve both light absorption and photo-carrier collection in graphene detectors. The coupled antennas concentrate free space light into the nano-scale deep-subwavelength antenna gaps, where the graphene light interaction is greatly enhanced as a result of the ultra-high electric field intensity inside the gap. Meanwhile, the metallic antennas are designed also as electrodes to collect the generated photo-carriers very efficiently. We have demonstrated room temperature mid-infrared (mid-IR) antenna-assisted graphene detectors with more than 200 times enhancement of responsivity (0.4 V/W at λ_0=4.45 μm) compared to devices without antennas (<2 mV/W).

2. Design of antenna-assisted graphene detectors

Figure 1 (a) shows the top view of an end-to-end coupled linear antenna array on a graphene sheet and the electrical field intensity ($|E|^2/|E_0|^2$) enhancement distribution obtained by the finite difference time domain (FDTD) simulation. Light incident from free space is tightly concentrated into the near-field in the antenna gaps (gap size ~100 nm), which can greatly enhance the light-graphene interaction [2] and thus increase light absorption in graphene. The

simulated current density distribution in a portion of the graphene-antenna structure (indicated by the dashed line on the top view) is shown in Fig. 1 (b). The current density distribution clearly shows that the current flows from one antenna to the graphene in the gap and then to the next antenna, as indicated by the dash-dotted arrows on the cross-section view. Thus the antenna rods also act like nano-electrodes, which can effectively collect photo-carriers generated in the nanogap between them since the maximum travelling distance for the photo-carriers generated in the gap to reach the antenna electrodes is the gap size (<100 nm in our designs). In this nano-detector, the regions with high carrier collection efficiency automatically overlap with the region where the light is focused and the majority of photo-carriers are generated. Therefore, the light absorption and photocarrier collection efficiency can be enhanced simultaneously. In our experiment, we designed the end-to-end coupled antenna structures (antenna length 900 nm, gap size 60 nm) in a 2D array to increase the light collection cross-section, as shown in Fig. 2 (c). During the device fabrication, a monolayer graphene grown via Chemical Vapor Deposition (CVD)) was first transferred onto a 30 nm dry thermal oxide layer on a highly doped silicon substrate. Then the antenna array was fabricated on the graphene sheet by electron beam lithography (EBL), electron beam evaporation of 10 nm Pd and 30 nm Au, and a lift-off process.

3. Detector performance characterization

The wavelength dependent responsivity of the antenna-assisted graphene detector is measured with a wavelength tunable QC laser (wavelength range: 4.3 μm to 4.7 μm). Due to the resonant nature of the plasmonic antennas, the responsivity (photo-voltage divided by the total incident power on the sample) exhibits strong wavelength dependence, as shown in Fig. 2 (a) for a device with the same structure design as that in Fig.1 (c). The responsivity reaches its maximum around 4.45 μm, which is very close to the peak wavelength (4.46 μm) of the electric field enhancement in the antenna gap calculated with FDTD simulation, also shown in Fig. 2 (a). As the bias current becomes larger, the detector responsivity increases monotonically and reaches its maximum ($R_V \approx 0.4$ V/W) at $I_{DS} \approx 4$ mA, as shown in Fig. 2 (b). Further increasing the bias leads to reduced responsivity, probably because the electric field in the graphene channel (>2 MV/m) reaches its breakdown field. A comparison between the photo-response of the graphene detectors with and without antennas is shown in Fig. 2 (c). With antenna-enhanced photo-carrier generation and collection, the photo-voltage is increased by more than 200 times compared to that of the reference sample at the same laser power. According to the FDTD simulations, the absorption at

the antenna resonance wavelength is enhanced by about 4~5 times (from ~2.3% to ~10%, see more details in supplementary information III) compared with a pure monolayer graphene sheet. We attribute the additional 40~50 times improvement to the much more efficient carrier collection via metallic antennas. Moreover, the-antenna assisted graphene detector shows a linear photo-response as the incident laser power increases up to 16 mW, indicating that the absorption is not saturated despite the strong field enhancement in the antenna gaps.

4. Discussion and conclusion

We have demonstrated the use of metallic optical antennas to simultaneously enhance the optical absorption and photo-carrier collection efficiency in graphene detectors and achieved room temperature mid-IR antenna-assisted graphene detectors with more than 200 times enhancement of responsivity compared to reference devices without antennas. By shrinking the detector element to deep subwavelength size, it is a promising solution to achieve high speed, ultra-compact detectors with bandwidth up to THz range. This design concept can also be applied to the graphene detectors in other wavelength ranges, such as near IR and visible wavelength, and other thin film detectors.
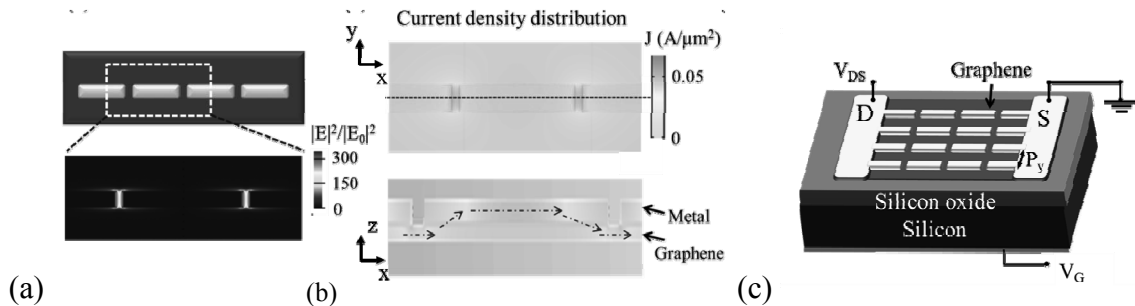
Figure 1 (a) Top view of the end-to-end coupled antennas on graphene (top) and the electric field intensity enhancement distribution on the surface of the graphene sheet (bottom). (b) Top view of the current density distribution on the surface of the graphene sheet (top) and cross-section view of the current density distribution in the middle plane of the antenna (indicated by the dashed line on the top view). The dash-dotted arrows indicate the path of the current flow. (c) A 3D schematic of the antenna-assisted graphene photodetector on a silicon substrate.
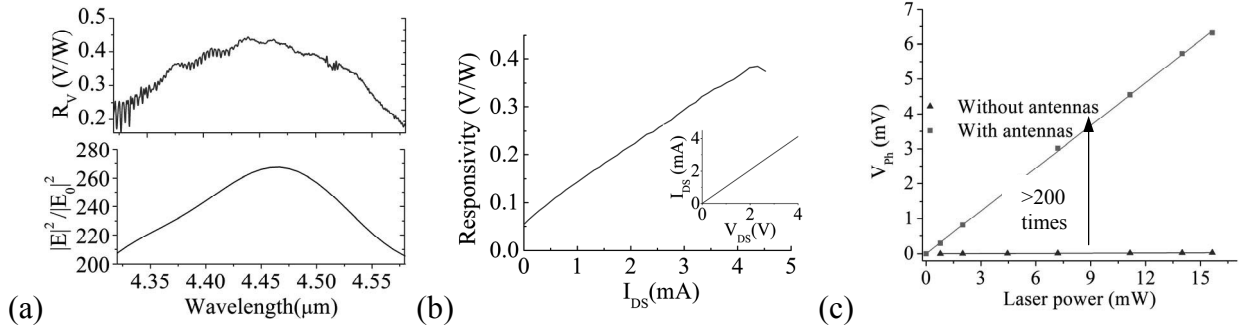
Figure 2. (a) Measured wavelength dependent photo-response of the antenna-assisted graphene detector (top) and electric field intensity enhancement in the center of the nano-gap between the plasmonic antennas obtained with FDTD simulation (bottom). The narrow dips on the photo-response curve are due to absorption lines of gas molecules in the air or on the sample (mainly CO_2). (b) Measured responsivity of the antenna-assisted graphene detector as a function of the biased current IDS at VGS=4 V. The inset shows the VDS-IDS plot of the same detector when the laser is off. (c) Measured photovoltage response of the graphene detectors with and without antennas as a function of incident laser power.

5. Acknowledgment

References

[1]   A. Urich, K. Unterrainer, and T. Mueller, "Intrinsic Response Time of Graphene Photodetectors," *Nano Letters,* vol. 11, pp. 2804-2808, Jul 2011.

[2]   Y. Yao, M. A. Kats, P. Genevet, N. F. Yu, Y. Song, J. Kong, and F. Capasso, "Broad Electrical Tuning of Graphene-Loaded Plasmonic Antennas," *Nano Letters,* vol. 13, pp. 1257-1264, Mar 2013.

Numerical modeling of SRH and tunneling mechanisms in HOT MWIR HgCdTe photodetectors

Marco Vallone [*], Marco Mandurrino [*], Michele Goano [*†], Francesco Bertazzi [*†],

Giovanni Ghione [*], Wilhelm Schirmacher [‡], Stefan Hanna [‡], and Heinrich Figgemeier[‡]

marco.vallone@polito.it

[*] DET, Politecnico di Torino, Corso Duca degli Abruzzi 24, 10129 Torino, Italy

[†] IEIIT-CNR, Politecnico di Torino, Corso Duca degli Abruzzi 24, 10129 Torino, Italy

[‡] AIM Infrarot-Module GmbH, Theresienstraße 2, D-74072 Heilbronn, Germany

Substantial reduction of dark current in photodetectors is a prerequisite for High Operation Temperature (HOT). HOT MWIR detectors are typically meant to be operated at $150\,\mathrm{K}$ and beyond while preserving performance characteristics formerly only obtained at substantially lower temperatures (typically $80\,\mathrm{K}$ to $100\,\mathrm{K}$). We compare here two sets of $\mathrm{Hg}_{1-x}\mathrm{Cd}_x\mathrm{Te}$ back-illuminated MWIR photodetectors grown by liquid-phase epitaxy (LPE): *set A* is p-doped by Hg vacancies ($N_A = 2 \times 10^{16}\,\mathrm{cm}^{-3}$), while in *set B* Au is used as acceptor ($N_A = 5 \times 10^{15}$ cm^{-3}) [1]. The photodiode junctions are defined by ion implantation into the p-type layer, with maximum donor density $N_D = 10^{18}\,\mathrm{cm}^{-3}$. The number of Hg vacancies, well known to be connected with Shockley-Read-Hall (SRH) recombination centers [2], is expected to be much lower in the Au-doped devices. Indeed, the experimental dark current density $J_{\mathrm{dark}}(V)$ (Figs. 1 and 2) is substantially lower in *set B*.

We calculated $J_{\mathrm{dark}}(V; T)$ for both sets of devices with a 3D numerical simulator [3] which takes into account SRH, Auger and radiative generation-recombination (GR) mechanisms, band-to-band tunneling (BTBT), and trap-assisted tunneling (TAT). Impact ionization was also included according to [4]. Auger and radiative GR rates were treated as in [3], whereas the SRH GR rate was described with the standard model by Shockley and Read [5], [6]:

$$R_{\mathrm{SRH}} = \frac{np - n_i^2}{\tau_p \left(n + n_i e^{\beta(E_t - E_{\mathrm{Fi}})}\right) + \tau_n \left(p + n_i e^{-\beta(E_t - E_{\mathrm{Fi}})}\right)} \, . \tag{1}$$

Within the same general formulation (1), two alternative descriptions of SRH processes were compared. First, in a simplified description (SRH-1), the lifetimes $\tau_{n,p}$ were directly assigned for each operating temperature, and the trap energies were set as $E_t = E_{\mathrm{Fi}}$ [2], where E_{Fi} is the intrinsic Fermi level. In a second, possibly more physics-based approach (SRH-2), recombination lifetimes were formulated as $\tau_{n,p} = 1/(N_t \sigma_{n,p} v_{th,n,p})$ [7]. Here N_t is the trap density, $v_{th,n,p}$ is the electron/hole thermal velocity, $\sigma_{n,p}$ is the electron/hole cross section on traps, and the trap energies are assumed to be constant with respect to the band edges. In principle, Eq. (1) should be able to better describe the temperature dependence of trap-assisted processes within the SRH-2 approach, thanks to the presence of thermal velocities $v_{th\,n,p}$ in the expressions of $\tau_{n,p}$. In the present analysis, the $N_t\sigma$ product was assumed to be the same for electrons and holes [8], [9] and to be temperature-independent.

Within the SRH-1 approach, a good fitting of the $J_{\mathrm{dark}}(V; T)$ characteristics for *set A* up to the largest value of

reverse bias $V_{\text{bias}} = -3\,\text{V}$ required the inclusion of both BTBT and TAT (Fig. 1, left). With SRH-2, on the contrary, the $J_{\text{dark}}(V;T)$ curves were well reproduced (especially up to $V_{\text{bias}} = -0.5\,\text{V}$) without the inclusion of TAT (Fig. 1, right).

The simulation of *set B* did not require any tunneling contribution up to $V_{\text{bias}} = -3\,\text{V}$, at all temperatures. The dark currents obtained with the SRH-1 and SRH-2 formulations are presented in Fig. 2, where the significantly better agreement allowed by the SRH-2 approach for all values of V_{bias} and T may be appreciated.

Tables I and II report the parameters of the SRH-1 and SRH-2 models determined in the present analysis, corresponding to the calculated characteristics of Figs. 1 and 2. These parameters strongly suggest that not only the lower dark current observed in *set B* can be ascribed to a lower density of SRH recombination centers, but also that the performance of this set of detectors is essentially Auger-limited.

In summary, the more recent technology corresponding to *set B* allows a significant reduction of the dark current because its reduced trap density allows both a decrease of R_{SRH} and a suppression of tunneling mechanisms. From a modeling perspective, the contribution of impact ionization seems crucial to obtain a good fitting for *set B*, whereas BTBT appears to dominate in *set A*. The present study also underlines the advantages of the SRH-2 description, based on a much smaller set of physically meaningful parameters, over the simpler but less predictive SRH-1 approach.

The analysis of the complex interplay between SRH, BTBT and impact ionization processes is currently in progress.

[1] R. Wollrab, W. Schirmacher, T. Schallenberg, H. Lutz, J. Wendler, and J. Ziegler, "Recent progress in the development of hot MWIR detectors," in *6th International Symposium on Optronics in Defence and Security (OPTRO 2014)*, (Paris), Feb. 2014.

[2] M. A. Kinch, F. Aqariden, D. Chandra, P.-K. Liao, H. F. Schaake, and H. D. Shih, "Minority carrier lifetime in *p*-HgCdTe," *J. Electron. Mater.*, vol. 34, no. 6, pp. 880–884, 2005.

[3] M. Vallone, M. Goano, F. Bertazzi, G. Ghione, R. Wollrab, and J. Ziegler, "Modeling photocurrent spectra of single-color and dual-band HgCdTe photodetectors: Is 3D simulation unavoidable?," *J. Electron. Mater.*, vol. 43, no. 8, pp. 3070–3076, 2014.

[4] M. A. Kinch, J. D. Beck, C.-F. Wan, F. Ma, and J. Campbell, "HgCdTe electron avalanche photodiodes," *J. Electron. Mater.*, vol. 33, pp. 630–639, June 2004.

[5] W. Shockley and W. T. Read, "Statistics of the recombinations of holes and electrons," *Phys. Rev.*, vol. 87, no. 5, pp. 835–842, 1952.

[6] J. G. Fossum and D. S. Lee, "A physical model for the dependence of carrier lifetime on doping density in nondegenerate silicon," *Solid-State Electron.*, vol. 25, pp. 741–747, 1982.

[7] S. M. Sze and K. K. Ng, *Physics of Semiconductor Devices*. Hoboken, NJ: John Wiley & Sons, 3rd ed., 2007.

[8] S. Krishnamurthy, M. A. Berding, Z. G. Yu, C. H. Swartz, T. H. Myers, D. D. Edwall, and R. DeWames, "Model for minority carrier lifetimes in doped HgCdTe," *J. Electron. Mater.*, vol. 34, no. 6, pp. 873–879, 2005.

[9] S. Krishnamurthy, M. A. Berding, and Z. G. Yu, "Minority carrier lifetimes in HgCdTe alloys," *J. Electron. Mater.*, vol. 35, no. 6, pp. 1369–1378, 2006.
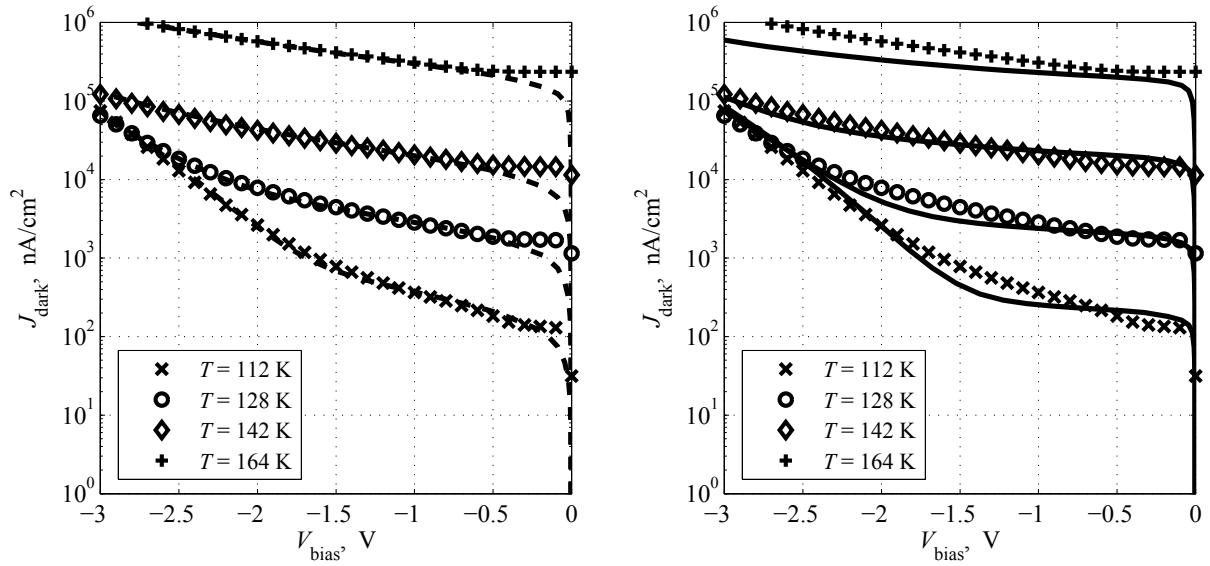
Fig. 1. Set A: comparison between experimental (symbols) and simulated dark current densities. The model includes: (left, dashed lines) Auger, radiative, BTBT, impact ionization, TAT and R_{SRH} according to the SRH-1 description; (right, solid lines) Auger, radiative, BTBT, impact ionization and R_{SRH} according to the SRH-2 description.
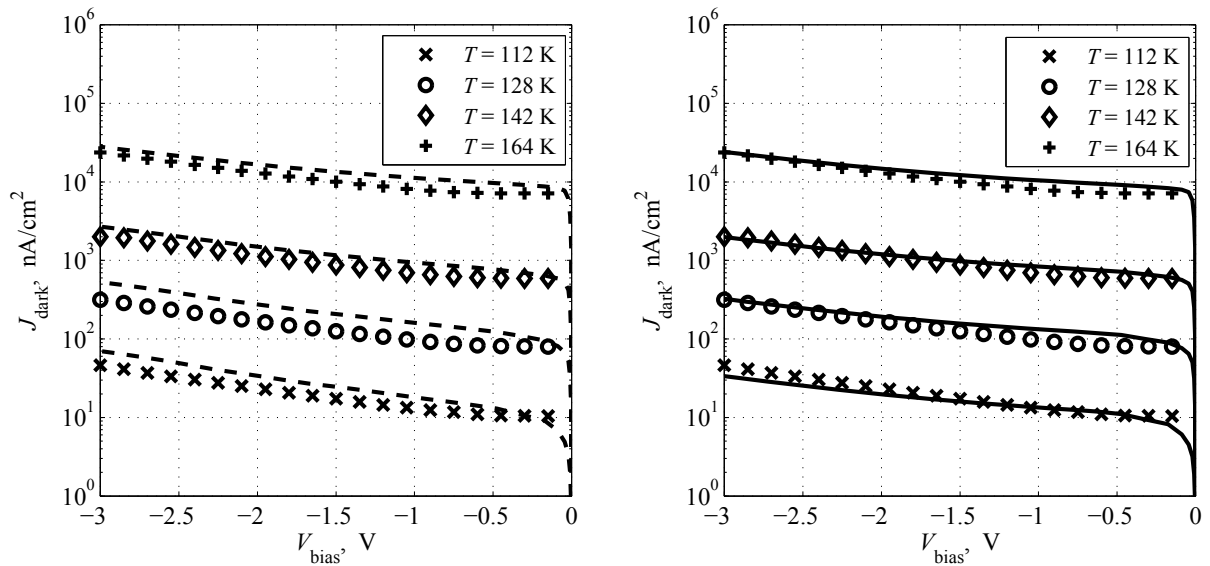
Fig. 2. Set B: comparison between experimental (symbols) and simulated dark current densities. The model includes: (left, dashed lines) Auger, radiative, impact ionization and R_{SRH} according to the SRH-1 description; (right, solid lines) Auger, radiative, impact ionization and R_{SRH} according to the SRH-2 description.

TABLE I
PARAMETERS ADOPTED FOR THE SRH-1 DESCRIPTION.

T, K	$\tau_{0\,\text{(n-region)}}$, μs	$\tau_{0\,\text{(p-region)}}$, μs	$E_t - E_{\text{Fi}}$, meV
set A			
112	2.6	0.9	0
128	7.4	2.6	0
142	9.6	3.3	0
164	9.6	3.3	0
set B			
all	2.4	0.05	0

TABLE II
PARAMETERS ADOPTED FOR THE SRH-2 DESCRIPTION

region	$N_t\sigma$, cm^{-1}	$E_c - E_t$, meV
set A		
p-doped	0.01	30
n-doped	0.8	70
set B		
p-doped	0.001	30
n-doped	0.0018	120

Development of MBE HgCdTe for HDVIP® focal plane arrays

Christopher Schaake[1,*], Roger Strong [1], Mike Kinch[1], Fred Harris[1], Lance Robertson[1], Jun Zhao[2], Fikri Aqariden[2]

[1]DRS Technologies, Dallas, TX

[2]EPIR Technologies, Bolingbrook, IL

*chris.schaake@drs.com, 214-996-2490 (phone), 972-560-6105 (fax)

DRS Technologies is interested in using molecular beam epitaxy (MBE) HgCdTe as an alternative to its standard liquid phase epitaxy (LPE) double-sided interdiffused (DSID) process for small pitch, large area high-density vertically integrated pixel (HDVIP®) focal plane arrays (FPAs). The HDVIP architecture uses vias to connect the HgCdTe to the read-out integrated circuit (ROIC). Reducing the via diameter, necessary for small pitch FPAs, is limited by the thickness of the HgCdTe. LPE material is typically grown >60 μm thick, which must be thinned and passivated prior to mounting on an ROIC. The thinning process can result in thickness non-uniformity, which can lead to regions of disconnected pixels as vias fail to reach the ROIC. Unlike LPE, MBE material can be grown to the desired thickness. Additionally, one or both passivation layers may be grown in situ with MBE, greatly reducing handling and processing time for DSID material.

CdZnTe (CZT) substrates were grown at DRS by the horizontal Bridgman method. They were sawn to a (211) orientation and polished. The CZT substrates were then shipped to EPIR for MBE growth. EPIR grew MWIR MBE films that were 8 μm thick and were capped with CdTe. The MBE films were shipped back to DRS, where they were annealed in a Hg ambient. MBE films went through a hybrid DSID process, shown in Figure 1, which is similar to how LPE is processed. The in situ CdTe cap was used for B-face passivation. MBE material was epoxy-mounted to sacrificial CZT substrates, followed by growth substrate removal and thinning of the HgCdTe absorber to 4 μm. The A-face was passivated with CdTe and ZnS. The samples were then annealed to interdiffuse the CdTe layers and convert the material to p-type. 16 hybrid DSID bars and 4 LPE DSID control bars were mounted on DRS1048 ROICs (480x640, 12 μm pitch). FPAs were fabricated using an established HDVIP process flow.

FPAs were tested in lab Dewars from 110 K to 170 K. LPE FPAs behaved as expected, indicating there were no processing issues with the lot. 15 of the 16 MBE FPAs passed the DRS micro-IDCA specification at 110 K with an average operability of 99.84%. MBE FPA performance degraded as operating temperature was increased due to noise defects. The RMS noise defects of both LPE and MBE FPAs are plotted in Figure 2 at 110 K, 140 K, and 160 K, along with n_i and n_i^2 curves. RMS noise defects of LPE and MBE FPAs followed the n_i curve and not the n_i^2 curve. Despite MBE and LPE material having similar etch pit densities of 1e5 cm-2, the MBE FPAs had 10 times more RMS noise defects at 160 K than the LPE FPAs.   The larger number of noise defects observed in MBE FPAs could be explained by a short lifetime in the depletion region [1].

Further evidence of a short lifetime was observed in dark current measurements from 100 K to 200 K, shown in Figure 3. The dark current was modeled with two components: diffusion current from the p-side and SRH current from the depletion region [2]. The p-side diffusion current consisted of Auger7 and vacancies, and it fit the data at temperatures above 120 K. However, at 100 K and 110 K, the dark current could not be modeled with p-side diffusion current alone. A SRH depletion current with a 150 μs lifetime was needed to fit the data at 100 K and 110 K. A 150 μs lifetime is considerably shorter than the 5 ms lifetime typically observed in LPE DSID. A 150 μs lifetime is consistent with poor FPA performance at 160 K [3]. Work is underway to understand the origin of the short lifetime observed in MBE films.
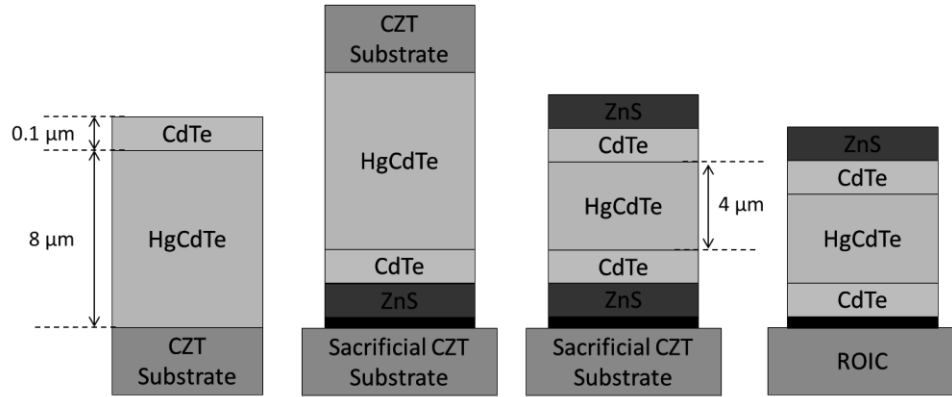
Figure 1. Hybrid DSID process used to prepare MBE material for HDVIP FPAs. The as-grown MBE structure (far left) is mounted onto a sacrificial CZT substrate, followed by substrate removal and thinning. The HgCdTe is then passivated and annealed prior to mounting onto an ROIC.
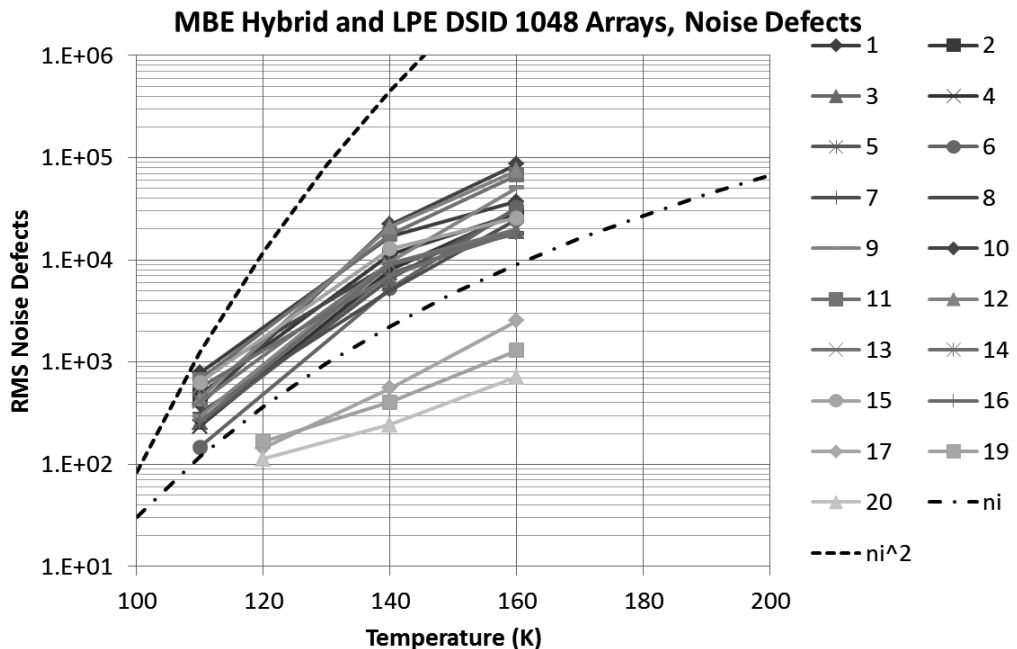
Figure 2. RMS noise defects on LPE (#'s 17,19, and 20) and MBE hybrid DSID FPAs (#'s 1-16) at 110 K, 120 K, 140 K, and 160 K. Also plotted are n_i and n_i^2 curves for reference.
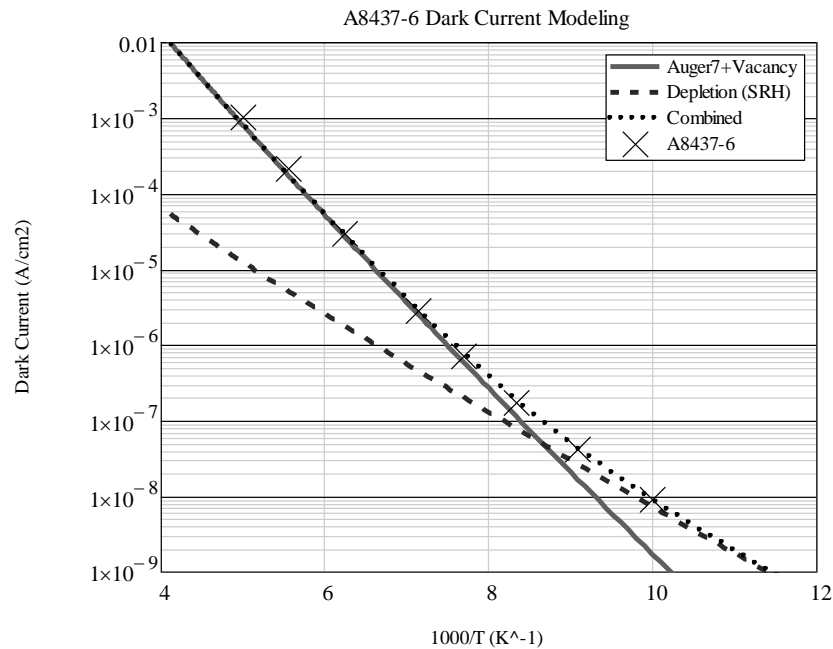
Figure 3. Dark current measured on A8437-6 and modeled dark current components. The dark current deviates from the Auger7+Vacancy curve at low temperatures, which can be explained by a depletion current with a SRH lifetime of 150 us.

References

[1] M. A. Kinch, C.-F. Wan, H. Schaake, and D. Chandra, "Universal 1/f noise model for reverse biased diodes," *Appl. Phys. Lett.*, vol. 94, no. 19, pp. 193508–3, May 2009.

[2] M. A. Kinch, *Fundamentals of Infrared Detector Materials*. 1000 20th Street, Bellingham, WA 98227-0010 USA: SPIE, 2007.

[3] M. A. Kinch, R. L. Strong, and C. A. Schaake, "1/f Noise in HgCdTe Focal-Plane Arrays," *Journal of Elec Materi*, vol. 42, no. 11, pp. 3243–3251, Nov. 2013.

MTF Consequences of Planar Dense Array Geometries

B. Pinkie*, A. R. Wichman*, and E. Bellotti*

*ECE Department, Boston University, 8 Saint Mary's Street, Boston, MA 02215
Contact information: email **bpinkie@bu.edu**, Tel. 617-353-5885

The current trend in IR photon detector array development is towards very small pixels for high resolution, low dark current imaging. Arrays with pitches as small as 10 μm have been demonstrated [1] and 5 μm pixels are being investigated in the DARPA AWARE program [2]. Long minority carrier lifetimes, necessary to maintain low dark currents, lead to diffusion lengths which can be several times larger than the pixel pitch. Special consideration must be made in the design and analysis of these dense arrays due to electronic interaction between neighboring pixels. In this work, we explore the MTF consequences of dense array operation.

Previously, we have used our numerical simulations to investigate crosstalk in two-color detectors [3], nBn devices [4], and photon trapping arrays [5]. Here we focus on planar ion-implanted *p*-on-*n* arrays which fit the dense array formalism ($\frac{P}{2} < L_D$ and $t < L_D$). Our models have been used to investigate the origin and geometry dependence of lateral diffusion currents in InGaAs double-layer heterostructures [6]. In this work, we extend the models to the HgCdTe material system with a focus on how the pixel geometry, and specifically the shape of the implanted junction and depleted region, influences the imaging capabilities of the array. The modulation transfer function (MTF) is calculated and used to quantify results as shown by the authors in [7]. Use of numerical models allows the exploration of non-ideal behavior. Three dimensional finite difference and finite element simulations allow us to perform a wide parametric study of the variables influencing MTF performance of dense arrays. Design suggestions for improved MTF performance are made and the trade-offs of such explored. Results are specific to HgCdTe detectors, but applicable across material systems.

References

[1] O. Gravrand *et al. J. Electron. Mater.* **42**, 3349 (2013).

[2] W. E. Tennant *et al. J. Electron. Mater.* **in press**,, available online, DOI: 10.1007/s11664-014-3192-4.

[3] B. Pinkie and E. Bellotti *J. Electron. Mater.* **42**, 3080 (2013).

[4] M. Reine, J. Schuster, B. Pinkie, and E. Bellotti, *J. Electron. Mater* **42**, 3015 (2013).

[5] J. Schuster and E. Bellotti, *Opt. Expr.* **21**, 14712 (2013).

[6] A. R. Wichman, R. E. DeWames, and E. Bellotti *Proc. SPIE* **9070-3**, in press. (2014)

[7] O. Gravrand *et al.* *J. Electron. Mater.* **in press**,, available online, DOI: 10.1007/s11664-014-3185-3.
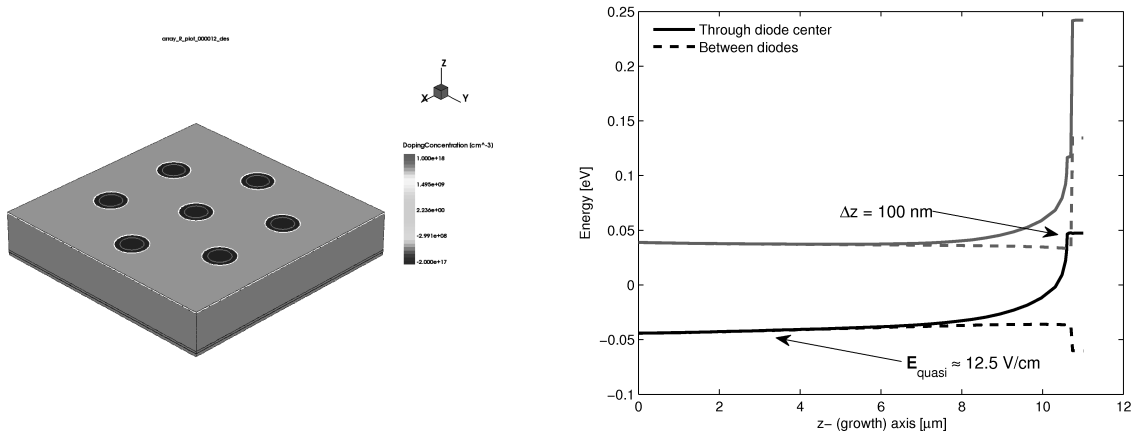
Figure 1: 3D schematic view of the planar HgCdTe arrays considered (left). A hexagonal arrangement of the diodes are shown, but other configurations are modeled as well. Resulting energy band diagram (right) of the device shown.
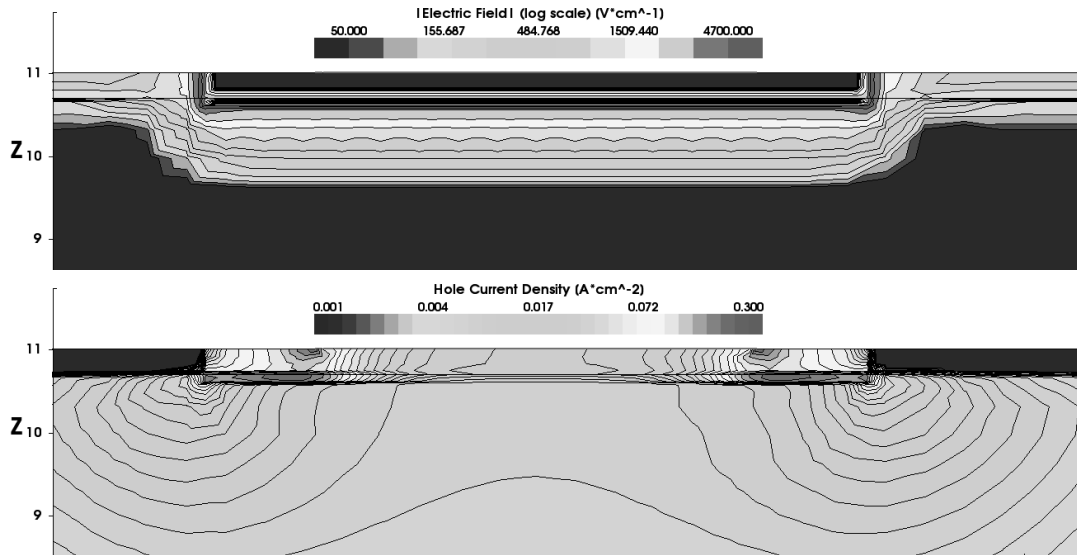
Figure 2: Spatial profiles of the magnitude of the electric field (top) and the hole current density (bottom) at 60 mV reverse bias showing field and current bunching at the corners of the implant. The geometry of the implant, and therefore the depleted region influences the collection behavior and MTF of diffusion dominated dense arrays.

Modeling and characterization of MTF and spectral response at small pitch on Mercury Cadmium Telluride

Jocelyn Berthoz[1], R. Grille[1], L. Martineau[1], L. Rubaldo[1], F. Chabuel[1], D.Leclercq[1], O. Gravrand[2]

[1] SOFRADIR, 364 Route de Valence, Actipole - CS10021 38113 Veurey-Voroize

[2] CEA Leti-MINATEC Campus, 17 rue des Martyrs, 38054 Grenoble Cedex 9, France

Phone:+33 4.76.28.77.00, Fax : +33 4.76.53.85.97, e-mail: jocelyn.berthoz@sofradir.com

Student paper

INTRODUCTION

Spatial applications are challenging infrared (IR) technologies requiring the best system performances. It requires to covering the entire infrared spectrum from SWIR to VLWIR with various pixel sizes. This is possible thanks to a well mastered Mercury Cadmium Telluride technology. Because of its adjustable gap, it can achieve all the infrared bands. Nevertheless, technology optimization requires a deep understanding of physical mechanisms.

This paper presents computations by finite element modeling for electro-optical performances as spectral response and modulation transfer function. Computations and characterizations for all infrared bands are shown to highlight the accuracy of our simulation and the state of the art of our technology, with the physics limited performances obtained.

EXPERIMENTAL AND COMPUTATION RESULTS

Computation by finite element is frequently used in order to compute MTF and spectral Response [1][2][3]. The computations presented here are made with the software Atlas

form Silvaco. First, the model is calibrated with measurement on 30µm pitch in the entire infrared band. Figure 1 shows measured and calculated spectral Response for SWIR to VLWIR. A good agreement is found for the entire infrared band. Then the parameters obtained are used for MTF's computations. Figure 2 shows a comparison between measured and calculated MTF. This graph shows that it is possible with the same parameter to compute spectral response and MTF. Moreover, MTF is better when the cut-off is lower. This is linked to the variation of the diffusion length with Cadmium composition which is larger for the SWIR band.

Then, computations for smaller pitch are achieved and compared to the measurement. Figure 3 presents MTF for the MWIR band with different pitch from 30µm to 10µm. As expected, when the pitch is reduced, MTF get higher. However as illustrated by figure 4 the Cross-talk also increased because of the lateral diffusion of carriers[4]. Nevertheless state of the art crosstalk results are obtained down to the 10µm pitch [5],
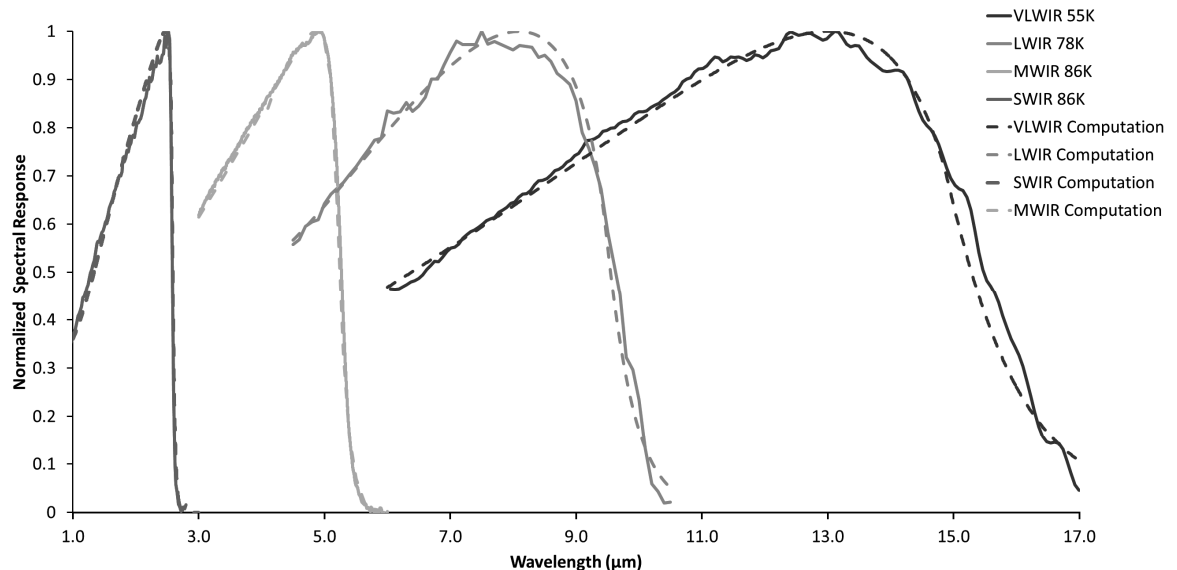
Figure 1. Normalized spectral response for different infrared band
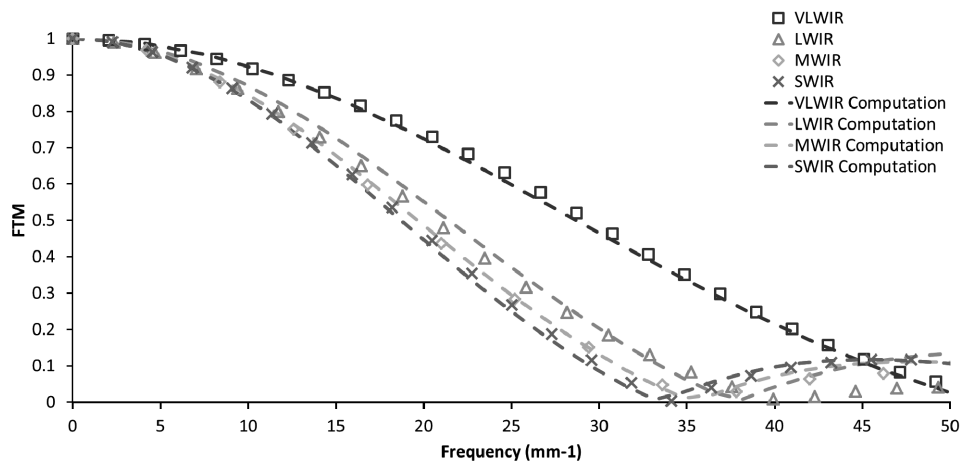
Figure 2. MTF measurements and computations for different infrared-band at 30μm pitch
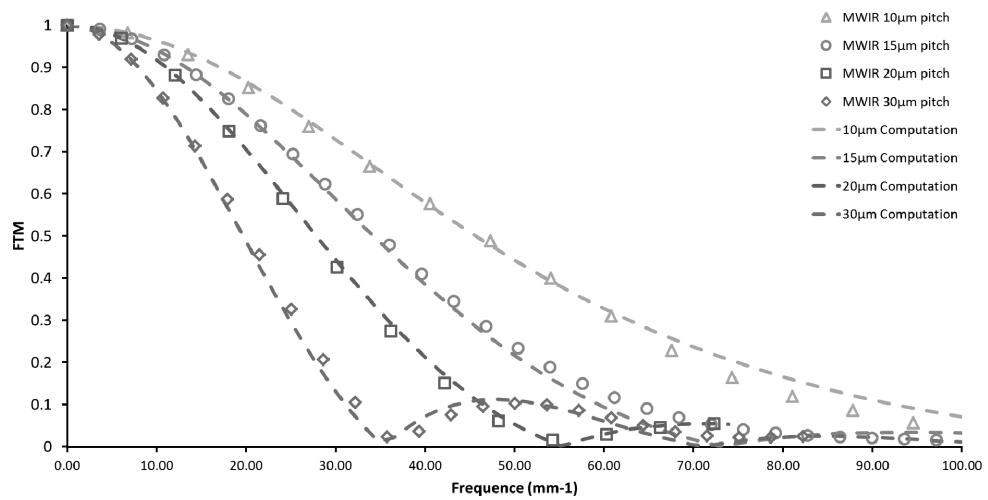
Figure 3. MTF measurements and computations for different pitch at MWIR band

Figure 4. Electrical cross-talk function of the pitch

REFERENCES

[1]   O. Gravrand and S. Gidon, "Electromagnetic modeling of n−on−p HgCdTe back−illuminated infrared photodiode response," *Journal of electron devices*, vol. 37, no. 9, 2008.

[2]   B. Pinkie, J. Schuster, and E. Bellotti, "Physics−based simulation of the modulation transfer function in HgCdTe infrared detector arrays.," *Optics letters*, vol. 38, no. 14, pp. 2546-9, Jul. 2013.

[3]   T. Fishman, V. Nahum, E. Saguy, Z. Calahorra, I. Shtrichman, S. D. Scd, and P. O. Box, "3D simulation of detector parameters for backside illuminated InSb 2−D arrays," *Proc. SPIE*.

[4]   O. Gravrand, J. Desplanches, C. Delbe, G. Mathieu, and J. Rothman, "Study of the Spatial Response of Reduced Pitch Hg 1−x Cd x Te Dual−Band Detector Arrays," *Journal of Electronic Materials*, vol. 35, no. 6, pp. 1159-1165, 2006.

[5]   G. Gershon, A. Albo, M. Eylon, O. Cohen, Z. Calahorra, M. Brumer, M. Nitzani, and E. Avnon, "Large Format InSb Infrared Detector With 10 μ m Pixels," *Optro-2014*, 2014.

A Systems Analysis of the Benefits of Small Infrared Detectors

We investigate the dependence of the performance of a background limited sensor on pixel size. The examination of resolution and sensitivity includes diffraction and detector size parameters, but good well capacity is assumed, antenna effects are ignored (and is appropriate) and a quality optical system that corrects for aberrations is assumed.   We show that smaller detectors can provide the same performance as larger detectors while providing reduced system swap, a less complicated system, and reduced overall cost. One result is a solid state imager with no moving parts and field of view switch for different magnifications.   These small detectors will require advances in optical system design and detector technology including the readout integrated circuits.

Ronald G. Driggers, Ph.D.
CEO, St. Johns Optical Systems
1130 Business Center Drive
Lake Mary, FL 32746
407-205-3577

Evaluation of MBE grown MCT on GaAs for HOT applications

J. Wenisch[*], W. Schirmacher, R. Wollrab, D. Eich, S. Hanna, R. Breiter, H. Lutz, H. Figgemeier

AIM Infrarot-Module GmbH, Theresienstr. 2, 74072 Heilbronn, Germany

Molecular beam epitaxy (MBE) is a key upcoming technology for cost-effective production of MCT infrared focal plane arrays (FPAs) as well as for the development of novel 3rd generation IR detectors. A separate predominant topic in the MCT community is the demand for high-operating temperature (HOT) IR detectors across all wavelengths. However, little has been published to date about the viability of MBE-grown material for HOT applications, especially for MCT grown on alternative substrates such as GaAs, Si or Ge. This is understandable, since MBE is still a relatively new technology for the fabrication of MCT material. HOT development usually is built upon the basis of a more mature and better understood fabrication technique such as liquid phase epitaxy (LPE). AIM is no exception in this regard and has achieved much progress over the last years in the development of HOT technology for detectors fabricated by LPE [1].

In parallel, MBE technology at AIM has achieved a high level of maturity and reliability [2]. To further improve and make full use of the benefits of MBE technology, efforts are being started to incorporate insights and techniques from the development of LPE-based material, especially with regard to HOT applications, into MBE-based projects.

Some aspects which were found to improve the performance of devices fabricated from LPE-grown material are actually much easier to achieve with MBE technology. A prime example is the growth of a cap layer with a graded composition region leading to the MCT detector layer [1,2].

In this contribution, we will present MWIR detectors fabricated from MCT grown by MBE which benefit from some aspects of the LPE-based HOT development. All MBE layers were grown on 100-mm (211)GaAs substrates. The FPAs were processed in standard planar *n*-on-*p* technology in a 640 x 512 pixel, 15 µm pitch design.

During electro-optical characterization, pixel operabilities above 99.5% for operating temperatures up to 120 K were measured. Fig. 1 shows the improvement in defective pixel

*Corresp. author: jan.wenisch@aim-ir.com, Phone: +49-7131-6212-187, Fax: +49-7131-6212-199

percentage between two MWIR detectors before (ball-shaped symbols) and after (triangle-shaped symbols) incorporation of HOT technology.
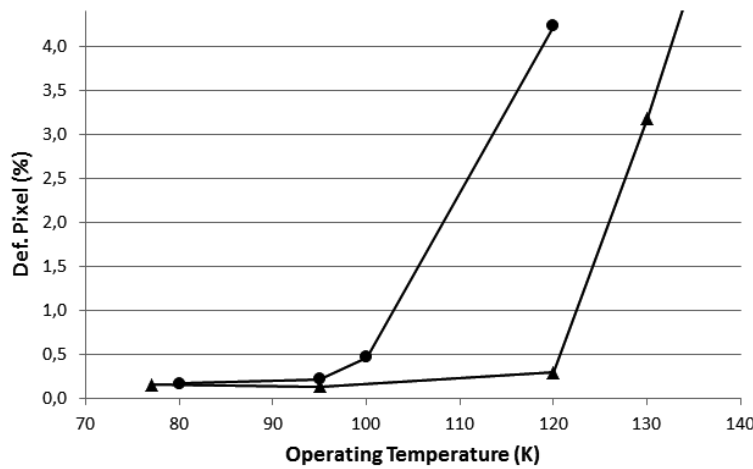
Fig. 1. Comparison of two MWIR detectors (640 x 512 pixels, 15 µm pitch) fabricated from MCT grown by MBE on GaAs substrates. Detector A (ball-shaped symbols) represents the state of development before the incorporation of HOT-technology in Detector B (triangle-shaped symbols).

References:

[1] W. Schirmacher, R. Wollrab, H. Lutz, T. Schallenberg, J. Wendler, and J. Ziegler, *J. Electr. Mater.* **43**, published online, DOI 10.1007/s11664-014-3033-5, 2014.

[2] J. Ziegler, J. Wenisch, R. Breiter, D. Eich, H. Figgemeier, P. Fries, H. Lutz , and R. Wollrab, *J. Electr. Mater.* **43**, published online, DOI 10.1007/s11664-014-3149-7, 2014.

Investigation of ICPECVD Silicon Nitride Films for HgCdTe Surface Passivation

J. Zhang*, G. A. Umana-Membreno, R. Gu, W. Lei, J. Antoszewski,
J. M. Dell, and L. Faraone

School of Electrical, Electronic and Computer Engineering,
The University of Western Australia, 35 Stirling Highway,
Crawley, WA 6009, Australia
*Email: jing.zhang@research.uwa.edu.au   Phone: +61-8-6488 3745   Fax: +61-8-6488 1095

ABSTRACT

Silicon nitride films of high dielectric quality deposited at low temperatures are attractive for surface passivation of HgCdTe devices. However, there are few reported studies on SiN_x as a passivation layer for HgCdTe and related compounds. In this paper, we report results of a study of SiN_x films deposited on HgCdTe epitaxial layers by inductively-coupled plasma-enhanced chemical vapor deposition at substrate temperatures between 80°C and 100°C. Capacitance-voltage measurements on SiN_x/n-HgCdTe metal-insulator-semiconductor structures indicated that Si-rich SiN_x films deposited at 100°C exhibit characteristics that make them suitable as surface passivation layers for HgCdTe-based devices.

Conventionally, high quality SiN_x films for surface passivation layers are typically deposited at temperatures, in the 200°C -750°C range, that are relatively much higher than the maximum allowed HgCdTe processing temperature (<120°C). However, inductively-coupled plasma-enhanced chemical vapour deposition (ICPECVD) offers the ability to deposit relatively high quality SiN_x films at temperatures as low as 80°C. Low-temperature (80°C-130°C) SiN_x films deposited employing ICPECVD have been reported to be characterised by low etch rates in wet-chemical etchants, minimal damage to substrate surface during deposition, low stress and high breakdown voltage [1]. The low ion energy of the plasma source in the ICPECVD systems enables SiN_x films to be deposited on HgCdTe without significant surface damage, and this was confirmed using magnetic-field dependent Hall measurements and high-resolution mobility spectrum analysis (HR-MSA) carried out before and after SiN_x deposition. The HR-MSA results indicated an increase in

the mobility of the dominant bulk electron after SiN_x, an effect that is likely due to hydrogen passivation of defect centers as a consequence of H incorporation during the ICPECVD process.

In order to determine ICPECVD SiN_x deposition conditions suitable for surface passivation of HgCdTe, a series of low-temperature (80°C-100°C) SiN_x films were deposited on CdTe/GaAs and Si substrates under different deposition conditions. The Si substrates were employed as reference samples. The deposition conditions employed are detailed in Table I. The influence of ICP power on the quality of the deposited films SiN_x films was assessed through the infrared (IR) absorbance of the films. The IR absorbance of each film was measured on the day of the deposition and was monitored during the six month period (Fig. 1). The SiN_x/CdTe/GaAs sample labelled C5-SiN_x deposited using ICP power of 600W appeared to be porous and more susceptible to oxidation under conventional ambient conditions, with the Si-O-Si stretching peak appearing at 1080 cm^{-1}, as shown in Fig. 1. This Si-O-Si oxidation peak has been reported to become evident when SiN_x films undergo oxidation in air, as reported by Liao et al. [2], Chang et al. [3] and Westerhout et al. [4]. H_2O in the air (moisture) has been found to be responsible for the oxidation of the SiN_x films [2].It is noted that although the SiN_x/Si reference sample showed good stability over six months, the results from SiN_x/CdTe/GaAs samples suggest that high ICP power conditions are not suitable for CdTe or HgCdTe substrates. Deposition conditions C2, C3, C4, D1 and D4 showed good time stability in terms of the IR absorbance peaks associated with exposure to O_2 and H_2O in the atmosphere.

The HgCdTe epilayers employed in this work were grown in a Riber-32 molecular beam epitaxy. A layer of 2 um-thick n$^+$ $Hg_{0.6}Cd_{0.4}Te$ was grown on CdZnTe substrate followed by a 5um-thick $Hg_{0.68}Cd_{0.32}Te$ layer. The HgCdTe wafer was then diced into four pieces, and on each piece SiN_x was deposited under the conditions detailed in Table II. For samples labelled D1-80C, D1-90C and D1-100C, the SiN_x films were deposited under similar conditions, varying only the temperature of the substrate, with samples D1-100C and D4-100C differing only in the SiH_4/NH_3 ratio employed.

The quasi-static method was applied to extract the density of interface states D_{it} at 77K, as shown in Fig. 2. All the four D_{it} curves were found to have similar mid-gap value but differ from each other when the surface potentials bend more towards valence and conduction band edges. D_{it} levels in the D4-100C labelled sample were lower than under other SiN_x deposition conditions, except for the sharp increase in D_{it} as the HgCdTe surface potential bends near the edge of valence band. The SiN_x deposition conditions for sample D4-100C were found to results in a SiN_x/HgCdTe MIS structure characterised by a negative fixed charge density of -1.2×10^{11} cm^{-2}, a slow interface charge density of 4.3×10^{10} cm^{-2}, and interface state density D_{it} of 4.0×10^{10} eV^{-1}cm^{-2}. These results are significant improvement on the best reported ECR-PCVD deposited SiN_x film on HgCdTe, which indicated a negative fixed charge density of -1.4×10^{11} cm^{-2} and an interface state density D_{it} of 1×10^{11} eV^{-1}cm^{-2} [5]. These characteristics suggest that ICPECVD SiN_x films deposited at relatively low temperatures (80°C-100°C) have significant potential as surface passivation films for HgCdTe-based devices.

Acknowledgments

Keywords - mercury compounds, hydrogenated silicon nitride, surface passivation.

TABLE I
Summary of deposition conditions for silicon nitride films on CdTe/GaAs and Si substrates

Batch name	Temperature (°C)	ICP RF power (W)	Gas flow rates (sccm)
C2-SiN$_x$	80	350	I[*]
C3-SiN$_x$	80	450	I[*]
C4-SiN$_x$	100	450	I[*]
C5-SiN$_x$	100	600	I[*]
D1-SiN$_x$	100	350	I[*]
D4-SiN$_x$	100	350	II[**]

[*]Flow I (sccm): SiH$_4$: 6.9, NH$_3$: 10.3, Ar: 120, He: 131.1, SiH$_4$/NH$_3$ = 0.67;
[*]Flow II (sccm): SiH$_4$: 7.5, NH$_3$: 9.7, Ar: 120, He: 131.1, SiH$_4$/NH$_3$ = 0.77.

TABLE II
Summary of deposition conditions for silicon nitride films
on HgCdTe substrates

Sample name	Temperature (°C)	SiH$_4$ flow rate (sccm)	NH$_3$ flow rate (sccm)	SiH$_4$/NH$_3$ ratio	SiN$_x$ thickness (nm)	[N]/[Si] ratio
D1-80C	80	6.9	10.3	0.67	285	1.17
D1-90C	90	6.9	10.3	0.67	267	1.07
D1-100C	100	6.9	10.3	0.67	244	1.02
D4-100C	100	7.5	9.7	0.77	202	0.90
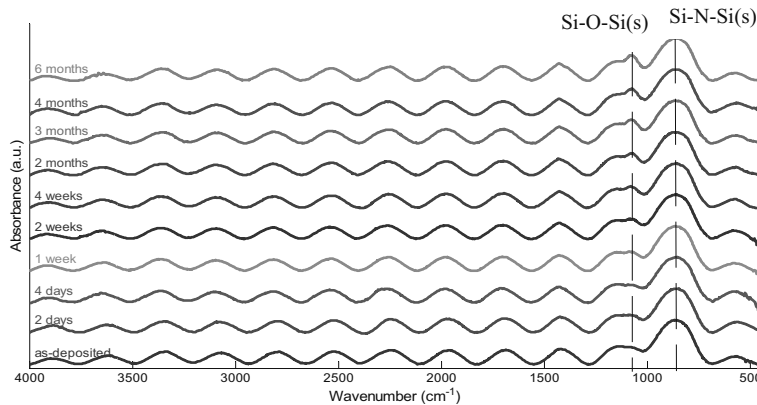
Fig. 1 The IR absorbance spectra of the C5-SiN$_x$ film on CdTe/GaAs substrate monitored in six-month period. The films were allowed to age in laboratory atmosphere. Text on the left indicate the time after fabrication that the measurement was taken.
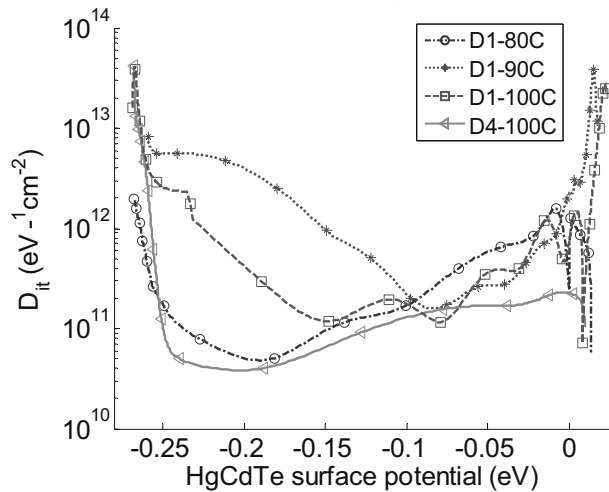
Fig.2 Comparison of the interface state densities (D$_{it}$) of the SiN$_x$/n-Hg$_{0.68}$Cd$_{0.32}$Te MIS structures extracted by the quasi-static method at 77K.

References:
[1] R. Wolf, K. Wandel, and B. Gruska, *Surface and Coatings Technology,* vol. 142-144, pp. 786-791, 2001.
[2] W.-S. Liao, C.-H. Lin, and S.-C. Lee, *Applied physics letters,* vol. 65, pp. 2229-2231, 1994.
[3] H.-Y. Chang, C.-Y. Meng, C.-W. Huang, and S.-C. Lee, *Journal of applied physics,* vol. 98, pp. 084501-084501-5, 2005.
[4] R. J. Westerhout, C. A. Musca, R. Sewell, J. Antoszewski, J. M. Dell, and L. Faraone, *IEEE Conference on Optoelectronic and Microelectronic Materials and Devices,* pp. 78-81, 2008.
[5] N. N. Kajihara, N. G. Sudo, N. Y. Miyamoto, and N. K. Tanikawa, "Silicon Nitride Passivant for HgCdTe n+p Diodes," Journal of the Electrochemical Society, vol. 135, pp. 1252-1255, 1988.

A NOVEL METHOD TO OBTAIN HIGHER DEPOSITION RATE OF CdTe USING LOW TEMPERATURE LPCVD FOR SURFACE PASSIVATION OF HgCdTe

Sneha Banerjee, Rajendra Dahal and Ishwara B. Bhat

Electrical, Computer and Systems Engineering Department, Rensselaer Polytechnic Institute, Troy, NY 12180

Phone: 518 276 2786; Fax: 518 276 6261; email: baners6@rpi.edu

Cadmium telluride (CdTe) has gained immense importance in the infrared (IR) detector industry as a surface passivant for mercury cadmium telluride ($Hg_{1-x}Cd_xTe$). CdTe is nearly lattice-matched with $Hg_{1-x}Cd_xTe$, which helps reduce the number of dangling bonds significantly. Since, it is a higher bandgap material than $Hg_{1-x}Cd_xTe$, it acts as a good minority carrier reflector, which in turn increases the minority carrier lifetime. A high minority carrier lifetime is a very important factor in the performance of IR detectors. Additionally, CdTe is transparent to IR radiation, has a high resistivity and is also mechanically harder than $Hg_{1-x}Cd_xTe$. With the increase in complexity of IR detector structures, conventional methods of CdTe deposition like evaporation became outdated and chemical vapor deposition (CVD) gained prominence [1, 2]. Earlier work reported in the 2013 workshop had demonstrated the conformal deposition of CdTe on high aspect ratio $Hg_{1-x}Cd_xTe$ structures at temperatures as low as 135°C [3]. A significant improvement in minority carrier lifetime was also reported on $Hg_{1-x}Cd_xTe$ samples with a thin passivation layer of CdTe deposited at 135°C. The major drawback of the entire process was the slow rate of deposition of CdTe (50 -60 nm/hr) at such a low temperature. This work presents a new reactor design and process to increase the rate of deposition of CdTe at temperatures less than 150°C.

A home-built horizontal hot-wall metalorganic CVD reactor was used for the deposition of CdTe passivation films. Ultra high purity (UHP) hydrogen was used as the carrier gas. Dimethylcadmium (DMCd) and Di-isopropyltellurium (DIPTe) were used as the metalorganic sources for cadmium and tellurium respectively. The hot-wall configuration consists of two clamshell heaters. All experiments were carried out with the front heater set to 600°C and the back heater turned off. This helped to maintain the temperature of the sample below 150°C. Commercial GaAs (100) and Si (110) were used as substrates to optimize the growth conditions. A new graphite cracker cell with integrated diffuser was designed and incorporated inside the hot-wall reactor to increase the growth rate. Precursors carried by UHP H_2 enter the graphite diffuser maintained at higher temperature and crack into elemental Cd and Te in the enclosed volume between the integrated graphite diffusers. They are then ejected as jets through the small holes on the outlet side and get deposited on the sample placed at the middle of the back heater. The pressure of the reactor chamber was maintained between 6 and 9 Torr for all depositions. The temperature of the samples did not exceed 145°C.

With the implementation of this cracker cell set up, the CdTe deposition rate has increased from 50 – 60 nm/hr (without graphite cracker cell) to over 420 nm/hr using a total H_2 flow of 3.1 standard litres per min (slm) at a temperature of 140°C. A set of experiments have been carried out by varying the hydrogen flow through the main line and keeping the precursor flows constant. Hydrogen flow has been varied from 1.5 slm to 3 slm in steps of 0.5 slm. Increase in deposition rates have been obtained with the increase in total hydrogen flow. Energy-dispersive X-ray (EDX) confirmed the Cd to Te ratio of 1:1 in the deposited CdTe films. The higher growth rate of CdTe passivation layer shortens the total deposition time for a required thickness, which further helps to keep the sample at lower temperature. Scanning electron microscope (SEM) has been used to characterize these samples. Figure 1 shows SEM cross-sectional images of CdTe films with varying hydrogen flow depicting the increase in film thickness with the increase in hydrogen flow. The surface morphology of the deposited CdTe films also varied with different hydrogen flow. As seen from the top view SEM images, the grain sizes increase with increase in the hydrogen flow. This is illustrated in Fig. 2.

After optimization of the growth conditions, the best conditions with the highest deposition rate of CdTe were used to deposit a passivation film on planar as well as patterned HgCdTe substrates. Maintaining the sample at a lower temperature prevents the depletion of mercury from the HgCdTe substrates, thereby reducing the chance of defects and interfacial traps. A uniform CdTe film was obtained on HgCdTe substrates. Though the coverage is not fully conformal, adequate deposition is obtained even on the bottom of the pattern. The thickness of CdTe film deposited in one hour on the top of the trench structure was ~440 nm whereas the thickness on the side walls was only ~165 nm and that at the bottom of the trench was ~270 nm. Figure 3 shows the conformal coverage obtained on a patterned HgCdTe substrate.

Additional work is being done to improve the conformal coverage on patterned HgCdTe substrates. The optimized results will be reported at the workshop. Other characterization results of the deposited CdTe films, like photoconductive decay, will also be presented later.

References:

[1] Y. Nemirovsky, N. Amir, and L. Djaloshinski, J. Electron. Mater. 24, 647 (1995).

[2] V. Ariel, V. Garber, D. Rosenfeld, G. Bahir, V. Richter, N.Mainzer, and A. Sher, J. Electron. Mater. 24, 1169 (1995).

[3] S. Banerjee, P. Y. Su, R. Dahal, I. B. Bhat, J. D. Bergeson, C. Blisset, F. Aqariden, and B. Hanyaloglu, J. Electron. Mater., 43 (8), 3012 (2014).

Figures:
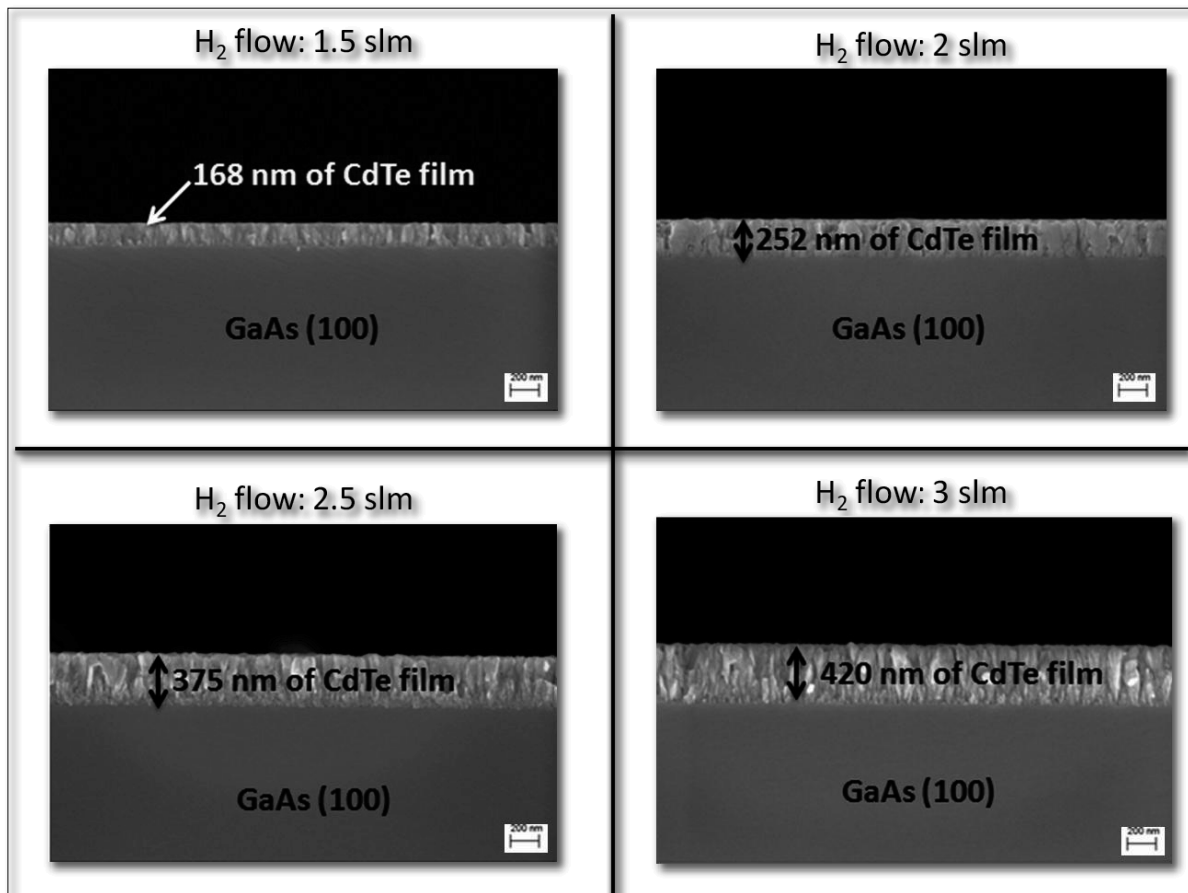
Fig. 1: SEM cross-sectional images showing the increase in the thickness of deposited CdTe films with increasing hydrogen flow.
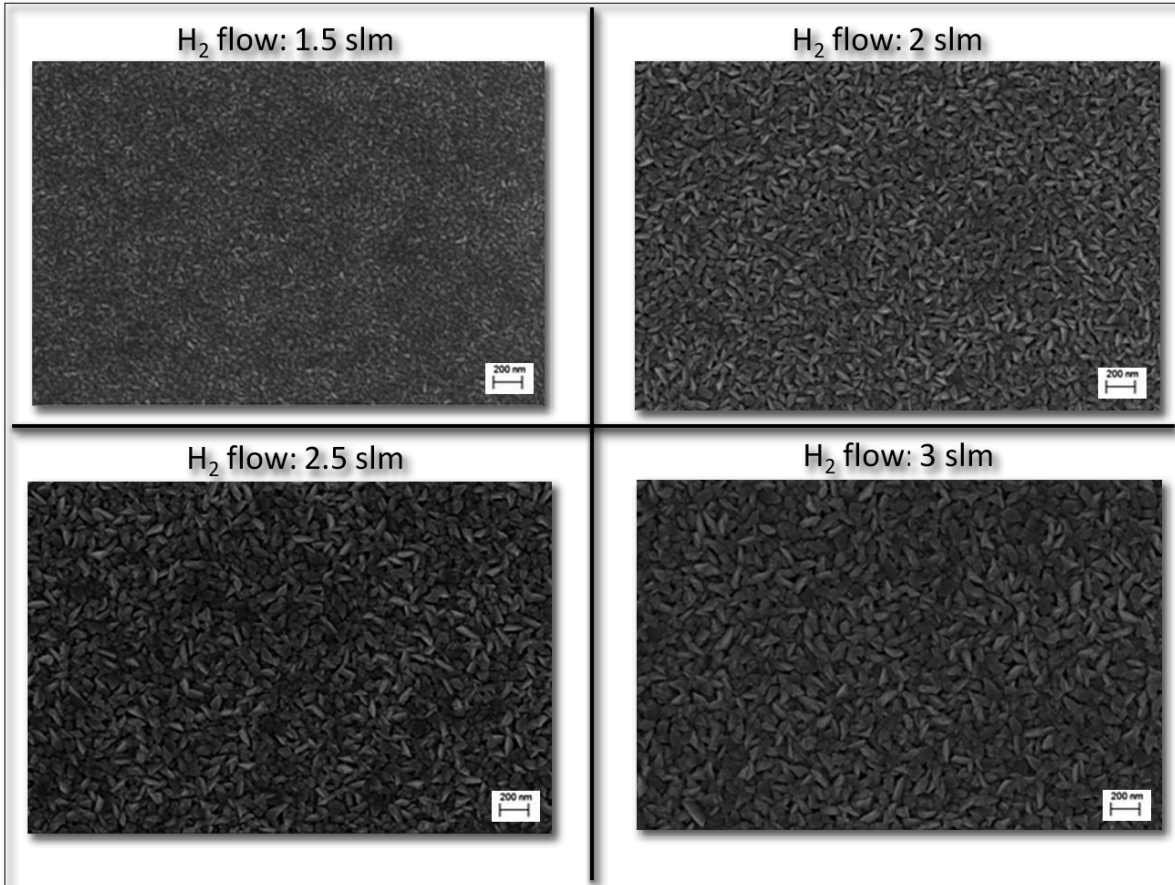
Fig. 2: SEM top view images showing the increase in the grain size of the deposited CdTe film with the increase in hydrogen flow.
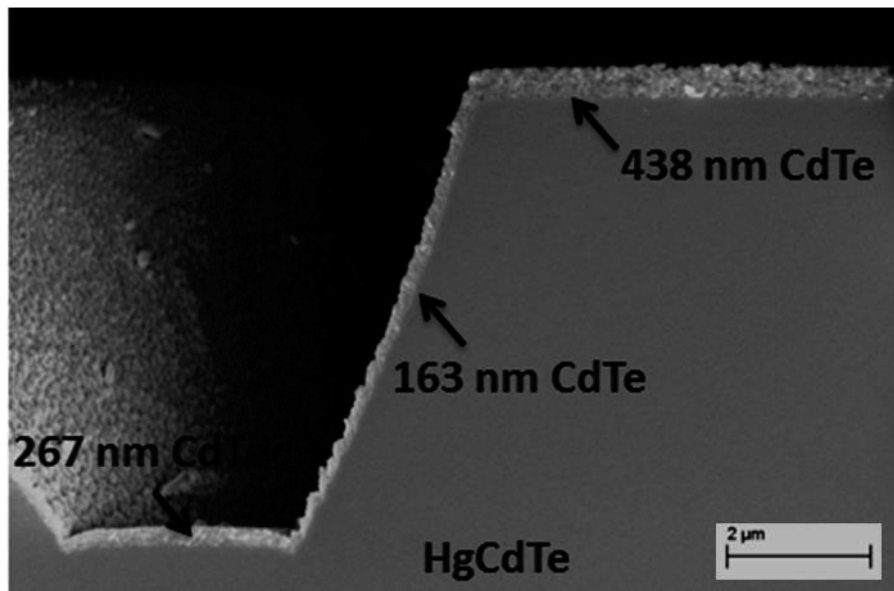
Fig. 3: SEM cross-sectional image of CdTe deposited on a patterned HgCdTe substrate for passivation; coverage is not fully conformal, but adequate deposition on the bottom of the trench structure.

Student Paper

Comparison of Auger and Radiative Recombination Lifetime in HgCdTe, InAsSb and InGaAs

Hanqing Wen, Benjamin Pinkie and Enrico Bellotti*
*ECE Department, Boston University, 8 Saint Mary's Street, Boston, MA 02215
E-mail: bellotti@bu.edu

Due to the adjustable cut off wavelength ranging from 0.7µm to 30µm and the available lattice-matched substrates, HgCdTe has been widely used for applications from the short-wavelength IR (SWIR), mid- and long-wavelength IR detector (MWIR and LWIR). The emerging InAsSb/AlAsSb material system has also found application in MWIR barrier detectors that are particularly desirable for their high working temperature and nearly zero valence band offset [1]. However, despite of the consistent efforts in exploring new device architectures to reduce dark current and improve quantum efficiency, the radiative and Auger recombination originating from the intrinsic properties of the material, impose a fundamental limit to the device performance. Although some work has been done in modeling the Auger and radiative recombination in these materials [2-4], no direct comparison is made among these materials within the same theoretical framework.

In this work direct and phonon-assisted (PA) indirect Auger and radiative recombination is investigated in HgCdTe, InAsSb and InGaAs using Green's function theory and full band structures. Electron self energies with the corresponding spectral density function is calculated under electron-phonon interaction and are subsequently used to find the PA recombination rate [5-6]. In particular, Monte Carlo method is adopted to evaluate the 4-fold integration over Brillouin zone for Auger calculation. The full band structures employed in the calculation is computed from the empirical pseudopotential method (EPM) which is calibrated and fitted to the real band features from experiment such as effective masses and band gap energies. Fig. 1 shows the band structures of (a) $Hg_{1-x}Cd_xTe$ with x = 0.29 at 150K and (b) $InAs_{1-x}Sb_x$ with x = 0.21 at 150K. A preliminary result about the radiative recombination lifetime in HgCdTe and InAsSb is presented in Fig. 2. As is shown, at both 150K and 200K, the HgCdTe has a slightly larger radiative lifetime than that of InAsSb in all the n-type doping considered. On the other hand, at 200K the radiative lifetime for both materials deviates from a line due to the high intrinsic carrier concentration at this temperature, while at 150K, the logarithm of lifetime shows a perfect linear relation with the logarithm of doping concentration. In the presentation, we will further demonstrate the results of Auger recombination where both direct and phonon-assisted indirect transition will be discussed.

Student Paper

Reference

[1]. Carras, M., J. L. Reverchon, G. Marre, C. Renard, B. Vinter, X. Marcadet, and V. Berger. "Interface band gap engineering in InAsSb photodiodes." *Applied Physics Letters* 87, no. 10 (2005): 102103-102103. [2]. Bertazzi, Francesco, Michele Goano, and Enrico Bellotti. "Calculation of auger lifetimes in HgCdTe." *Journal of electronic materials* 40, no. 8 (2011): 1663-1667.

[3]. Krishnamurthy, S., M. A. Berding, Zhi Gang Yu, C. H. Swartz, T. H. Myers, D. D. Edwall, and R. DeWames. "Model for minority carrier lifetimes in doped HgCdTe." *Journal of electronic materials* 34, no. 6 (2005): 873-879.

[4]. Metzger, W. K., M. W. Wanlass, R. J. Ellingson, R. K. Ahrenkiel, and J. J. Carapella. "Auger recombination in low-band-gap n-type InGaAs." *Applied Physics Letters* 79, no. 20 (2001): 3272-3274.

[5]. Bertazzi, Francesco, Michele Goano, and Enrico Bellotti. "Numerical analysis of indirect Auger transitions in InGaN." *Applied Physics Letters* 101, no. 1 (2012): 011111.

[6]. Wen, Hanqing, and Enrico Bellotti. "Numerical Analysis of Radiative Recombination in Narrow-Gap Semiconductors Using the Green's Function Formalism." *Journal of Electronic Materials* (2014): 1-8.
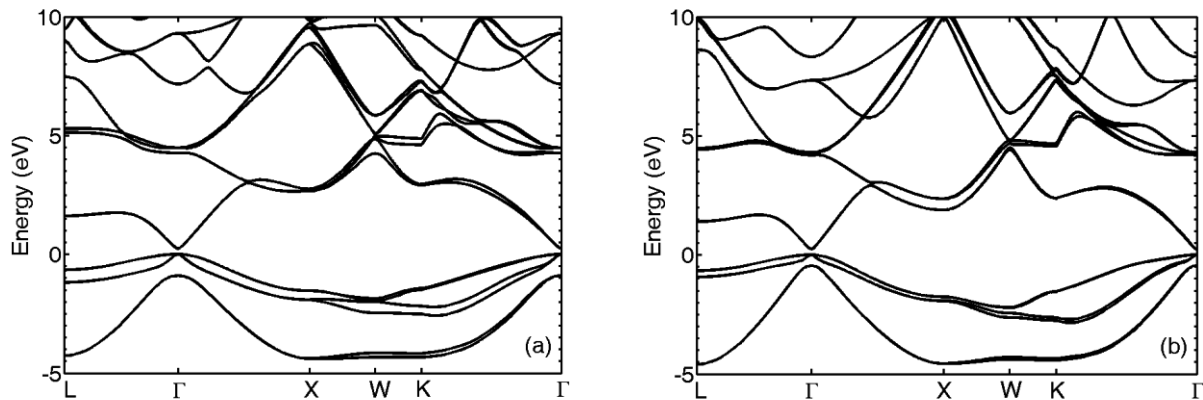
FIG. 1. Band structures for (a) $Hg_{0.71}Cd_{0.29}Te$ at 150K, (b) $InAs_{0.79}Sb_{0.21}$ at 150K.
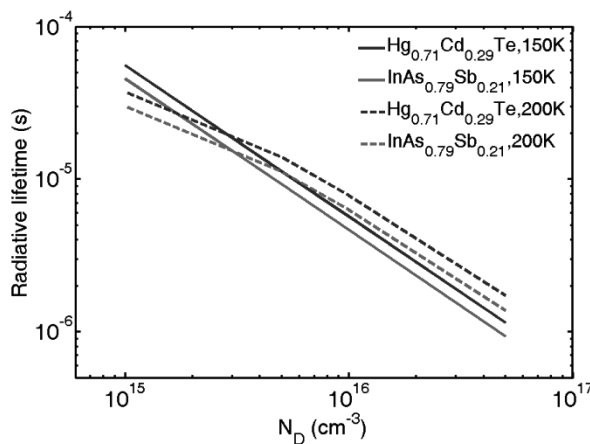
FIG. 2. Radiative recombination lifetime as a function of n-type doping concentration for $Hg_{0.71}Cd_{0.29}Te$ at 150K (blue, solid), $InAs_{0.79}Sb_{0.21}$ at 150K (red, solid), $Hg_{0.71}Cd_{0.29}Te$ at 200K (blue, dashed), $InAs_{0.79}Sb_{0.21}$ at 200K (red, dashed).

The Future of Infrared; III-Vs or HgCdTe?

Michael A. Kinch

DRS Technologies, Dallas Texas

The future of infrared systems for all spectral bands is being driven towards ever-smaller pixel pitches and ever-higher operating temperatures. The performance requirements of such systems with regard to both dark current and noise will be examined for the materials technologies and device architectures that are in vogue today. The possibility for extending the operation of mid- and long-wavelength focal plane arrays to room temperature with background- and diffraction-limited performance will be discussed, together with the potential issues that must be addressed in order to achieve this ultimate goal.

Effects of Annealing on Point Defects in CdZnTe, CdMgTe, and CdMnTe Crystals Grown by Bridgman and Floating Zone Techniques

Rubi Gul, A. Bolotnikov, G. Camarda, A.Hossain, C. Yonggang, G. Yang, U. Roy and R. James

Brookhaven National Laboratory, Upton, NY 11973, USA

Email: gul@bnl.gov

Abstract

The performance and resolution of nuclear-radiation detectors is substantially affected by crystal defects. The main factor in the degradation of the detector's performance is the presence of extended and point defects within the band-gap of the material. We investigated the effects of annealing on the nature and the densities of the point defects, and related the properties of the carrier traps with the resistivity of the material, and ultimately to the performance of the detectors. The main technique used in the study was Deep-Level Transient Spectroscopy (DLTS). We studied detectors annealed under different conditions, such as annealing under vacuum, a Cd over-pressure, a dopant-containing atmosphere, and a Te over over-pressure. We observed that the material's electrical resistivity changed drastically after annealing. The DLTS results show that the nature, behavior and density of the traps changed under different annealing conditions. Some defects vanished while others emerged in the DLTS spectrum, leading to changes in the relative concentration of most carrier traps. In this research the relationships between the performance of detectors, the bulk electrical resistivity, concentration of specific deep traps, and annealing conditions will be reported.

Keywords: CdZnTe; DLTS; point defects; annealing; trap densities; resistivity

Fabrication and Simulation of II-VI tunnel insulators for InGaAs Nonvolatile Memory Devices

Ernesto Suarez[1], Pik-Yiu Chan[2], Mukesh Gogna[2], Fuad Al-Amoody[2], Barry Miller[2], Evan Heller[2], John E. Ayers[2], Faquir Jain[2]

1. University of Hartford 200 Bloomfield Ave West Hartford CT 06117
    ersuarez@hartford.edu
2. University of Connecticut Storrs CT 06269

Abstract:

This study shows the use of a ZnS ZnMgS/ZnS heteroepitaxial tunneling layer in a non-volatile memory FET to maintain threshold voltage stability. This quantum well layer replaces instable oxides. We show graphical simulations of this high K tunneling layer and fabrication of InGaAs device.

Keywords: InGaAs, Non-volatile memory FETs, FET Simulation, MOCVD fabrication

1. INTRODUCTION:

Recently II-VI tunneling insulators have shown stability in threshold voltages by reduction of interface charge.[1,2] This paper focuses on the use of these II-VI layers for InGaAs nonvolatile memory field effect transistors (FETs). In traditional NVMFET, the tunneling insulator is SiO_2, this yields a variable oxide charge, leading to a variable threshold voltage, creating a hurdle to continue to scale down memory devices. The ZnS/ZnMgS/ZnS tunnel insulator provides the high band gap needed as an energy barrier. Since this barrier is single crystalline in nature, charge trapping at both interface is negligible, leading to a consistent threshold voltage. The device schematic, shown in figure 1, uses a InP substrate for the InGaAs FET. A control insulator is fabricated on the floating gate. The floating gate is comprised of

individually cladded germanium-oxide- germanium (GeO$_x$-Ge) quantum dots. This creates a favorable threshold voltage shift and minimizes gate leakage. Non-volatile memory field effect transistors (NVMFET) threshold voltage is determined by equation 1. The contribution from the individually-cladded quantum dots ins shown in equation 2.

$$V_T = \phi_{ms} + 2\phi_F - \frac{Q_{ox}}{C_{ox}} - \frac{Q_d}{C_{ox}} - \frac{Q_{fg}}{\varepsilon_{ox}/d}$$

equation 1

$$V_{th\_QDNVM} = V_{TH} + \frac{qmn_{dct}}{\varepsilon_0\varepsilon_{ox}}\left(t_1 + \frac{\varepsilon_{ox}}{2\varepsilon_{S1}}D_{dot}\right)$$

equation 2

2. INGAAS NON-VOLATILE MEMORY SIMULATION

Schrodinger's equation is self-consistently solved to provide simulation data for the states of the InGaAs non-volatile memory FET.[3,4] These simulations are shown in figure 2 . This simulation shows the charge trapped in the first layer oif germanium-oxide cladded germanium quantum dots. The II-VI tunneling layer has trapped this charge because of its high band gap. This device is in the "1" state. As you lower V$_G$ the charge is tunneled back into the channel.

3. INGAAS NON-VOLATILE MEMORY FABRICATION

These devices are fabricated using metal-organic chemical vapor epitaxy (MOCVD). The ZnS/ZnMgS/ZnS are grown epitaxially on the InGaAs gate material. Each layer is approximately 50 Å thick.[5] Even though there is large lattice constant mismatch between the tunneling layer and the substrate, the grown layers are smaller than the critical layer thickness and do not relax. These fabricated InGaAs FETs are tested and give the characteristic I$_D$-V$_G$ graph shown in figure

4. FIGURES
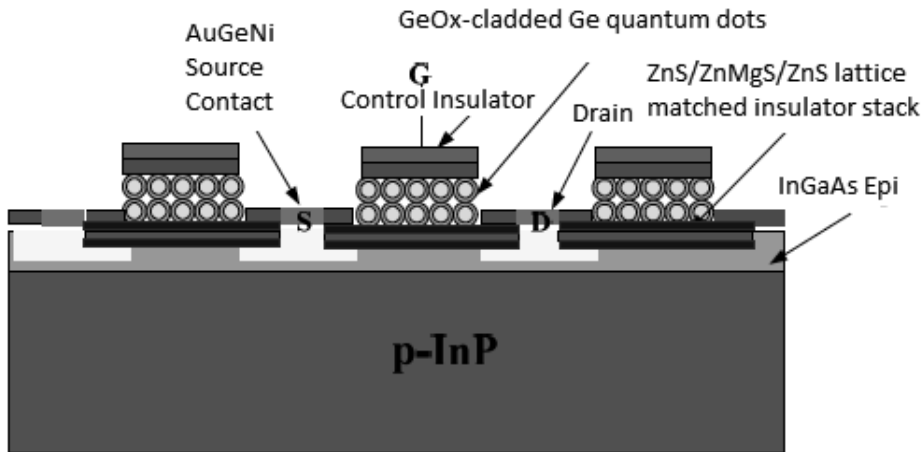
Figure 1. Design of InGaAs II-VI insulator InGaAs FET
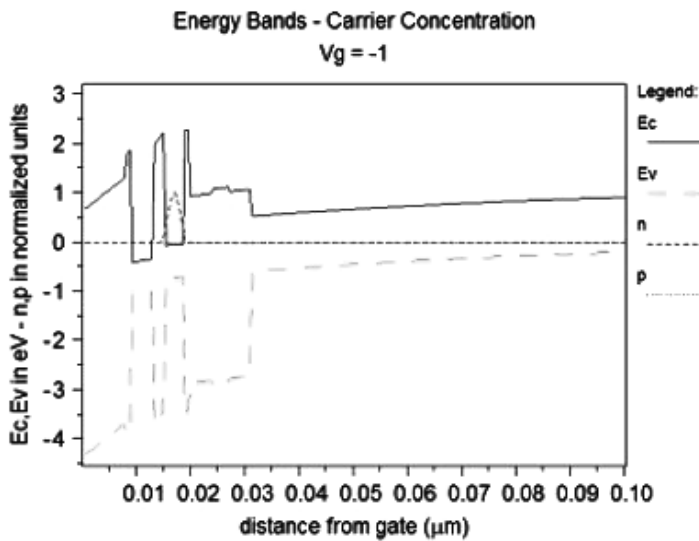
Figure 2. Simulation of Charge in the GeOx-Ge floating gate of an II-VI InGaAs non-volatile memory FET
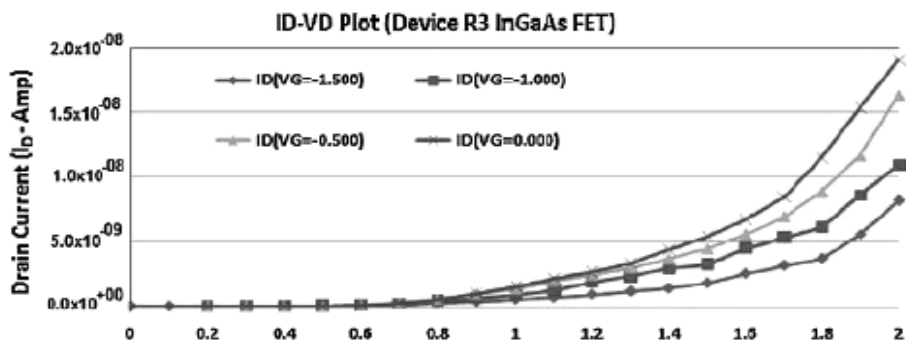
Figure 3. ID-VD plot of a InGaAs FET

5. REFERENCES

[1]E.Suarez, P-Y Chan, M. Gogna, J. E. Ayers, E. Heller, F. Jain, "ZnS/ZnMgSeTe/ZnS II-VI Energy Barrier for InGaAs Substrates, "International Journal of High Speed Electronics and Systems, Vol. 23, No 1&2, 1450013-7, (June 2014)

[2]P. Y. Chan, M. Gogna, E. Suarez, F. Al-Amoody, S. Karmakar, B. I. Miller, E. K. Heller, J. E. Ayers, and F. C. Jain, "Fabrication and Simulation of an indium gallium arsenide quantum-dot-gate field effect transistor (QDC-FET) with ZnMgS as a tunnel gate insulator," J. Electron. Mater., Vol 42, No. 11, pp.3259-3266 (2013).

[3]E. Suarez, F. C. Jain, M. Gogna, F. Alamoody, D. Butkiewicus, R. Hohner, T. Liaskas, S. Karmakar, P-Y. Chan, B. Miller; J. Chandy, and E. Heller. "Non-volatile Memories Using Quantum Dot (QD) Floating Gates Assembled on II-VI Tunnel Insulators," J. Electron. Mater., Vol 39, No 7, pp.903-907 (2010)

[4] P. Chan, E. Suarez, M. Gogna, B. Miller, E. Heller, J. Ayers, F. Jain, "Indium Gallium Arsenide Quantum Dot Gate Field-effect Transistors Using II-VI Tunnel Insulators Showing Three-State Behavior," J. Electron. Mater., Vol 41 N 10, pp.2810-2815 (2012).

[5]E.Suarez, P-Y Chan, M. Gogna, J. E. Ayers, E. Heller, F. Jain, "ZnS/ZnMgSeTe/ZnS II-VI Energy Barrier for InGaAs Substrates, "International Journal of High Speed Electronics and Systems, Vol. 23, No 1&2, 1450013-7

Floating Gate Nonvolatile Memory Structure
Using cladded Germanium Quantum Dot Channel (QDC)

J. Kondo[1*], M. Lingalugari[1], P-Y. Chan[1], E. Heller[2], and F. Jain[1]

[1]University of Connecticut, 371 Fairfield Way, Storrs, CT 06269

[2]Synopsys Inc., 400 Executive Boulevard, Ossining, NY 10562

*Presenter's contact information; phone (860)817-4615, fax (860)486-2447, email jun.kondo@uconn.edu

Abstract: This paper aims at studying the effect of incorporating lattice matched II-VI layers grown on Ge quantum dot channel (QDC) for field effect transistors (FETs) and nonvolatile floating gate memory structures. The I_D-V_G characteristics are expected to be significantly improved by the deposition of lattice matched II-VI layers at the gate of the QDC-FET. The device operations are explained by carrier transport in narrow energy mini-bands which are manifested in a quantum dot superlattice (QDSL) transport channel.

Keywords: quantum dot channel, mini-band, quantum dot superlattice

1. QDC-FET and Nonvolatile Floating Gate Memory Structures

This paper describes modeling of QDC FETs which consists of two layers of Germanium cladded quantum dots in the channel region, and two layers of ZnSe and ZnMgSe in the gate insulator. The actual I_D-V_G characteristics of the QDC FET without the II-VI gate insulator are shown in Figure 1. This paper also describes modeling of the nonvolatile floating gate memory structure where two layers of Germanium cladded quantum dots are added to form the floating gate. These device structures are shown in Figure 2[1]. GeOx cladded forms the thin-barrier (~1nm) over Ge quantum dots (~3nm), and an array of these cladded quantum dots behaves as a quantum dot superlattice (QDSL)[2]. The Kronig-Penney model will be used to determine the mini-energy band locations and energy band width, and the simulation will use a self-consistent solution of Schrodinger and Poisson's equations[2].

2. <u>Theory and Simulation</u>

The drain current I_D is expressed by Equation 1[1]. It depends on number of mini-energy bands (i) and V_{DS}, (signified by integer j)[1]. The threshold shift ΔV_{TH} depends on transfer of charge to the mini-bands (i) due to the formation of quantum dot superlattice in quantum dot layers in the gate region[1]. In addition, the saturation current I_D (sat) is expressed by Equation 2[1].

$$I_D = \left(\frac{W}{L}\right) C_o^" \, \mu_n \left[\sum_{i=0}^{m} \sum_{j=0}^{n} \, \{V_G - (V_{THi} + \Delta V_{THi}) - \frac{1}{2} V_{DSj}\} \, V_{DSj} \right] \tag{1}$$

$$I_D(\text{sat}) = \frac{1}{2}\left(\frac{W}{L}\right) C_o^" \, \mu_n \left[\sum_{i=0}^{m} \, \{V_G - (V_{THi} + \Delta V_{THi})\} \right]^2 \tag{2}$$

These two equations were used to simulate I_D-V_D characteristics of QDC FETs, and simulation results are shown in Figure 3, and twenty one V_G values were used in this simulation. In order to simulate I_D-V_G characteristics, these I_D-V_D characteristics were transposed to I_D-V_G characteristics and shown in Figure 4. These results show the three state characteristics, and the I_D current peak differentiates the first and the second states, and the current saturation state is considered as the third state. Multi-state FETs are needed in multi-valued logic (MVL) that can reduce the number of gates and transistors in digital circuits[3].

3. <u>Figures</u>
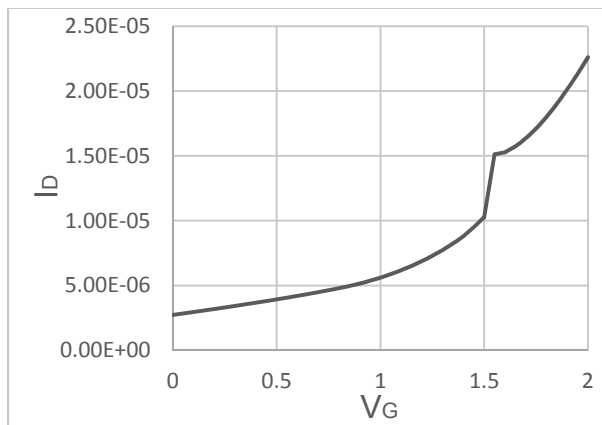
Figure 1: I_D-V_G Characteristics of QDC FET (V_D=0.75V)
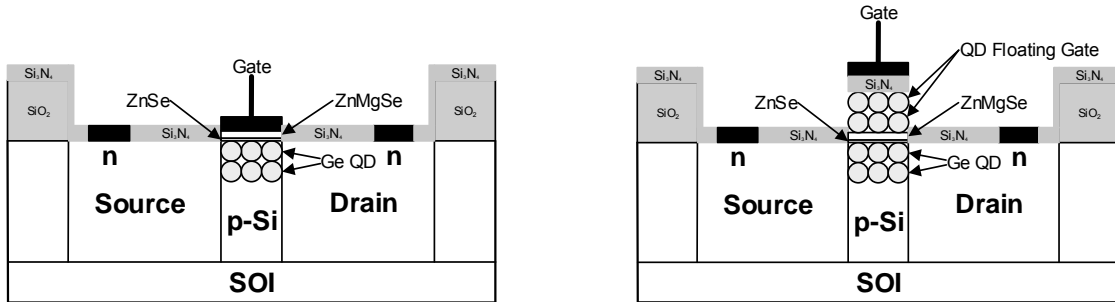
Figure 2: Structure of Ge QDC FET (left) and Floating Gate Nonvolatile Memory (right)
Source; F. Jain, et al. "Four-State Sub-12-nm FETs Employing Lattice-Matched II-VI Barrier Layers." [1]
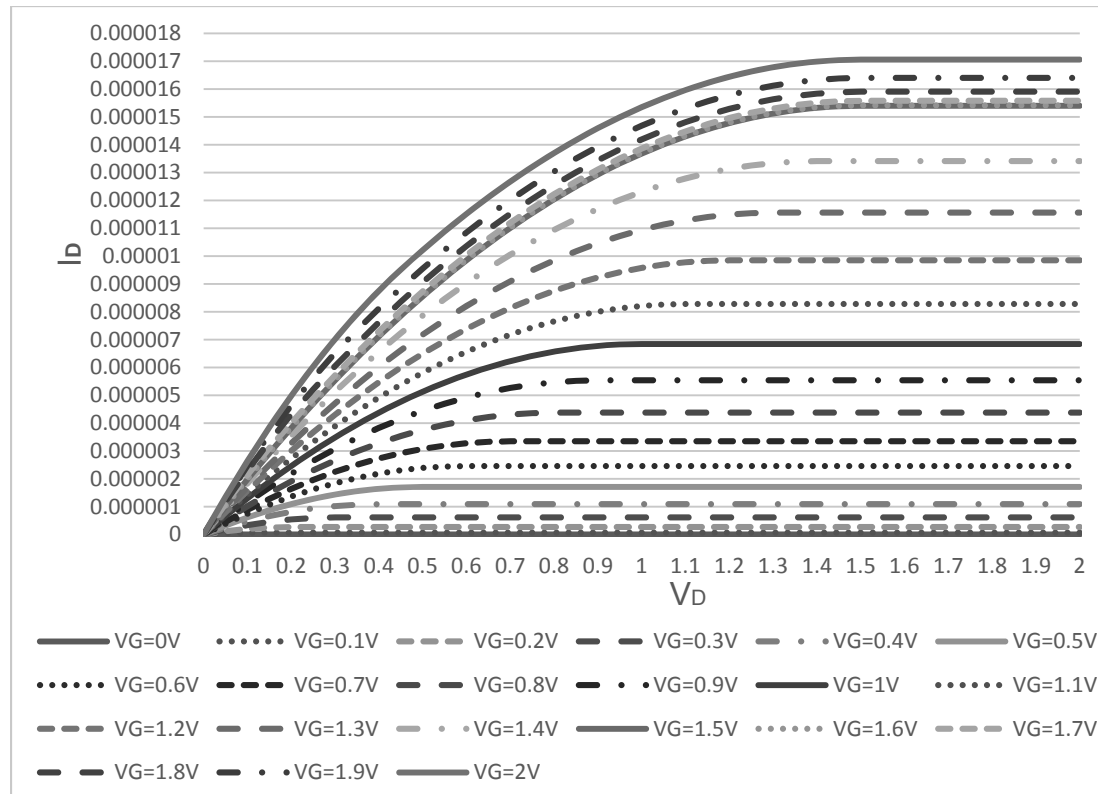
Figure 3: I_D-V_D Simulation of QDC FET
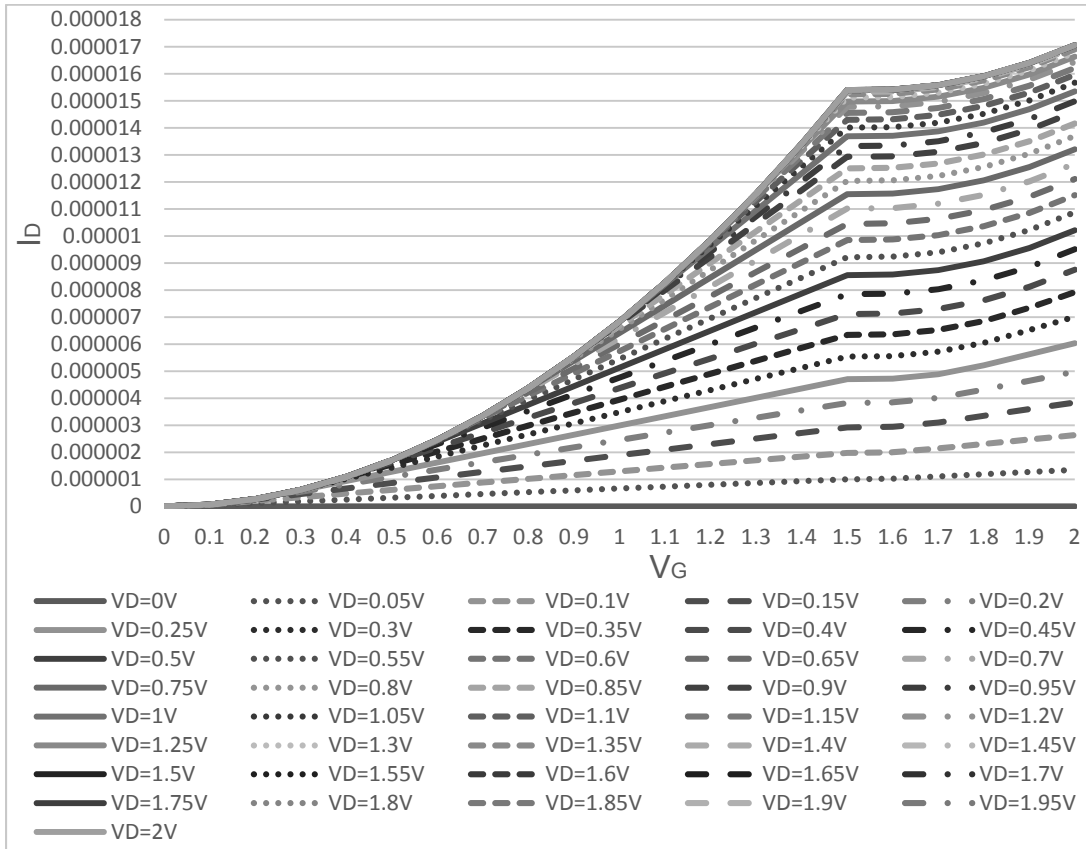
Figure 4: I_D-V_G Simulation of QDC FET

4. References

[1] F. Jain, P.-Y. Chan, E. Suarez, M. Lingalugari, J. Kondo, P. Gogna, B. Miller, J. Chandy, and E. Heller, "Four-State Sub-12-nm FETs Employing Lattice-Matched II-VI Barrier Layers." *Journal of Electronic Materials*, Vol. 42, No. 11, p. 3199-3201, 2013.

[2] F. Jain, S. Karmakar, P.-Y. Chan, E. Suarez, M. Gogna, J. Chandy, and E. Heller, "Quantum Dot Channel (QDC) Field-Effect Transistors (FETs) Using II-VI Barrier Layers." *Journal of Electronic Materials*, Vol. 41, No. 10, p. 2780-2781, 2012.

[3] J. Chandy and F. Jain, *Proc. of International Symposium on Multiple Valued Logic*, p. 186, 2008.

Minimization of the Surface Leakage Currents in the High-Resistivity (Cd,Mn)Te Crystal Plates

A. Markowska[1,2], M. Witkowska-Baran[2], D. Kochanowska[2], A. Mycielski[2]

ola_markowska@interia.pl

[1] *Institute of Radioelectronics, Warsaw University of Technology, Plac Politechniki 1, Warsaw, Poland*
[2] *Institute of Physics PAS, Al. Lotników 32/46, Warsaw, Poland*

Abstract: The purpose of the study was to find method of minimization of the surface leakage current (SLC) and of slowing down degradation of the surfaces (increase of the SLC with time).

Keywords: passivation, (Cd,Mn)Te, surface leakage current, detectors.

1. INTRODUCTION

The seminsulating (Cd,Mn)Te crystal was grown using a vertical Bridgman method. The (Cd,Mn)Te is naturally a p-type semiconductor with a low resistivity due to Cd vacancies acting as acceptor centers and produced when Cd atoms escape during the growth proccess[1]. In order to increase crystal resistivity, we used compensation of free holes by doping with indium. Samples, cut from (Cd,Mn)Te crystal, were used in the investigations. The size of the platelets was $5 \times 5 \times 2$ mm^3. Thereafter, we annealed samples in Cd for reducing the concentration of acceptors and also for improve the overall quality of the crystal by reduction the numer of second phase defects and inhomogeneities[2]. The material's resistivity were mapped by a contactless method with the use of EU-ρ-SCAN and it was in the range of 10^8-10^9 Ωcm.

2. EXPERIMENTAL PROCEDURE

The two types of electrical contacts were used for the electrodes:
1) an amorphous/nanocrystalline layer (300 µm) of heavily-doped ZnTe:Sb plus an Au layer

(200 μm), as shown on *Figure 1*, both evaporated on the surfaces of the platelets in the ultra--high vacuum (10^{-7} - 10^{-10} Pa) by using a molecular beam epitaxy (MBE) apparatus, and 2) a chemically deposited Au layer. Before depositing the contact layers in MBE aparatus, we prepared surfaces of the crystal platelets by the following steps:

- grinding with 9.5 μm Al_2O_3 powder,

- mechano-chemically polisheding in a 2 % solution of Br in methanol + glycol,

- selective etching (about 15 s) in a 1 % solution of Br in methanol, and,

- thoroughly rinsing in methanol.

The chemical deposition of Au as the only contact layer was preceded by the following processes:

- grinding with 9.5 μm Al_2O_3 powder,

- mechano-chemically polisheding in a 2 % solution of Br in methanol + glycol,

- etching in a 10 % solution of Br in methanol, and,

- thoroughly rinsing in methanol.

Subsequently, Au was chemically deposited from a solution of $AuCl_3 \cdot HCl \cdot 4H_2O$ (gold chloride acid + distilled H_2O_2) in a reaction between the solution and the crystal's surface.

Both the contacts from amorphous layer, and chemically deposited Au were made in two configurations: 1) center-spot, and 2) covering both parallel faces of the platelets. *Figures 2. (a)* and *(b)* present both cases.

Before any chemical treatment of the surfaces between electrodes (lateral surfaces), the electrodes were covered with a protecting layer. Various chemical treatments: 1) etching in 10 % solution of Br in methanol (60 s), 2) etching in 10 % solution of Br in methanol (30 s) and then etching in 1 % solution of Br in methanol (120 s), and 3) etching in 10 % solution of Br in methanol (30 s), etching in 1 % solution of Br in methanol (30 s) and passivation with ammonium sulfide $(NH_4)_2S$ (120 s), were tested in order to optimize passivation of the inter-

-electrode surfaces. We used a Keithley 617 Programmable Electrometer with very high input resistance ($> 10^{14}$ Ω) and with an internal voltage source (up to 100 V) to study the evolution of the current-voltage characteristics in time by multiple repeating the measurements after hours and days. We used "two-electrode" measurements, where the applied voltage is distributed between the first contact region, the bulk, and the second contact region, see *Figure 3*.

The best combination of chemical substances (based on $(NH_4)_2S$) for passivation has been chosen.

The secondary ion mass spectroscopy (SIMS) was used to investigate time evolution of the oxidation level of the (Cd,Mn)Te crystal surfaces after various treatments, beginning from the surfaces just after polishing.

3. FIGURES
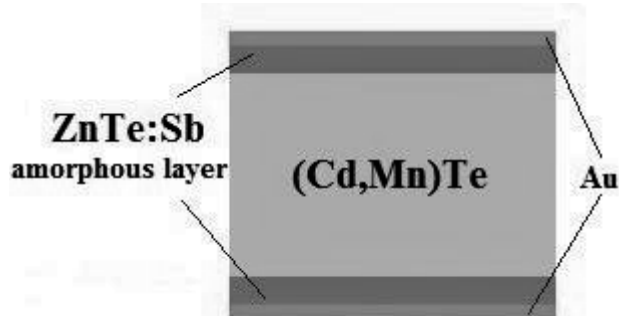
Figure 1. Sample with the contact layers deposited in MBE aparatus.
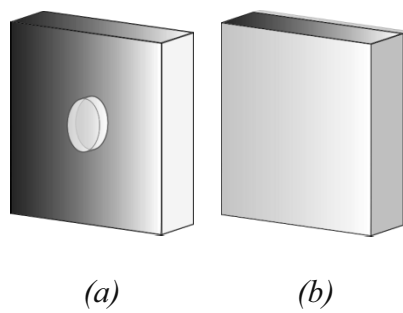
Figure 2. Samples with electrodes (a) center-spot contacts, and (b) covering both parallel faces of the platelets.
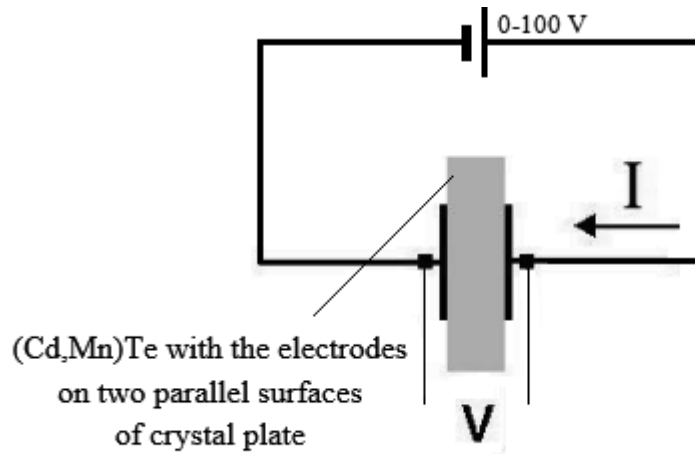
Figure 3. Geometry of electrodes for measuring the current-voltage characteristics.

Current flow is represented by I, and voltage by V.

4. REFERENCES

[1] KiHyun Kim, ShinHang Cho, JongHee Suh, Hong, Jinki, SunUng Kim, „Gamma-Ray Response of Semi-Insulating CdMnTe Crystals", IEEE Trans. Nucl. Sci., Vol. 56, no. 3 (2009).

[2] M. Witkowska-Baran, D. M. Kochanowska, A. Mycielski, R. Jakieła, A. Wittlin, W. Knoff, A. Suchocki, P. Nowakowski, K. Korona, „Influence of annealing on the properties of (Cd,Mn)Te crystals", Phys. Status Solidi C. doi: 10.1002/pssc.201300746, (2014).

ABOUT THE NATURE OF n-TYPE CONDUCTIVITY OF AS-GROWN MBE Hg$_{1-x}$Cd$_x$Te LAYERS AND ITS CHANGING WITH ANNEALING IN QUASI-EQUILIBRIUM AND EQUILIBRIUM Hg VAPOR

Boris Aronzon[1], Galina Chekanova[2], Mikhail Nikitin[*2] and Niyaz Talipov[3]

[1]Russian Research Center "Kurchatov Institute", Moscow, Russia

[2]JSC Shvabe-Photodevice, Moscow, Russia

[3]Peter the Great Military Academy of Strategic Rocket Forces, Moscow, Russia

Introduction

Low temperature (< 100 K) Hall-effect measurements performed at low magnetic field B < 0.03 T on as-grown MBE Hg$_{1-x}$Cd$_x$Te (x ≈ 0.180-0.350) heterostructures show every time n-type conductivity. That differs radically from situation with as-grown bulk single crystal material and as-grown Liquid Phase Epitaxy (LPE) layers where p-type conductivity is evidenced always due to high concentration of Hg vacancies.

Objective of the present work was to measure Hall-effect on as-grown Hg$_{1-x}$Cd$_x$Te (x ≈ 0.215-0.230 and 0.250-0.350) heterostructures in wide range of temperature (4.2 K - 300 K) and magnetic field up to 8 T and examine the impact on electro-physical parameters an annealing in quasi-equilibrium and equilibrium Hg vapor.

MBE-grown multi-layer structures

Study was accomplished on multilayer Hg$_{1-x}$Cd$_x$Te (x ≈ 0.215-0.230 and 0.250-0.350) heterostructures grown by MBE on GaAs (013) substrates with ZnTe/CdTe buffer layers [1]. Typical composition profile is shown on Fig. 1. As-grown hetrostructures were either undoped or In-doped during growth. Electron concentration determined on as-grown absorber (working) layer at low magnetic field was every time as low as n$_{77}$=(1-8)×10^{14} cm^{-3}.

Heterostuctures were annealed in quasi-equilibrium and equilibrium Hg vapor. Annealing was performed in evacuated quartz ampoule with independent Hg source at temperatures

T_{Hg}/T_{HgCdTe}=228/248 ^{0}C and T_{Hg}/T_{HgCdTe}=230/230 ^{0}C traditionally used for conversion of highly doped (p_{77}=10^{17}-10^{18} cm^{-3}) p-type as-grown bulk single crystal wafers and LPE layers into n-type with low electron concentration n_{77}=(1-8)×10^{14} cm^{-3}. Single step time of annealing was equal to 48-72 hours that provides mercury atoms diffusion through-the-thickness. Total annealing time of 7-8 steps was equal to 408-456 hours.

Results

Hall constant of as-grown samples was negative in temperature interval 4.2 K – 300 K and demonstrates seriously non-linear dependence on magnetic field up to 8 T (Fig. 2&3). Samples look like n-type with significant contribution of another type of charge carriers with lower mobility. Calculated electron concentrations and Hall mobility are shown on Fig. 4.

After first annealing step last from 48 to 63 hours we have observed conversion of conductivity type in undoped and In-doped heterostructures from low electron concentration n-type to p-type with hole concentration p_{77}=(1-10)×10^{16} cm^{-3}. During further annealing steps hole concentration has grown up to p_{77}=(1.3-2.2)×10^{18} cm^{-3} and then stabilized at level p_{77}=(1.1-1.3)×10^{18} cm^{-3} (Table).

Total optical transmission in infrared spectral range was lowered significantly from approximately 60 % to 32-42 % that indicates on serious growth of heavy free charge carriers' concentration (Fig. 5).
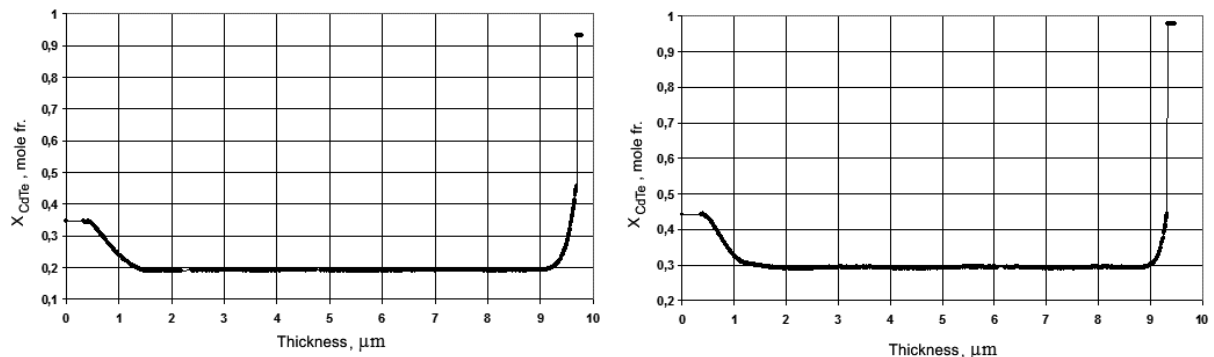
Fig. 1. In-situ measured composition "x" profile of three-layer MBE-grown Hg$_{1-x}$Cd$_x$Te epitaxial structure (point 0 μm means front surface of CdTe buffer layer)
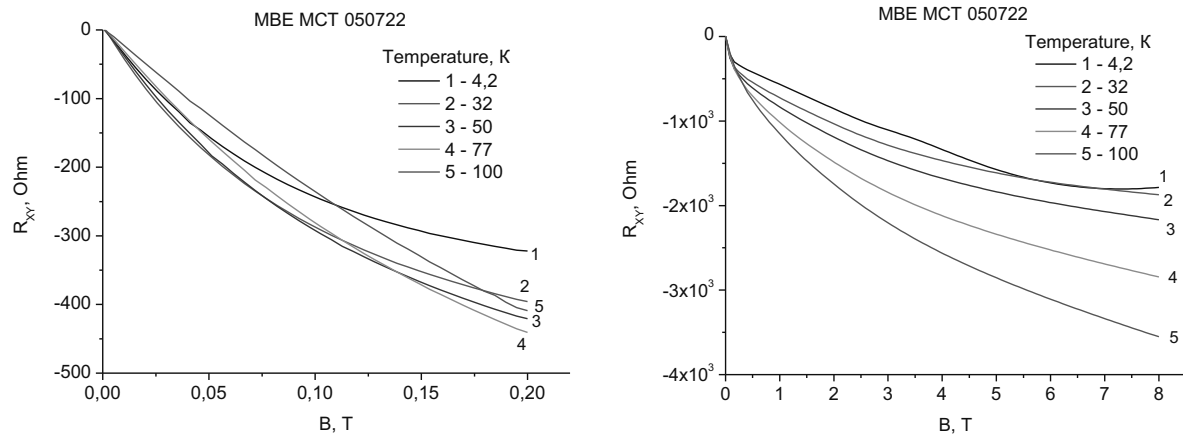
Fig. 2. Dependences of Hall coefficient on magnetic field at different temperatures: as-grown absorber (working layer) x ≈ 0,220. Composition "x" profile - on Fig. 1 (left)
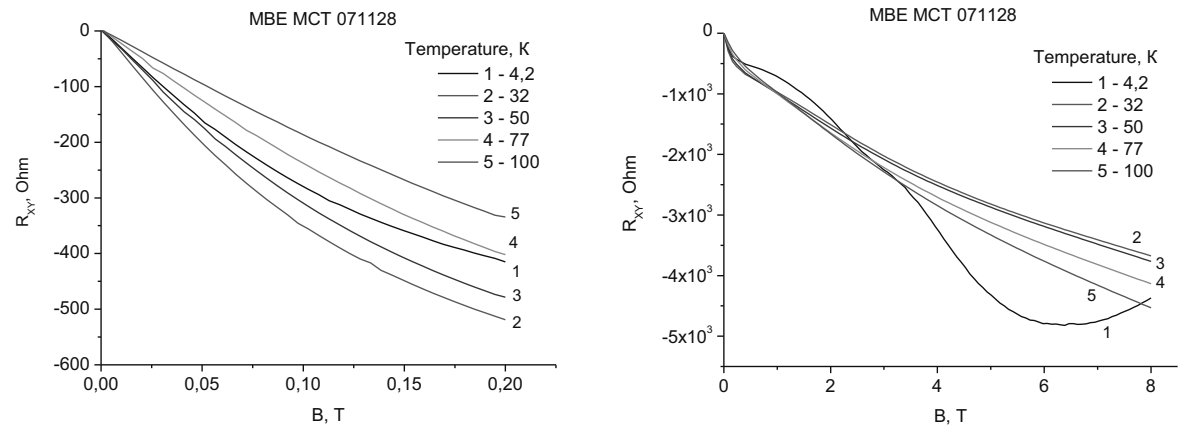
Fig. 3. Dependences of Hall coefficient on magnetic field at different temperatures: as-grown absorber (working layer) x ≈ 0,292. Composition "x" profile - on Fig. 1 (right)
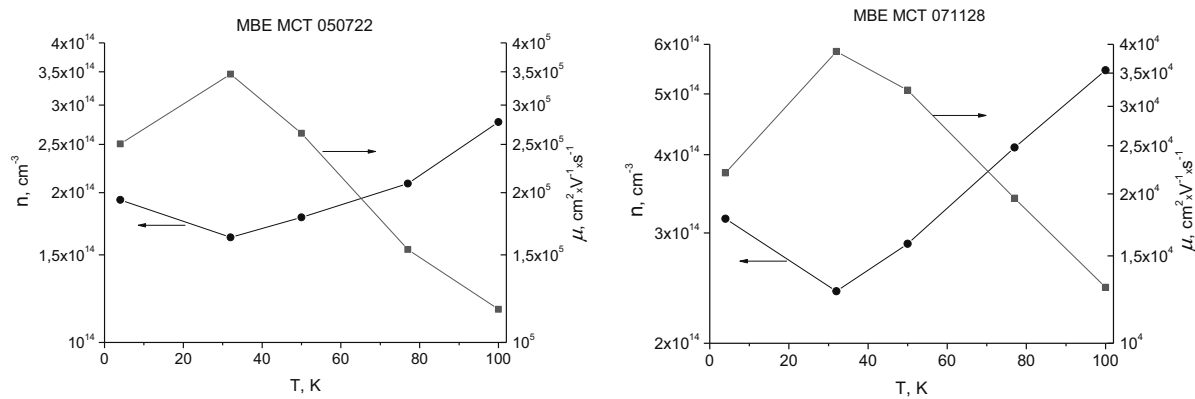
Fig. 4. Dependences of calculated electron concentrations and Hall mobility on temperature in as-grown absorber (working layer)

Table

Typical annealing results

Step No.	Annealing conditions $T_{Hg}/T_{HgCdTe}/t_{ann}$	σ, Ohm$^{-1}\times$cm^{-1}	R_H, cm^3/C	p, cm^{-3}	μ_p, cm$^2\times$V$^{-1}\times$s^{-1}
1	228/ 248^0 C/48 hrs	2,8	144,7	$4,4\times10^{16}$	410
2	228/ 248^0 C/63 hrs	7,8	33,4	$1,8\times10^{17}$	260
3	228/ 248^0 C/68 hrs	12,6	19,5	$3,0\times10^{17}$	260
4	228/ 248^0 C/72 hrs	39,6	5,7	$1,1\times10^{18}$	220
5	228/ 248^0 C/63 hrs	39,6	5,2	$1,2\times10^{18}$	200
6	325/ 345^0 C/8 hrs	42,3	3,7	$1,7\times10^{18}$	160
7	228/ 248^0 C/72 hrs	35,1	5,3	$1,2\times10^{18}$	190
8	228/ 248^0 C/62 hrs	39,0	4,8	$1,3\times10^{18}$	190
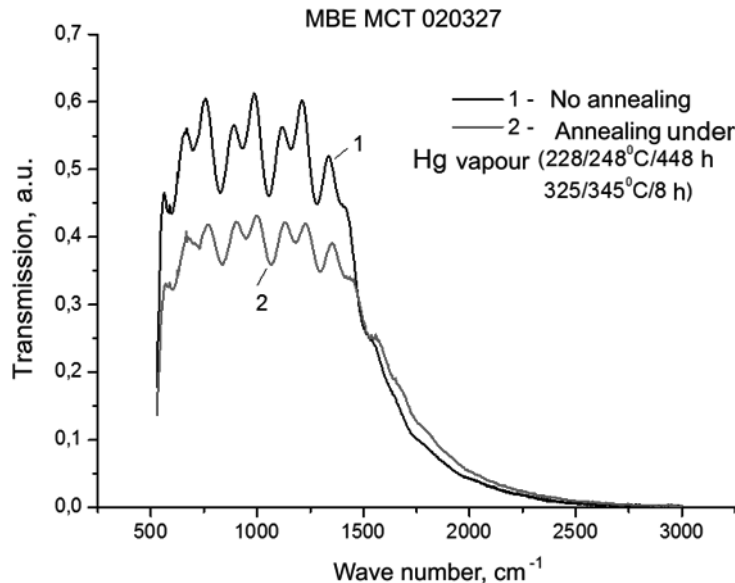
Fig. 5. Room temperature total infrared transmission spectra of heterostructure

REFERENCES

[1] V.V. Vasiliev, V.S. Varavin, S.A. Dvoretsky, I.M. Marchishin, N.N. Mikhailov, A.V. Predein, I.V. Sabinina, Yu.G. Sidorov, A.O. Suslyakov and A.L. Aseev, "LWIR Photodiodes and Focal Plane Arrays Based on Novel HgCdTe/CdZnTe/GaAs Heterostructures Grown by MBE Technique", Chapter 4 in Book [Photodiodes – From Fundamentals to Applications], Ilgu Yun (Ed.), InTech Publisher, Rijeka, p. 133-172 (2012)

Characterization of CdTe Growth on GaAs with Using Different Etching Techniques

E. Bilgilisoy, M. Günnar, S. Özden, M. Polat, Y. Selamet

elifbilgilisoy@iyte.edu.tr — *+90 554 640 47 73*

Izmir Institute of Technology, Departmant of Physics, Urla 35430, Izmir, TURKEY

Abstract: CdTe/GaAs(211)B buffer layers which were grown by molecular beam epitaxy (MBE) have been used to analyze the crystal quality and dislocation density. The optical properties of the sample were characterized by ex-situ spectroscopic ellipsometry (SE). Ex-situ SE was also used to assess thicknesses of the layers and the results were compared with x-ray reflectivity (XRR) measurement. A portion of the material was exposed to different defect decoration methods in order to investigate their effect on CdTe buffer layer.

Keywords: defect decoration, molecular beam epitaxy, CdTe, etch pit density.

1. INTRODUCTION

In order to minimize the lattice mismatch between alternative substrates and HgCdTe needs to be grown on a buffer layer such as CdTe, CdZnTe or ZnTe. Surface defects of the buffer layer leads to some problems which reduce the detector and focal plane array performance. Hence, the crystal quality and dislocation density of CdTe grown on alternative substrate needs to be grown high performance HgCdTe infrared devices.

Wet chemical etching is the most common process to reveal dislocations which are caused by the large lattice mismatch and some surface imperfections of substrate. Different etch techniques leave the different pit shapes on the crystalline surface. Crystal symmetry along the direction perpendicular to the surface can be understood by monitoring the shape of etch pits. In order to determine etch pit density, we can use some different etch methods and calculate the density of

dislocations by counting the number of etch pits per unit area. Defect decoration etching creates etch pits at about the crossing point of two dislocations. In this work, we compare and analyze etch pit density results of CdTe samples grown under different growth conditions by using Everson, Nakagawa, Benson etch and different characterization methods.

2. **EXPERIMENTAL PROCEDURE AND RESULTS**

CdTe buffer layers on GaAs(211)B substrates were grown by MBE. To measure the thickness of a buffer layer, we performed the SE and XRR measurements and examined the results. Both measurements showed that the thickness of a CdTe buffer layer was approximately 2µm (Figure 1). CdTe sample was cut into several pieces and used standard etch pit density (EPD) methods; however, etching times were kept shorter than normal etching times due to thickness at room temperature. We focus our investigation three different etch methods: Everson [1], Nakagawa [2] and Benson [3].

Table 1. Defect decoration process, volume ratio, etching time and EPD resulting values.

Etch Method	Volume Ratio	Etch time (s)	EPD (cm^{-2})
Everson (Lactic acid:HNO_3:HF)	25:4:1	15	7.9×10^7
	25:4:2	15	9.3×10^7
	25:8:1	20	—
	25:4:0.5	20	8.6×10^7
Nakagawa (H_2O:H_2O_2:HF)	20:20:30	20	—
		7	1.4×10^7
Benson(H_2O:HCl:HF:HNO_3:CrO_3)	150:5:5:5:4	15	—

In order to apply the etching procedures, wet chemical etchants were prepared with different volume ratios in polypropylene beakers at room temperatures. Next, a piece of the sample was dipped into these mixtures which were specified at Table 1 at room temperature. The whole procedure of wet chemical etching included application of different EPD etches, cleaning with DI water and drying with N_2 blower for this study. The etch pits were observed using SEM and AFM to investigate diameter and depth of etch pits Figure 3 and Figure 2. The areal density of etch pits was obtained by manual counting and by using software program from the SEM images (Figure 3). We considered the effect of dislocations on Te, CdTe and GaAs vibrational modes which were measured with Raman spectroscopy mapping. In the Raman spectroscopy experiment, Ar^+ laser was used with 488 nm wavelength at room temperature (Figure 4).

3. <u>FIGURES</u>

Figure 1. Ex-situ SE measurement results of CdTe thickness value (MSE:8.837).
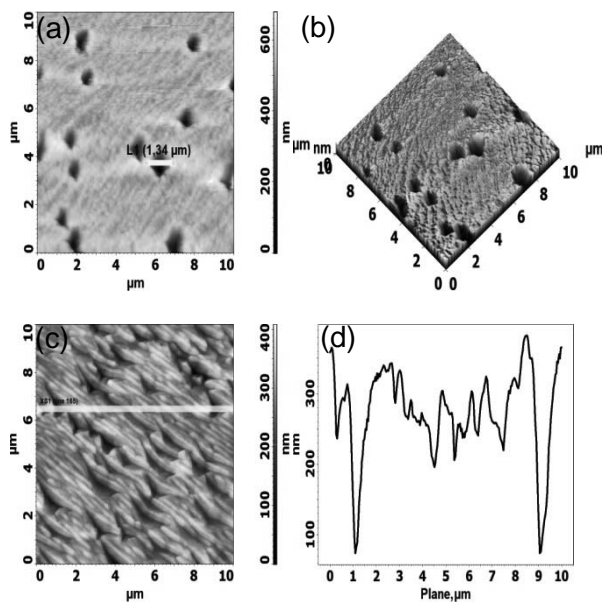
Figure 2. CdTe (211)B sample after Nakagawa etching (20H₂O:20H₂O₂:30HF); (a) 2D Topographical image (10μmx10μm) size of pits~0.74-1.29 μm, (b) 3D Topographical image (10μmx10μm). Same sample after Everson (25Lactic acid:4HNO3:0.5HF) etching; (c) 2D Topographical image (10μmx10μm), (d) cross section line analysis of depth of etch pits~255-265nm.
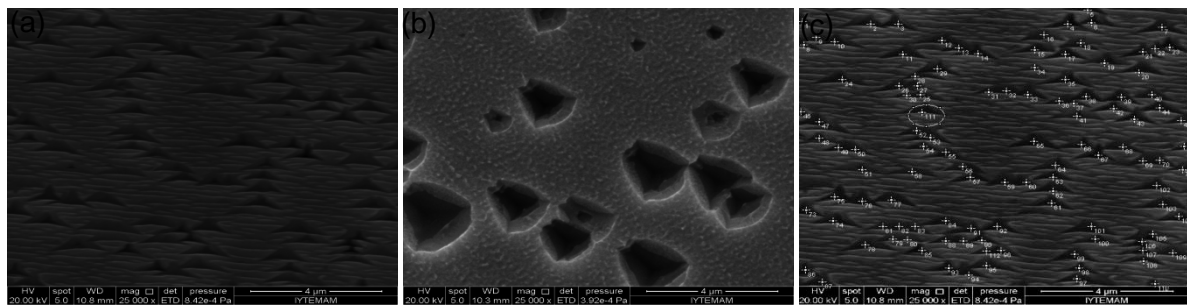
Figure 3. Topographic SEM images of CdTe sample after (a) Everson (25Lactic acid:4HNO3:0.5HF), (b) Nakagawa (20H_2O:20H_2O_2:30HF) etching and (c) counting pits by a software program [4].
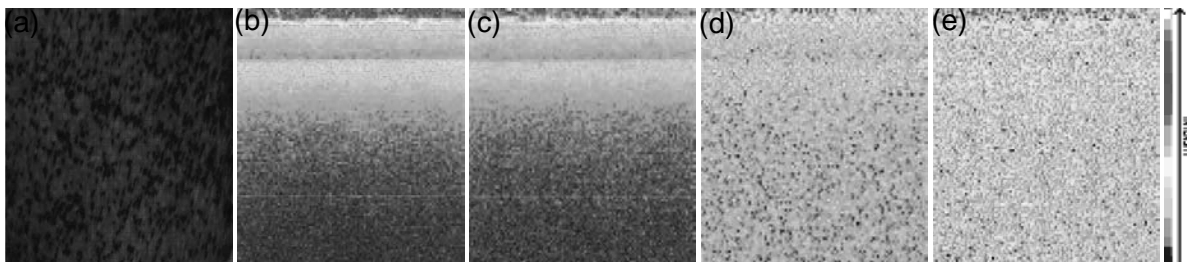
Figure 4. (a) Optical microscope image (40μmx40μm) of CdTe sample after Everson EPD etching. (b) 125.262 cm^{-1} A_1 symmetry Te phonon mode [5], (c) 143.797 cm^{-1} CdTe-like TO phonon mode [5], (d) 169.403 cm^{-1} CdTe-like LO phonon mode [5], (e) 275.379 cm^{-1} GaAs-like TO phonon mode [6] Raman intensity changes.

4. <u>REFERENCES</u>

1. Everson, W., et al., *Etch pit characterization of CdTe and CdZnTe substrates for use in mercury cadmium telluride epitaxy.* Journal of electronic materials, 1995. 24(5): p. 505-510.
2. Nakagawa, K., K. Maeda, and S. Takeuchi, *Observation of dislocations in cadmium telluride by cathodoluminescence microscopy.* Applied Physics Letters, 1979. 34(9): p. 574-575.
3. Farrell, S., et al., *Effect of Cycle Annealing Parameters on Dislocation Density Reduction for HgCdTe on Si.* Journal of electronic materials, 2011. 40(8): p. 1727-1732.
4. Abràmoff, M.D., P.J. Magalhães, and S.J. Ram, *Image processing with ImageJ.* Biophotonics international, 2004. 11(7): p. 36-43.
5. Levy, M., et al., *Characterization of CdTe substrates and MOCVD Cd< sub> 1− x</sub> Zn< sub> x</sub> Te epilayers by Raman, photoluminescence and X-ray diffraction techniques.* Journal of crystal growth, 1998. 187(3): p. 367-372.
6. Allwood, D., et al., *Monitoring epiready semiconductor wafers.* Thin Solid Films, 2002. 412(1): p. 76-83.

Use of sub-bandgap illumination to improve radiation detector resolution of CdZnTe

Martine C. Duff, Aaron L. Washington, II, Lucile C. Teague, Jonathan S. Wright,
Arnold Burger, Michael Groza, and Vladimir Buliga

martine.duff@srnl.doe.gov – 803 725 2054

Abstract: We investigated the performance improvement of $Cd_{1-x}Zn_xTe$ (CZT) crystals with previously known levels of intrinsic defects and secondary phases (SP), at various voltages, LED light wavelengths and shaping times. Although our setup was clearly not optimized for radiation detector performance, it demonstrated substantial resolution improvements (based on FWHM of the 662 keV gamma (γ) peak from ^{137}Cs upon illumination with 950 nm light) of 16 to 38% in comparison to un-illuminated CZT under similar conditions. This presentation will include discussion of the electro-optic behavior and its effect on performance. Additional testing and fabrication of a detector that incorporates such LED light optimization could lead to improved performance with existing detector-grade materials.
Keywords: NIR, secondary phases, CZT.

1. INTRODUCTION

CdZnTe or CZT can be used as an X-ray spectrometer and X-ray imaging in the medical and aerospace industries. The development, fabrication and spectrometer performance of CZT has significantly improved over the last 20 yrs with performance benefits that under certain conditions begin to approach that of commercial Si and Ge detectors.[1,2,3,4,5] One performance gap was narrowed through a better knowledge of internal electric field distribution by focusing on charge traps and reducing charge collection times for enhancing γ interaction.[6,7,8,9] As previously shown, the internal electric field of CZT can be altered through post growth manipulation using a variety of mechanisms.[10,11,12] One of the least invasive methods of post-growth manipulation is the use of superficial illumination to interact with the embedded defects located in mid-gap energy states. The wavelength of illumination acts on the defect density in the mid-gap states to alleviate traps, induce in some cases, an electro-optic effect, and significantly increasing the carrier collection.[10,13,14,15,16] An electro-optic effect with CZT can be examined using a Pockels-like cell. Recently, the electro-optic effect was used to calibrate nuclear reactor pulses.[17] During Pockels, near-infrared (NIR) radiation interacts with charge carriers within the crystal and causes a polarization of the internal electric field toward the cathode (negative).[18]

The internal electric field of CZT has been examined with materials that either have or possess the potential of high spectral resolution. We have previously investigated the influence of applying external LED illumination (at an optimal power) to show visual evidence of the liberation of charge carriers that are trapped in low energy mid gap states and in higher energy low gap states through Pockels imaging.[18] A possible explanation for the enhanced electric field polarization includes the formation of a soliton resonance intensity, which is a self-focusing process that occurs in illuminated and electrically-biased CZT crystals.[19] This room-temperature-based electro-optic behavior has been observed in materials that have electrons and holes as charge carriers, such as CZT and

InP:Fe.[20] For CZT, this type of extreme electro-optic performance is limited to material doped at the ~10^{17} cm^{-3} level; this self-focusing behavior does not occur in undoped material.[19,21] Schwartz and colleagues (2002)[19] have shown that in the absence of an applied electric field, the path of a circular 15 μm diameter light beam passing (or propagating) through a CZT wafer will increase in diameter by roughly three-fold indicating that there is a natural divergence within the crystal. Under bias, light beams can be focused to create a soliton in doped CZT. Schwartz and colleagues[19] determined that there is a linear relationship between soliton intensity (self-focusing behavior for a fixed wavelength and entrance beam size) and illumination background intensity (in mW cm^{-2}) and that this linear relationship extends for more than four orders of magnitude.

2. PERFORMANCE TESTING AND DISCUSSION

The two CZT materials in this presentation perform very well as radiation detectors under more optimized conditions. For example, our prior work with these crystals has shown that the Redlen crystal had a FWHM of 1.6% for the 662 keV peak of ^{137}Cs, using a 1600 V bias, a 0.5 μs shaping time and single pixel geometry. The YT 3-7-8 crystal had a FWHM 1.7% for the 662 keV peak of ^{137}Cs using a bias of 1000 V, a 0.3 μs shaping time and a single pixel geometry. Because our current study's focus was to examine the effect of sub-bandgap illumination on radiation detection, there were substantial changes in detector performance setup that were required. *Figure 1* provides an image of the detector performance measurement setup. Prior work with these crystals in other geometries demonstrated that they had very high leakage currents (data not shown). Although measurements of detector resolution were possible, they were of poor quality—in the several tens of percent. To compensate for the high leakage currents, a layer of Au was added to four sides of the crystal and a hemi-spherical geometry was used with both crystals as noted in the methods. Due to high leakage currents with the Redlen crystal in particular, a Frisch grid was also used.

Table 1 shows that sub-bandgap light illumination improved the resolution under all conditions. At a shaping time of 2.0 μs, there was better energy resolution at low voltage (500 V) for the 1000 nm illumination but in the absence of illumination, better resolution was obtained at 1000 V. At a lower shaping time (0.5 μs), a voltage of 1500 V and illumination at 1000 nm, the energy resolution was better than that at a higher shaping time of 2.0 μs at 1500 V. Lowering the illumination wavelength from 1000 nm to 950 nm produced the best total energy resolution improvements regardless of shaping time or voltage applied with. For the Redlen crystal, the resolution was better at an illumination of 950 nm as opposed to 1000 nm for the same bias and shaping time conditions. Additionally, the amount of resolution improvement was higher at 950 nm than at 1000 nm. Higher biases did not always produce better resolution when that was the only condition parameter that was changed for the study of this crystal. *Table 1* also shows the percent improvement in resolution with illumination, which were the greatest when the crystal was illuminated at 950 nm as opposed to 1000 nm, regardless of the other setup parameters. Some example spectra for the data in *Table 1* are shown in *Fig. 2.*

The amount of energy resolution improvement was considerably greater at 950 nm than at 1000 nm with the exception of high voltage settings (2000 V for the Redlen crystal and 1500 V for the YT crystal, data for YT crystal not shown) when there was little effect of wavelength on resolution improvement. The results from the YT testing differ from that with the Redlen crystal, which had fewer defects than that of the YT 3-7-8. According to oru prior transmission IR measurements with the two crystals, the Redlen crystal clearly has a lower number of SP relative to the YT and may also have relatively fewer types or numbers of traps that could be excited upon illumination. Additionally, the YT crystal which was more sensitive/responsive to the light may have had more trap "diversity" that were excitable with light, due to its greater number of defects and SP.

When the bias on the crystal was greatly increased (e.g., with 1500 and 2000 V with the YT and Redlen crystals, respectively in this study), additional noise degraded the signal quality in terms of resolution improvement. The decrease in resistivity upon illumination may be (due to the freeing of traps that contribute to the bulk resistivity) could provoke the decreased number of counts that are observed on the ROI for the 662 keV peak of ^{137}Cs so there are some tradeoffs for the improved resolution.

Our study also did not directly determine the direct physical processes that helped improve the energy resolution but there are several possible explanations for this. Given previously discussed work on the effects of sub-bandgap light on the electrical behavior of biased CZT. The de-trapping of mid- and deep-level traps which should lead to greater charge collection is supported by a slow current decay after illumination during current transient measurements.[22] Additional detector development would be required to have the flexibility to utilize 950 nm lighting during γ-spectroscopy when resolution is most important but have the option of working without the illumination for less power consumption of the detector.

3. TABLE AND FIGURES

Table 1. Results of the illumination studies with Redlen 64039B crystal with hemispherical contacts and exposure to a ^{137}Cs source.

Shaping time (μs)	Light wave-length (nm)	Voltage (V)	FWHM with LED off (keV)	FWHM with LED on (keV)	FWHM Improvement (keV)	Resolution with LED off (%)	Resolution with LED on (%)	Resolution improvement (Δ%)	Total resolution improvement with illumination (%)
0.5	950	1500	24.1	16.5	7.5	3.7	2.7	1.0	27.1
2.0	950	500	28.6	19.4	9.1	4.3	2.9	1.4	31.9
0.5	1000	1500	26.3	20.6	5.7	4.0	3.1	0.9	21.6
2.0	1000	500	27.5	21.7	5.9	4.2	3.3	0.9	21.3
2.0	1000	750	27.3	21.9	5.4	4.1	3.3	0.8	19.7
2.0	1000	1000	26.5	22.2	4.3	4.0	3.4	0.7	16.2
2.0	1000	1500	29.9	24.0	5.9	4.5	3.6	0.9	19.6

LED

Optical density filter on top of collimator

Band-pass filter

Anode

Cathode

[137]Cs source (underneath cathode)
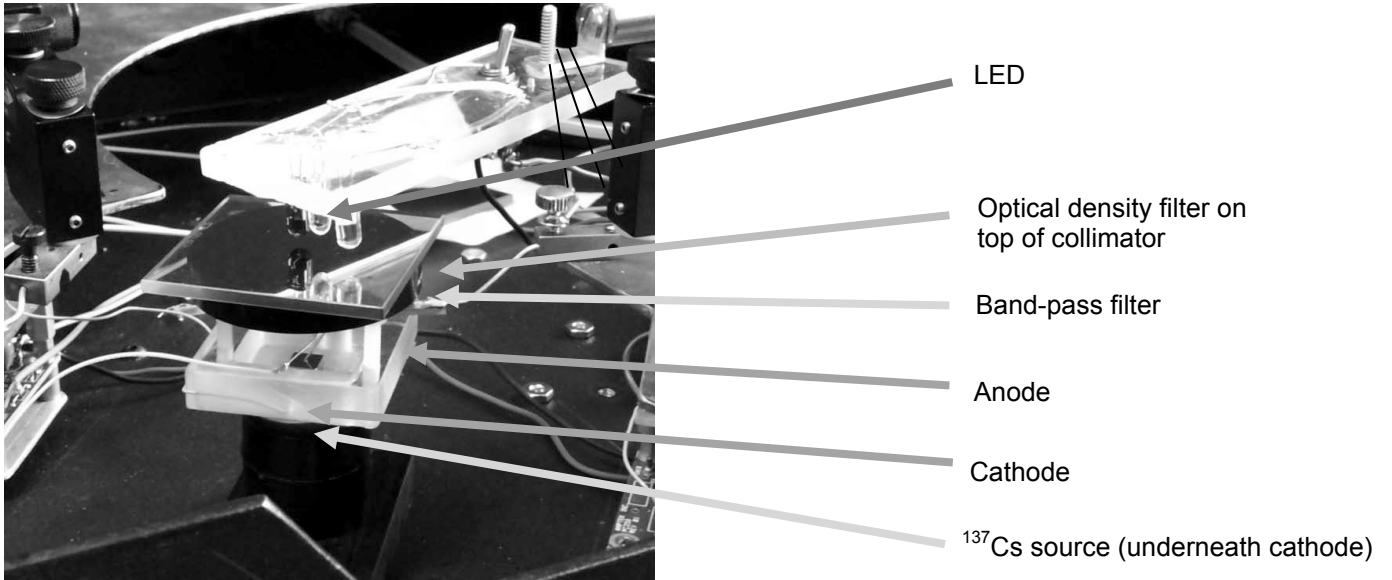
Fig. 1. (Above) The general setup of the illuminated detector studies with the YT 3-7-8 CZT crystal using hemispherical contact geometry. The studies with the YT crystal required optical density filters (0.5 and 1.0). The distance between the [137]Cs-137 source and the CZT was kept constant throughout the study. The same setup was used with the Redlen crystal.

Fig. 2. (Right) The ^{137}Cs with crystal 64039B in hemispheric configuration in black and IR (950 nm) illumination in red. With IR illumination the energy resolution was improved from 3.7 to 2.7%
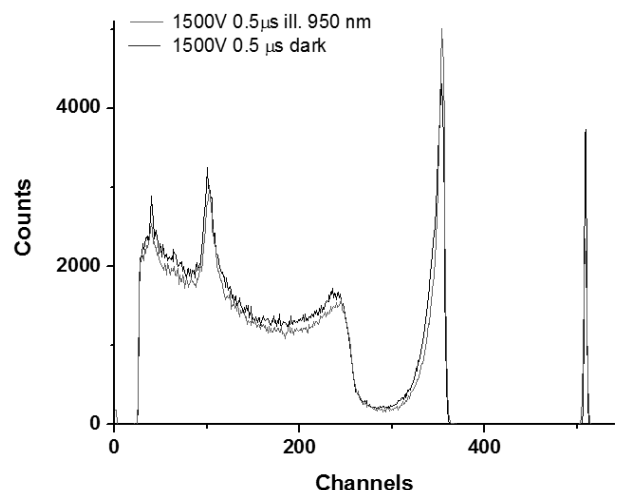
4. REFERENCES

[1] T. E. Schlesinger et al., *Mater. Sci. Eng. R-Rep.* 2001, *32* (4-5), 103-189.
[2] J. F. Butler et al., *IEEE Trans. Nucl. Sci.* 1992, *6*, 605.
[3] J. F. Butler et al., *IEEE Trans. Nucl. Sci.* 1998, *45* (3), 359-363.
[4] C. L. Lingren et al., *IEEE Trans. Nucl. Sci.* 1998, *45* (3), 433-437.
[5] A. E. Bolotnikov et al., *Nucl. Instr. Meth. Phys. Res. Sect. A-Accel. Spectrom. Dect. Assoc. Equip.* 1999, *432* (2-3), 326-331.
[6] M. Groza et al., *J. Appl. Phys.* 2010, *107* (2), 023704-8.
[7] G. Yang et al., *J. Elect. Mat.* 2009, *38* (8), 1563-1567.
[8] A. Zumbiehl et al., *J. Cryst. Growth* 1999, *197* (3), 650-654.
[9] P. DeAntonis, et al., *IEEE Trans. Nucl. Sci.* 1996, *43* (3), 1487-1490.
[10] P. J. Sellin, et al., *Appl. Phys. Lett.* 2010, *96* (13), 133509-3.
[11] A. Burger, et al., *J. Electron. Mater.* 2003, *32* (7), 756-760.
[12] A. Cola and I Farella, *Appl. Phys. Lett.* 2009, *94* (10).
[13] S. Shwartz et al., *Appl. Phys. Lett.* 2008, *93* (10).
[14] S. Shwartz et al., *Phys. Rev. B* 2009, *79* (19).
[15] H. W. Yao et al., *Proc. SPIE*; Doty, F. P., Ed.; pp 62-68, July 7, 1997.
[16] H. W. Yao et al., *Proc. SPIE*, James, R. B., Ed.; 330, Oct. 19, 1999.
[17] K. A. Nelson et al., *Appl. Rad. Isotopes* 2012, *70,* 1118-1120.
[18] A. L. Washington et al., *J. Appl. Phys.* 2011, *110* (7), 3119-3124.
[19] T. Schwartz et al., *Opt. Lett.* 2002, *27,* 1229-1231.
[20] M. Chauvet et al., *Opt. Lett.* 1996, *21,* 1333-1335.
[21] S. Shwartz et al., *Optics Express*, 2006, *14* (20), 9385-9391.
[22] J. S. Wright et al., *J. Electron. Mat.* 2013, *42,* 3119-3121.

RELATIONSHIP OF ZnTe-BASED CONTACT PROCESS

TO CdS/CdTe SOLAR CELL PERFORMANCE

T.A. Gessert, J.N. Duenow, S. Ward, J.F. Geisz, and B.R. Faulkner*

tim.gessert@nrel.gov - 303-384-6451

National Renewable Energy Laboratory (NREL), 15013 Denver West Parkway,

Golden, Colorado 80401 USA

**Colorado School of Mines, 1500 Illinois Street, Golden, Colorado 80401 USA*

Introduction and Experimental Details

It has been suspected that contacts historically used for polycrystalline CdTe PV films/devices may demonstrate reduced functionality when used with crystalline materials. [1] One important historical back contact is ZnTe:Cu/Ti. [2,3] When this contact is used on bulk (or thick epitaxial) CdTe, a concern exists that the CdTe could *sink* Cu from the ZnTe:Cu – because the crystalline CdTe is generally much thicker than polycrystalline films. This could lead to a reduction in Cu-related acceptor concentration in the ZnTe:Cu, thus limiting the formation of the quasi-tunneling barrier at the ZnTe:Cu/Ti interface needed for low-resistance electrical transport. In this study, we apply the ZnTe:Cu/Ti contacting process developed at NREL for *polycrystalline* CdS/CdTe device research activities [2] to *crystalline* CdTe surfaces. The crystals were purchased from JX Nippon and were 0.5-cm x 0.5-cm x 800-μm thick, (211) oriented, polished on both sides, and were either nominally undoped ($\sim$2x10^{14} cm^{-3}, residual p-type) or Na-doped to a concentration of $\sim$5x10^{15} cm^{-3} as measured at NREL by room-temperature Hall. These bulk crystalline CdTe were attached to Si handles to enable processing needed for sequential transmission-line method (TLM) analysis of specific contact resistance (ρ_c) and other characterization of the ZnTe:Cu/Ti back contact structure. [4]

Results and Discussion

The processes described above yielded A-, B-, and C-Type structures (see **Fig. 1**) that enabled I-V and TLM analysis on all samples in this set (i.e., doped and undoped CdTe substrates, with ZnTe:Cu layers deposited at $\sim$30°C or $\sim$320°C, as described in **Table I**). **Fig. 2** shows I-V curves of Type-B structures indicating conductivity between the two nearest

contact pads (25-µm separation). Although all samples demonstrate ohmic behavior, **Fig. 2** reveals that samples with ZnTe:Cu deposited at ~320°C have lower total resistance (i.e., total resistance = combined sheet resistance [R_s] and ρ_c) than samples deposited at ~30°C. TLM measurements of these samples reveal further that *both* the R_s and ρ_c are significantly lower for the samples formed at ~320°C. Note that at this stage in the analysis (i.e., analysis of B-Type structures), the TLM analysis is primarily probing resistivity of the ZnTe:Cu layer and ρ_c at the ZnTe:Cu/Ti interface (i.e., not the ZnTe/CdTe interface). Although the TLM-indicated R_s could be impacted (i.e., reduced) by the lower resistance of the Na-doped CdTe substrate, the opposite is observed. Specifically, **Fig. 2** shows, for samples where the ZnTe:Cu is deposited at either ~30°C and ~320°C, the samples fabricated with Na-doped CdTe indicate *higher* total resistance than the undoped samples. Further, **Table I** indicates that this higher total resistance is due to both higher R_s and ρ_c. This observation is still being considered, but suggests that the Na-doped CdTe substrate may impact the ZnTe:Cu layer and related interfaces - at the contacting temperatures used here.

In contrast to the TLM measurements of the B-type structures, current flow for the C-Type structures is intended to occur primarily through the CdTe substrate (i.e., the relatively conductive ZnTe:Cu layer between the pads is removed during the third etch step). **Fig. 3** shows that the resistance between pads is generally much higher for the C-Type than for the B-Type structures, and that many of the samples now reveal a noticeable non-linearity in their I-V response. Further, the samples in **Fig. 3** with the lowest resistance between the pads are now the two samples that include a Na-doped CdTe substrate. These observations strongly suggest that the current in the C-Type samples flows primarily through the bulk CdTe layer.

Although TLM measurements were attempted on all C-Type samples, only the sample that included both Na-doped CdTe, and a ZnTe:Cu layer deposited at 320°C (Sample #130, **Table I**), produced TLM data that was sufficiently reliable to extract R_s and ρ_c values. This is not unexpected because it is much more difficult to flow current through the CdTe for the two samples produced with the undoped substrates. The resulting TLM analysis (**Fig. 4)** shows the resulting fit if data points 1, 3, and 4 are used to compute R_s and ρ_c. Although these values (~15K Ω/sq and ~40 Ω-cm^2) depend on which data points are incorporated (or excluded) in the TLM analysis, in all cases the resulting ρ_c would remain significantly higher than ~1 Ω-cm that would be expected to yield a dominant external loss for even a 1-Sun PV device. [5]

Conclusions

Although this work should be viewed as preliminary, initial observations suggest: ρ_c at the outer ZnTe:Cu/Ti interface presently appears to be sufficiently low (0.1-0.5 Ω-cm^2) to minimize its effect on total external loss of resulting PV devices operated at 1 sun - as long as the ZnTe:Cu and Ti are deposited at a temperature >250°C. This suggests that Cu diffusion into the bulk CdTe substrate does not reduce the N_A of the ZnTe:Cu layer sufficiently to limit emission at the ZnTe:Cu/Ti interface (i.e., low-resistance quantum-mechanical tunneling at the outer contact remains the dominant current-transport mechanism). Unfortunately, the present processing conditions appear to yield a ρ_c at the CdTe/ZnTe:Cu interface that is sufficient to dominate total external losses for any resulting 1-sun device (~40 Ω-cm^2). This result is unexpected because the valence-band continuity at the CdTe/ZnTe interface has been assumed to yield low resistance current transport at this interface. The related NREL processes (e.g., the ion-beam mill step) are presently being investigated with a view to reduce this ρ_c.

Acknowledgements

TABLE 1. RESULTS OF TLM ANALYSIS FOR FOUR SAMPLES ANALYZED IN THIS STUDY

ID	Structure	CdTe Substrate	ZnTe:Cu Temp (°C)	TLM (first 2 pts*) R_s (Ω/sq)	ρ_c (Ω-cm^2)
127	A-Type	UD	30	50K	2.2
128	A-Type	Na	30	70K	7.3
129	A-Type	UD	320	4.6K	0.09
130	A-Type	Na	320	7.7K	0.9
127	B-Type	UD	30	63K	1.3
128	B-Type	Na	30	85K	4.6
129	B-Type	UD	320	5.4K	0.08
130	B-Type	Na	320	5.1K	0.42
127	C-Type	UD	30	-	-
129	C-Type	Na	30	-	-
129	C-Type	UD	320	-	-
130	C-Type	Na	320	17K	40

*Except as shown in Figure 4 for Sample 130.
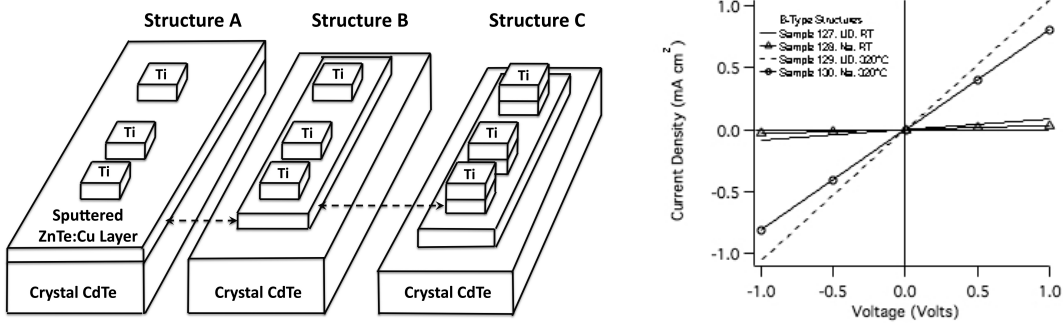
Figure 1. (Left) Schematic of samples with a current-confinement layer indicated. The dashed arrows show the sputtered ZnTe:Cu layer in B-Type and C-Type samples. Note that only three of the six pads are illustrated, and the Si handle is not shown.

Figure 2. (Right) I-V analysis for all B-Type structures shown in Fig. 1 for current flow between the pads separated by 25 μm.
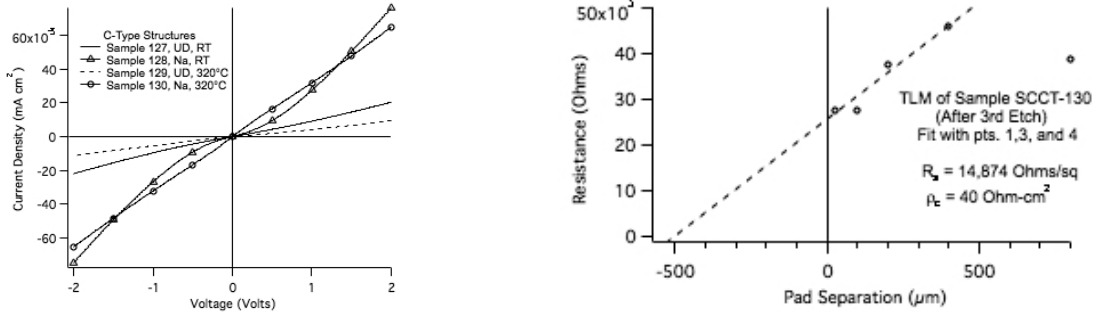
Figure 3. (Left) I-V curves for C-Type structures (shown in Fig. 1) for current flow between the pads separated by 25 μm.

Figure 4. (Right) TLM data for all pad separations for the C-Type structure (shown in Fig. 1) for Na-doped CdTe substrate and ZnTe:Cu/Ti layers deposited at 320°C.

References

[1] T.A. Gessert, R. Dhere, D. Kuciauskas, and E. Colegrove, "Development of CdTe on Si Heteroepilayers for Controlled PV Material and Device Studies," MRS Proceedings Vol. 1538, pp. 243-248 (2013)..

[2] T.A. Gessert, S. Asher, S. Johnston, A. Duda, and M.R. Young, Proc. 4th World Conf. PV Energy Conv., IEEE, Piscataway, NJ, USA, 2006, p. 432.

[3] N. Strevel, L. Trippel, C. Kotarba, and I. Khan, "Improvements in CdTe Module Reliability and Long-Term Degradation through Advances in Construction and Device Innovation," Photovoltaics International, **22** pp. 66-74 (2013).

[4] H.H. Berger, "Contact Resistance and Contact Resistivity," *J. Electrochem. Soc.: Solid-State Sci. and Technol.* **119** (4) pp. 507-514 (1972).

[5] T.A. Gessert and T.J. Coutts, "Development and Analysis of Cu-Doped ZnTe for use as a Back Contact Interface for CdS/CdTe Solar Cells," AIP Conf. Proc. #306 (AIP, Woodbury, New York, 1994), pp. 345-353.

Study of grain boundary and dislocation core structures using CdTe bi-crystals

T. Paulauskas,[1] C. Buurma,[1] M. K. Y. Chan,[2] C. Sun,[3] M. J. Kim,[3] S. Sivananthan,[1] R. F. Klie[1]

[1] *Department of Physics, University of Illinois Chicago, Chicago, IL*

[2] *Center for Nanoscale Materials, Argonne National Laboratory, Argonne, IL*

[3] *Department of Materials Science and Engineering, University of Texas at Dallas, TX*

Poly-crystalline Cu-doped CdTe is commercially used in thin film photovoltaics (PV). Despite intense research and development of the cells the current efficiency 20.4% laboratory record is still ~10% shy of the theoretical Shockley-Quisser limit. One of the main challenges in CdTe PVs is increasing the open-circuit voltage (V_{oc}) beyond 900 mV, which is a critical parameter closely related to electron-hole recombination. Grain boundaries are believed to play an important role in decreasing the minority carrier lifetimes by providing carrier recombination centers and better understanding of their effects on CdTe solar cell performance is needed.

In this study, we systematically analyze ultra-high vacuum (UHV) bonded CdTe bi-crystals with pre-defined misorientions, which are intended to mimic real grain boundaries in poly-crystalline CdTe. Atomic-scale characterization of the interfaces is carried out in an aberration-corrected cold-field emission scanning transmission electron microscope (STEM) using high-angle annular dark field (HAADF) imaging and atomic-column resolved X-ray energy dispersive spectrum imaging (XEDS). The associated strain fields are calculated using the geometrical phase analysis (GPA).

The (100)|(100) wafer bonding geometry in Fig 1 causes formation of a high energy interface whereby Te columns are facing Te columns at the interface. A novel triple-atom column configurations are seen to be forming at the interface. Figures 2a,b presents a low-angle tilt grain boundary with (110) interface plane which is composed mainly of Lomer dislocations ~5nm apart.

[1] Sun, C., N. Lu, J. Wang, J. Lee, X. Peng, R.F. Klie, and M.J. Kim, "Creating a single twin boundary between two CdTe (111) wafers with controlled rotation angle by wafer bonding," Applied Physics Letters **25** 103, 2013.

[2] T. Paulauskas, C. Buurma, E. Colegrove, B. Stafford, M. K. Y. Chan, M. J. Kim, S. Sivananthan, R. F. Klie *"Atomic-scale study of polar Lomer-Cottrell and Hirth lock dislocation cores in CdTe", submitted to* Acta Crystallographica (2014).
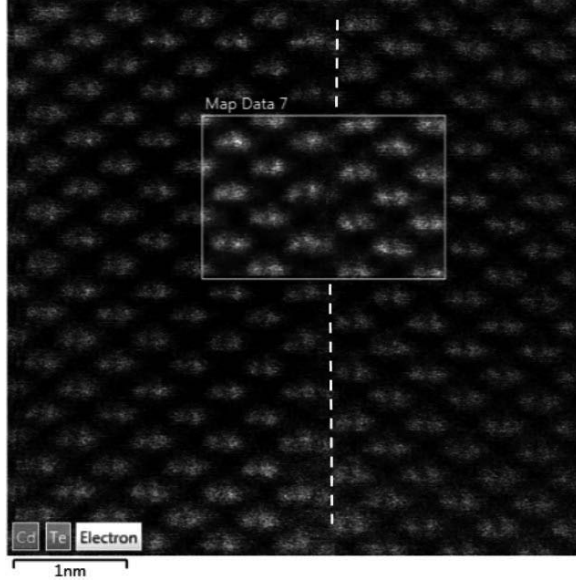
Figure 1: Atomic-column resolved X-ray spectrum image (color inset) across the interface (dashed line) of (100)|(100) bi-crystal. Triple-atom columns can be seen forming at the interface.
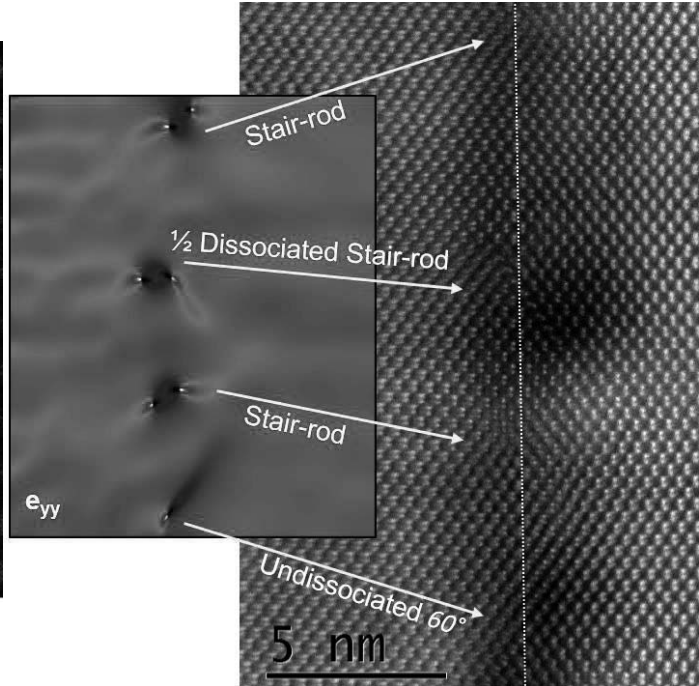
Figure 2a: HAADF image (right) of symmetrical low-angle (2°) tilt grain boundary with (110) interface plane (dashed line). The boundary is composed of arrays of discrete dislocation cores. Associated strain fields (GPA) are presented on the left.
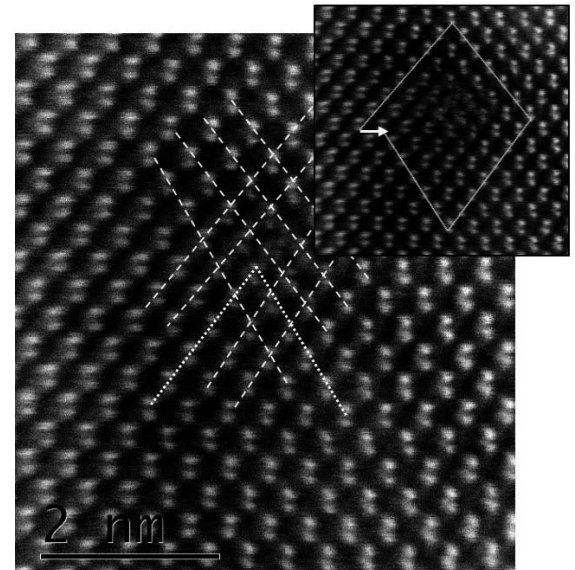
Figure 2b: Majority of dislocations in the low-angle tilt grain boundary above are made of pure-edge sessile Lomer dislocations which have Burgers vector of the form *a*/2[-110]. These can be seen to form due to two intersecting extra {111} planes at an acute angle. Burgers circuit is drawn in the inset.

THE CRYSTALLOGRAPHIC CHARACTERIZATION OF AgGaTe$_2$ AND AgAlTe$_2$ GROWN BY CLOSED SPACE SUBLIMATION

Aya. Uruno[1]*, Ayaka. Usui[1] and Mamakazu. Kobayashi[1,2]

[1] *Waseda Univ., Dept. of Elec. Eng. & Biosci., Tokyo. Japan*

[2] *Waseda Univ., Kagami Mem. Res. Inst. for Mat. Sci. & Technol., Tokyo, Japan*

*phone, fax: +81-3-5286-1684 e-mail: a.uruno@fuji.waseda.jp

Introduction

CdTe is one of the most promising photovoltaic materials available for use in low-cost and high-efficiency solar cells [1]. Also, ternary I-III-VI$_2$ group compounds with chalcopyrite structure are widely used for solar cells. I-III-Te$_2$ compounds replace Cd in CdTe with group I and III elements, and are hence expected to be another attractive candidate for novel solar cell materials. The bandgap of AgGaTe$_2$ at room temperature is around 1.3 eV [2]. This value is slightly lower than the optimum value for fabricating solar cells. Formation of solid solutions of AgAlTe$_2$ (Eg = 2.2 eV [2]) and AgGaTe$_2$ is an approach to optimize the bandgap energy. The growth of AgGaTe$_2$ and AgAlTe$_2$ and understanding of the growth mechanism with respect to the substrate surface are inevitable tasks to achieve high quality alloy layers of Ag(Al,Ga)Te$_2$. AgGaTe$_2$ and AgAlTe$_2$ layers were grown by the closed space sublimation (CSS) method. The CSS method is widely used in the fabrication of CdTe thin film solar cells since it has many advantages for the fabrication of low cost solar cells [1]. In this study, the AgGaTe$_2$ and the AgAlTe$_2$ layers were grown on sapphire substrates

by the CSS method, and the crystallinity and the stoichiometry of grown layers were studied. From these results, the growth of Ag(Al,Ga)Te$_2$ was performed, and the optical property was studied to confirm the solid solution.

Experimental

AgGaTe$_2$, AgAlTe$_2$ and Ag(Al,Ga)Te$_2$ layers were grown on a- and c-plane sapphire substrates. The source temperature was varied from 750 ^{o}C to 850 ^{o}C. The source used was the mixture of powdered AgGaTe$_2$ and AgAlTe$_2$ with various ratios when the Ag(Al,Ga)Te$_2$ layer was grown. Its crystallographic properties were evaluated by X-ray diffraction (XRD). The transmittance in visible range was measured by a ultra-violet to visible spectrophotometry (UV-VIS) and the bandgap of the grown layer was evaluated.

Results and Discussions

The XRD spectra of AgGaTe$_2$ and AgAlTe$_2$ layers grown on c-plane sapphire substrate are shown on in Fig. 1. Source temperatures for the AgGaTe$_2$ and the AgAlTe$_2$ layer were 750 ^{o}C and 800 ^{o}C, respectively. The XRD spectrum of grown layers contained peaks originating from AgGaTe$_2$ and AgAlTe$_2$, and the 112 peak was the strongest peak for both samples. From this, layers exhibited the strong preference for the (112) orientation. The optimal source temperature to grow AgGaTe$_2$ and AgAlTe$_2$ was around 750 ^{o}C and 800 ^{o}C, respectively.

The solid solution of AgGaTe$_2$ and AgAlTe$_2$ was grown on c-plane sapphire. Figure 2 shows a transmittance spectra of AgAlTe$_2$ and Ag(Al,Ga)Te$_2$ layers. The source temperature for the

Ag(Al,Ga)Te$_2$ layer was 775 $^{\circ}$C.   The weight ratio of AgGaTe$_2$:AgAlTe$_2$ was 1:5.   As shown in Fig. 2, there were rapid decreases in transmittance value near absorption edges.   Absorption edges of AgAlTe$_2$, and Ag(Al,Ga)Te$_2$ were appeared about 550 nm and 600 nm, respectively.   The value of optical bandgap at the room temperature was evaluated from the transmittance curve, and values were about 2.3 eV and 2.0 eV, respectively.   From this, it was cleared that the growth of the solid solution of AgGaTe$_2$ and AgAlTe$_2$ was successfully achieved.   Based on the transmittance spectrum, the Ga mole fraction was about 30%.

Conclusion

AgGaTe$_2$ and AgAlTe$_2$ layers were grown on c-plane sapphire substrate with varying the source temperature.   The optimal condition to grow the AgGaTe$_2$ and AgAlTe$_2$ was source temperature of around 750 $^{\circ}$C and 800 $^{\circ}$C, respectively.   And both layers grown on c-plane sapphire substrates exhibited the strong preference for the (112) orientation.   From these results, the growth of the Ag(Al,Ga)Te$_2$ layer was performed.   It was cleared that the solid solution of AgGaTe$_2$ and AgAlTe$_2$ which has the bandgap value of about 2.0 eV was achieved.

Acknowledgments
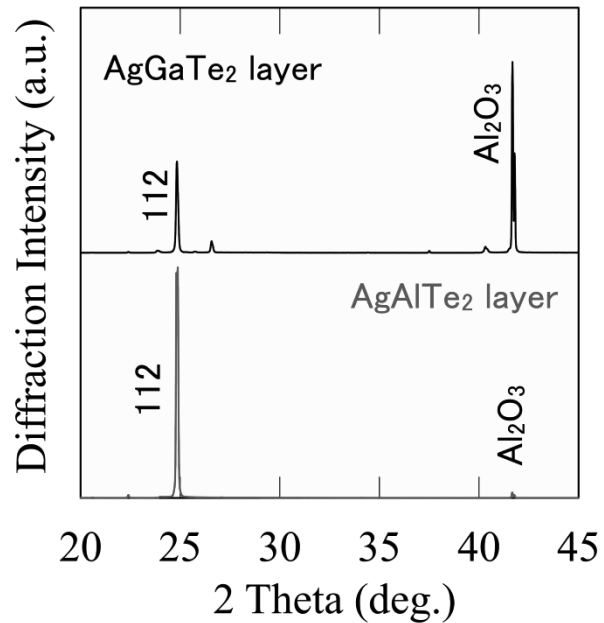
Fig. 1. XRD θ-2θ scans of the AgGaTe$_2$ and the AgAlTe$_2$ layers grown on c-plane sapphire.
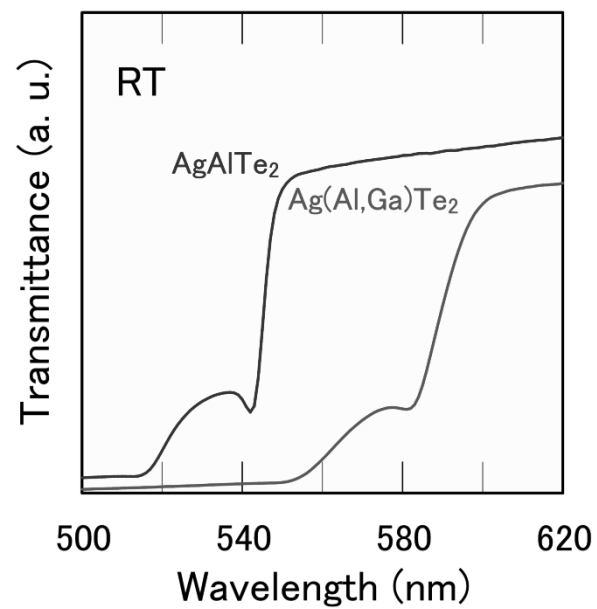
Fig. 2. Transmittance spectra of the AgGaTe$_2$ and the Ag(Al,Ga)Te$_2$ layers grown c-plane sapphire.

References

[1] X. Wu, Sol. Energy. 77, 803 (2004).

[2] B. Tell, J. L. Shay, and H. M. Kasper, Phys. Rev. B 9, 5203 (1974).

High-Efficiency Flexible CdTe Superstrate Devices

T.M. Barnes,[1] W. L. Rance,[1] J. M. Burst,[1] M. O. Reese,[1] D. M. Meysing,[2] C. A. Wolden,[2] H. Mahabaduge,[1] J. Li,[2] J. D. Beach,[2] T. A. Gessert,[1] S. M. Garner,[3] Pat Cimo,[3] and W. K. Metzger[1]

[1]NREL, Golden, CO 80401, USA

[2]Colorado School of Mines, Golden, CO 80401, USA

[3]Corning Incorporated, Corning, NY 14831, USA

Abstract — Flexible, superstrate CdTe devices combine the advantages of a commercially demonstrated, low-cost manufacturing process with a lightweight, flexible form factor. Here, we present data on cell efficiencies greater than 16%, and the critical processing changes that have enabled recent efficiency increases.

The devices in this study were made on Corning® Willow® Glass, which is a highly transparent, flexible, hermetic, and dimensionally stable substrate that can withstand high processing temperatures. To date, we have produced devices with several different combinations of front and back contacts on this glass and have found that it is compatible with most of our standard processing steps. One of our best devices to date has a certified efficiency of 16.4%, and here we will discuss the critical process advancements that enabled this high efficiency compared to our previous 14% baseline.

(Cd,Mn)Te crystal plates for radiation detectors:

Electrical contacts and surface passivation.

M. Witkowska-Baran[1], A. Mycielski [1], D. Kochanowska[1], A. J. Szadkowski[1], M. Juchniewicz[2], E. Kamińska[2]

[1]Institute of Physics Polish Academy of Sciences ,Al. Lotników 32/46, 02-668 Warsaw, Poland

[2]Institute of Electron Technology, Al. Lotników 32/46, 02-668 Warsaw, Poland

M. Witkowska-Baran- phone: (+48) 22 116 26 21, fax: (+48) 22 843 09 26, e-mail: mwitkow@ifpan.edu.pl

1. INTRODUCTION

The (Cd,Mn)Te monocrystalline plate is a good candidate for X and gamma-ray detector owing to properly wide band-gap, good charge collection efficiency and high resistivity of (Cd,Mn)Te crystals. [1] The ability to grow the (Cd,Mn)Te crystals at relatively low temperatures ensures a high yield for manufacturing detectors with good parameters.

The main aim of our study was to develop, for the semi-insulating (Cd,Mn)Te monocrystalline plates, a technique of repeatable making good electrical contacts and a technique of passivation of the surfaces between electrodes. Our investigations of the electrical contacts were focused on the amorphous/nanocrystalline contact layers ("ACL" in the further text). The effects of passivation of the inter-electrode surfaces on the magnitude of the surface leakage currents (SLC) were studied. The properties of the metal-semiconductor interface as an electrical contact to the semiconductor crystal used as a radiation detector are governed by many phenomena at this interface like inter-diffusion between metal and semiconductor, formation of various chemical species, formation of defects, and all these processes effect the detector's performance [3].

2. CRYSTALS AND PREPARATION OF THE CRYSTAL PLATES

The high-quality single crystals of (Cd,Mn)Te, doped (for compensation) with vanadium (or Cl, or In) were grown by the Low Temperature Bridgman Method. The high resistivity was achieved not only due to proper compensation at growth, but also by subsequent annealing of the crystal plates in the cadmium vapors (this procedure reduces the concentration of cadmium vacancies, present in the as-grown crystals. [1] For the deposition of the contact layer - the crystal surface has to be properly prepared. Especially - excess of cadmium at the surface must be avoided, as Cd quickly becomes oxidized, and then it is difficult to remove. A special selective etching (described in details in [1]), used for obtaining the so called "epi-ready" surfaces, was applied. This etching creates a tellurium-rich layer, about 20Å thick. Fig. 1 illustrates the distribution of atoms in the surface region. The effects of choice of the parameters of the selective etching (the time of etching, the concentration of Br in the solution etc.) on the quality of the surface, prepared for contact deposition, and on the properties of the subsequently made contacts were studied.

3. AMORPHOUS CONTACT LAYERS

The contact layers (ACL) were made by vacuum deposition of the layers of heavily-doped ZnTe:Sb or CdTe:In on the "epi-ready" surfaces of the good-quality, high-resistivity (10^8–10^{10} Ωcm) single crystals of (Cd,Mn)Te. The evaporation was carried out in the medium-high vacuum of about 10^{-7}Tr.

The ACL were covered by an evaporated Au top layer for electrical connections. The obtained electrical contacts were characterized. The ACL were studied with scanning electron microscope (SEM). The secondary-electron images gave the "look" of the very surface, energy dispersive scanning of the X-ray luminescence response supplied information on the local atomic composition of the ACL, i.e. – on its homogeneity.

In Fig. 3. the secondary-electrons images of the surfaces of the ACL deposited on the (Cd,Mn)Te crystal surface are shown (left-hand side of the figure). The thicknesses of the ACL for A1), A2) and A3) were: 100 nm, 300 nm and 1000 nm respectively. The small areas of the ACL, containing specific objects (later identified as "holes"), presented in the insets, were studied by scanning of the intensity of the X-ray luminescence characteristic for the related elements: Cd, Zn, Te and Sb. For each of the three ACL surface images we have a set of four (right-hand side of the figure) distributions (maps) of the element content. One can see deficiency of Sb and strong presence of Cd in the objects. As Sb is contained in the ACL, while Cd is a constituent of the underlying (Cd,Mn)Te crystal - the observation allows us to interpret the objects as holes in the ACL. Obviously, holes in the contact layer are detrimental for the contact operation (they spoil the uniformity of the detector). It was observed that the number and size of those holes depends on the thickness of the ACL, so the best thickness was looked for. It has been found that the most appropriate thickness is 300-500 nm. In order to study the effect of the ACL thickness on the performance of the contact, the current-voltage characteristics of the (Cd,Mn)Te crystal plates with the two ACL electrodes, were measured for different thicknesses of the ACL. On the same crystal plate the electrode was deposited, the I-V characteristic measured, the electrode removed from the surface and a new electrode, of different ACL thickness, was deposited, and so on. Both ZnTe:Sb and CdTe:In ACL were studied as electrodes. See Fig 3. A and B. For the voltages up to 100 V, all the characteristics for various ACL thicknesses and for both ZnTe:Sb and CdTe:In ACL, turned out to be linear, as it can be seen in Fig. 3.

4. SURFACE LEAKAGE CURRENTS (SLC) AND PASSIVATION PROCEDURES

When the current flows between two electrodes attached to the crystal plate, part of it flows along the surface between electrodes. Sometimes, due to specific electrical properties of the crystal surface, this current can be large with respect to the current in the bulk. In this situation this current, called "surface leakage current" (SLC), can completely distort operation of the crystal plate as a radiation detector. SLC should be evaluated and minimized. To evaluate the SLC, the I-V characteristics of the current flowing between electrodes attached to the crystal plates were measured with a "guard-ring" circuit. The scheme is shown in Fig. 4. For connection **I** – the whole current (bulk current plus SLC) flows through the ammeter. For connection **II –** only the bulk current flows through the ammeter. SLC is caught by the guard ring and passes by the ammeter. The difference between the current values for **I** and **II** gives the evaluation of the SLC.

It was observed that the SLC are low for the (Cd,Mn)Te surface freshly etched in the Br(9%)-CH$_3$OH solution. For example, a high-resistivity (10^8 Ωcm) (Cd,Mn)Te plate, with (ZnTe:Sb) ACL, 500 nm thick, on both faces, was studied. The inter-electrode surfaces were etched and the I-V characteristics for the circuit configurations **I** and **II** (consult Fig. 4.) were measured immediately after etching. The results are shown at Fig. 5.

There is practically no difference between **I** (the whole current) and **II** (the bulk current only), which means that SLC was negligible in this case. The situation changed with time. Because of some kind of degradation of the inter-electrode surface, the SLC increased. Chemical treatments of the inter-electrode surfaces were studied as methods of persistent diminishing of the SLC. Before those treatments the electrodes were protected by a layer of Apiezon W. Mainly $(NH_4)_2S$ (*Ammonium sulfide*) was used as the solution for the final passivation of the (Cd,Mn)Te surface. Appropriate preparation of the surface before the final passivation turned out to be crucial and various chemicals were tested. Fig. 6. presents the influence of time on the current voltage characteristics of a (Cd,Mn)Te plate with two ACL electrodes deposited after passivation. The sample was first etched (30 sec.) in Br(1%)-CH_3OH, then etched (6 min.) in $(NH_4)_2S$. The characteristics were measured: immediately after chemical treatment, after 10 days, and after 30 days.

5. FIGURES
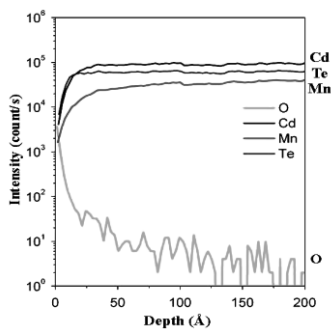
Fig. 1. Spatial distribution of atoms, obtained by SIMS, near the surface of a (Cd,Mn)Te crystal plate after etching. A layer with excess of tellurium exists near the surface. [3]
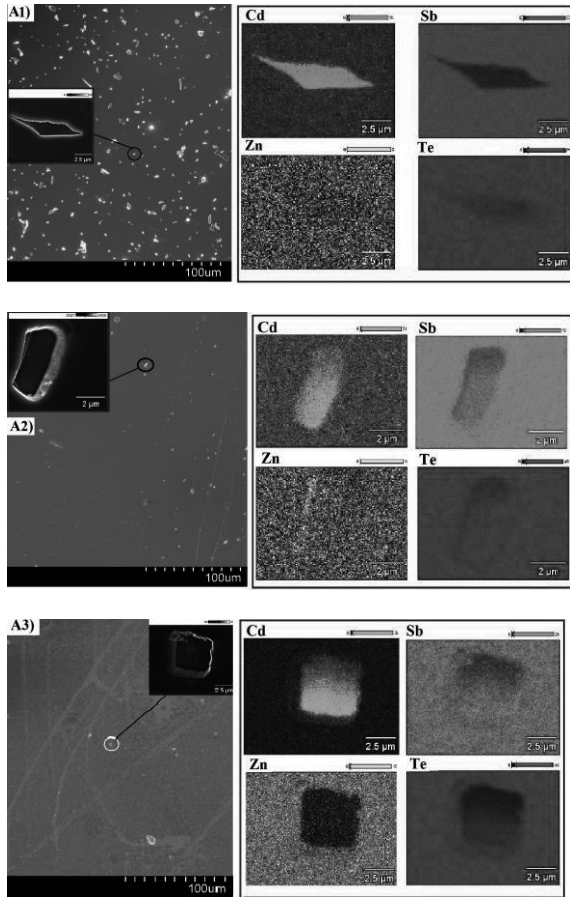
Fig. 2. The surfaces of the amorphous ZnTe:Sb contact layers, deposited on the (Cd,Mn)Te crystal surface, for the three different thicknesses of the layer: 100, 300 and 1000 nanometers. Investigations by SEM. Left hand side images – the secondary-electron images. The insets show magnified pictures of the selected small objects on the surface. Right-hand side images – distributions of the four elements – Sb, Cd, Zn and Te, obtained by scanning of the intensity of the characteristic X-ray luminescence in the regions of the objects. Description in the text.
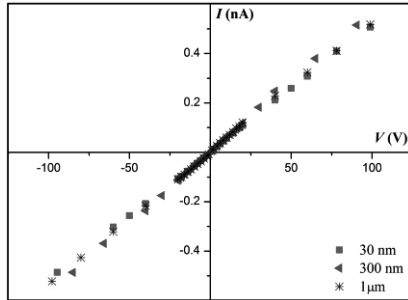
Fig. 3A. I-V characteristic of a high-resistivity (Cd,Mn)Te crystal plate with the **CdTe:In** ACL as the electrodes, for the ACL thicknesses 30, 300 and 1000 nm.
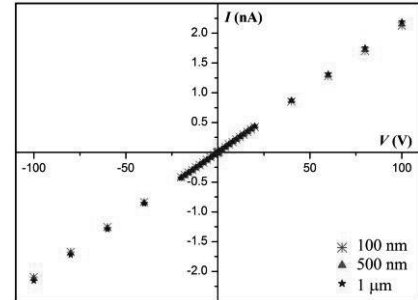
Fig. 3B. I-V characteristic of a high-resistivity (Cd,Mn)Te crystal plate with the **ZnTe:Sb** ACL as the electrodes, for the ACL thicknesses 100, 500 and 1000 nm.

Fig. 4. Scheme of the measuring system for evaluation of the SLC. (The crossection of the sample, perpendicular to the electrode surfaces is shown). On the right hand side - the "guard-ring" configuration of the bottom electrodes is depicted. d = 8.8 mm, x = 1 mm.
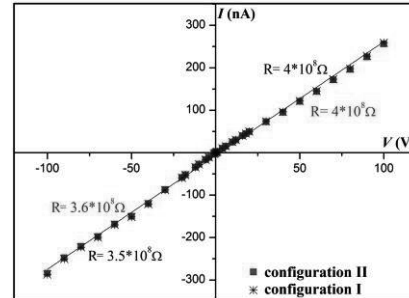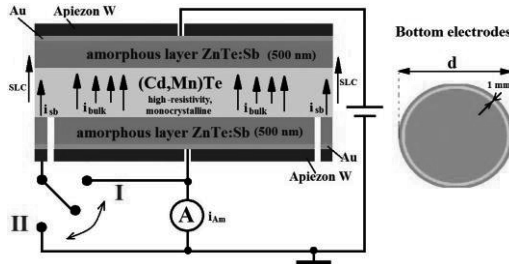
Fig. 5. The I-V characteristics for a high-resistivity (Cd,Mn)Te plate with (ZnTe:Sb) ACL on both sides. The two curves correspond to the circuit configurations **I** and **II** (consult Fig. 4.). The inter-electrode surfaces were freshly etched in the Br(9%)-CH₃OH solution.
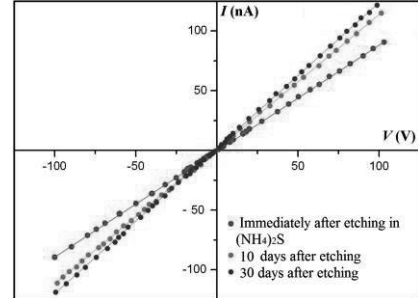
Fig. 6. The I-V characteristics of a (Cd,Mn)Te plate with two ACL electrodes: immediately after chemical treatment, after 10 days, and after 30 days.

6. REFERENCES

[1] A Mycielski, A. Burger, M. Sowińska et al. „Is the (Cd,Mn)Te crystal a prospective material for X-ray and gamma ray detectors?" Phys. Stat. Sol. (c) vol. 2, No. 5, (2005) pp. 1578-1585

[2] M. Witkowska-Baran, A. Mycielski, D. Kochanowska et al. „*Amorphous contact layers on (Cd,Mn)Te crystals*" Journal of Crystal Growth vol. 320 (2011) pp.1–5

[3] M. Witkowska-Baran, A. Mycielski, D. Kochanowska et al. „Contacts for High-Resistivity (Cd,Mn)Te Crystals" IEEE Transactions on Nuclear Science, vol. 58, No. 1, (2011) p. 347

Properties of sputter deposited contact materials on CdZnTe for radiation detector applications

S. Tari, F. Aqariden, Y. Chang

Sivananthan Laboratories, 590 Territorial Dr, Unit H Bolingbrook, IL 60440

C. Grein

University of Illinois at Chicago, Physics Department, Chicago, IL 60607-7059

M. S. Miao, D. Odkhuu, N. Kioussis

W. M. Keck Computational Materials Theory Center

California State University at Northridge, Northridge, CA 91330-8268

Radiation detectors with high gamma-ray energy resolution, linear energy response and the capability of room temperature operation are highly desirable for many applications such as medical diagnostics, homeland security, counter-terrorism inspections, as well as non-or counter-proliferation detection. State-of-the-art, room temperature, high resolution x-ray and gamma-ray detectors are usually based on CdZnTe semiconductors. The structural and electronic properties of CdZnTe surfaces, especially surface/contact metal interfaces, have a significant impact on radiation detector performance, such as leakage current, signal to noise ratios and energy resolution, particularly for relatively soft x-ray photons and large pixilated arrays. The choices of contact material and deposition technique determine the electronic properties to a large extent. We present a detailed study on the structural and electronic properties, hence detector performance, of various metal contacts deposited by sputtering on chemically polished (CP) CdZnTe surfaces of about 1 nm roughness. X-ray photoemission spectroscopy results indicate that contacts deposited on CP-finished CdZnTe surfaces are oxide-free and no atomic intermixing is observed. High resolution scanning transmission electron micrographs show a smooth and defect-free interface. I-V measurements show either ohmic or rectifying behaviour depending on the contact metal. Energy resolution measurements of fabricated detectors will also be presented.

Keywords: CdZnTe, radiation detector, polishing, leakage current, contacts, sputtering, interface, barrier.

EFFECTS OF CHEMO-MECHANICAL POLISHING ON CADMIUM ZINC TELLURIDE X-RAY AND GAMMA-RAY DETECTORS

Stephen U. Egarievwe[1], Anwar Hossain[2], Ifechukwude O. Okwechime[1], and Ralph B. James[2]

[1] Alabama A&M University, Normal, AL 35762, USA

[2] Brookhaven National Laboratory, Upton, NY 11973, USA

Abstract

In this paper, we compare the results of using two chemicals to chemo-mechanically polish cadmium zinc telluride (CdZnTe) wafers after mechanical polishing. The chemicals studied in this experiment include 1) bromine-methanol-ethylene glycol (BME) solution and 2) hydrogen bromide in hydrogen peroxide and ethylene glycol (HBr + H_2O_2 + $C_2H_6O_2$) solution. Current-voltage measurements show that the HBr-based solution produced lower leakage current compared to the BME solution. However, spectral response results for the 59.5-keV peak of Am-241 gave 7.5% FWHM for both chemical solutions. X-ray photoelectron spectroscopy (XPS) indicates that the tellurium oxide peaks $Te3d_{5/2}O_2$ and $Te3d_{3/2}O_2$ were reduced significantly by the BME solution compared to the HBr-based solution.

Introduction

Major sources of electronic noise that degrade the energy resolution in semiconductor x-ray and gamma-ray detectors include surface and bulk leakage currents.[1-3] While bulk leakage current depends on the crystal quality, the surface leakage current is mainly caused by surface roughness, dangling bonds, and the nonstoichiometric surface, formed during cutting of detector wafers from the as-grown crystal ingots. These fabrication-induced defects are often reduced through surface polishing and etching processes. This experimental work compares the effects of using two chemicals to chemo-mechanically polish cadmium zinc telluride (CdZnTe) wafers after mechanical polishing. The chemical are 1) bromine-methanol-ethylene glycol (BME) solution and 2) hydrogen bromide in hydrogen peroxide and ethylene glycol (HBr + H_2O_2 + $C_2H_6O_2$) solution.

Experiment

Three samples of sizes 6.4 x 6.4 x 2.8 mm^3 were sliced from a detector-grade CZT wafer grown by the Bridgman method. All three samples, A1, A2 and A3, were mechanically polished with 800-grit and 1200-grit silicon carbide abrasive papers, followed by polishing in 3.0 and 0.9 micron alumina powder (Al_2O_3). Samples A2 and A3 were further polished chemo-mechanically using 1) bromine-methanol-ethylene glycol (BME) solution and 2) hydrogen bromide in hydrogen peroxide and ethylene glycol (HBr + H_2O_2 + $C_2H_6O_2$) solution, respectively. Sample A1 was kept as a control.

X-ray photoelectron spectroscopy (XPS) experiment was conducted using a RHK Technology UHV 7500 system in an ultrahigh-vacuum setup at pressure below 8 x 10-10 Pa to scan for peaks of cadmium (Cd), tellurium (Te) and tellurium oxide (TeO_2) on the surfaces of the samples. Current-voltage measurement were made after the deposition of electrical contacts using a 5% gold chloride ($AuCl_3$) solution on the center of the two opposite planar surfaces of each CZT wafer. Spectral responses of the three samples were measured for Am-241 at an applied voltage of 200 V.

Results

The resistivity of each of the CZT samples is of the order of 10^{10} Ω-cm. As shown in Figure 1, the hydrogen bromide-based solution produced lower leakage current compared to the BME solution. The spectral responses of the three samples for the 59.5-keV peak of Am-241, shown in Figure 2, do not indicate any significant changes to the spectral performance. The spectral response for each sample gave 7.5% FWHM for the 59.5-keV peak of Am-241.

As for the surface chemistry, the XPS results shown in Figures 3 revealed prominent $Cd3d_{5/2}$ and $Cd3d_{3/2}$ peaks at 405 eV and 409 eV, respectively, corresponding with the elemental peak of cadmium. The Cd peaks remained fairly stable for the three samples, thus indicating no significant changes on the Cd peaks by each of the chemo-mechanical polishing solutions. The native oxide on the mechanically polished sample, shown by the tellurium oxide peaks $Te3d_{5/2}O_2$ and $Te3d_{3/2}O_2$ in Figure 4, was reduced significantly by chemo-mechanical polishing in BME solution compared to the HBr-based solution.
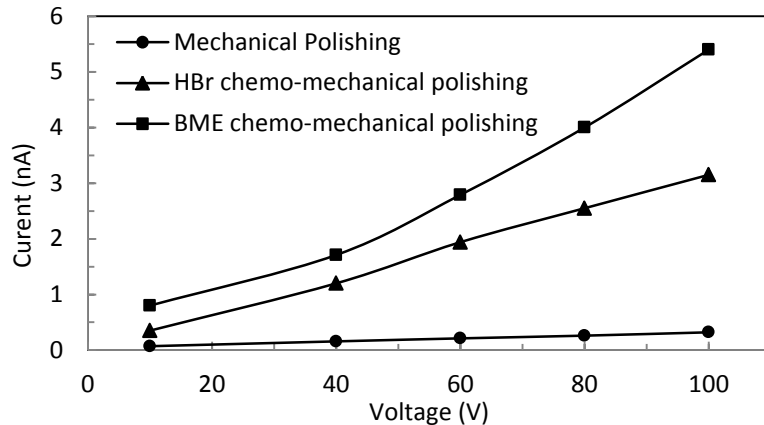
Figures

Figure 1. Current-voltage measurements for the three CZT samples.
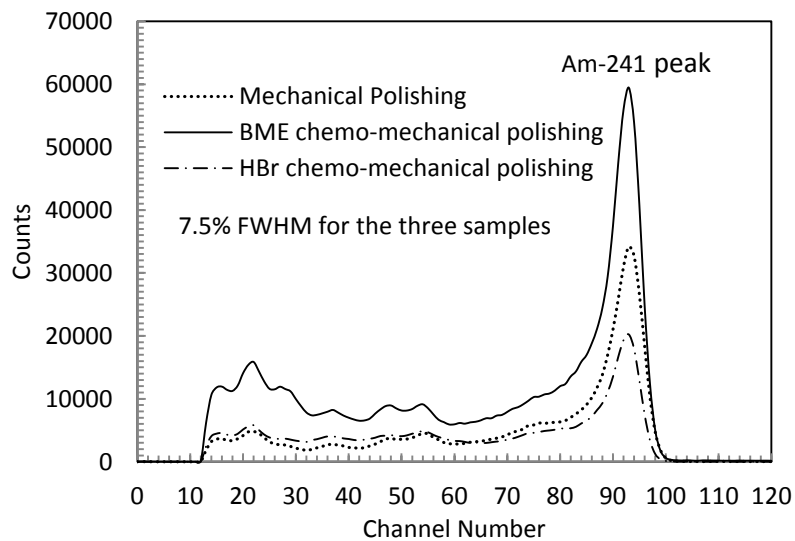
Figure 2. Am-241 spectral responses of CZT for the three polishing processes.
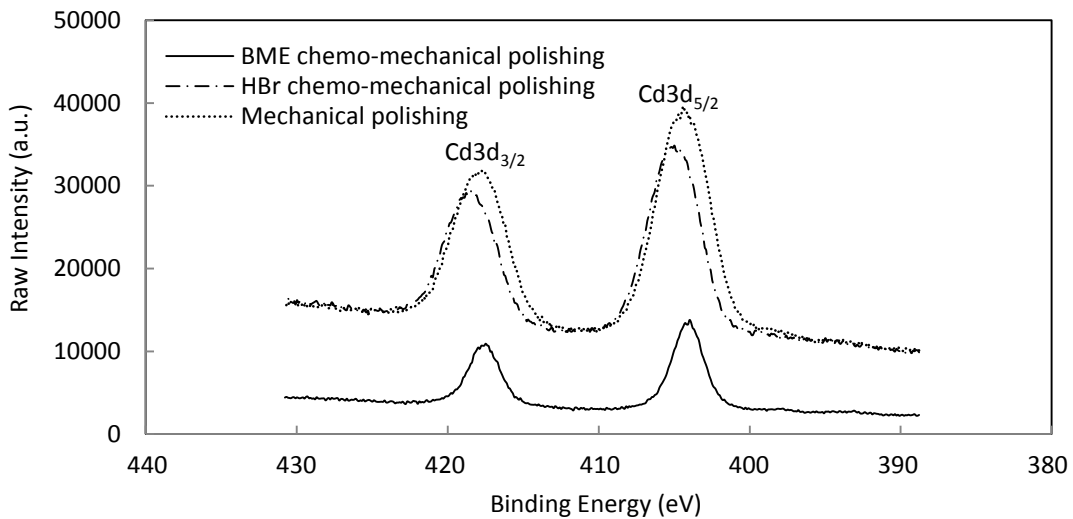
Figure 3. XPS spectra showing $Cd3d_{3/2}$ and $Cd3d_{5/2}$ peaks.
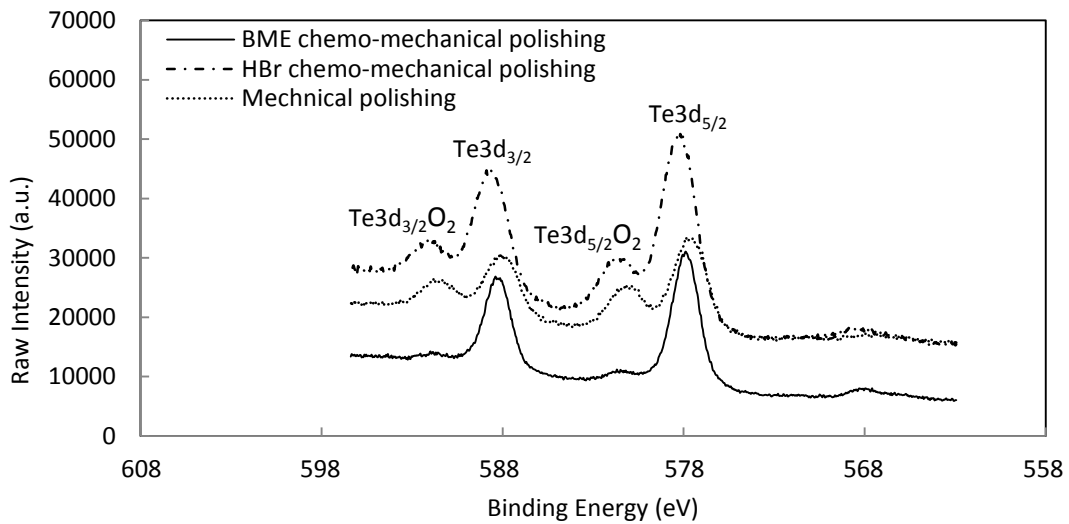
Figure 4. XPS spectra showing the TeO_x peaks.

References

[1] M. C. Duff, D. B. Hunter, A. Burger, M. Groza, V. Buliga, and D. R. Black, *Applied Surface Science* 254, 2889 (2008).

[2] T. H. Prettyman, F. P. Ameduri, A. Burger, J. C. Gregory, M. A. Hoffbauer, P.R. Majerus, D. B. Reisenfeld, S. A. Soldner, and C. Szeles, Proc. SPIE 4507, 25 (2001).

[3] A. Hossain, A. E. Bolotnikov, G. S. Camarda, Y. Cui, S. Babalola, A. Burger, and R. B. James, *Journal of Electronic Materials* 38, 1356 (2008).

Influence of annealing on the native defects in the (Cd,Mn)Te and (Cd,Mn)(Te,Se) crystals

Dominika Kochanowska, Marta Witkowska-Baran, Andrzej Mycielski

Institute of Physics Polish Academy of Sciences, Al. Lotników 32/46, 02-668 Warsaw, Poland

*e-mail: dmkoch@ifpan.edu.pl, phone: (+48) 22 116 21 26, fax: (+48) 22 843 09 26,

Abstract: Observations, by IR microscopy, of the tellurium inclusions in the (Cd,Mn)Te and (Cd,Mn)(Te,Se) crystals, and resistivity mapping, are described. Both as-grown and annealed crystals were studied.

Keywords: defects, inclusions, annealing, (Cd,Mn)Te.

1. Introdution

The (Cd,Mn)Te and (Cd,Mn)(Te,Se) belong to the family of CdTe based compounds. These materials are considered as a base for X and gamma ray detector devices [1]. For such applications a material with high resistivity and low concentration of native defects like second phase inclusions (Te inclusions) is necessary [2]. Post growth annealing is one of common methods used for increase of the resistivity and minimization of the number of inclusions.

2. Experimental procedure and results

The (Cd,Mn)Te and (Cd,Mn)(Te,Se) crystals grown by the Low Pressure Bridgman method were investigated. The growth at high temperatures and the shape of the phase-diagrams of these compounds favour formation of the second-phase inclusions during the

growth process. The Te inclusions in the CdTe-based materials have polyhedral shape. Increased density of such defects is observed at grain and twin boundaries, as it is shown in Fig. 1 and 2 (secondary electron images from a scanning electron microscope). We are going to present influence of different annealing conditions on the inclusions in the crystals and on the resistivity.

Two kinds of procedures were applied to the crystals after growth: 1) - thermal relaxation of the entire ingot at high temperature in vacuum, and 2) - annealing of the samples cut from the ingot in the saturated Cd vapours. We studied a few series of samples (as grown, relaxed only, annealed only, and both relaxed and annealed). The investigations were made by IR transmission microscopy and by measurements of the material resistivity maps (by contactless TDCM method [4]). The results were compared. Par example Fig. 3 and 4 allow us to compare the density and size of Te inclusions in the (Cd,Mn)Te:Cl samples, as-grown and annealed respectively.

The paper will present comparison of the results obtained for the two different materials - (Cd,Mn)Te and (Cd,Mn)(Te,Se). Before subsequent procedures, i.e.- as-grown, these materials contain a lot of native defects (such as cadmium vacancies and tellurium inclusions) typical for this family of compounds, and the resistivity is in the range 10^4-10^5 Ωcm. It has been observed that: 1) Thermal relaxation results in the decrease of size and concentration of the inclusions, more homogenous resistivity, and a few times higher value of the resistivity. 2) Annealing in Cd vapours at proper conditions (time and temperature) results in the increase of the resistivity by about 2-3 orders of magnitude (up to 10^9 Ωcm), and in the further diminishing of the size and concentration of the Te inclusions (Fig. 4).

3. Figures
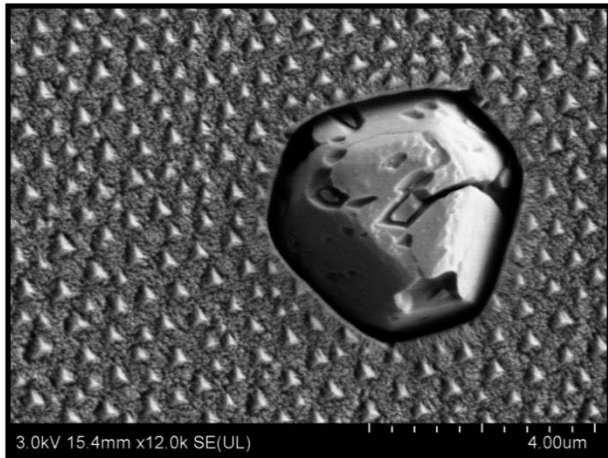
Figure 1 SEM image of Te inclusion in (Cd,Mn)Te crystal [5].
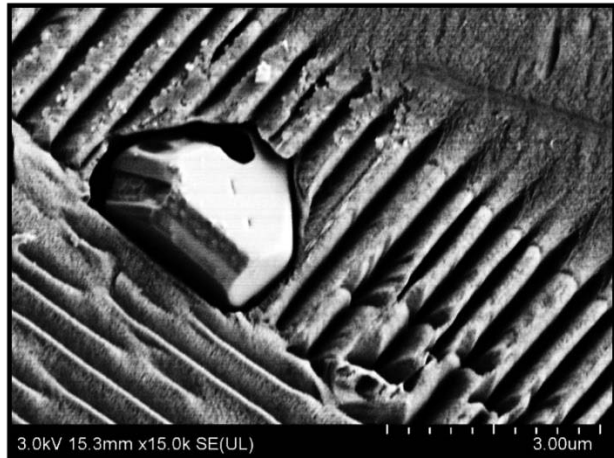
Figure 2 SEM image of Te inclusion at a twin boundary [5].
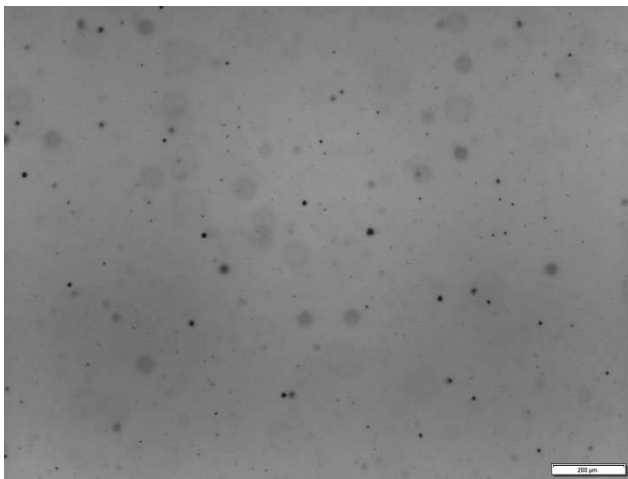
Figure 3 IR image of (Cd,Mn)Te as-grown sample with resistivity above 10^5 Ωcm.

Figure 4 IR image of (Cd,Mn)Te sample after annealing in Cd vapours at uniform temperature. Annealing of the sample results in the increase of resistivity.

4. References

[1] A. Mycielski, A. Burger, M. Sowinska, M. Groza, A. Szadkowski, P. Wojna, B. Witkowska, W. Kaliszek, P. Siffert, *Phys. Stat. Sol. (c)*, vol. **2**, no. 5, (2005), pp. 1578–1585;

[2] T. E. Schlesinger J. E. Toney, H. Yoon, E. Y. Lee, B. A. Brunett, L. Franks, R. B. James, *Mat. Science Eng.* **32**, (2001), pp. 103-189;

[3] H. R. Vydyanath, J. A. Ellsworth, J. B. Parkinson, J. J. Kennedy, B. Dean, C. J. Johnson, G. T. Neugebauer, J. Sepich, P. K. Liao, J. Elect. Materials, vol. 22, no. 8, (1993), pp. 1073-1080;

[4] R. Stibal, J. Windscheif ,W. Jantz; *Semicond. Sci. Technol.*, **6**, (1991), pp. 995-1001;

[5] D. Kochanowska, M. Rasinski, M. Witkowska-Baran, M. Lewandowska, A. Mycielski, Phys. Status Solidi C **11**, No. 9, 1523–1527 (2014) / **DOI** 10.1002/pssc.201300711;

Study on Floating-zone-grown CdMnTe Crystals for Radiation-Detector Applications

Ge Yang[1]*, Genda Gu[1], Aleksey E. Bolotnikov[1], Yonggang Cui[1], Giuseppe S. Camarda[1], Anwar Hossain[1], Utpal N. Roy[1], Nicholas Kivi[1,2], Tiansheng Liu[1], and R. B. James[1]

1. Brookhaven National Laboratory, Upton, NY 11973, USA

2. University of Tennessee, Knoxville, TN 37916, USA

* Corresponding author: Ge Yang, Building 197D, Brookhaven National Laboratory, Upton, NY 11973, USA. Tel: 1-631-344-4341, Email: gyang@bnl.gov

1. INTRODUCTION

CdMnTe (CMT) has recently attracted increasing interest, since it is considered a promising material for fabricating high performance room-temperature X-ray and gamma-ray detectors.[1-5] Compared with CdZnTe (CZT), a current leading material in such applications, CMT offers several distinct advantages that make it a good candidate in this field. First, the segregation coefficient of Mn in CdTe is nearly unity in contrast to 1.35 for Zn in CdTe. This difference accounts for a more uniform distribution of Mn in CdTe, compared to the relatively high variation of Zn concentration in CdZnTe. This would increase the yield of suitable crystals for detectors, and help to reduce the costs of producing large-area detector arrays. Another significant advantage of CMT crystals is their greater tunability of the band-gap due to the large compositional influence of Mn, i.e., adding Mn increases the room-temperature band gap at a rate of 13 meV/[at% Mn] in contrast to 6.7 meV/[at% Zn] after the addition of Zn to CdTe. Most of the crystal growth attempts for CMT have been accomplished with various Bridgman methods. In Bridgman-grown CMT crystals, a common phenomenon is the presence of a high density of Te inclusions. High densities of Te inclusions can entail significant fluctuations in the total collected charge by trapping free charge-carriers generated by incident radiation, thereby strongly degrading the energy resolution of thick detectors. As a result, it is important to explore new growth approaches to improve the crystal quality of CMT. In this work, we used the modified floating zone (MFZ) technique to grow CMT crystals. To our knowledge, this is the first attempt to grow CMT crystals using the floating-zone method. The detailed structural, electrical and optical properties of MFZ-grown CMT crystals were investigated, and they were compared with those grown by Bridgman methods as well. In particular, we demonstrate that the MFZ

technique can be used to produce CMT crystals free of Te inclusions. A large temperature gradient across the growth interface could play a crucial role during the corresponding growth process.

2. RESULTS AND DISCUSSION

Figure 1 (a) shows the morphology of a representative MFZ-grown CMT wafer. The wafer consists of one large-size grain, one small grain starting from the wafer edge, and two tiny grains embedded inside the large grain. It is noteworthy that many twins prevail within the majority of the crystals. For comparison, Figure 1 (b) exhibits the IR transmission image of the same wafer. Clearly one can see that the single crystalline portions of MFZ-grown CMT are totally free of Te inclusions. Furthermore, there are no Te inclusions decorating either grain boundaries or twin boundaries, although both provide energetically-favorable sites for the formation of inclusions. We noted several tiny dark areas exist at the edge of the wafer, which could originate from the excess Te of the starting materials. The absence of Te inclusions in MFZ-grown CMT crystals offers a distinct feature not seen in CMT ingots grown by the Bridgman method. In the latter, it was commonly observed that a high density of Te inclusions is formed in as-grown crystals, especially along grain or twin boundaries. These inclusions can distort the local internal electric field in CMT detectors, entail significant fluctuations in the total charge-collection by trapping free charge-carriers and therefore, seriously deteriorate the performance of radiation detectors. A concave growth interface of CMT material can result in the trapping of Te-rich liquid droplets as a consequence of morphological instability, and therefore, a high density of Te inclusions may be formed during the following cool-down period. This is considered as the main origin of large-size Te inclusions in as-grown CMT and CZT crystals. The shape of the melt/crystal growth interface is closely related to the convection behavior in the melt zone. In our MFZ-growth process, the optical heating by halogen lamps forms a narrow melting zone within the feed rod, where the temperature gradient at the interface between the liquid and the solid is very high, much larger than that of Bridgman growth. In this case, thermo-capillary convection dominates over natural convection of the melt zone, which tends to increase the convexity of the melt/crystal growth interface. In fact, it has been recognized that a convex or flat growth interface offers a unique advantage in terms of producing larger crystals and preventing the

trapping of Te-rich droplets during the growth. The rotation of the feed rod/crystal applied in our crystal growth also helps to promote the shape of the growth interface towards 'flat' in addition to making the heating more uniform.

We measured the low-temperature (4.2 K) photoluminescence spectrum of the MFZ-grown CMT crystal, as illustrated in Figure 2. The spectrum consists of three regions: I: near-band-edge region; II: donor–acceptor pair (DAP) recombination region; and III: defect-related region associated with some impurity-complex energy levels ($D_{complex}$) and extended defect levels. The two peaks at 1.659 eV and 1.645 eV are ascribed to the neutral donor-bound exciton (D^0,X) transition and the neutral acceptor-bound exciton (A^0,X) transition separately. A peak from the donor-acceptor pair (DAP) recombination at 1.596 eV and its phonon replica at 1.575 eV can be clearly distinguished. In the defect-related region III, the feature peak at 1.482 eV originates from the A center, a cation-Cd vacancy complex. Another peak at 1.5562 eV most probably is due to an (eA^0) emission, i.e., a recombination of free electrons on the acceptor. We also observed the so-called Y band at 1.467 eV, which is related to dislocations. The peak at 1.445 eV, on the lower energy shoulder of the Y band, is the corresponding phonon-replica. It should be noted that the intensity of the Y band is much higher than that of the exciton peaks, indicating that the crystalline quality is deteriorated by the high stress field in as-grown CMT. A long-term in-situ or post-growth thermal annealing phase will probably help to release such type of stress to improve crystalline quality.

ACKNOWLEDGEMENTS

REFERENCES

(1) A. Mycielski, A. Burger, M. Sowinska, M. Groza, A. Szadkowski, P. Wojnar, B. Witkowska, W. Kaliszek, and P. Siffert, Phys. Status Solidi (c), **2005**, 2, 1578–1585.

(2) Y. Cui, A. E. Bolotnikov, A. Hossain, G. S. Camarda, A. Mycielski, G. Yang, D. Kochanowska, M. Witkowska-Baran, and R. B. James, Proc. of SPIE, **2008**, 7079, 70790N-1-70790N-1.

(3) G. Yang, A. E. Bolotnikov, L. Li, G.S. Camarda, Y. Cui, A. Hossain, K. Kim, V. Carcelen, R. Gul and R. B. James, Journal of Electronic Materials, **2010**, 39, 1053-1057.

(4) A. Hossain, Y. Cui, A. E. Bolotnikov, G. S. Camarda, G. Yang, D. Kochanowska, M. Witkowska-Baran, A. Mycielski, and R. B. James, Journal of Electronic Materials, **2009**, 38, 1593-1599.

(5) J. Zhang, L. Wang, J. Min, J. Huang, X. Liang, K. Tang, P. Shen, M. Shen, W. Liang, N. Huang and Y. Xia, Phys. Status Solidi C, **2014**, 11, 1–4.

(a)   (b)
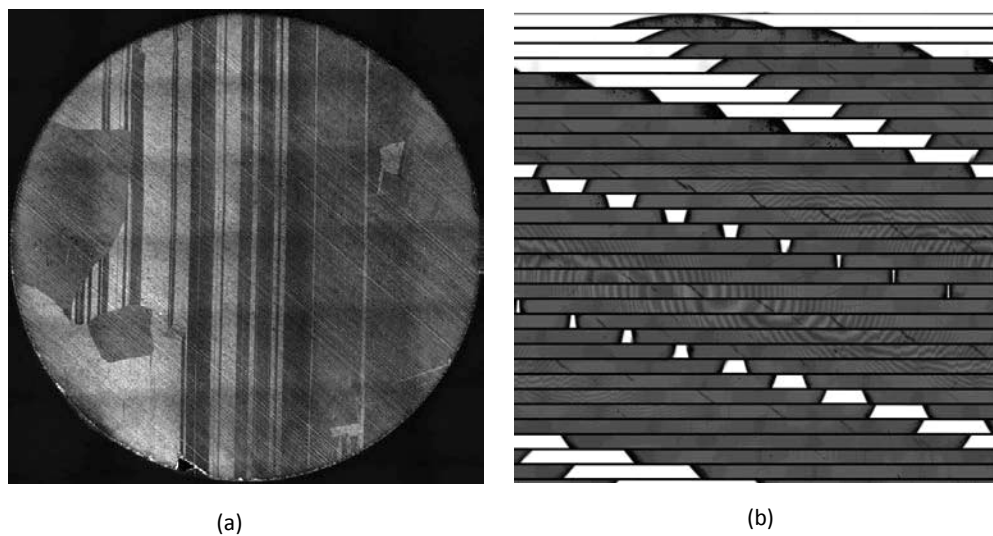
Figure 1 Morphology of a representative MFZ-grown CMT wafer (The diameter of the wafer is 19 mm). (a) Polarized light microscopy image; (b) Infrared (IR) transmission image.
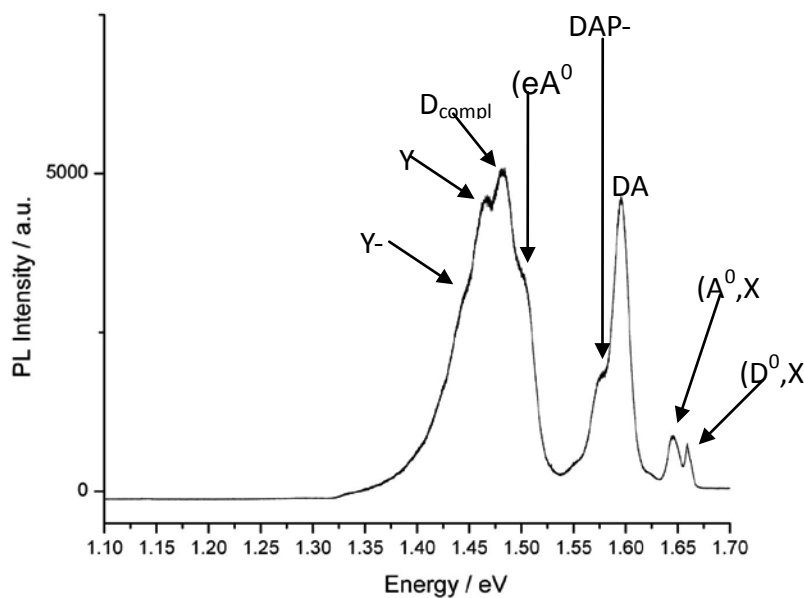

Figure 2 Representative photoluminescence (PL) spectrum of a MFZ-grown CMT crystal. The PL spectrum was measured at 4.2 K.

Recent developments of CdZnTe in JX Nippon Mining & Metals

R. Hirano[1], A. Noda[2], K. Murakami[2], H. Kurita[2]

JX Nippon Mining & Metals Corporation
Compound Semiconductor Materials Department
[1]*6-3, Otemachi 2-chome, Chiyoda-ku, Tokyo 100-8164, Japan*
[2]*187-4, Usuba, Hanakawa, Kitaibaraki, Ibaraki 319-15, Japan*

Without compromising any crystal properties, we are now producing the 6 inch CdZnTe ingots routinely. The crystal properties of the 6 inch CdZnTe is identical to that of the 5 inch crystal. Thanks to the development of the quality CdZnTe ingots, high performance astronomical immersion gratings have been developed by one of the Japanese science teams [1-4]. To expand our scope, we have started the CZT production for the radiation detectors. We will show some spectra using the Pt-Pt or Pt-In contacts.

1. Introduction

CdZnTe crystals have been mainly used for the IR detectors. The IR detector market needs large size single crystal substrates with the high quality properties. In order to meet their needs, we have developed the 6 inch single crystals. On the other hand, CdZnTe crystals are also used for the radiation detectors. Unlike the IR market, the larger size substrates, are not required, however, new applications such as X-ray FPD, X-ray CT would need the larger size substrates than ever with the higher quality of defect density. The CdZnTe crystals are also used for the other applications such as immersion gratings, Electro-optical modulator module for CO_2 laser and solar cells. In the present paper, we report on our recent developments of CdZnTe

2. 6 inch CdZnTe growth

6 inch CdZnTe crystals were grown by VGF method with a Cd reservoir in the lower part of the VGF furnace for controlling the Cd pressure, thereby minimizing stoichiometric defects (precipitates). Figure 1 shows the typical example of the 6 inch CdZnTe after grinding. The maximum sized substrates with 95mm x 95mm were obtained as shown in Fig. 2. Some important crystal properties such as Zn distributions, precipitates, EPD, FWHM and carrier concentrations were investigated and no remarkable differences between the 5 inch and the 6 inch crystals were found. Fig. 3 shows the typical example of the Zn distributions of the 6 inch CdZnTe.

3. CdZnTe for the radiation detectors

4.5~5 inch CdZnTe crystals were grown by VGF method to get the high resistivity

materials for the radiation detector applications with In doping. Pt –Pt contacts were

Fig. 1. 6 inch CdZnTe
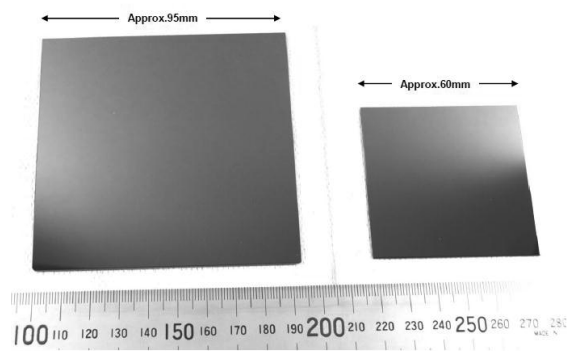
Fig. 2. 95mm x 95mm Single CdZnTe wafer

used for the spectra evaluations. In doped CdTe and Cl doped CdTe crystals were also grown to check the difference of radiation properties between the CdZnTe crystals and the CdTe crystals. These crystals were grown under the Cd reservoir controlling and we have confirmed that the high resistivity CdZnTe crystals with the smaller precipitates can be grown by optimizing the several steps annealing methods. Figure 4 shows the typical examples of the spectra with the Pt-Pt contacts. The present results suggest the uniformity of the spectra and the PC channels are very uniform. We also confirmed that no polarization was seen for the In-Pt contacted In doped CdTe and the In doped CdZnTe. The spectra of In doped CdTe were improved by using the In-Pt contact.

Zn Concentration mapping

5.0	5.1	5.0	5.0	5.0	5.1	5.1	5.0	4.9
5.0	5.0	5.0	5.0	5.0	5.1	5.1	5.0	4.9
5.0	5.0	5.0	4.9	4.9	5.1	5.0	5.0	4.9
5.0	5.0	4.9	4.9	4.9	5.0	5.0	5.0	4.9
5.0	5.0	4.9	4.9	4.9	5.0	5.0	5.0	4.9
5.2	5.2	5.1	5.1	5.1	5.1	5.1	5.1	5.0
5.2	5.2	5.1	5.0	5.1	5.1	5.1	5.1	5.0
5.1	5.1	5.1	5.1	5.0	5.1	5.0	5.0	4.9
5.0	5.1	5.1	5.0	5.0	5.0	5.0	4.9	4.8

(%)

approx.10x10mm2
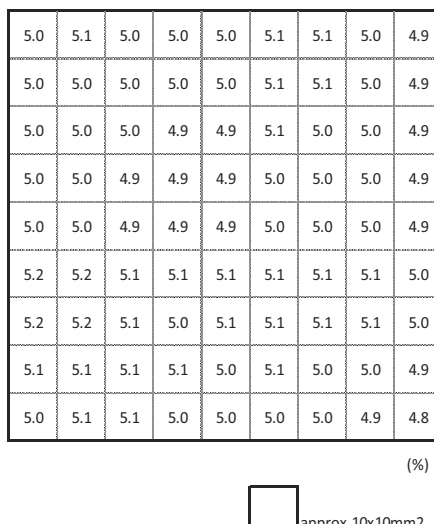
**Fig. 3. Zn concentration distribution of
95mm x 95mm wafer taken from a 6 inch ingot.**
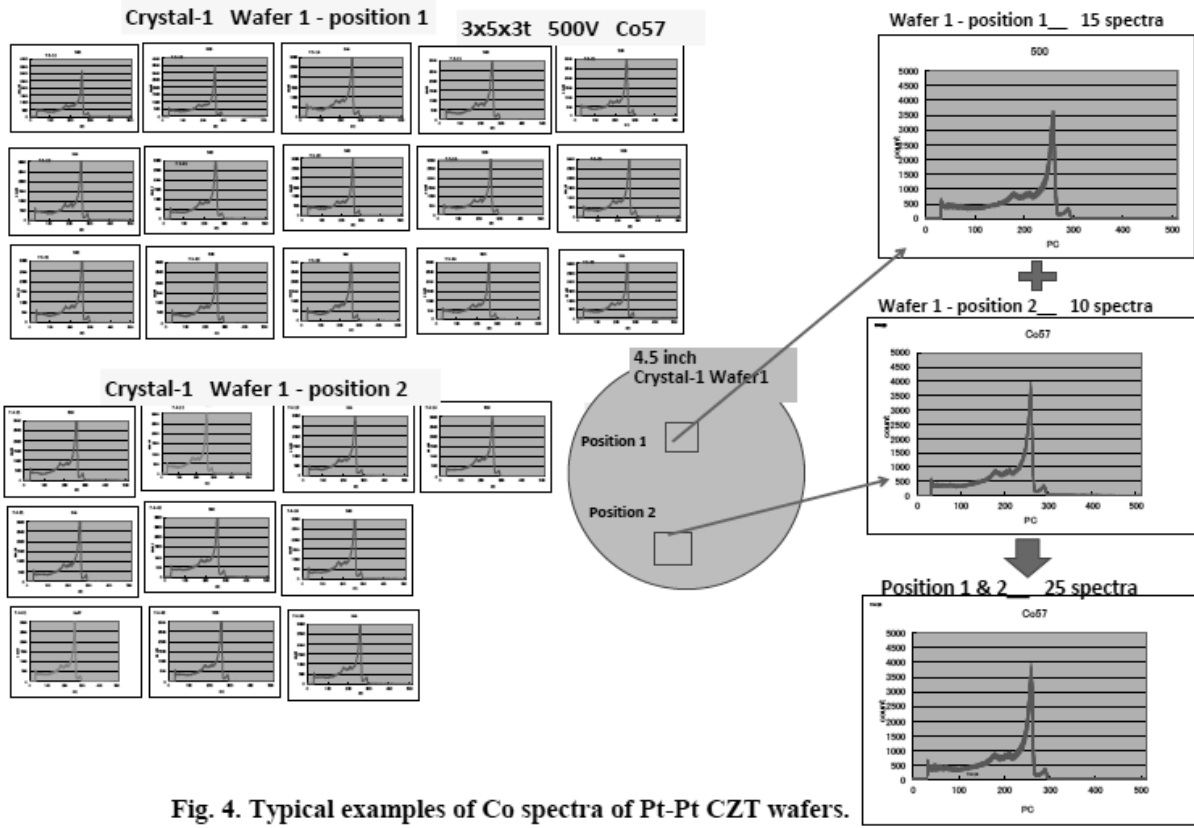
Fig. 4. Typical examples of Co spectra of Pt-Pt CZT wafers. These spectra taken from the different position

4. Other applications

4-1. Immersion gratings

We have grown the 5 inch CdZnTe crystals for the immersion grating for high-resolution spectroscopy in the mid-infrared (MIR). Sukegawa et al. [2] and Ikeda et.al [3] have developed the CdZnTe immersion grating for space-borne application. This application requires large sized CdZnTe ingots with high quality crystal properties; especially the transmittance is extremely important [1]. As we previously confirmed that higher resistivity materials have better IR transmittance, we prepared the 5 inch CdZnTe with higher resistivity for their applications. Sarugaku et al. [4] have measured the IR transmittance accurately.

4-2. Solar cells

We sometimes grow the 4.5-5 inch CdTe crystals for the solar cell studies. J. N. Duenow et al. have shown [5] the studies of Single-crystal CdTe solar cells with Voc greater than 900mV. In order to study the CdTe solar cell properties, many of our customers are now using the Na doped CdTe. As shown by Deunow et.al, the Na concentration measured by ICP is much higher than that of the carrier concentration by Hall measurements. Previously, we had found that the Na concentration can be reduced by stopping the crystal growth at the half solidified position. We think that it would be related to the redistribution speed of Na in CdZnTe.

We are also studying the correlation between the polycrystalline properties and the solar cells properties with Kisarazu National College of Technology [6].

5. Conclusion

This paper presents our recent developments of CdZnTe and CdTe crystals for the various applications, such as IR detectors, Radiation detectors, Immersion gratings and the Solar cells. The recent studies have shown that the crystal quality, especially the uniformity of crystal properties in such large size ingots will be very important.

References)
[1]. T. Sukegawa, S. Sugiyama, T. Kitamura, Y. Okura and M. Koyama, Proc. of SPIE Vol. 8450 84502V-2

[2]. Y. Sarugaku, Y. Ikeda, N. Kobayashi, T. Sukegawa, S. Sugiyama, K. Enya, H. Kataza*a*, H. Matsuhara, T. Nakagawa, H. Kawakita, S. Kondo, Y. Hirahara, C.Yasui, Proc. of SPIE Vol. 8442 844257-1

[3]. Ikeda et al. in prep.

[4]. Sarugaku et al. in prep.

[5]. J. N. Deunow, J. M. Burst, D. S. Albin, D. Kuciauskas, S. W. Johnston, R. C. Reedy and W. K. Metzger,
Appl. Phys. Lett. 105, 053903 (2014)

[6]. T. Okamoto, S. Ikeda, S. Nagatsuka, R. Hayashi, K. Yoshino, Y. Kanda, A. Noda and R. Hirano, Japanese Journal of Applied Physics 51 (2012) 10NC12

Dynamic curvature and stress studies for
MBE CdTe on Si and GaAs substrates

R. N. Jacobs,[1] C. Nozaki,[1] M. Jaime Vasquez,[1] C.M. Lennon,[2] L.A. Almeida,[1] J. Arias,[3] J. Pellegrino,[1] C. Taylor,[4] and B. Wissman.[4]

1- U. S. Army RDECOM, CERDEC Night Vision and Electronic Sensors Directorate
2- Fulcrum Corporation.
3- CACI Corporation.
4- k-Space Associates, Inc.

ABSTRACT

Infrared focal plane arrays (IRFPA) based on HgCdTe semiconductor alloys have been shown to be ideal for tactical and strategic applications. High density (>1M pixel), high operability HgCdTe detectors on large area, low-cost composite substrates such as CdTe buffered Si or GaAs,[1-3] are envisioned for next-generation (IRFPAs). Thermal expansion mismatch is among various material parameters that govern the structural properties of the final detector layer. It was previously shown that the thermal expansion mismatch plays the dominant role in the residual stress characteristics of the heteroepitaxial structure.[1] The wafer curvature (bowing) that can result from this stress, may cause problems for subsequent processing. This includes pixel-disregistery during the mating of large-area HgCdTe/CdTe/Si detector wafers to large area read-out wafers.

In this work, we demonstrate the monitoring of dynamic curvature and stress during molecular beam epitaxy (MBE), of CdTe on Si and GaAs substrates. The effect of temperature changes on wafer curvature throughout a growth sequence is documented using a multi-optical sensor tool developed by K-Space Associates, Inc. Figure 1, shows dynamic curvature data during the periodic annealing of CdTe/Si in a typical growth run. Both obvious and subtle changes in the curvature profile can be understood through the framework of lattice and thermal stress. The oscillations are the result of compressive stress (negative curvature), and tensile stress (positive curvature) exerted on the film during heating and cooling, respectively. The overall decreasing curvature is interpreted to be the result of residual lattice mismatch induced stress.   This interpretation is supported by the gradual compressive stress observed for a separate CdTe/Si growth without periodic annealing (dashed line in figure 1). This monitoring technique makes

possible, the study of growth sequences which employ annealing schemes and/or interlayers to influence the final residual stress state of the heteroepitaxial structures.
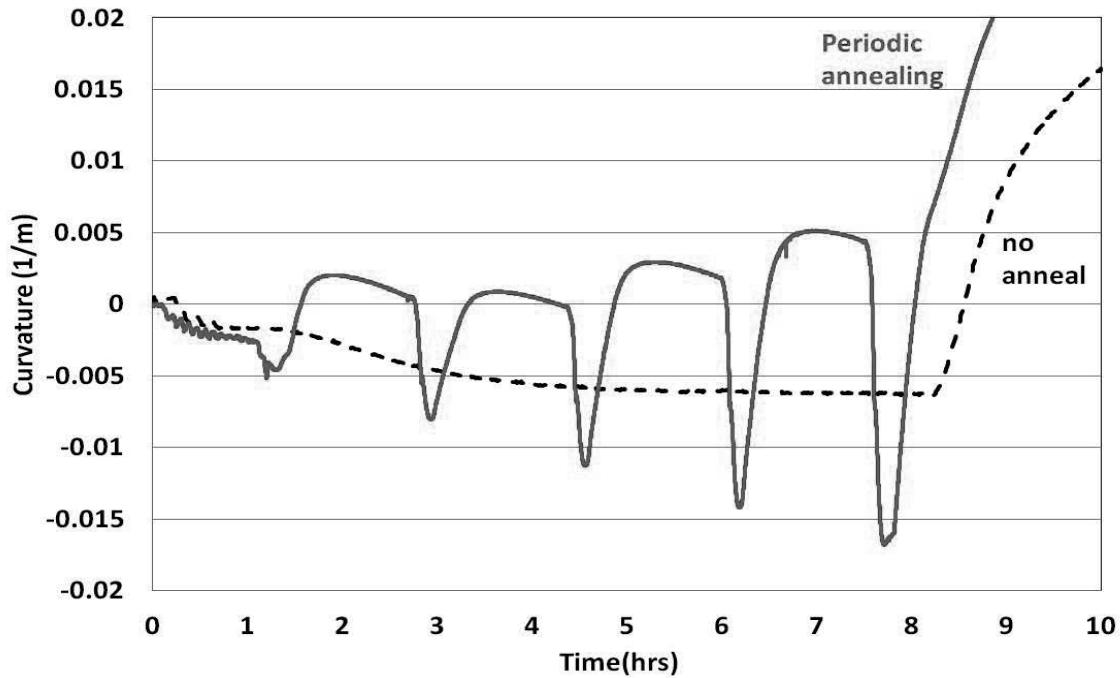
Figure 1: Curvature profiles observed for typical MBE CdTe/Si growth runs with periodic annealing (solid line), and without periodic annealing (dashed line).

1. R.N. Jacobs, J. Markunas, J. Pellegrino, L.A. Almeida, M. Groenert, M. Jaime-Vasquez, N. Mahadik, C. Andrews, S.B. Qadri, *J. Cryst. Growth.* **310**, 2960 (2008).
2. C.M. Lennon, L.A. Almeida, R.N. Jacobs, J.K. Markunas, P.J. Smith, J. Arias, A.E Brown, J. Pellegrino. *J. Electron. Mater.,* **41**, 2965 (2012).
3. L.A. Almeida, L. Hirsch, M. Martinka, P.R. Boyd, and J.H. Dinan, *J. Electron. Mater.* **30**, 608 (2001).

ANALYSIS OF DEFECT SIZE IN HgCdTe GROWN BY MBE

K. R. Olsson*, M. F. Vilela, M. Reddy, and D. D. Lofgreen

Raytheon Vision Systems, 75 Coromar Drive, B2/8, Goleta, CA 93117.

*kurt_olsson@raytheon.com

INTRODUCTION

One of the primary performance limiters in HgCdTe-based infrared detectors is the formation of defects during the growth process. In HgCdTe layers grown by molecular beam epitaxy (MBE), the majority of material defects are a result of imperfections in the substrate surface or deviations from optimum growth conditions. Understanding the formation mechanism of these defects is crucial to reducing their density and increasing device operability.

The preferred method for analysis of HgCdTe defects is microscopy; surface images via an optical microscope or scanning electron microscope (SEM) show the shape of a defect, and SEM cross-sectional images using focused ion beam (FIB) milling can reveal the origin of the defect in the film or at the substrate.[1] Unfortunately, these methods are time consuming and can be destructive to the grown layers, a major drawback in a production environment. Full wafer defect mapping can quickly provide the precise location and size (expressed as diameter) of all defects that can be resolved with the microscope. By analyzing statistical trends in the defect sizes found on a wafer, defect formation mechanisms can be identified without using microscopy.

EXPERIMENTAL RESULTS

At Raytheon Vision Systems (RVS), full wafer defect mapping is done with the NSX 105 defect inspection tool from August Technology. A custom software tool is then used to create

wafer maps and analyze defect counts by binning the defects by size (Figure 1).[2] The defect density histogram can then be examined to determine which size defects are most common on the surface. Defects are customarily identified as either macrovoids, defects larger than 10µm in diameter and a result of Hg-deficient growth conditions, or microvoids, defects smaller than 10µm in diameter and a result of Hg-rich growth conditions or substrate precipitates. It is hypothesized that under optimum growth conditions, the large majority of defects will be microvoids which initiate at the substrate and increase in size uniformly during material growth, leading to a large population of defects of the same size. To test this hypothesis, a subset of wafers grown under near-optimum growth conditions on a 5-inch Riber Epineat (System A) and a 10-inch VG Semicon V100 (System B) were selected for study. These wafers met two criteria: they met the qualifying defect specifications, and showed a Gaussian defect distribution with a strong peak, reflecting a large number of uniformly sized defects. A strong correlation between layer thickness and average defect size is shown in Figure 2, demonstrating that these defects are initiated at the substrate.

CONCLUSION

With a baseline for growth under optimal conditions established, this paper will examine several wafers with wafer maps and defect density histograms that do not follow a Gaussian defect distribution. Defect patterns will be studied both with the defect analysis tool and with SEM to confirm that both methods can identify the formation mechanism of the defect. This method of defect analysis is a fast and powerful means of determining the source of defects and the appropriate growth decision to minimize them.
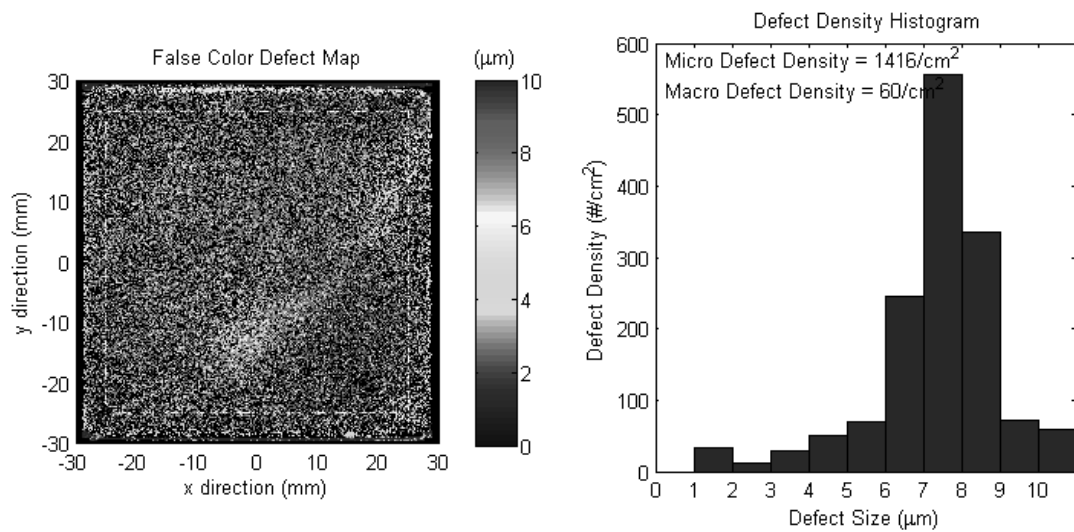
Figure 1. (a) Map of defect location and size and (b) defect histogram sorting defects by diameter
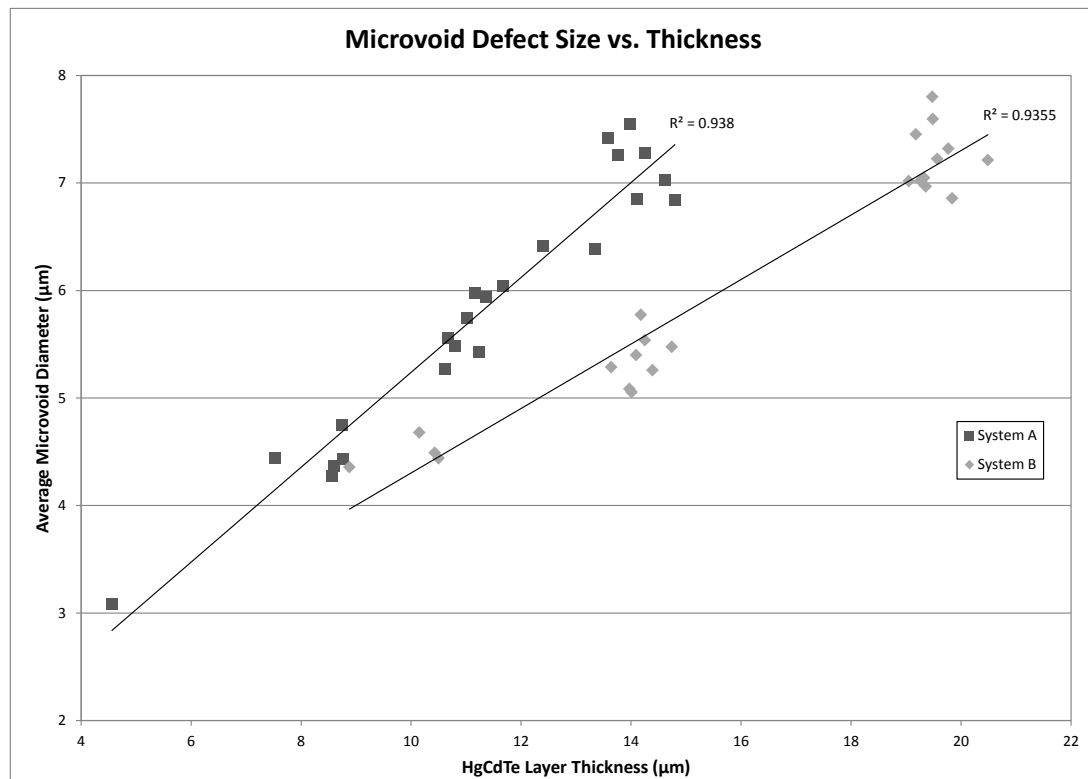
Figure 2. Microvoid defect size as a function of layer thickness for wafers grown on Systems A and B.

REFERENCES

[1] M. Reddy, J. Wilde, J.M. Peterson, D.D. Lofgreen, S.M. Johnson, *J. Electron. Mater.* 41, 2957 (2012).

[2] D.D. Lofgreen, M.F. Vilela, E.P. Smith, M.D. Newton, D. Beard, S.M. Johnson, *J. Electron. Mater.* 36, 958 (2007).

CdZnTe Substrate Preparation for MBE HgCdTe Deposition

J. D. Benson, L. O. Bubulac, P. J. Smith, R. N. Jacobs, J. K. Markunas, M. Jaime-Vasquez, L. A. Almeida, A. Stoltz, P. S. Wijewarnasuriya*, B. VanMil*, G. Brill*, Y. Chen*,

U. S. Army RDECOM, CERDEC Night Vision and Electronic Sensors Directorate

*U. S. Army Research Laboratory

The highest sensitivity, lowest dark current HgCdTe infrared focal plane arrays (IRFPAs) are currently produced on CdZnTe substrates. A yield limiting factor in MBE HgCdTe/CdZnTe detector fabrication is the presence of macro-defects.[1] Two categories of HgCdTe epilayer macro-defects have recently been associated with defects originating from the (112)B CdZnTe substrate surface.[2] Cross-sectional transmission electron microscopy (TEM) analysis traced micro-void defects to pits on the surface of the (112)B CdZnTe substrate.[3] Additional cross-sectional TEM analysis traced morphological defects to raised protrusions on the surface of the (112)B CdZnTe substrate.[2] From both TEM analyses, the defective area was confined to a small region surrounding the CdZnTe pit/protrusion and the HgCdTe epilayer micro-void/morphological defect.

An MBE preparation/clean-up etch of the CdZnTe substrate is required before epitaxial deposition of HgCdTe. The MBE preparation etch is used to remove ~ 2-10 µm of CdZnTe from the surface. The MBE preparation etch reduces the native oxide and removes residual organic contamination.[4-6] The MBE preparation etch is also required to remove surface and near-surface damage induced to the CdZnTe crystal during wafer production. The standard MBE preparation/clean-up etch technique is: solvent soak, Br: methanol etch, solvent soak, N_2 blow dry, and mounting to a wafer holder.[4] After the MBE preparation etch, pits and raised protrusions are observed on the CdZnTe (112)B

surface.[7] The combined density of pits/bumps is $\sim 3 \times 10^3$ cm^{-2}. Pit/bump formation has been associated with MBE preparation etching of Te precipitate 'strings' in the near surface region of the (112)B CdZnTe substrate as shown in figures 1-3.[7]

In the current state-of-the-art HgCdTe detector there is no buffer layer between the HgCdTe epilayer and the CdZnTe substrate. This makes the starting CdZnTe as-received surface and substrate preparation extremely critical for high performance detector fabrication. The objective of this research is two-fold: 1) analyze the initial 'out of the box' wafers for surface contamination and defects, 2) mitigate the formation of pits/protrusions in the CdZnTe substrate by investigating/altering the MBE preparation etch chemistry. The minimization of pits/protrusions and the impurity contamination surrounding these defects in CdZnTe substrates should lead to a reduction in mico-voids and morphological defects in MBE HgCdTe/CdZnTe, which should in turn increase FPA operability.
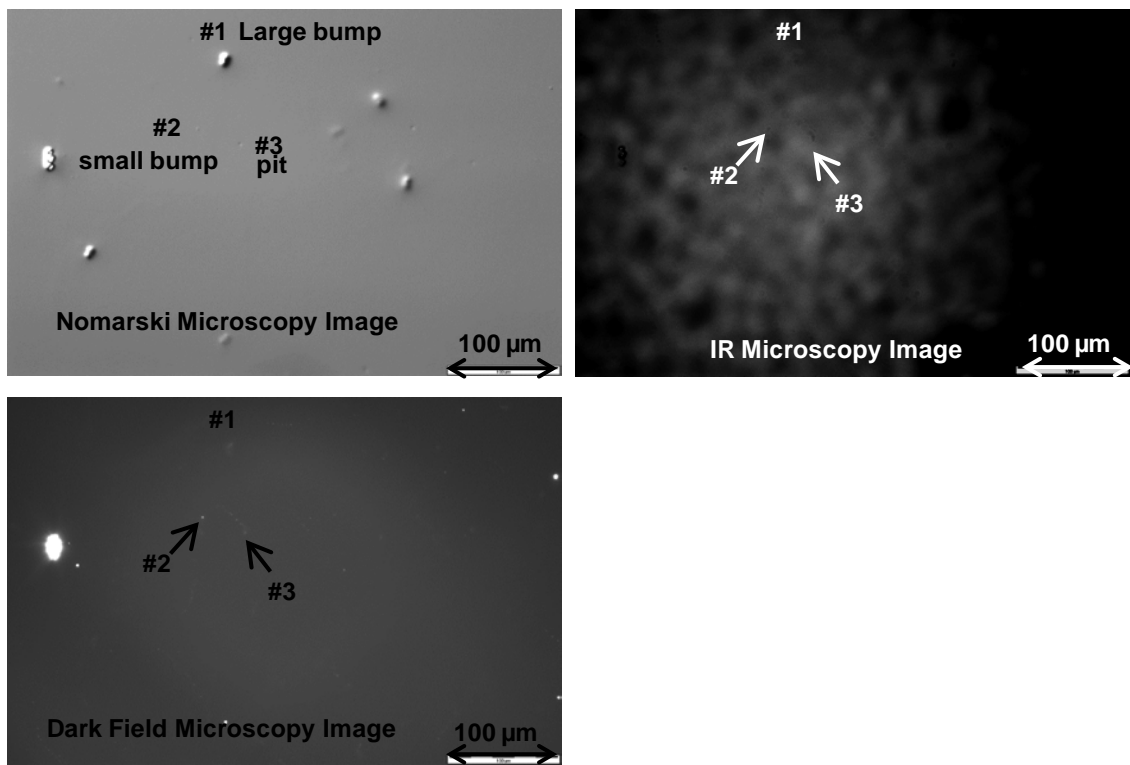
Figure 1. Distinctive large bump cluster near the center of a 2×3 cm CdZnTe wafer after MBE preparation etch. Nomarski phase contrast, near IR, and dark field microscopy images of the distinctive bump cluster showing Te precipitate 'strings' associated with pits/bumps.
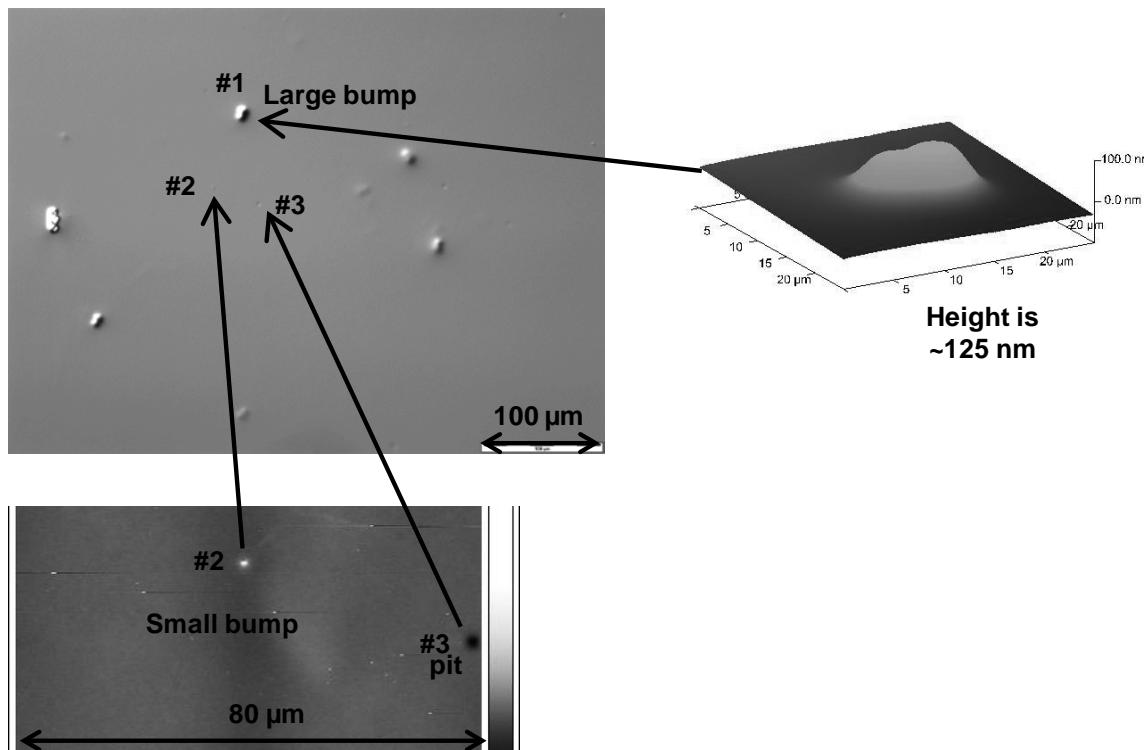
Figure 2. Nomarski phase contrast of the distinctive bump cluster and AFM images of some of the bumps and pits.
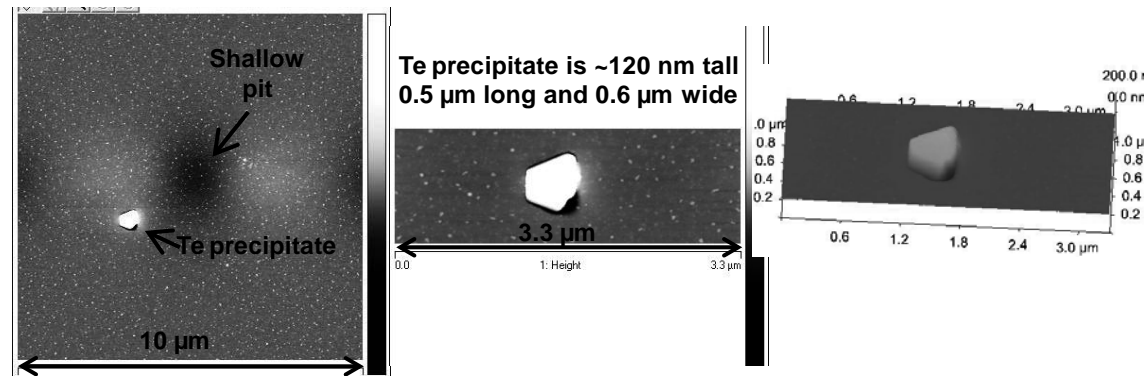
Figure 3. High resolution AFM images of the pit and a Te precipitate exposed during the MBE preparation etching.

References

1). M. Reddy, J. Wilde, J. M. Peterson, D. D. Lofgreen, and S. M. Johnson, *J. Electron. Mater.* **41**, 2957 (2013).

2). M. Reddy, W. A. Radford, D. D. Lofgreen, K. R. Olsson, J. M. Peterson, and S. M. Johnson, *submitted to J. Electron. Mater. (2014).*

3). M. Reddy, D. D. Lofgreen, K. A. Jones, J. M. Peterson, W. A. Radford, J. D. Benson, and S. M. Johnson, *J. Electron. Mater. **42**, 3114 (2013).*

4.) J. D. Benson, A. B. Cornfeld, M. Martinka, K. M. Singley, Z. Derzko, P. J. Shorten, J. H. Dinan, P. R. Boyd, F. C. Wolfgram, B. H. Johs, P. He, and J. A. Wollam, *J. Electron. Mater. **25**, 1406 (1996).*

5.) J. N. Johnson, L. A. Almeida, M. Martinka, J. D. Benson, and J. H. Dinan, *J. Electron. Mater. **28**, 817 (1999).*

6.) P. Moravec, V. G. Ivanits'ka, J. Franc, Z. F. Tomashik, V. M. Tomashik, K. Masek, P. I. Feychuk, L. P. Shcherbak, P. Hoschl, R. Grill, and J. Walter, *J. Electron. Mater. **38**, 1645 (2009).*

7). J. D. Benson, L. O. Bubulac, P. J. Smith, R. N. Jacobs, J. K. Markunas, M. Jaime-Vasquez, L. A. Almeida, A. Stoltz, P. S. Wijewarnasuriya, G. Brill, Y. Chen, J. Peterson, M. Reddy, M. F. Vilela, S. M. Johnson, D. D. Lofgreen, A. Yulius, G. Bostrup, M. Carmody, D. Lee, and S. Couture, *submitted to J. Electron. Mater. (2014).*

X-ray Topography Studies of MBE-HgCdTe Layers on bulk-grown CdZnTe and MBE-CdTe on Si Substrates

Syed B. Qadri[3] ,Priyanthi Amarasinghe[1,3]and Priyalal S. Wijewarnasuriya[2],

[1] National Research Council Postdoc, Washington, DC 20375
[2] U.S. Army Research Laboratory, Adelphi, MD 20783
– Contact – priyalal.s.wijewarnasuriya.civ@mail.mil
[3] U.S. Naval Research Laboratory, Washington, DC 20375

Abstract

Large-format, low-cost, reliable and high-performance IR focal plane arrays (IRFPA) are essential for the Army's 3rd generation IR imaging technology. Current state-of-the-art IRFPAs are fabricated using HgCdTe. Bulk-grown $Cd_{0.96}Zn_{\sim0.04}Te$ (CZT) substrates are the natural choice for HgCdTe epitaxy, since CZT is lattice matched to the LW-HgCdTe. However, the lack of large-area CZT substrates, their high production costs, and more importantly, the difference in thermal expansion coefficients between CZT substrates and Si readout integrated circuits (ROIC) are some of the inherent drawbacks of CZT substrates for 3rd generation applications. Developments in molecular beam epitaxy (MBE) chalcogenide buffer layer growth technology on Si substrates have opened up new HgCdTe research and have offered a new dimension to HgCdTe-based IR technology. Si substrates provide advantages in terms of their relatively large area (3- to 8-inch diameter is easily obtained) compared to CZT substrate materials, durability during processing, and reliability during thermal cycling.

In this paper, x-ray topography and rocking-curve of full-width at half-maximum (FWHM) data will be presented for two different MBE grown HgCdTe epilayers that were grown on high-quality bulk CdZnTe (211) and CdTe/Si (211) substrates. High resolution x-ray diffraction (HRXRD) rocking curves were measured on both HgCdTe and its substrates using a Rigaku high-resolution diffractometer with an 18-kW rotating-anode Cu source. A monochromator consists of two Ge(110) channel cut crystals is used to collimate only Cu Kα_1 x-rays. X-ray rocking curves were measured for (422) and (311) reflections and the lattice parameters were determined from $2\theta/\omega$ scans. HgCdTe on ZnCdTe substrate showed significantly less FWHM values compared to HgCdTe grown on CdTe/Si substrate. The FWHM values of HgCdTe (422) for ZnCdTe (211) and CdTe(211)/Si (211) substrates were determined to be 33 and 189 arc-secs, respectively.

X-ray topographic images were also taken by using a double-crystal topography setup using Cu Kα_1 radiation. In this system, the distance between the source and the sample was kept at roughly 1 m for allowing high-resolution measurements with minimal vertical angular divergence. The slit on the source side of the setup was set to an optimum size for further cutting down of vertical angular divergence. The monochromator consists of an asymmetrically cut Si(111) crystal. The samples are mounted on a manually adjustable four-

circle goniometer. During topographic imaging X-rays diffracted from the sample are collected by high-resolution film held in a film cassette on the detector side. Each sample was exposed to the X-ray radiation for more than 5 hours with the source set at 30 kV and 120 mA.

Figure 1(a) shows the x-ray topographs of HgCdTe on CdZnTe substrate taken from (211) reflection. Cross-hatch patterns were observed in three directions possibly due to growth conditions characterized by excessive Hg flux (Martinka, et al., 2001). X-ray topograph of HgCdTe on CdTe substrate taken from (211) reflection is shown in Figure 1(b). In this topograph cross-hatch patterns were observed only in two directions. The out-of-plane lattice constants of HgCdTe on CdZnTe and CdTe/Si substrates were calculated as 6.4669 Å and 6.4686 Å, respectively.
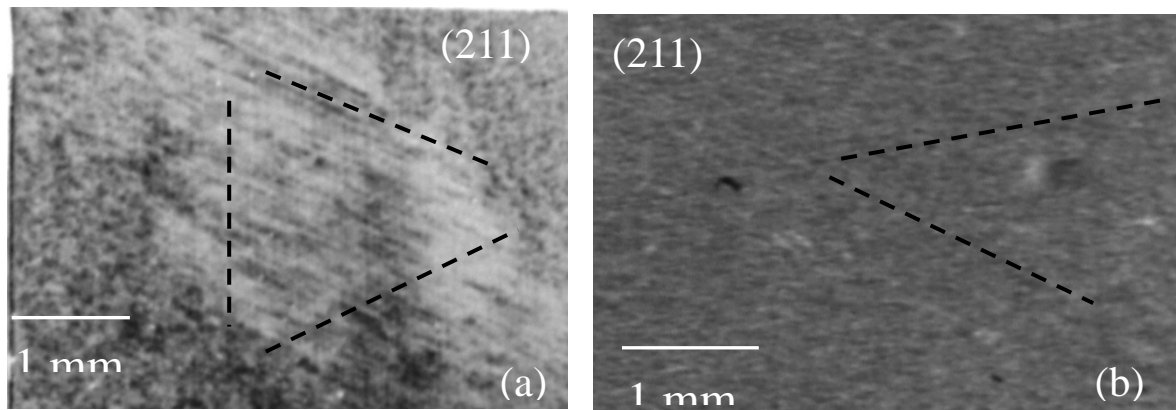

Figure 1. X-ray topographs of HgCdTe on CdZnTe (a) and CdTe (b) substrates taken from (211) reflection

Reference

Martinka, L.A., Almeida, J.D. Benson, J.D. and Dinan, J.H. (2001) J. Electronic Materials, 30, 6, 632-636.

State of the Art HgCdTe at Raytheon Vision Systems

C. Fulk, W. Radford, D. Buell, J. Bangs, K. Rybnicek

Raytheon Vision Systems, 75 Coromar Drive, Goleta, CA

HgCdTe continues to be the first choice for high performance infrared imaging and sensing. We examine and compare a range of detectors in a variety of formats, fabricated at RVS over the past 14 years. This includes single and dual color detector arrays with HgCdTe materials grown by liquid phase epitaxy (LPE) on CdZnTe and molecular beam epitaxy (MBE)on both silicon and CdZnTe substrates.

This study analyzed more than 165,000 current-voltage measurements of dark current densities from Test Structure Assemblies (TSAs) included on every detector wafer fabricated at RVS. Data spans 25 orders of magnitude for cutoff wavelengths from 1.7 µm to 8 µm and operating temperatures from 40 K to 300 K. A basis is derived for a simple manufacturing trend model to compare each technology over a wide range of cutoffs and temperatures. This model uses a function similar to W. Tennant's Rule'07 but includes a generation recombination (GR) term for diodes which are not diffusion limited. Dark current densities below the test set limit are extrapolated assuming GR limited performance. The model assumptions are tested using SCA median dark current density values at the same inverse cutoff-temperature products. This extends the model predictive values ~10-15 orders of magnitude below the test set limit.

The large data set allows for probabilistic determination of array manufacturability and prediction of yield given a set of performance and operating requirements. SCA details such as dark current, QE, and noise distributions, are also illustrated in selected cases to further highlight each technology's advantages and disadvantages.
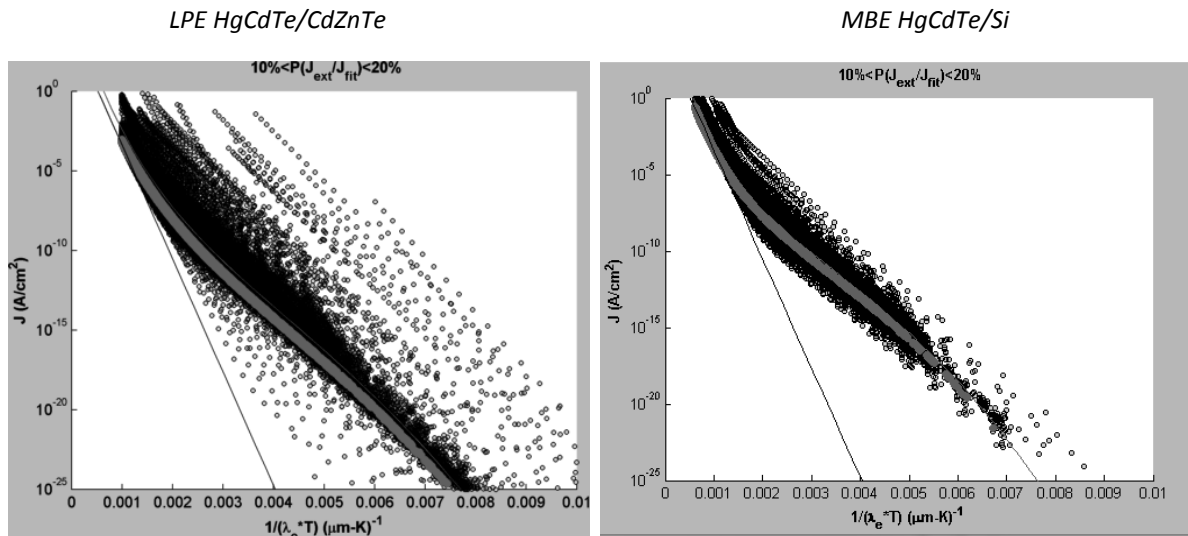
Figure 1: ~165000 dark current density measurements are taken versus temperature to determine dark current density distribution as a function of the inverse temperature-cutoff product. LPE HgCdTe/CdZnTe on the left, MBE HgCdTe/Si on the right.

Sub-wavelength photonic structure to add spectral capabilities to MWIR and LWIR HgCdTe photodiode.

F. Boulard, O. Gravrand, D. Fowler, G. Badano, P. Ballet, M. Duperron, S. Boutami, and R. Espiau de Lamaestre
*tel : +33 4 38 78 22 70, fax: +33 4 38 78 51 67, e-mail : francois.boulard@cea.fr
Univ. Grenoble Alpes, F-38000 Grenoble, France
CEA, LETI, Minatec Campus, F-38054 Grenoble, France

Key words: HgCdTe, MWIR, LWIR, photonic structure, IRFPA

In this paper, we present simulation and experimental results on design and integration of sub-wavelength photonic structure to add spectral functionalities to MWIR and LWIR HgCdTe photodiode. The relationship between metallic grating's design and optical excited mode is illustrated by numerical simulations. The agreement with spectral response and dispersion relation measurement on test photodiode array is discussed. Finally, first results on small format MWIR IRFPA are presented with operability as high as 99.7%.
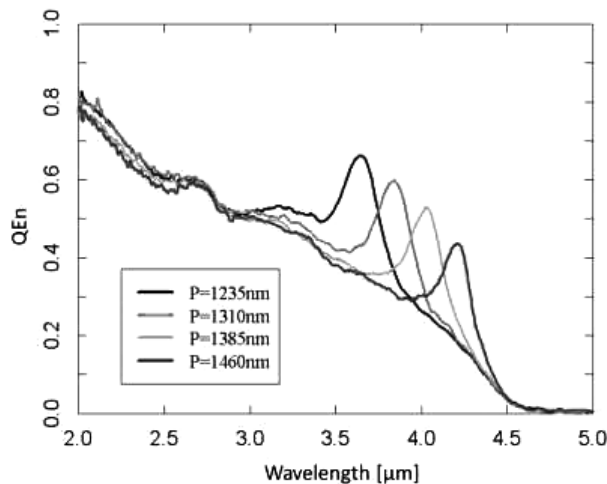
Figure 1 : Normalized spectral response of MWIR HgCdTe photodiode test array

Comparison of HgCdTe and InAsSb Photon-Trapping Structures for Broadband Infrared Detection

J. Schuster and E. Bellotti

ECE Department, Boston University, 8 Saint Mary's Street, Boston, MA 02215
Contact information: email **js382@bu.edu**

HgCdTe and InAsSb focal plane arrays are normally backside illuminated where the incident light is absorbed through the transparent substrate on which the detector array is grown. Such conventional detectors suffer from significant reflection losses at the air/semiconductor interfaces. Consequently, an anti-reflection (AR) coating is incorporated to reduce these losses. Unfortunately, it is very difficult to engineer an AR coating that works effectively over a wide spectral range, that is one that offers nearly zero reflectance and consequently 100% external QE, assuming unity internal QE. Additionally, an AR coating can introduce stress into a detector limiting its interoperability or lifespan. An alternate approach is to instead remove the substrate and etch a photon-tapping (PT) structure directly into the detector absorber layer (AL). When properly engineered, the PT structure will significantly reduce reflection losses, negating the need for an AR coating [1, 2]. Furthermore, by removing device volume, the detector dark current is potentially lowered, allowing higher operating temperatures to be achieved. However, this technique exposes the narrow gap AL mandating that the surface be properly passivated to reduce surface recombination current and maintain high device performance.

In this paper we will perform a detailed comparison of various PT structures, including pillars, pyramids and holes based on two separate detector architectures: HgCdTe *P*-on-*n* photodiodes [1, 3] (see Fig. 1 left) and InAsSb nBn detectors [4] (see Fig. 1 right). In the analysis we will assess the performance of the PT structures by computing the reflectance (see Fig. 2), quantum efficiency and crosstalk of these structures. To simulate the performance of these devices we first solve the electromagnetic problem using the finite-difference time-domain method (FDTD) which yields the optical generation rate in the pillars. We incorporate this optical generation rate into the finite element method (FEM) to perform the drift-diffusion analysis by simultaneously solving the carrier continuity and Poisson equations on a three-dimensional finite element grid. A detailed description of the modeling techniques is outlines in [5].

Abstract compiled from material that has previously been approved for public release by the responsible authorities.

References

[1] C. A. Keasler and E. Bellotti, *Appl. Phys. Lett.* **99**, 091109 (2011).

[2] B. D. MacLeod and D. S. Hobbs, *Proc. SPIE* **6940**,69400Y2008

[3] J. Schuster and E. Bellotti, *Opt. Express* **21**,14712–147272013

[4] A. I. D'Souza, E. Robinson, A. C. Ionescu, D. Okerlund, T. J. de Lyon, H. Sharifi, M. Roebuck, D. Yap, R. D. Rajavel, N. Dhar, P. S. Wijewarnasuriya, and C. Grein, *J. Electron. Mater.* **41**,2671–26782012

[5] J. Schuster, B. Pinkie, S. Tobin, C. Keasler, D. D'Orsogna, and E. Bellotti, *IEEE J. Select. Topics Quantum Electron.* **19**,38004152013
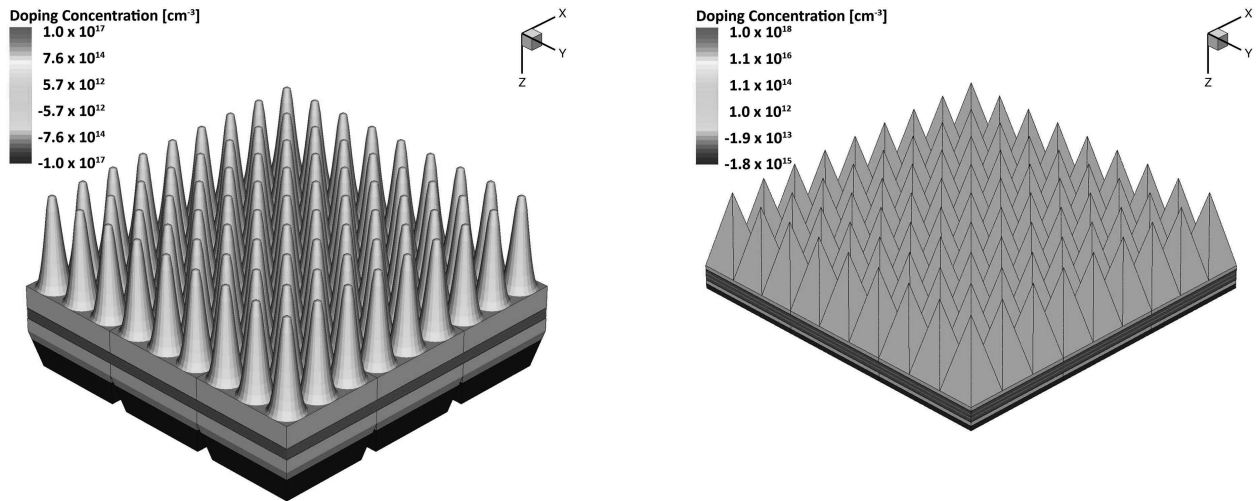
Figure 1: Left: Geometrical representation of HgCdTe photodiode array incorporating a periodic lattice of pillars. Right: Geometrical representation of InAsSb nBn array incorporating a periodic lattice of pyramids.
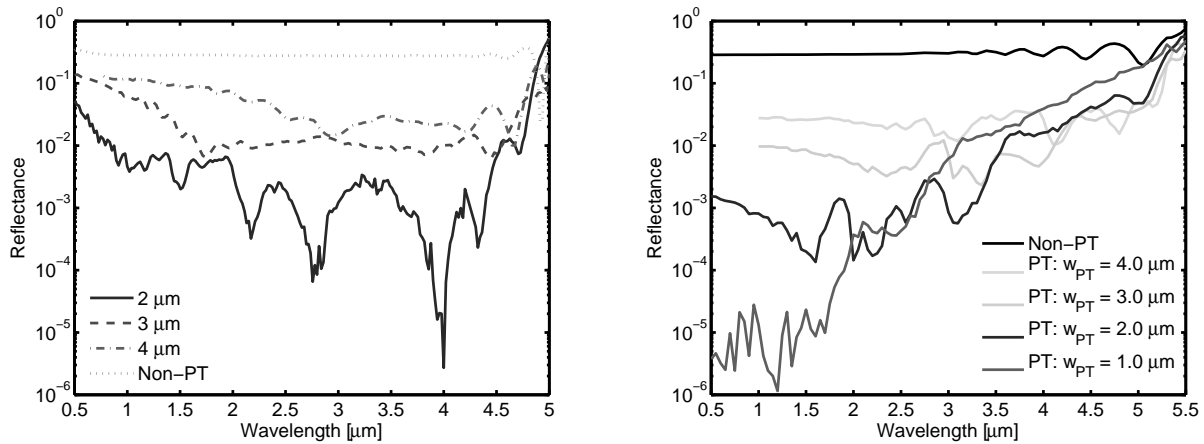

Figure 2: Left: Calculated reflectance spectra for Fig. 1 (left) with lattice periods (pillar base diameter) ranging from $2-4\,\mu$m (figure coutesry of Dr. Craig Keasler [1]). Right: Calculated reflectance spectra for Fig. 1 (right) with lattice periods (pyramid base length) ranging from $1-4\,\mu$m.

Mid-Wave and Long-Wave Infrared cut-off wavelengths HgCdTe FPA based on P on N technology at Sofradir and DEFIR : HOT and small pitch developments

Alexandre Kerlain (a), Florent Rochette (b), Laurent Rubaldo (a), Nicolas Péré-Laperne (a), Loïc Dargent (a), Christine Cassillo (a), Rachid Taalat (a) Laurent Mollard (b)

SOFRADIR, Avenue de la Vauve - CS20018 91127 PALAISEAU, France

(b) Univ. Grenoble Alpes, CEA, LETI, MINATEC campus,

F-38054 Grenoble, France

Abstract : In this paper we report recent results on P on N HgCdTe developed at SOFRADIR and DEFIR laboratory focusing on HOT applications and pitch size reduction.

Key words: MWIR, LWIR, HgCdTe, P on N

1. INTRODUCTION

Today IR technologies are facing two main challenges: increasing operating temperature (for SWAP applications[1]) and reducing the pixel pitch[2].

Increasing operating temperature:

Sofradir legacy technology is based on planar N/P photodiode with V_{Hg} P doped LPE HgCdTe, it has demonstrated its ultimate performances in term of operating temperature[3]. In order to respond to high operating temperature (HOT) challenges, extrinsic planar technology using Indium N-type doped LPE with As P+ implantation has been developed in the DEFIR joint laboratory (CEA-LETI / SOFRADIR). This technology is now currently in production in Sofradir for LWIR band (640x512 15um pitch). Up to 110K operation has been demonstrated for λ_c = 9µm@80K. MWIR band using this technology has demonstrated performances up to 150K at F/2[1]. Red band (λ_c = 5.2 µm) has been first developed. Thanks to HgCdTe tunable bandgap capability, there is a real interest in going into the blue band (λ_c = 4.2 µm). A

significant reduction in dark current (I_{dark}) compensates the signal loss[4]. We present

in this paper first results in dark current comparing blue and red bands in HgCdTe.

Pixel pitch reduction:

Sofradir has recently demonstrated 10um pitch FPA up to 110K using legacy

technology[2]. We present here recent development within DEFIR Laboratory,

concerning small pitches in planar P on N technologies in MWIR and LWIR bands.

2. HgCdTe HOT technologies

In the case of diffusion limited dark current with significantly high lifetime (i.e.

diffusion length > thickness of the absorbing layer) the expression of dark current can

be expressed as $Jsat=q.n_i^2.e/(N_D.Tau)$ (eq 1) with $ni \sim exp(-Eg(T)/kT)$ (eq 2).

In the case of Auger 1 lifetime limited diffusion current, to minimize the dark current,

the designer must choose a relatively low doping level (closed to 1.10^{15} cm^{-3} or less)

and expect a Auger 1 lifetime of few µs. Lower doping may be more difficult to control

and performances may be limited *in fine* by SRH lifetime.

Teledyne P on N DLPH structure has a doping concentration from mid 10^{14} cm^{-3} to

1.10^{15} cm^{-3} associated with a thickness equal to the cut-off wavelength. Best diodes

results are corresponding to rule07 behavior[5].

N on P extrinsic technology can theoretically have the same dark current with higher

N_D. As underlined in recent papers Rule07 is still today the reference in terms of best

IR detectors I_{dark} performances even with extrinsic n/p technologies[6].

The P on N technology at Sofradir is based on Indium N-type doped HgCdTe LPE on

CZT substrate. P+ planar diodes are made by Arsenic implantation. Indium doping

concentration varies from 1 to 5.10^{15} at/cm². Figure 1 shows I_{dark} results obtained on

5.2µm@80K and 4.2µm@80K 15µm pitch FPAs. Dark current is compared with a

diffusion limited modeling (equation 1) and Rule07. We show that dark current follows

diffusion trend with lifetime compatible with Auger process (Tau > 2µs with N_D>1.10^{15} at/cm²) for both bands.

3. P ON N TECHNOLOGY PITCH REDUCTION

Defir is the joint laboratory between CEA-LETI and SOFRADIR. One of the aim of the laboratory is to optimize p-on-n photodiodes. Pitch reduction is a real challenge in terms of performances and process[5]. In order to evaluate our planar *p-on-n* technology for pitches smaller than 15µm, we have fabricated and characterized small arrays of detectors with pitches from 15µm to 5µm both in MWIR (cutoff wavelength of 5.3µm at 80K) and LWIR (cutoff wavelength of 9µm at 80K). Dark current in LWIR band were measured and compared to rule07.

Figure 2 shows I(V) characteristics for confined diodes in LWIR band from 15µm down to 5µm pixel pitch under photonic flux. The reduction in photonic current corresponds to the pitch reduction, a similar BTB tunneling behavior is observed with no pitch dependence.

Figure 3 compares measurements with Rule07, there is no departure from Auger compatible diffusion trend down to 8µm pitch diodes. Diodes with pixel pitch lower than 8µm have not been measured here. These results show the good behavior of our technology to the small pixel pitches with diffusion limited currents on Rule07 down to 70K.

4. FIGURES
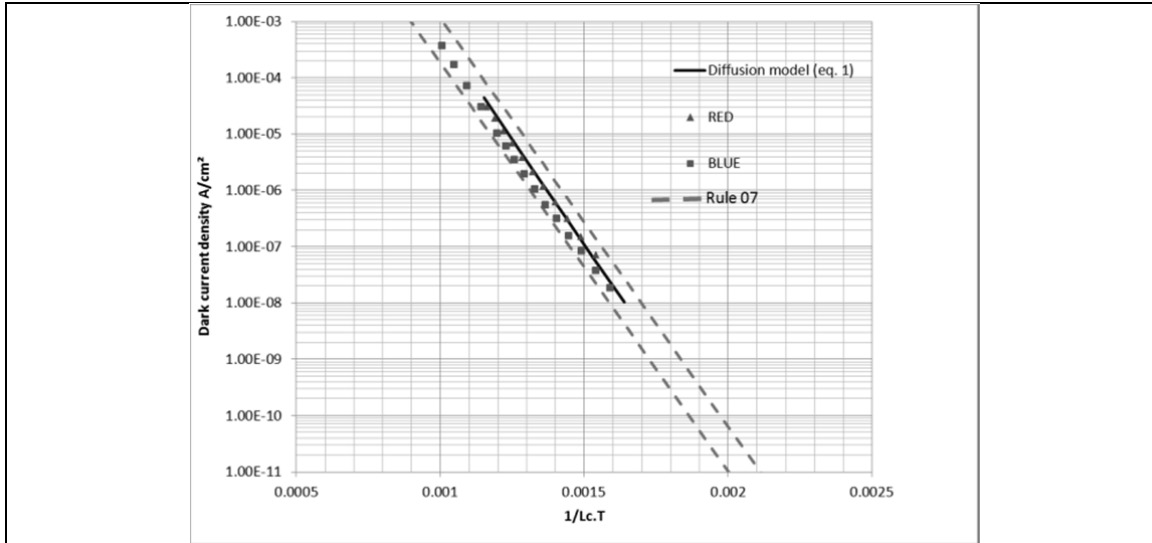
Figure 1 : Dark current density in MWIR bands (red and blue) compared to Rule07
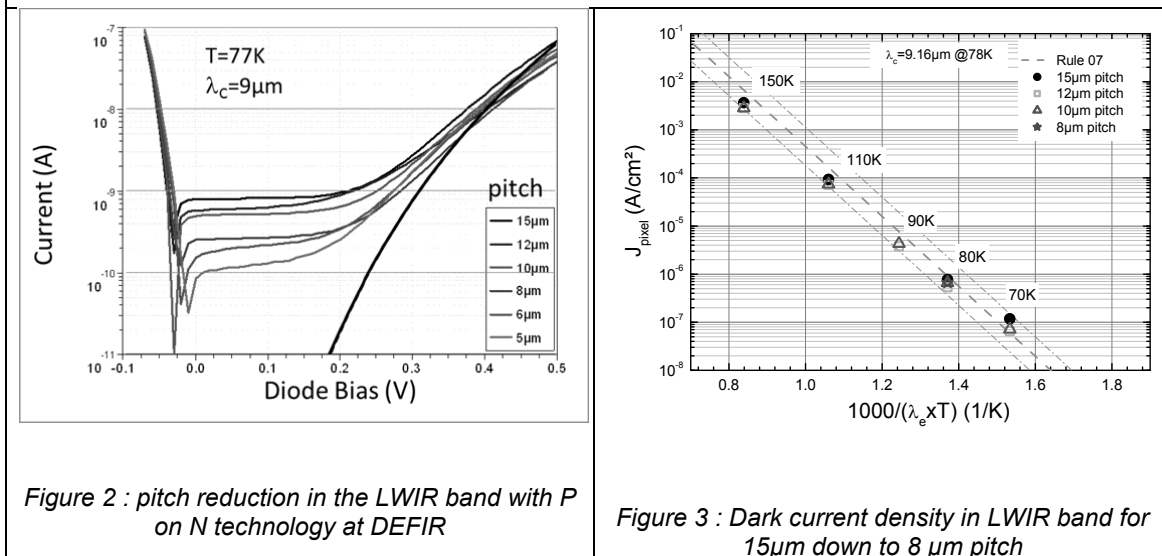

Figure 2 : pitch reduction in the LWIR band with P on N technology at DEFIR

Figure 3 : Dark current density in LWIR band for 15μm down to 8 μm pitch

5. REFERENCES

[1] Alain Manissadjian et Al, Proc. SPIE 8353, Infrared Technology and Applications XXXVIII, 835334 (31 May 2012)

[2] Y. Reibel et Al , Proc. SPIE 9070, Infrared Technology and Applications XL, 907034 (24 June 2014)

[3] Xavier Brenière; Laurent Rubaldo; Frederic Dupont
Proc. SPIE 9070, Infrared Technology and Applications XL, 90702W (24 June 2014)

[4] Y. Reibel et Al,; Proc. SPIE 8896, Electro-Optical and Infrared Systems: Technology and Applications X, 88960B (25 October 2013)

[5] W. E. Tennant et Al, Journal of Electronic Materials August 2014, Volume 43, Issue 8, pp 3041-3046,

[6] W. Schirmacher, R. Wollrab, H. Lutz, T. Schallenberg, J. Wendler, J. Ziegler, Journal of Electronic Materials August 2014, Volume 43, Issue 8, pp 2778-2782

Invited Paper: Advances in M/L Dual-Color Focal-Plane Technology

D. Lofgreen, W. Radford, C. Rabkin
Raytheon Vision Systems, Goleta, CA, USA

As 3rd Generation dual-color focal plane arrays (FPAs) mature into production, there is a continued push to drive cost down. Yield improvements, yield stabilization, and wafer size help to drive down the cost of the FPA. One must be mindful when scaling wafer size to maintain current yields and look for opportunities to stabilize them given the reality that wafer volume may decrease as wafer size increases. In this invited talk, we will discuss the yield limitations and the recent results of scaling dual-color technology to larger substrates. Molecular beam epitaxy (MBE) yield will be shown as it pertains to uniformity challenges while scaling substrate size. Processing challenges as well as FPA test results will be discussed as well.